Next-generation oligonucleotide-conjugates for enhanced potency and versatile functionality

Disha Kashyap
Exeter College
University of Oxford

A thesis submitted for the *Degree of Doctor of Philosophy*

Michaelmas 2025

Declaration

I declare that the work presented in this thesis is my own, unless otherwise stated in the Results and Methods, such as when collaborators contributed to experiments or analysis. This thesis has not been submitted, either partially or in full, for another qualification of this University, or for a qualification at any other institution.

Contributions by collaborators:

Chapter 2:

Microscopy data for the sub-cellular localisation of (+)-JQ1-ASO conjugates was generated by Martina Caddedu, at MRC NATA. Catherine Charhour, in the Milne Lab, processed the RNA-seq data with the Seqnado pipeline. This pipeline was developed by Catherine Chahrour and Alastair Smith, Milne lab.

Chapter 5:

Molecular modelling for the generation of the OligoPROTAC-BRD4-VHL complex was carried about Prof. Shozeb Haider, UCL Chemistry.

This work has resulted in the following publications:

- **Kashyap, D.**; Booth, M. Nucleic Acid Conjugates: Unlocking Therapeutic Potential. *ACS Bio & Med Chem Au, 2024*, doi: 10.1021/acsbiomedchemau.4c00092.
- **Kashyap, D.**; Caddedu, M; Oliver, P; Milne, T.; Booth, M. Harnessing BET-bromodomain assisted nuclear import for targeted subcellular localization and enhanced efficacy of antisense oligonucleotides. *Journal of the American Chemical Society, 2025*, doi:10.1021/jacs.5c09544.

◇ **Kashyap, D.**; Milne, T.; Booth, M. Engineering antisense oligonucleotides for targeted mRNA degradation through lysosomal trafficking. *Chemical Science, 2025*, doi:10.1039/D5SC03751D.

◇ **Kashyap, D.**; Haider, S; Milne, T.; Booth, M. DNA-Programmable Protein Degradation: Dynamic Control of PROTAC Activity via DNA Hybridization and Strand Displacement. *JACS Au, 2025*, doi:10.1021/jacsau.5c00422

Disha Kashyap 26 September 2025

Signature *Date*

Abstract

Nucleic acids are powerful biopolymers. As therapeutics, they enable interventions at various stages of gene expression through Watson-Crick base pairing, while as polymers they allow programmability, stimuli responsiveness, and incorporation of diverse functionalities. Covalent modifications with small molecules or ligands can further expand therapeutic potential. This DPhil research aimed to develop innovative strategies for targeted mRNA and protein degradation using such oligonucleotide conjugates — exploring new designs to unlock biological functionality and advance molecular medicine.

The thesis is divided into two parts. *Part I* focused on the development of antisense oligonucleotide (ASO) conjugates for targeted sub-cellular nuclear localisation **(Chapter 2)** and for establishing new mechanisms of RNA degradation **(Chapters 3, 4)**.

In **Chapter 2**, ASOs were linked to (+)-JQ1, a BET bromodomain ligand that promotes nuclear import. These conjugates enhanced splice-switching and mRNA knockdown across diverse targets and backbone chemistries. Notably, (+)-JQ1-Oblimersen, a late-stage clinical ASO, showed improved efficacy in an acute myeloid leukemia model.

Chapters 3 and **4** focused on attempts to optimize ASOs for enhanced cytoplasmic activity. **Chapter 3** explored coupling ASOs to an RNase L–recruiting ligand for

cytoplasmic mRNA degradation. This RNase L-recruitment approach for mRNA degradation also involved the optimisation of an ASO sequence for targeting MLL-AF4 fusion leukemias. **Chapter 4** aimed at the development of LyTONs (lysosomal trafficking antisense oligonucleotides) by conjugating ASOs to an autophagosome-tethering compound. LyTONs were shown to achieve potent lysosome-dependent knockdown of Menin (*MEN-1*) mRNA, an important leukemia target, and boost the activity of conventional gapmers.

Together, these strategies demonstrated how chemical conjugation expands ASO activity and mechanism, offering opportunities to target otherwise inaccessible transcripts.

Part II aimed at the development of Oligonucleotide-linked proteolysis targeted chimeras (OligoPROTACs) for oligonucleotide-guided protein degradation. Classical PROTACs, while powerful, suffer from off-target effects and limited control. **Chapter 5** presents OligoPROTACs: hybridisation-assembled DNA scaffolds that configure PROTAC warheads in space for distance-dependent degradation. Crucially, this system has been engineered to contain a reversible off-switch for activity — achieved via toehold-mediated strand displacement. This first demonstration of programmable, controllable PROTACs highlights the potential of nucleic acid conjugates to enhance the precision and safety of targeted protein degradation therapies.

Acknowledgements

First and foremost, I would like to thank my supervisors, Mike and Tom. You have both been incredible mentors, generous with your time, encouragement, and wisdom. From our many discussions, whether deeply scientific or simply supportive, I always came away reassured, motivated, and full of ideas. You both deepened my appreciation for nucleic acids and transcription, and for the beauty that lies where chemistry meets molecular biology.

I am also indebted to the Booth and Milne labs. Ellen, thank you for your steady warmth and kindness, and for making me feel so supported throughout. Hannah, Alex, Charlie, Ina, Charlotte, Kia and Chelsea — thank you for sharing your excellent science and company. From the Milne lab, I am grateful to Vassi, Alastair, and Nick, for helping this organic chemist find her feet in molecular biology, and to Catherine, for her brilliant bioinformatics and solid life advice. Nicole, Lucia, Ana, and Gianna — thank you for your help, ideas, and for always listening.

A special thank you to the CJS group, who never let me face organic chemistry alone. Christine, Siddhant, Sakshi, Zhuxin, Damon, and Justin — your kindess and readiness to help never went unnoticed. Thanks also to the Bayley and Qing labs, especially Duhan, Zhong, and Lemuel, for the stimulating discussions and for making the Chemistry Research Lab a brighter place, and to Antoine and Alistair from the Conway lab, whose company made even troubleshooting enjoyable. A big

thank you also to my CDT programme director and manager, Angie and Tracey — thank you for believing in me and supporting me through it all.

Outside the lab, love and support made this work possible. Gregory, thank you for being my constant—your unconditional love and support have held me firm and carried me forward. Riccardo, thank you for being my other constant: for reminding me that even when I hate the science, I actually love it. Thank you both for celebrating the highs with me and standing by me through the lows. Ada, thank you for always dancing beside me, and lifting me up when I needed it most. Caroline, thank you for your special mix of laughter, support, and glitter. Gavin, thank you for your warmth and for the music that has carried me through many phases of this journey. Arunima and Ryan, thank you for your kindness and keeping things in perspective. To my lovely flatmates, Ludovico, Liam, Noelia, and Fien, thank you for creating a home away from home, filled with joy and laughter. And to more spectacular people who have made Oxford unforgettable: Nikhil (a true gem and very rare find in my last year); Meghana, Shanthi, Carol (a sisterhood that has been my strength since my first year); Amir, Chris, Julian; thank you all.

Finally, I would like to thank my family, my ultimate foundation: to my brilliant brother, Adhiraj, for constantly inspiring me to be better; to my father, Mangesh, whose quiet strength, humor, and wisdom keep us all going; to my mother, Anjana — my light, my strength, my greatest role model, and the truest embodiment of love, selflessness, and utter grace; this thesis is dedicated to you.

List of abbreviations

2′-5′ — 2′ to 5′-linked oligoadenylate

2′-MOE — 2′-O-Methoxyethyl

2′-OMe — 2′-O-Methyl

AA-tRNA — Aminoacyl-Transfer RNA

AF4 — ALL1-fused gene from chromosome 4

Ago2 — Argonaute 2 protein

ALL — Acute Lymphoblastic Leukemia

ALAS1 — 5-Aminolevulinic Acid Synthase 1

AML — Acute Myeloid Leukemia

AMV — Amuvuttra (drug context, keep only if needed)

APP — Amyloid Precursor Protein

apoB-100 — Apolipoprotein B-100

apoCIII — Apolipoprotein C-III

ASCVD — Atherosclerotic Cardiovascular Disease

ASGPR — Asialoglycoprotein Receptor

ASO — Antisense Oligonucleotide

AOC — Antibody-Oligonucleotide Conjugate

ATP — Adenosine Triphosphate

ATTEC — Autophagosome tethering compound

AUC — Area Under Curve

AUG — Start Codon

Bafa — Bafilomycin

BCA — Bicinchoninic Acid Assay

BBB — Blood-Brain Barrier

BC-DNA — Bicyclo-DNA

BET — Bromodomain and Extra-Terminal domain

BRD4 — Bromodomain-containing protein 4

CB1 — Cannabinoid Receptor 1

CD — Cluster of Differentiation

Chol — Cholesterol

CLIPTAC — Click-formed Proteolysis Targeting Chimera

CMV — Cytomegalovirus

COF — Cofactor

CPP — Cell-Penetrating Peptide

CTCF — CCCTC-binding Factor

CTD — C-Terminal Domain

DCA — Docosanoic Acid

DMD — Duchenne Muscular Dystrophy

DNA — Deoxyribonucleic Acid

DNA-PAINT — DNA Points Accumulation for Imaging in Nanoscale Topography

dsDNA — Double-Stranded DNA

DTT — Dithiothreitol

eEFs — Eukaryotic Elongation Factors

eIFs — Eukaryotic Initiation Factors

eRFs — Eukaryotic Release Factors

EPA — Eicosapentaenoic Acid

ETF — Elongation Transcription Factor

FCS — Familial Chylomicronemia Syndrome

Fc — Fragment Crystallizable Region

FRET — Fluorescence Resonance Energy Transfer

GalNAc — N-Acetylgalactosamine

G3139 (Oblimersen) — Clinical ASO targeting BCL-2

G4 — G-quadruplex

GTF — General Transcription Factor

HAO1 — Hydroxyacid Oxidase 1 (glycolate oxidase)

HeFH — Heterozygous Familial Hypercholesterolemia

HDO — Heteroduplex Oligonucleotide

HoFH — Homozygous Familial Hypercholesterolemia

HSA — Human Serum Albumin

hATTR — Hereditary Transthyretin-mediated Amyloidosis

Inr — Initiator Element

IRE — Iron-Responsive Element

IRES — Internal Ribosome Entry Site

IRP — Iron Regulatory Protein

IVT — In vitro transcription

LNA — Locked Nucleic Acid

m6A — N6-Methyladenosine

m7G — 7-Methylguanosine

miRNA — MicroRNA

MLL — Mixed Lineage Leukemia

MLL-AF4 — Fusion of MLL and AF4 Genes

MLL-r — MLL-rearranged Leukemia

mRNA — Messenger RNA

mTOR — Mechanistic Target of Rapamycin

NELF — Negative Elongation Factor

NIR — Near-Infrared

nt — Nucleotide

OAS — 2′-5′ Oligoadenylate Synthetase

PABPC — Cytoplasmic Poly(A)-Binding Protein

PABPN — Nuclear Poly(A)-Binding Protein

PBMC — Peripheral Blood Mononuclear Cell

PCSK9 — Proprotein Convertase Subtilisin/Kexin Type 9

PEG — Polyethylene Glycol

PFP — Pentafluorophenyl

PIC — Pre-Initiation Complex

PMO — Phosphorodiamidate Morpholino Oligomer

PNAs — Peptide Nucleic Acids

PO — Phosphodiester

PROTAC — Proteolysis Targeting Chimera

PS — Phosphorothioate

PMSA — Prostate-Specific Membrane Antigen

PTM — Post-Translational Modification

qPCR — Quantitative PCR

RBP — RNA-Binding Protein

RISC — RNA-Induced Silencing Complex

RNA — Ribonucleic Acid

RNAi — RNA Interference

RNase H — Ribonuclease H

RNase L — Ribonuclease L

RNP — Ribonucleoprotein

RSV — Respiratory Syncytial Virus

SAR — Structure-Activity Relationship

SELEX — Systematic Evolution of Ligands by Exponential Enrichment

SEM — Human leukemia cell line with MLL-AF4 translocation

siMA6 — A specific siRNA targeting MLL-AF4

siRNA — Small Interfering RNA

SMA — Spinal Muscular Atrophy

SNA — Spherical Nucleic Acid

SPAAC — Strain-Promoted Azide-Alkyne Cycloaddition

SPR — Surface Plasmon Resonance

SSO — Splice-Switching Oligonucleotide

ssDNA — Single-Stranded DNA

TAD — Topologically Associating Domain

TFIIB (BRE) — TFIIB Recognition Element

TLR9 — Toll-like Receptor 9

TTR — Transthyretin

UPS — Ubiquitin-Proteasome System

UTR — Untranslated Region

VEGF — Vascular Endothelial Growth Factor

VH032 — VHL E3 Ligase Ligand

VHL — Von Hippel–Lindau Protein

Z-DNA — Left-Handed DNA Helix Form

μ**M** — Micromolar

2D — Two-Dimensional

3D — Three-Dimensional

Contents

List of Figures

List of Tables

Part I

Chapter 1

Introduction

1.1 Nucleic acids structure and function

Nucleic acids, 2′-deoxyribonucleic acid (DNA), and ribonucleic acid (RNA) are fundamental biopolymers consisting of repeating monomeric motifs. Encoded within their sequences and chemical structure is the molecular information that directs and regulates all of biology.

The discovery of DNA as the hereditary material was built on decades of foundational work. In 1869, Friedrich Miescher first identified a phosphorus-rich substance from cell nuclei, which he named "nuclein"[1]. Early in the 20th century, Phoebus Levene elucidated the basic chemical components of DNA, including the sugar, phosphate, and nitrogenous bases[2]. In 1944, Avery, MacLeod, and McCarty demonstrated that DNA, and not protein, was the biomolecule that carried heredity information[3]. Building on this, Rosalind Franklin and Raymond Gosling's X-ray diffraction studies revealed the helical structure of DNA, providing crucial insight into its molecular structure[4]. In 1953, James Watson and Francis Crick integrated

these findings to propose the double helix model[5], explaining how DNA could store and replicate genetic information—laying the foundation for modern molecular biology.

1.1.1 Chemical structure

Nucleotides

The biological roles of DNA and RNA are rooted in their chemical structure. The most basic unit of nucleic acids is the nucleotide[2]. Each nucleotide consists of three components (Figure 1.1):

- ◇ A Nitrogenous Base: Either a purine (adenine [A], guanine [G]) or a pyrimidine (cytosine [C], thymine [T] in DNA, uracil [U] in RNA)
- ◇ A Pentose Sugar: Deoxyribose in DNA and ribose in RNA, differing by the absence (DNA) or presence (RNA) of a 2′-hydroxyl group
- ◇ A Phosphate Group: Links adjacent nucleotides through phosphodiester bonds between the 3′- hydroxyl and 5′- phosphate of neighbouring sugars, creating a sugar-phosphate backbone

The phosphodiester linkage forms the covalent backbone of nucleic acids, providing both structural integrity and resistance to cleavage under physiological conditions[6]. Beyond the backbone, the 3D conformation of nucleic acids is also heavily influenced by the configuration of individual nucleosides. A key aspect of this configuration

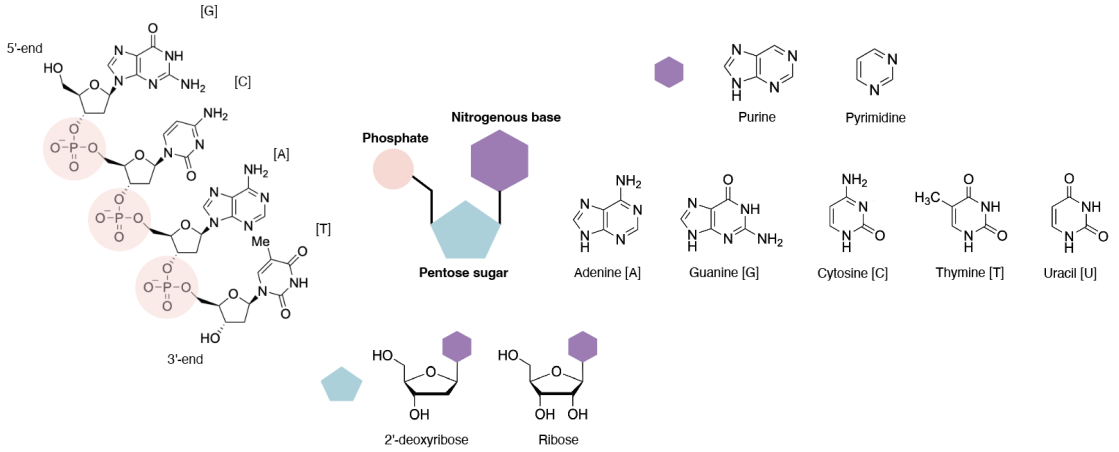

Figure 1.1: Tripartite nucleic acid structure: Nitrogenous bases [A], [T], [G], [C] for DNA and [U] in place of [T] for RNA; pentose sugar 2′- deoxyribose for DNA and ribose for RNA; phosphate group for nucleic acid backbone linked via covalent phosphodiester bonds.

is the anomeric form of the glycosidic bond: natural nucleic acids overwhelmingly favor the β-anomer over the α-anomer, due to its stereochemical compatibility with enzymes and stable duplex formation (Figure 1.2a)[7,8].

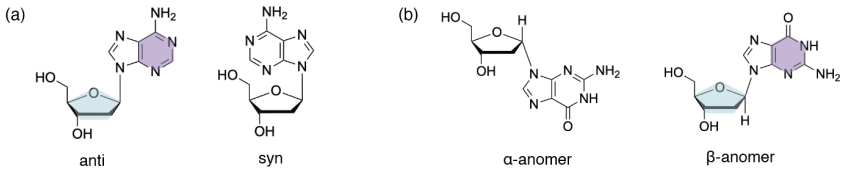

Figure 1.2: (a) Syn-, anti- configurations of the nitrogenous base relative to the sugar; (b) α-, β-anomeric forms of the glycosidic bond between nitrogenous base and pentose sugar.

The orientation of the nitrogenous base relative to the sugar, described as syn or anti, plays a pivotal role in base stacking, geometry, and secondary structure formation (Figure 1.2b). While purines can adopt both conformations, the anti conformation is typically predominant in B-form and A-form RNA (see section on

Tertiary Structure), positioning the base favorably for canonical hydrogen bonding[9][10]. Conversely, syn conformations appear in specific contexts such as Z-DNA and modified nucleosides, highlighting their structural and regulatory significance in chromatin biology and therapeutic oligonucleotide design[11][12].

This tripartite structure endows nucleic acids with directionality (5′ to 3′) and chemical polarity (5′-phosphate and 3′-hydroxyl), which are essential for replication (DNA copying) and transcription (RNA synthesis, see subsection 1.1.2). The nitrogenous bases project inward, allowing for sequence-specific interactions that form the basis of information storage and genetic regulation.

One of the most defining structural features of nucleic acid structure is base pairing, governed by hydrogen bonding. Watson–Crick base pairing[5] refers to a three-dimensional (3D) secondary structure assembled through specific hydrogen bond geometries between nitrogenous bases (Figure 1.3a).

- ◇ Adenine [A] pairs with Thymine [T] in DNA (or Uracil [U] in RNA) through two hydrogen bonds.
- ◇ Guanine [G] pairs with Cytosine [C] via three hydrogen bonds.

These canonical pairs support the antiparallel alignment of nucleic acid strands. The base pairings are pseudosymmetric, ie, overlay of A-T base pair on any other base pair (T-A, G-C or C-G) show aligned phosphodiester backbones (Figure 1.3b).

Furthermore, π –π stacking between adjacent bases contributes significantly to the thermodynamic stability of the DNA and RNA duplexes. Together, these features are critical for high-fidelity base recognition during DNA replication and RNA transcription (see subsection 1.1.2).

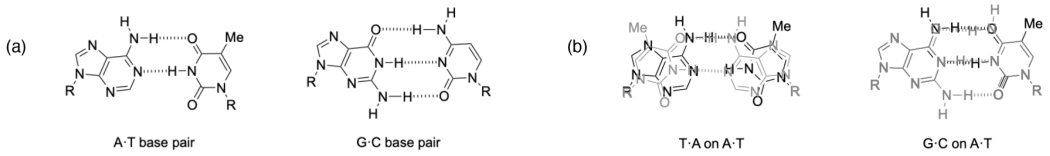

Figure 1.3: (a) Hydrogen-bonding patterns between base pairs, [A]-[T] and [G]-[C]. (b) Structures of the T · A base pair overlaid on the A · T base pair, and the G · C base pair overlaid on the A · T base pair.

Secondary Structure

The linear nucleotide sequence (primary structure) folds into defined local geometries that constitute the secondary structure of nucleic acids. These structures arise from intramolecular or intermolecular base pairing and stacking interactions, typically governed by Watson–Crick and non-canonical base pairs. Here, these secondary structures are discussed in the context of the biological cell.

In DNA, secondary structure is largely defined by the formation of the double helix. In contrast, RNA exhibits a richer repertoire of structural motifs due to its single-stranded nature and 2′-hydroxyl group of the ribose. The 2′-hydroxyl-ribose facilitates tighter binding and more complex folding patterns[13,14] (Figure 1.4), as manifested in the following.

◇ Helices: Continuous stretches of base-paired nucleotides form double-stranded helices, typically adopting specific geometries in RNA as opposed to DNA[15].

◇ Hairpin Loops: Short sequences that fold back on themselves to form a stem-loop structure, stabilized by internal base pairing within the stem and unpaired bases in the loop[16].

◇ Bulges and Internal Loops: Mismatched or unpaired nucleotides interrupting helices introduce local flexibility and recognition sites for proteins or ligands[17].

◇ Pseudoknots: Higher-order motifs in which nucleotides in a loop base-pair with a complementary region outside the loop, contributing to structural stability and catalytic activity in functional RNAs[16][18].

These secondary structures serve as critical intermediates between the nucleotide sequence and complex tertiary folds. They play key roles in molecular recognition, catalysis, and the regulation of biological processes such as translation, RNA splicing, and degradation[17][14].

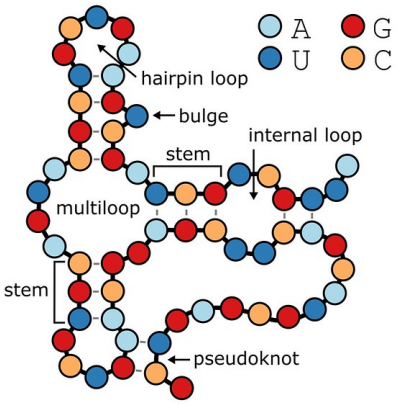

Figure 1.4: Various secondary structures formed in RNA via Watson-Crick base pairing. *Figure adapted from "bpRNA: large-scale automated annotation and analysis of RNA secondary structure" by Danaee et. al, under CC BY-SA 2.0.*

Tertiary Structure

The specificity of Watson–Crick pairing forms the double-stranded B-form DNA structure, its most physiologically predominant form, and also allows for the the formation of short duplexes in RNA. However, DNA can adopt alternate secondary structures depending on sequence composition, hydration state, and superhelical stress[19]. These forms expand the functional and structural versatility of the genome (Figure 1.5).

- ◇ B-form: The canonical right-handed helix, with ∼10.5 base pairs (bp) per turn—wide major and narrow minor grooves. B-DNA is the preferred conformation of DNA under physiological conditions; it is stabilised by regular Watson–Crick base pairing, strong π –π stacking interactions, electrostatic shielding of the phosphate backbone by cations, and extensive hydration of the grooves[5]. This geometry supports compact chromatin organization while allowing dynamic access for gene regulation, including transcription initiation, replication, and repair.

- ◇ A-form: A right-handed helix that is more compact and dehydrated than the B-form, typically seen in RNA-DNA hybrids or double-stranded RNA. The A-form has ∼11 bp per turn and a deep, narrow major groove with a shallow minor groove[20].

- ◇ Z-form: In contrast to the right-handed helices, the Z-form is a left-handed helical form, favored by alternating purine-pyrimidine (especially GC-rich) sequences[21]

under high salt concentrations or negative supercoiling. Its distinctive zigzag sugar-phosphate backbone distinguishes it from the smoother helices of the B- and A-form. Z-form transiently forms behind RNA polymerase, and may act as a regulatory element that supports transcriptional bursting for optimizing promoter-protein turnover[22].

The structural repertoire of nucleic acids extends beyond this. Nucleic acids often utilize non-Watson–Crick base pairing to form a rich array of higher-order structures—observed particularly in RNA but also in certain specialized DNA contexts. These interactions play pivotal roles in biological recognition, catalysis, and regulation.

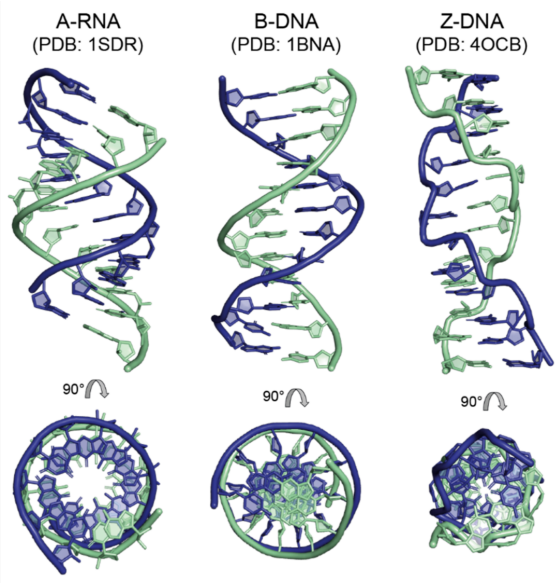

Figure 1.5: A-, B- and Z-forms of nucleic acid tertiary structure. *Figure adapted from "Symmetry in Nucleic-Acid Double Helices" by Heinamenn et. al., under CC BY license.*

Hoogsteen base pairing is a major alternative to the Watson–Crick scheme, named after Karst Hoogsteen, first described in 1959. In Hoogsteen geometry, the purine adopts a syn-conformation, allowing the hydrogen bond formation in an alternate geometry[23]. Hoogsteen interactions can coexist with canonical base pairs or substitute for them transiently, introducing conformational flexibility into duplex DNA[24]. Hoogsteen interactions have also been observed in

protein-bound DNA and damaged DNA[25].

Hoogsteen hydrogen bonding also underpins the formation of non-canonical higher-order DNA/RNA structures, such as:

◇ Triplex structures, where a third strand binds in the major groove of a duplex via Hoogsteen or reverse Hoogsteen pairing. These interactions form base triads such as T • A–T and C^+ • G–C, the latter requiring protonated cytosine under mildly acidic conditions[26]. Triplex DNA has been studied in the context of gene regulation, targeted gene inhibition, and antisense therapeutics[27] (Figure 1.6).

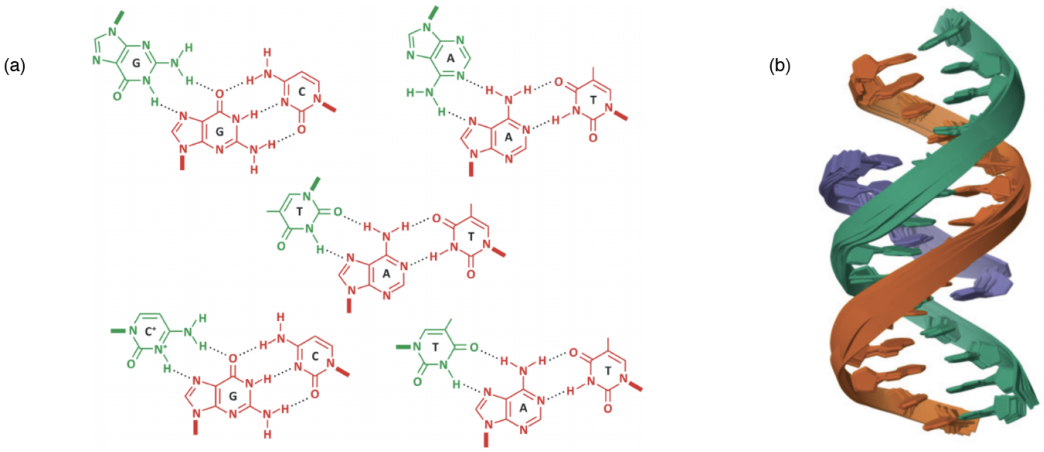

Figure 1.6: Triplex DNA formation and Hoogsteen base pairing. (a) Hydrogen-bonding patterns resulting in triplex DNA formation. Red represents Watson-Crick base pairing, green represents the Hoogsteen base pair. *Figure adapted from "Structures and stability of simple DNA repeats from bacteria" by Brazda et. al, under CC BY license*; (b) X-ray crystal structure of triplex DNA, PDB: 1WBG.

◇ G-quadruplexes (G4s) are formed by planar arrays of four guanine (G) bases interacting via Hoogsteen hydrogen bonds, stabilized by monovalent cations ($K^+ > Na^+ \gg Li^+$)[28]. Found in telomeres, oncogene promoters[29] (e.g., MYC, KRAS),

and untranslated regions (UTRs), G4s play key roles in transcriptional regulation, replication, and translation, and are being actively explored as therapeutic targets[30]. Their stability is highly sequence- and context-dependent, influenced by loop length, number of G-runs, and flanking sequences (Figure 1.7).

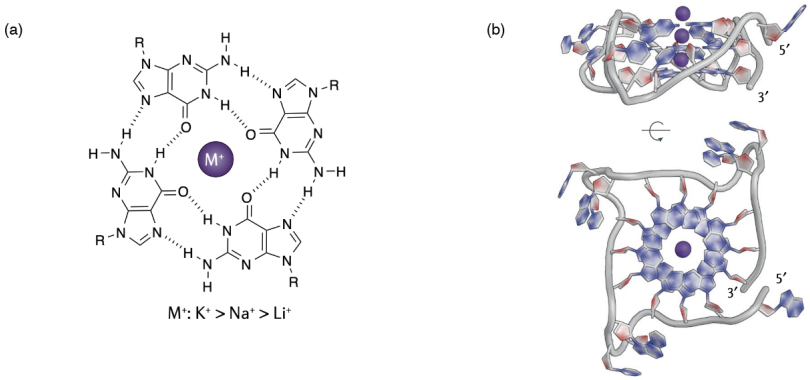

Figure 1.7: G-quadruplexes. (a) Guanine tetrad stabilized by Hoogsteen base-pairing and by cation (M+), preference for monovalent cations in the order of ($K^+ > Na^+ \gg Li^+$). b) X-ray crystal structure of G4 from a human telomere sequence, PDB: 1KF1. *Figure adapted from "The regulation and functions of DNA and RNA G-quadruplexes" by Varshney et. al, reproduced with permission from Springer Nature.*

In sum, DNA secondary structure extends far beyond the classic double helix. The interplay between Watson–Crick and Hoogsteen base pairing, along with the formation of triplexes and quadruplexes, reveals a rich conformational landscape that underlies the dynamic and functional versatility of nucleic acids.

1.1.2 Biological function

At the most fundamental molecular level, DNA is a linear sequence of nucleotides that comprises the genome. DNA serves not only as the long-term genetic storage

material but also as a highly organized regulatory landscape. It is the nucleotide sequence[31] and 3D architecture[32] that determines the functional output of genomes, guiding the synthesis of RNA and proteins, and directing the regulation of cellular processes.

Within the eukaryotic nucleus, genomic DNA is packaged into discrete, thread-like structures known as chromosomes[33]. Each chromosome consists of a single, continuous DNA molecule compacted by histones and other architectural proteins into higher-order chromatin (referred to as the quaternary structure of DNA). Chromatin is densely decorated with core histones, architectural proteins, and chromatin remodeling complexes. The fundamental unit of chromatin is the nucleosome, consisting of ∼147 base pairs of DNA wrapped around a histone octamer composed of two each of H2A, H2B, H3, and H4 (Figure 1.8).

These histone proteins act as scaffolds for the regulation of chromatin accessibility and influence the binding of transcription factors, chromatin remodelers, and structural proteins[34]. The N-terminal tails of histones undergo several chemical modifications such as methylation, acetylation, phosphorylation, and ubiquitination. These chemical marks play crucial roles in defining chromatin states: for example, H3K27ac and H3K4me3 are associated with active enhancers and promoters, respectively, whereas H3K9me3 and H3K27me3 mark transcriptionally repressed heterochromatin.

Chromatin fibers are also subject to active remodeling by ATP-dependent complexes and are constantly shaped by interactions with chromatin-binding proteins[35,36]. Among these, two of the most prominent are the chromosome cohesion factor cohesin and the CCCTC-binding factor (CTCF)—a sequence-specific DNA-binding protein initially identified at insulator elements[37]. Together, cohesin and CTCF play a central role in organizing the genome into topologically associating domains (TADs) and chromatin loops by mediating long-range DNA-DNA interactions[38]. These loops formed by CTCF binding sites are enriched at TAD boundaries. The deletion or inversion of these sites leads to the disruption of TAD structure and dysfunctional gene regulation[39,40,41].

Building upon this modular chromatin architecture, the spatial organization of the genome within the nucleus follows a highly ordered and dynamic architecture that plays a fundamental role in regulating genome function. Early structural studies revealed that transcriptionally active "euchromatin" and repressed "heterochromatin" are segregated into distinct nuclear compartments, demonstrating the presence of functional zoning within the eukaryotic nucleus[42,43]. In addition to this compartmentalization, the genome is further organized into TADs and chromatin loops, and genes are often positioned in preferential locations relative to the nuclear periphery or nuclear speckles[44,37]. The nucleus itself is also partitioned into discrete sub-nuclear bodies, including the nucleolus, Cajal bodies, and splicing speckles, which serve as hubs for specific molecular processes—composed of both proteins

and RNAs distributed in a non-random fashion[45,46].

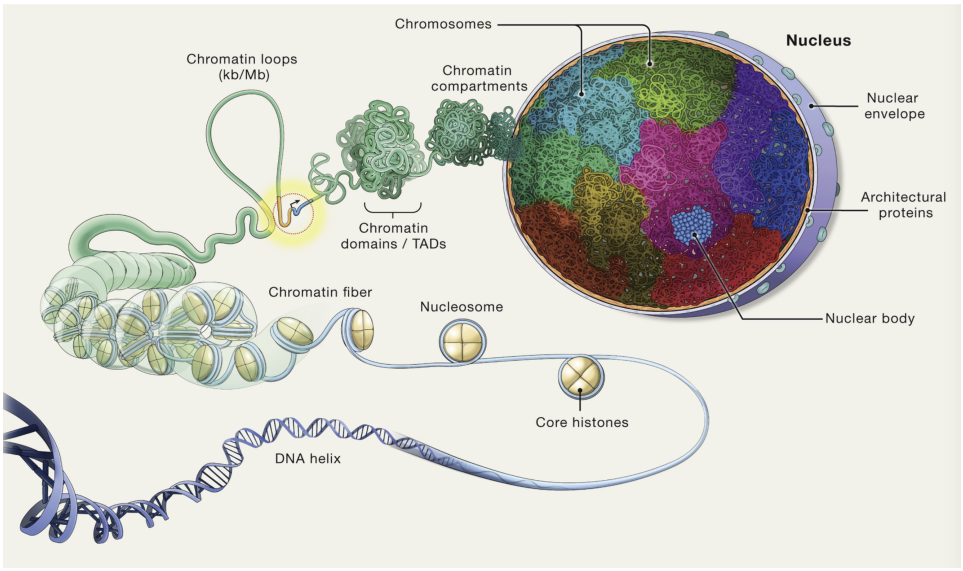

Figure 1.8: Genomes are organized at multiple levels. DNA is wrapped around the nucleosome, which is comprised of an octamer of core-histones, forming the chromatin fiber which folds into loops, often allowing upstream gene regulatory elements (yellow), such as enhancers, to come into the proximity of gene promoters (gold/blue) to control transcription (black arrow). This fiber then folds into TAD chromatin domains, which create chromatin compartments through association. The DNA of each chromosome occupies a specific volume, or chromosomal territory (multi-colored), within the cell nucleus. This results in non-random patterns of chromosome and genes. *Figure adapted from "The Self-Organizing Genome: Principles of Genome Architecture and Function" by Misteli et. al, reproduced with permission from Elsevier.*

Although these defined architectural patterns suggest a high degree of order, recent single-cell and live-cell imaging approaches have revealed substantial heterogeneity and variability in genome organization. For example, the two alleles of a given gene may occupy distinct spatial positions or exhibit different transcriptional states within the same nucleus. Similarly, many chromatin interactions detected in population-based assays occur with low frequency at the single cell level, and the

number and morphology of nuclear bodies fluctuate between individual cells[47,48,49]. This coexistence of order and variability suggests that genome organization is governed by self-organizing principles, where emergent properties arise from the collective behaviour of chromatin, regulatory proteins, and the nuclear environment[32].

Amidst this intricately regulated and dynamic chromatin landscape, genetic information encoded in DNA is interpreted and executed in biology through two fundamental processes: transcription and translation. These processes constitute the central dogma of molecular biology[5], converting the genetic code into active molecular processes. Together, transcription and translation drive gene expression, governing the synthesis of RNA and proteins—regulating every aspect of cellular development, differentiation, and physiological homeostasis.

Transcription

Transcription is the process by which genetic information encoded in DNA is copied into RNA. Transcription begins when the enzyme RNA polymerase binds to a promoter region upstream of a gene. In eukaryotes, this process is primarily mediated by RNA polymerase II, which transcribes all protein-coding genes and many non-coding RNAs[50]. The promoter contains core motifs such as the TATA box, initiator (Inr), and BRE (TFIIB recognition element), which facilitate the recruitment of the pre-initiation complex (PIC). While the TATA box is a well-characterized promoter element, many promoters are instead associated with GC-rich regions or other mo-

tifs, and the structural organization of these alternative promoter types remains less clearly defined[51].

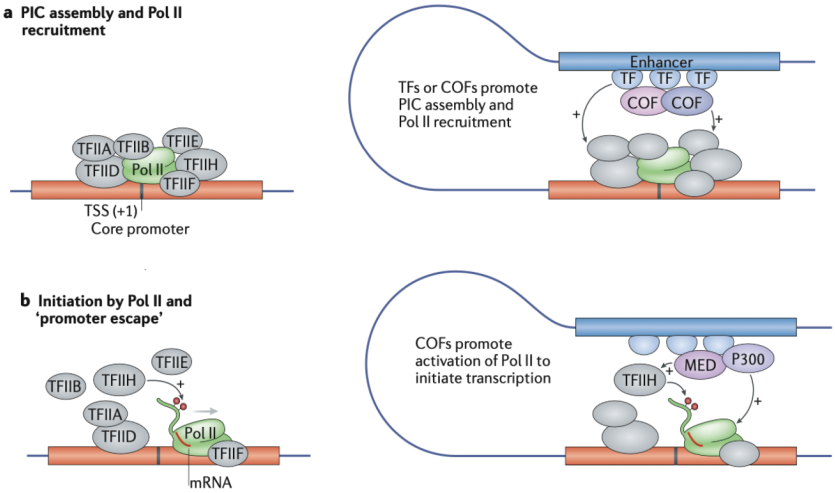

Figure 1.9: Functional mechanism of Transcription, part I.(a) PIC assembly and Pol II recruitment: Transcription begins with assembly of the PIC, including Pol II and GTFs. Enhancers aid this by recruiting transcription factors (TFs) and cofactors (COFs) that interact with GTFs or Pol II.; (b) Initiation and promoter escape: Pol II initiates transcription after DNA duplex melting at the transcription start site. TFIIH phosphorylates Pol II's CTD (Ser5/Ser7) to enable escape from the promoter. Enhancers facilitate this via recruiting COFs like Mediator and p300. *Figure adapted from "Eukaryotic core promoters and the functional basis of transcription initiation" by Haberle et. al, reproduced with permission from Springer Nature.*

Assembly of the PIC requires several general transcription factors (GTFs)—including TFIID, TFIIA, TFIIB, TFIIF, TFIIE, and TFIIH—which help position RNA polymerase II correctly, and unwind the DNA double helix to expose the template strand. Once correctly positioned, RNA polymerase initiates transcription by synthesizing a short RNA primer and escaping the promoter (Figure 1.9a).

After initiation, RNA polymerase II often pauses within 20–60 nucleotides (nts)

downstream of the transcription start site. This promoter-proximal pausing is regulated by Negative Elongation Factor (NELF) and DRB Sensitivity-Inducing Factor (DSIF) (Figure 1.9a). Release from pausing is driven by Positive Transcription Elongation Factor b (P-TEFb), which phosphorylates RNA polymerase and associated pausing factors, enabling the transition into productive elongation (Figure 1.10c)[52].

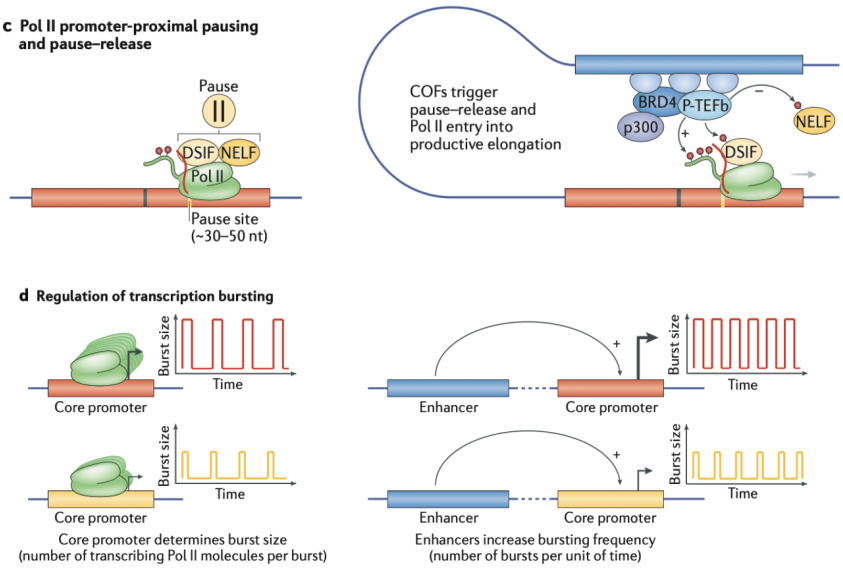

Figure 1.10: Functional mechanism of Transcription, part II. (c) Promoter-proximal pausing and release: Pol II pauses after early elongation, stabilized by DSIF and NELF. CDK9 (P-TEFb) phosphorylates these factors and Ser2 of Pol II CTD, enabling pause release. Enhancers promote this by recruiting CDK9, BRD4, or p300.; (d) Transcription bursting: Transcription occurs in bursts. Core promoters control burst size, while enhancers increase burst frequency. + denotes target activation and – denotes target inhibition. *Figure adapted from "Eukaryotic core promoters and the functional basis of transcription initiation" by Haberle et. al, reproduced with permission from Springer Nature.*

During elongation, RNA polymerase traverses the gene body, synthesizing a complementary RNA strand from the DNA template. The elongation complex includes

elongation factors that stabilize the RNA-DNA hybrid, maintain polymerase processivity, and coordinate with chromatin remodelers and histone-modifying enzymes to manage nucleosome barriers.

Transcriptional activity is tightly linked to the chromatin environment. Histone modifications, such as H3K4me3 at active promoters or H3K27ac at enhancers, serve as epigenetic marks that recruit or repel transcriptional machinery. Chromatin remodelers (for example, SWI/SNF) slide or evict nucleosomes to expose regulatory elements, while DNA methylation and repressive marks (for example, H3K9me3, H3K27me3) help silence transcription (Figure 1.10d)[34].

In addition, 3D genome architecture facilitates enhancer-promoter communication. Distant regulatory elements are brought into close spatial proximity with their target genes through chromatin looping, mediated by CTCF, cohesin, and other architectural proteins[53]. This spatial organization enables precise control of transcriptional responses to developmental cues, signaling pathways, and environmental stimuli. Once transcription is initiated within this three-dimensional regulatory landscape, the nascent RNA transcript undergoes co-transcriptional processing.
As transcription proceeds, the nascent RNA undergoes co-transcriptional processing to be converted into "mature mRNA" (Figure 1.11):

- $5'$ Capping: Addition of a 7-methylguanosine cap, (m^7G) that protects the transcript and facilitates nuclear export and translation.

◇ Splicing: Removal of introns and joining of exons by the spliceosome—this process enables multiple transcripts from a single gene.

◇ 3′ End Formation: Cleavage followed by poly-adenylation (poly(A)) tail addition, enhancing mRNA stability and enabling translation.

◇ RNA Editing and other related modifications: Includes A-to-I editing and N6-methyladenosine (m6A) modification[54].

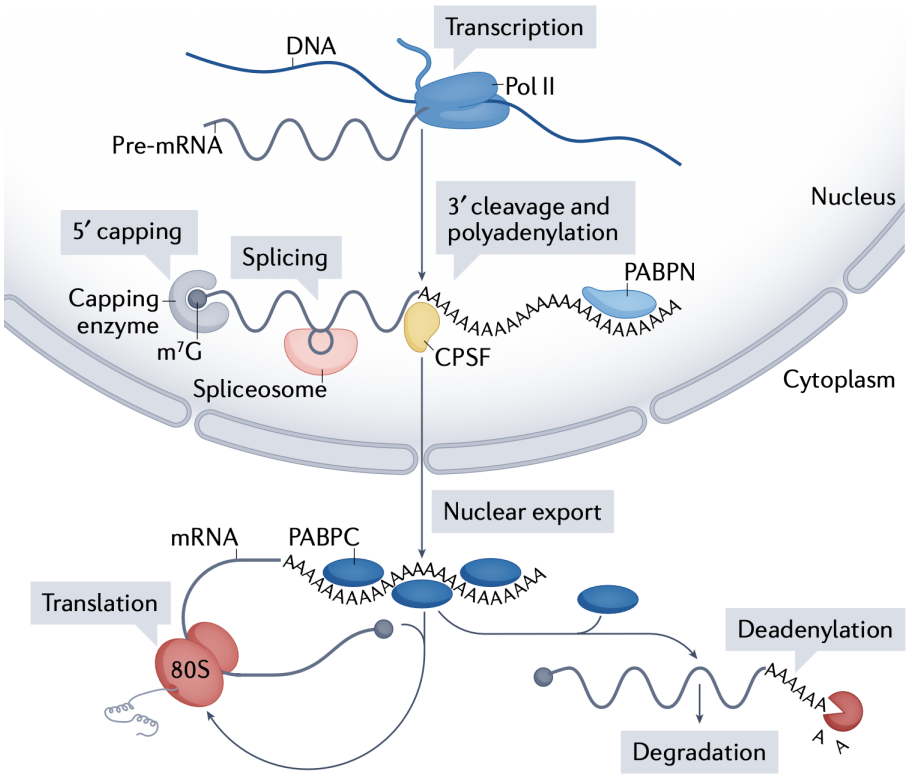

Figure 1.11: In the nucleus, pre-mRNAs are transcribed by RNA Pol II and undergo 5' capping with (m7G), splicing, and 3' cleavage with poly(A) tail addition. The nuclear poly(A)-binding protein (PABPN) regulates this process. In the cytoplasm, PABPC promotes translation and stability. Deadenylation leads to PABPC release and mRNA decay. *Figure adapted from "Roles of mRNA poly(A) tails in regulation of eukaryotic gene expression" by Passmore et al. Reproduced with permission from Springer Nature*

Translation

Translation is the process of decoding mRNA into a polypeptide chain, carried out by ribosomes. In eukaryotes, the ribosome consists of a 40S small subunit and a 60S large subunit. The subunits consist of rRNAs that form the structural and catalytic core, together with associated proteins that stabilize the complex and facilitate interactions with translation factors[55]. Translation occurs in three stages: initiation, elongation, and termination[56].

Translation initiation begins with the assembly of the pre-initiation complex, including eIFs (for example, elongation initiation factors such as eIF1, eIF2-GTP-tRNAi $^{\text{Met}}$, eIF3, eIF4F complex) and the 40S ribosomal subunit (Figure 1.12a). The 5′ cap structure is recognized by eIF4E, guiding the complex to the mRNA.

The ribosome scans the mRNA to find the start codon (AUG) within a Kozak consensus sequence. Once found, the 60S subunit joins to form the functional 80S ribosome and translational elongation begins. This cycle repeats for every codon. During the process of elongation (Figure 1.12a, b):

◇ Aminoacyl-transfer RNA (aa-tRNA) enters the A site.

◇ Peptide bond formation occurs in the P site.

◇ Ribosome translocates, moving tRNAs to P and E sites.

Termination occurs when a stop codon (UAA, UAG, UGA) enters the A site. Elongation release factors (eRF1, eRF3) mediate polypeptide release and disassembly of the ribosomal complex[57] (Figure 1.12a). Translation is tightly regulated by the following factors/processes:

- ◇ UTRs (untranslated regions) and RNA structure: Elements such as uORFs (upstream open reading frames) and IRESs (internal ribosome entry sites) regulate initiation efficiency.
- ◇ microRNAs: Inhibit translation or degrade mRNAs via RISC (RNA-induced silencing complex)[58].
- ◇ RBPs (RNA-binding proteins): Modulate localization, stability, and translation rates.
- ◇ Cell signaling: mTOR and eIF2α phosphorylation regulate global translation in response to stress[59].

Transcription and translation are functionally integrated processes. Transcription determines which mRNAs are produced. Post-transcriptional regulation results in the filtering and processing of functional transcripts. Translation controls the production of functional proteins. Moreover, feedback loops exist for the regulation of RNA transcription by translation products. For example, the translation of iron-storage proteins such as ferritin feeds back to regulate intracellular iron levels, which in turn modulate the activity of iron regulatory proteins (IRPs). These IRPs

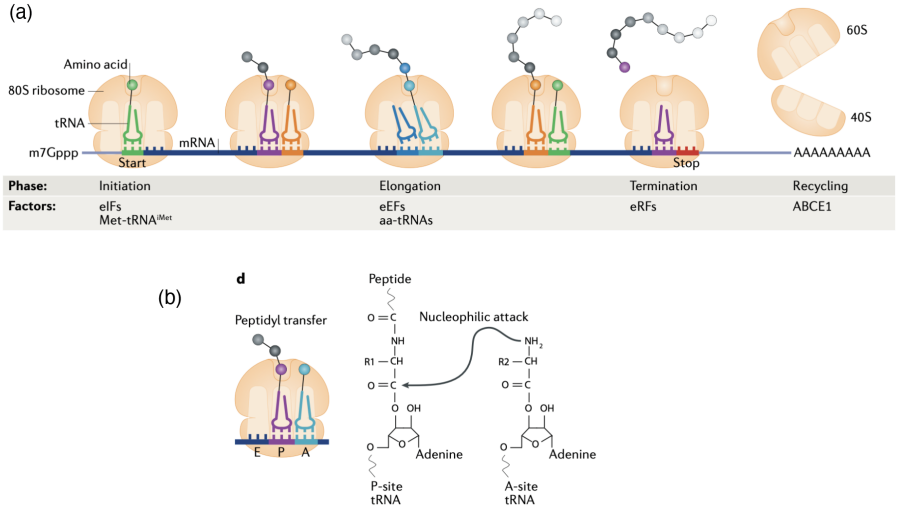

Figure 1.12: Functional mechanism of Translation. (a) Translation begins with initiation, where eukaryotic initiation factors (eIFs), Met-tRNAi $^{\text{Met}}$, ribosomal subunits, and mRNA assemble at the AUG start codon. During elongation, eukaryotic elongation factors (eEFs) and aa-tRNAs synthesize the peptide chain until a stop codon is reached. Termination then occurs via eukaryotic release factors (eRFs), releasing the peptide. Finally, ribosome recycling is mediated by ABCE1. (b) In elongation, the amino group of the A-site aa-tRNA attacks the ester bond of the P-site peptidyl-tRNA, transferring the growing peptide. *Figure adapted from "Roadblocks and resolutions in eukaryotic translation" by Schuller et. al, reproduced with permission from Springer Nature.*

bind to iron-responsive elements in target mRNAs to control their stability and translation[60].

Following translation, proteins undergo additional regulatory steps:

◇ Post-translational modifications (PTMs): Chemical modifications such as phosphorylation, acetylation, ubiquitination modify functional activity and cellular interactions[61].

◇ Chaperone-mediated folding: Ensures that newly synthesized proteins attain their correct 3D conformation, preventing misfolding and aggregation.

◇ Protein degradation: Proteasome and autophagy pathways clear misfolded or short-lived proteins[62].

Thus, together transcription and translation constitute the primary axis of gene expression—enabling cells to respond dynamically to developmental and environmental stimuli. Understanding these processes in molecular detail provides insight into cell identity, physiology, and mechanisms of disease.

Building on this foundational knowledge, recent advances have harnessed the principles of gene expression to develop nucleic acid–based therapeutics—a rapidly expanding class of therapies that target or manipulate RNA and DNA to modulate gene function with precision.

1.2 Nucleic Acid therapeutics

Nucleic acid therapeutics are a class of drugs comprising primarily of DNA or RNA as the therapeutically active agent. Nucleic acid-based drugs have emerged as a powerful class of therapeutics due to their sequence-specific targeting capability. To date, a total of 24 nucleic acid drugs have been approved by the FDA/EMA[63]. These include messenger RNA (mRNA) and CRISPR-Cas-based therapeutics, and short oligonucleotides such as short-interfering RNA (siRNAs), antisense oligonucleotides (ASOs), aptamers, and CpG deoxynucleotides.

1.2.1 Mechanism of action and therapeutic potential

ASOs are single-stranded oligonucleotides that modulate with RNA processing via multiple mechanisms[64]. Enzyme-active ASOs form DNA-RNA duplexes that are recognized and cleaved by RNase H, leading to reduction of the target transcript[65] (Figure 1.13a). Variants designed with Ago2-activating chemistries function analogously to single-stranded siRNAs[66]. Splice-switching ASOs, which do not activate RNase H, modulate exon inclusion or exclusion, stabilizing transcripts, or inhibiting nonsense-mediated decay[67] (Figure 1.13b). These diverse mechanisms permit ASOs to modulate gene expression beyond canonical degradation.

siRNAs are short, double-stranded RNA molecules that initiate gene silencing through the RNA interference (RNAi) pathway[68]. Endogenously or synthetically derived siRNAs are incorporated into the RNA-induced silencing complex (RISC), where Dicer, TRBP, and Ago2 are key effectors. The antisense strand guides RISC to complementary mRNA targets, where Ago2 executes site-specific cleavage—the rate-limiting catalytic step of RNAi[69]. Therapeutic siRNAs are designed to exploit this pathway for targeted mRNA knockdown (Figure 1.13c).

siRNAs and ASOs share mechanistic similarities—their mechanism of action can be divided into three stages: pre-hybridization, hybridization, and post-hybridization[64]. Pre-hybridization includes processes such as cellular uptake, subcellular trafficking, and localization—key determinants of intracellular bioavailability. The hy-

bridization phase refers to the base-pairing interaction between the therapeutic oligonucleotide and its RNA target, influenced by factors such as RNA secondary structure, sequence accessibility, and target RNA/nucleic acid drug half-life. Post-hybridization effects refers to the pharmacological effects exerted either via catalytic degradation or through steric blocking[64,70].

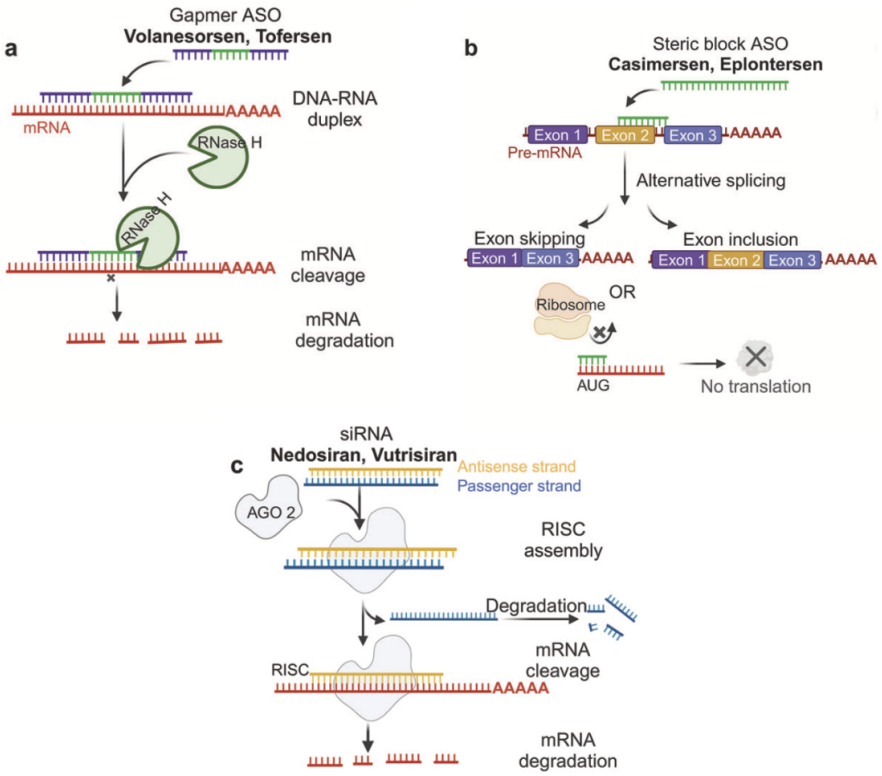

Figure 1.13: Mechanisms of action for antisense oligonucleotides and short interfering RNAs. (a) Gapmer ASOs, with a central DNA gap and RNA-like wings, bind mRNA to form RNA-DNA duplexes, triggering RNase H–mediated degradation.; (b) Steric block ASOs modulate gene expression by inducing exon skipping/inclusion or blocking translation by masking the start codon. (c) siRNAs load into RISC, where the antisense strand guides target mRNA binding, leading to translational repression.; *Figure adapted from "Nucleic acid drugs: recent progress and future perspectives" by Sun et. al, under CC BY-SA 4.0.*.

Aptamers are 2D- (two-dimensional) or 3D-structured single-stranded nucleic acids

selected for high-affinity binding to specific protein or small-molecule targets through processes such as SELEX[71]. They mimic antibodies in function but offer advantages in synthesis, stability, and cellular permeability[72].

CpG oligonucleotides are synthetic DNA sequences rich in unmethylated CpG motifs, which mimic bacterial DNA and stimulate innate immunity. These sequences activate Toll-like receptor 9 (TLR9), triggering cytokine release and dendritic cell activation[73]. Therapeutically, they are employed as vaccine adjuvants or immunomodulators in infectious and neoplastic diseases.

1.2.2 Chemical modifications of nucleic acids

DNA and RNA are not seemingly ideal drug candidates: they are large, negatively charged molecules, they cannot easily cross lipid bilayers, are rapidly degraded by endogenous nucleases, and can elicit potent immune responses. Over the past several decades, extensive chemical modifications have been developed to overcome these limitations to allow clinical translation—improving their pharmacokinetics, tissue distribution, and biological stability. These modifications fall into three primary categories: backbone, sugar, and base modifications.

Backbone alterations were among the first successful strategies for enhancing nucleic acid stability (Figure 1.14). The goal has been to increase nuclease resistance, prolong circulation time, and improve cellular uptake[63]. Key examples include:

Charged Backbone Analogues:

◇ Phosphorothioate (PS) Linkages: In this modification, a non-bridging oxygen in the phosphate group is replaced by a sulfur atom. This substitution enhances resistance to nuclease degradation and increases binding to serum proteins[74], resulting in an extended plasma half-life of approximately 2–3 days. PS linkages were first used in Vitravene (fomivirsen), the inaugural FDA-approved antisense oligonucleotide drug[75]. However, the strong protein interactions also contribute to toxicity and off-target effects[64].

Uncharged Backbone Analogues:

◇ Methylphosphonates: These analogues feature a methyl group replacing one of the non-bridging oxygens, yielding a neutral backbone[76]. This provides nuclease resistance and a charge-free profile, but results in poor aqueous solubility.

◇ Morpholinos (PMOs): The sugar-phosphate backbone is replaced with morpholine rings connected via phosphorodiamidate linkages. PMOs are completely resistant to nucleases and primarily used for splice modulation. They form the basis of several approved DMD therapies such as Eteplirsen, Golodirsen, Viltolarsen, and Casimersen[77][78][79][80][81].

◇ Thiomorpholino Oligonucleotides (TMOs): TMOs combine morpholino sugars with phosphorothioate linkages to improve delivery and pharmacological properties[82]. Though promising in preclinical studies, their long-term safety remains to be fully evaluated[82].

◇ Peptide Nucleic Acids (PNAs): In PNAs, the sugar-phosphate backbone is replaced with N-(2-aminoethyl)-glycine units. This provides exceptional stability and resistance to enzymatic degradation[83]. However, PNAs suffer from limited cellular uptake and poor bioavailability.

Conformationally Constrained Backbones:

◇ Locked Nucleic Acids (LNAs): LNAs incorporate a 2′-4′-linked methylene bridge that locks the sugar into a C3′-endo conformation. This rigidity enhances duplex thermal stability allowing for tighter RNA binding. Nonetheless, LNAs have been associated with adverse effects, including thrombocytopenia and organ toxicity.

◇ Tricyclo- or bicyclo-DNA (bc- or tcDNA): These analogues include cycloalkane rings fused to the sugar, offering conformational restriction and systemic delivery potential. However, the safety and toxicity profile of tcDNA remains under investigation[63].

Sugar and base modifications fine-tune hybridization kinetics, immune recognition, and enzyme compatibility (Figure 1.15).

2′-O-Methyl (2′-OMe) and 2′-O-Methoxy-ethyl (2′-MOE): This modification replaces the 2′-hydroxyl with a methyl (2′-OMe) or methoxy-ethyl group (2′-MOE), enhancing RNA duplex stability and reducing immunogenicity. It is used in approved ASOs like nusinersen for spinal muscular atrophy[84]. However, 2′-OMe or

2′-MOE modifications are not compatible with RNase H activity, and are limited to non-degradative mechanisms unless employed in the "gapmer" design.

2′-Fluoro (2′-F): The 2′-hydroxyl group in the sugar is replaced by fluorine, locking the sugar in the C3′-endo conformation and increasing binding affinity[85]. Often combined with 2′-OMe in siRNA drugs like Givosiran and Lumasiran[86,87], 2′-F can enhance potency but also has the potential to increase off-target interactions.

Gapmer design: Gapmers combine a central DNA "gap" flanked by 2′-modified sugar wings. This design allows for RNase H activity while improving ASO stability and binding affinity. Gapmers are employed in mipomersen, inotersen, and volanesorsen[88,89,90]. Their efficacy depends on the careful optimization of length and modification pattern.

Thus, many of these sugar modifications (e.g., 2′-F, LNAs) stabilize the C3′-endo sugar pucker conformation characteristic of RNA. This enhances duplex melting temperature and binding affinity—thereby improving targeting efficacy[91].

Chemical modifications to the *nucleobases* are employed to enhance the stability, binding affinity, and immunological tolerance of therapeutic oligonucleotides.

5-Methylcytosine improves hybridization strength and reduces detection by innate immune receptors by mimicking natural epigenetic marks[92]. However, excessive methylation may interfere with endogenous methylation-sensitive biological processes.

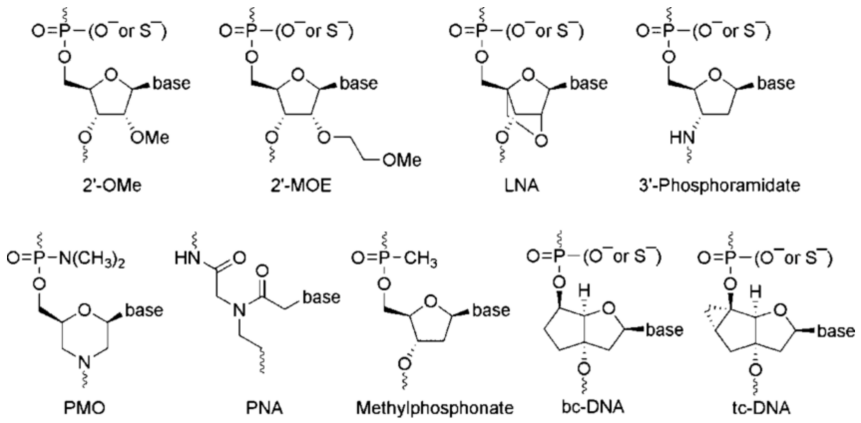

Figure 1.14: Chemical structures of a selection of oligonucleotide modifications that have been tested as antisense agents (2 OMe: 2 ′-O-Methyl, 2 MOE: 2 ′-O-Methoxyethyl, LNA: Locked nucleic acid, PMO: Phosphorodiamidate morpholino oligomer, PNA: Peptide nucleic acid, bc-DNA: Bicyclo-DNA, tc-DNA: Tricyclo-DNA). *Figure adapted from "Therapeutic Potential of Tricyclo-DNA antisense oligonucleotides" by Goyenvalle et al., under CC BY-NC 4.0.*

Inosine, the deaminated form of adenosine, acts as a wobble base that pairs preferentially with cytosine and can enhance codon flexibility. These base modifications are particularly important in siRNA, ASO, and mRNA platforms to improve efficacy and safety[88][89][90].

Excessive or poorly placed base modifications may interfere with endogenous RNA-binding proteins or editing enzymes, leading to unintended transcriptome-wide effects[63].

Together, all these chemical enhancements form the backbone of modern oligonucleotide therapeutics. Their rational design has enabled the transition of nucleic acids from promising modalities into breakthrough medicines (Figure 1.15), Table 1.1.

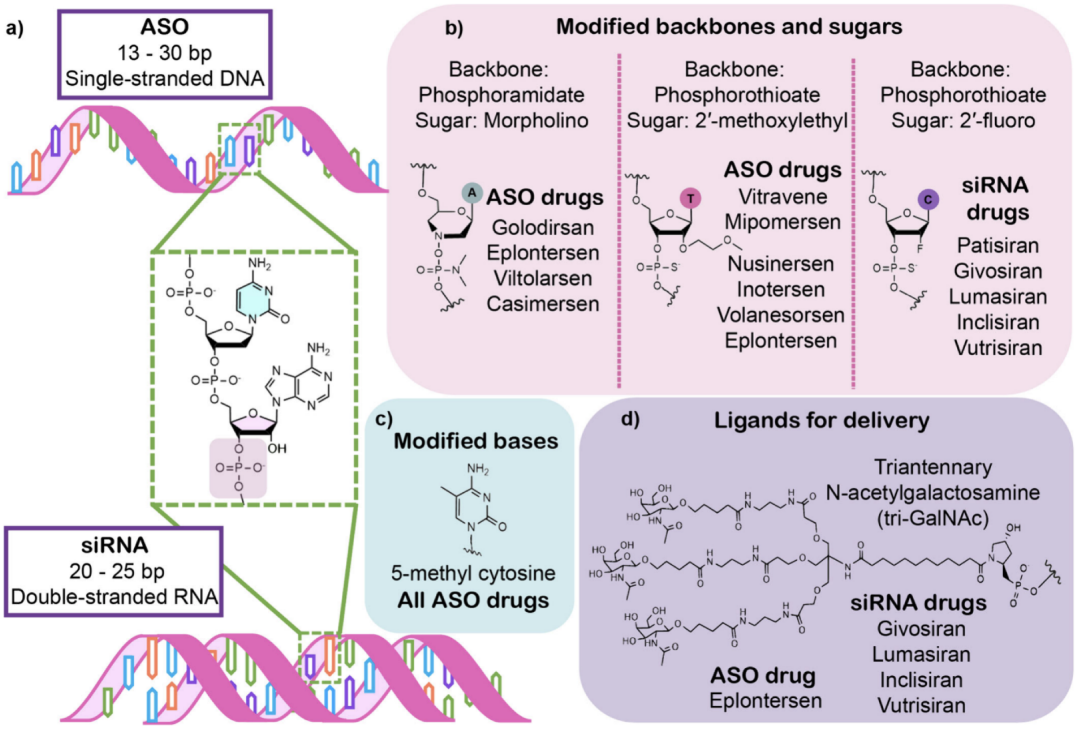

Figure 1.15: Chemical modifications featured in approved ASO and siRNA therapeutics.(a) ASOs are single-stranded and siRNAs are double-stranded. (b) Chemical modifications in the backbone and sugar, and (c) cytosine base are present in the approved ASO and siRNA therapeutics listed. (d) Enhanced hepatic delivery is achieved via the tri-GalNAc moiety through receptor–ligand interactions in the approved ASO and siRNA drugs. *Figure adapted from "Nucleic Acid Conjugates: Unlocking Therapeutic Potential" by Kashyap et al., under CC BY-SA 4.0.*

1.2.3 Covalent conjugation for enhancement of activity

Rational chemical optimisation of the components of nucleic acids has enabled nucleic acid therapeutics to be approved for clinical use. However, despite improvements in pharmacokinetics and target specificity, many current therapies remain limited to liver and muscle diseases[63]. A promising innovation in the field involves covalent conjugation—oligonucleotides are chemically linked to other molecules to enhance delivery, targeting, or functionality. This next generation of oligonucleotide

therapeutics has expanded the scope of treatable conditions and opened doors to more precise cell and tissue-specific interventions.

Two primary synthetic approaches are employed to generate oligonucleotide conjugates: pre-synthetic[93,94,95,96] and post-[97,98,99,100] synthetic modification:

- ◇ The pre-synthetic strategy involves incorporating pre-chemically modified phosphoramidite building blocks during oligonucleotide solid-phase synthesis. These monomers, functionalized with conjugate moieties, can be integrated at various points in the sequence, most efficiently at the $5'$ end. The $3'$ end presents synthetic challenges due to steric hindrance from the solid support. Although this method offers flexibility in conjugation sites, the synthesis of custom phosphoramidites can be technically demanding.

- ◇ The post-synthetic strategy involves the introduction of reactive functional handles (for example, amines, thiols, azides, etc.) into the oligonucleotide during synthesis. After purification, the oligonucleotide is coupled to the target molecule in solution. This modular approach facilitates optimization of both the oligonucleotide and conjugate separately, though reaction efficiency can be hindered by solubility mismatches and side product formation. Reactions such as copper-free click chemistry are often employed to overcome these limitations.

Both strategies are widely utilized, depending on the chemical nature of the conjugate and the desired application.

Table 1.1: List of approved ASO and siRNA therapeutics on the market. *When not stated, the sugar chemistry is fully 2′-H, apart from PMOs that have altered sugars themselves. PO, phosphate; PS, phosphorothioate; PMO, phosphorodiamidate morpholino oligomer; OMe, methoxyl; MOE, methoxyethyl; GalNAc, N-acetylgalactosamine.*

S.No.	**Drug Name (Year)**	**Target, Indication**	**Chemistry**	**Mechanism of Action**
1	VITRAVENE (1998)	CMV IE-2, CMV retinitis	21-mer ASO; Backbone: full PS	RNase H
2	KYNAMRO (2013)	ApoB-100, HoFH	20-mer ASO; full PS; Sugars: 2′-MOE, 2′-H (gapmer)	RNase H
3	EXONDYS 51 (2016)	Dystrophin, DMD	30-mer ASO; full PMO	Exon exclusion
4	SPINRAZA (2016)	SMN2, SMA	18-mer ASO; full PS; 2′-MOE	Exon inclusion
5	ONPATTRO (2018)	TTR, hATTR	21-mer siRNA; full PO; Sugars: 2′-OH, 2′-OMe, 2′-H	RISC / Ago2
6	TEGSEDI (2018)	TTR, hATTR	20-mer ASO; full PS; Sugars: 2′-MOE/2′-H (gapmer)	RNase H
7	GIVLAARI (2019)	ALAS1, acute hepatic porphyria	21/23-mer siRNA; PO, PS; Sugars: 2′-OMe, 2′-F; Conjugate: 3′-tri-GalNAc	RISC / Ago2
8	VYONDYS 53 (2019)	Dystrophin, DMD	25-mer ASO; full PMO	Exon exclusion
9	WAYLIVRA (2019)	apoCIII, FCS	20-mer ASO; full PS; Sugars: 2′-MOE/2′-H (gapmer)	RNase H
10	OXLUMO (2020)	HAO1, PH1	21/23-mer siRNA; PO, PS; Sugars: 2′-OMe, 2′-F; Conjugate: 3′-tri-GalNAc	RISC / Ago2
11	LEQVIO (2020/2021)	PCSK9, HeFH/ASCVD	21/23-mer siRNA; PO, PS; Sugars: 2′-OMe, 2′-F, 2′-H; Conjugate: 3′-tri-GalNAc	RISC / Ago2
12	VILTEPSO (2020)	Dystrophin, DMD	21-mer ASO; full PMO	Exon exclusion
13	AMONDYS 45 (2021)	Dystrophin, DMD	22-mer ASO; full PMO	Exon exclusion
14	AMVUTTRA (2022)	TTR, hATTR	21/23-mer siRNA; PO, PS; Sugars: 2′-OMe, 2′-F; Conjugate: 3′-tri-GalNAc	RISC / Ago2
15	WAINUA (2023)	TTR, polyneuropathy hATTR	20-mer ASO; PO, PS; Sugars: 2′-MOE/2′-H (gapmer); Conjugate: 5′-tri-GalNAc	RNase H

S.No.	Drug Name (Year)	Target, Indication	Chemistry	Mechanism of Action
16	TOFERSEN (2023)	SOD1, SOD1-ALS	20-mer ASO; PO, PS; Sugars: 2′-MOE/2′-H	RNase H
17	IMETELSTAT (2024)	Telomerase in MDS	13-mer ON; PS-Phosphoramidate; Conjugate: 5′-Palmitic (C16) acid	Telomerase inhibition

1.2.4 Conjugates for enhancing nucleic acid delivery

The efficient delivery of nucleic acids remains a major challenge[101]. Nucleic acids require active internalization mechanisms, predominantly endocytosis, which frequently traps them in endosomal compartments[102]. Only a small fraction of nucleic acids undergo endosomal escape to exert therapeutic effects[103]. To overcome these limitations, small molecule ligands have been used to exploit *receptor-mediated uptake*:

◇ N-Acetylgalactosamine (GalNAc) is the most clinically validated option for liver-specific delivery. GalNAc binds with high affinity to the asialoglycoprotein receptor (ASGPR), a receptor abundantly expressed on hepatocytes and characterized by rapid recycling, which facilitates efficient internalization and robust gene silencing responses[104]. Several FDA-approved drugs such as Lumasiran, Givosiran, and the 2024-approved Eplontersen utilize GalNAc conjugation in combination with second-generation backbone modifications like 2′-OMe and 2′F to achieve potent and durable RNAi effects in a cell- and tissue-specific manner.

◇ Anisamide targets sigma receptors, which are frequently upregulated in various

cancer cell types and are associated with signaling pathways involved in cell proliferation[105]. A triantennary anisamide moiety was chemically modified into a phosphoramidite, and incorporated during solid-phase synthesis to yield trivalent anisamide-conjugated ASOs. These triantennary-anisamide 2′-OMe ASOs exhibited a two-fold increase in cellular uptake and a four-fold enhancement in target protein expression relative to unconjugated controls.

◇ Anandamide, an endogenous fatty acid neurotransmitter and natural ligand of cannabinoid receptor 1 (CB1), has been associated with neurological and cardiometabolic disorders, obesity and cancer[95]. Various siRNA-anandamide conjugates have been synthesized using post-synthetic strategies. Monovalent conjugates have been shown to lead to a two-fold enhancement in cellular uptake[106]. Dendritic constructs that co-displayed anandamide and glucose enabled efficient gene knockdown in neuronal cells—while unconjugated siRNAs showed no activity[107].

◇ Folate receptors, which are overexpressed in many cancer types, serve as effective entry points for targeted nucleic acid delivery. Folate-polyethylene glycol (PEG)-siRNA conjugates have demonstrated selective and efficient silencing of genes in folate receptor-expressing cells[108]. Notably, monovalent folate-siRNA constructs reduced target expression by over 75% whereas unconjugated siRNAs have little to no effect[109].

The cellular membrane has been evolved to restrict the entry of large, negatively

charged biomolecules, and presents a formidable barrier to nucleic acid therapeutics. To address this, researchers have employed *lipid-based conjugates* to enhance the lipophilicity and cellular uptake of oligonucleotides:

- ◇ Cholesterol, a fundamental component of lipid membranes and a key regulator of steroid hormone synthesis and lipid metabolism, has shown promise when conjugated to siRNAs. Cholesterol (Chol)-siRNA conjugates have been detected in diverse tissues including heart, kidney, adipose, and lung, where they facilitate over 50% knockdown of target genes *in vivo*[110,111] compared to negligible activity of the unconjugated siRNAs. Moreover, cholesterol-conjugated ASOs achieved a five-fold increase in potency within skeletal muscle tissue in rodent models[112].

- ◇ Other lipid conjugates, such as palmitate and tocopherol (toc), showed enhanced activity in the skeletal tissue of rodents but less pronounced effects in primates, highlighting the influence of species-specific plasma protein interactions[112]. Chol- and toc-modified heteroduplex ASOs were capable of crossing the blood-brain barrier and achieving over fivefold knockdown of MALAT1 in neuronal and microglial cells, compared to unmodified ASO duplexes (Figure 1.16)[98].

- ◇ Studies demonstrate that pre-annealing chol-siRNA conjugates with serum lipoproteins such as HDL (high-density lipoprotein), LDL (low-density lipoprotein), or albumin further improved efficacy—HDL in particular yielded 5- to 18-fold greater mRNA silencing[113].

- ◇ The fatty acid chain length is also a crucial determinant of performance: while

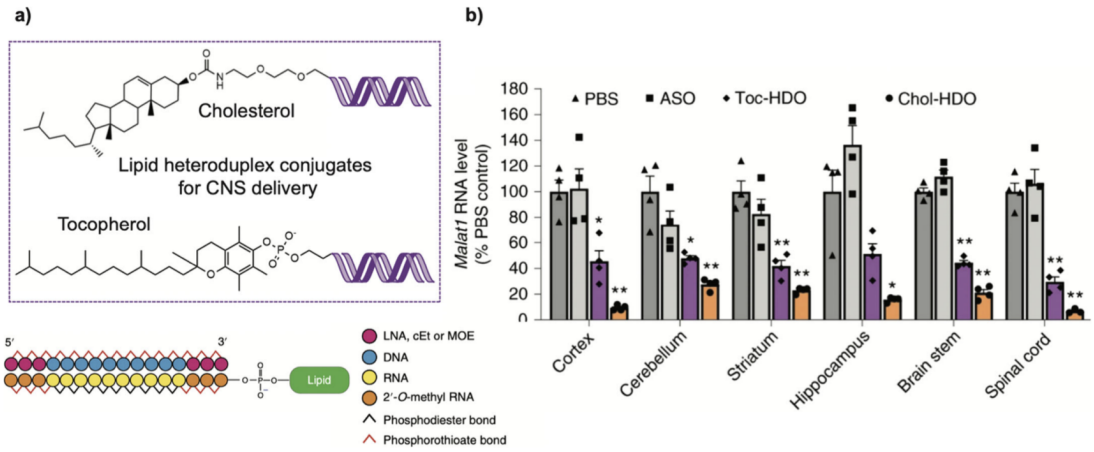

Figure 1.16: Cholesterol and tocopherol-conjugated ASOs for delivery across the blood brain barrier.(a) Chemistry of Chol- and Toc- heteroduplex ASOs.; (b) Widespread knockdown of MALAT1 across the CNS with Chol- and Toc-HDOs.*Figure adapted from "Nucleic Acid Conjugates: Unlocking Therapeutic Potential" by Kashyap et al., under CC BY-SA 4.0.*

short-chain fatty acids like lauroyl (C12), myristoyl (C14), and palmitoyl (C16) did not appreciably reduce target expression, longer chains such as stearoyl (C18) and docosanyl (C22) significantly enhanced mRNA knockdown in hepatic tissue[113]. In an alternative approach, dendritic long-chain alkyl phosphate esters pre-complexed with human serum albumin (HSA) improved nuclease resistance and reduced non-specific uptake by macrophages, thereby enhancing delivery efficiency[114].

◇ A distinct platform employing a 2′-O-hexadecyl (C16) chain enabled efficient and safe silencing in central nervous system (CNS), ocular, and pulmonary tissues. In an Alzheimer's disease mouse model, this 2′-O-C16-siRNA successfully suppressed amyloid precursor protein (APP) levels and ameliorated associated behavioral deficits[115].

◇ In another study, an effective multimeric platform for local lung delivery was determined[116]. By synthesizing and characterizing a panel of chemically modified siRNAs, varying in valency (mono- to tetravalent) and hydrophobic conjugates (eicosapentaenoic acid (EPA) or docosanoic acid (DCA)), it was demonstrated that a divalent siRNA scaffold achieved efficient pulmonary uptake and potent inhibition of SARS-CoV-2 infection (Figure 1.17).

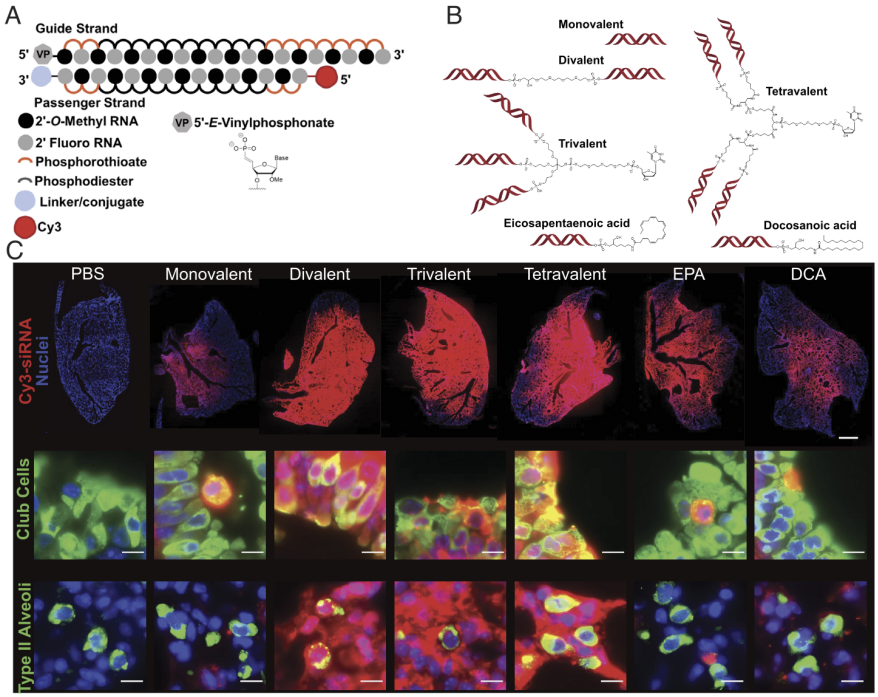

Figure 1.17: Diverse siRNA architectures and lipid conjugates explored for improved lung delivery. (a)Schematic of the fully chemically modified siRNA. Multivalent linker or hydrophobic moiety is conjugated to the 3′ end of the passenger strand. Cy3 dye labeled to the 5′ end of the passenger strand.; (b) Schematic for the multivalent and hydrophobic siRNA scaffolds tested.; (c) Representative fluorescence Images-Introduction of lung after intratracheal injection of siRNA in mice sacrificed at 24 hours postinjection (Top) Distribution of siRNA in red) with staining of DAPI in blue. Scale bar: 1 mm.*Figure adapted from "Divalent siRNAs are bioavailable in the lung and efficiently block SARS-CoV-2 infection" by Hariharan et al., under CC BY-NC-ND 4.0.*

◇ Another study revealed that Chol-conjugated siRNAs efficiently deliver to the placenta with primary liver clearance. A panel of fully modified siRNAs targeting Htt (Huntington) was synthesised, conjugated to Chol, docosahexaenoic acid (DHA), or docosanoic acid (DCA), with or without a phosphatidylcholine (PC) head group. Divalent and non-conjugated controls revealed that conjugate type and siRNA architecture significantly influence placental accumulation and tissue distribution (Figure 1.18)[117].

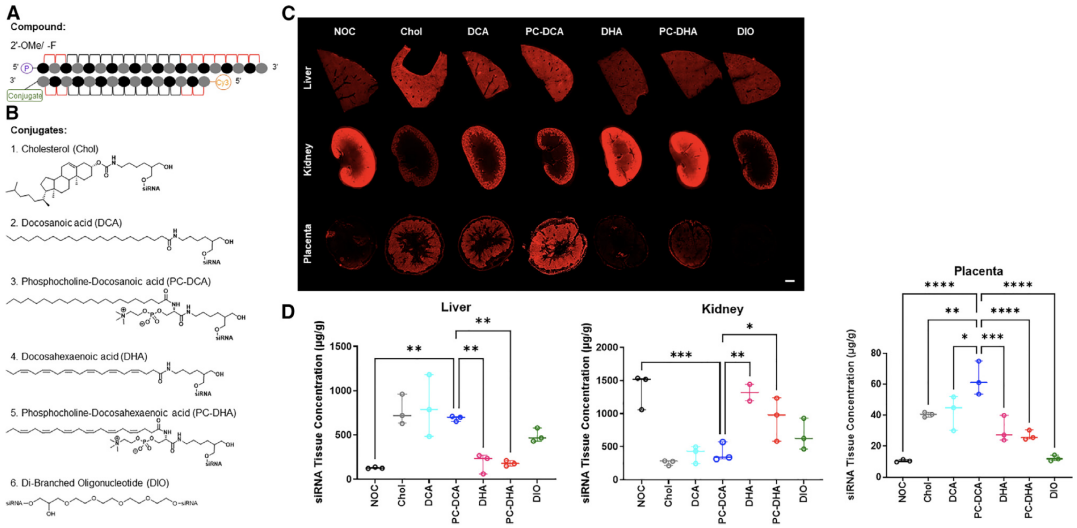

Figure 1.18: Lipid-modified siRNA for enhanced placental delivery. (a) Schematic for chemical modification of ASO scaffold. (b) Chemical structure of siRNA conjugates used for placental delivery. (c) Tissue fluorescence imaging; Scale bar, 1 mm. All Images-Introduction acquired at identical laser intensity. NOC refers to no conjugate. (d) Guide strand accumulation within various organs quantified after 48 hours.; *Figure adapted from "Chemical optimization of siRNA for safe and efficient silencing of placental sFLT1" by Davis et al., under CC BY-NC-ND 4.0.*

◇ A comparative evaluation of GalNAc and lipophilic targeting ligands such as cholesterol and tocopherol in hepatocyte systems demonstrated clear differences in performance. GalNAc conjugation led to approximately a 7-fold increase in

uptake and a 10-fold boost in efficacy relative to unconjugated ASOs. In comparison, cholesterol and tocopherol conjugates provided a 3- to 5-fold improvement in uptake and a 5-fold enhancement in silencing activity[118].

Small-molecule ligands can facilitate nucleic acid delivery to many cell types—even those once considered impervious to uptake. Peptides and, in particular, antibodies that act as ligands by binding to specific receptors and antigens respectively, have exceptional targeting capabilities extending beyond hepatocyte targeting.

Antibody-oligonucleotide conjugates have been employed across a variety of disease contexts, including CNS disorders, cardiac and skeletal muscle malignancies, as well as breast, lung, and hematological cancers[119].

◇ A particularly well-studied target is the transferrin receptor (TfR), known for its high expression in brain endothelial cells. Antibody-ASO conjugates directed against murine TfR enabled ASOs to achieve therapeutic concentrations in the mouse brain, improving survival in severe spinal muscular atrophy (SMA) models[120]. Enhanced delivery was also observed in peripheral tissues such as muscle—critical for treating neuromuscular conditions such as SMA. Another strategy used a modified Fc domain with low-affinity binding to human TfR to enhance transport across the BBB—achieved in both murine and non-human primate models[120].

◇ In the case of cancer, surface receptors like CD44 and EphA2, commonly overexpressed in glioblastomas, have been targeted with antibody-ASO conjugates,

resulting in efficient internalization and gene silencing[121].

◇ Transcription factor MXD3 in precursor B-cell acute lymphoblastic leukemia (preB-ALL) has been utilized in a anti-CD22 antibody-ASO conjugate. These constructs successfully reduced MXD3 expression and prolonged survival in both xenograft and murine leukemia models[122][99].

Peptide-based conjugates, especially those using cell-penetrating peptides (CPPs), have extensively employed for nucleic acid delivery:

◇ CPPs like Tat — composed primarily of arginine and lysine residues — enable intracellular delivery by crossing lipid membranes[123]. Tat-siRNA conjugates demonstrated functional delivery with strong RISC activity and peri-nuclear localization. However, excess positive charge is associated with toxicity; increasing arginine content in CPPs has been linked to cytotoxicity and renal impairment in mice[124][125], likely due to membrane disruption and non-specific interactions with endogenous nucleic acid-binding proteins[126].

◇ Charge-balanced alternatives such as the Pip5 and Pip6 series peptides, characterized by two arginine-rich regions flanking a hydrophobic core, have been conjugated to PMOs for use in Duchenne muscular dystrophy (DMD). These conjugates restored dystrophin protein expression across cardiac and skeletal muscle in mouse models following a single dose[127] with limited toxicity.

◇ In addition to CPPs, tissue-targeting peptides have been used to enhance specificity. A notable example includes a peptide ligand for the GLP-1 receptor—

abundantly expressed in pancreatic β-cells and the brain. An ASO conjugated to this GLP-1 targeting peptide successfully achieved functional delivery to β-cells, which are typically resistant to ASO uptake[128].

Nucleic acid aptamers represent a versatile class of targeting ligands that can be engineered to bind a wide array of protein targets with high affinity—often comparable to that of monoclonal antibodies[129]. The introduction of a single phosphorothioate modification to the backbone of an RNA aptamer dramatically enhanced its affinity for vascular endothelial growth factor (VEGF) and thrombin, achieving binding strengths in the 1–2 picomolar (pM) range—approximately 1,000 times stronger than the unmodified aptamer. In comparison, the typical target affinities for an antibody fall in the range of 10–100 pM[130].

Several aptamer-oligonucleotide conjugates have demonstrated therapeutic potential:

- The AS1411 aptamer, which targets nucleolin, a nucleolar protein overexpressed in many cancers, has been shown to internalize into prostate, lung, and pancreatic cancer cells— enabling ASO localisation to the nucleus. When conjugated to a splice-switching oligonucleotide (SSO), AS1411 significantly enhanced activity, achieving twice the splice correction efficiency compared to the free SSO alone[131].

- The A10 aptamer, designed to bind the prostate-specific membrane antigen (PSMA), has been conjugated to siRNAs for selective delivery to prostate cancer cells,

where it effectively induced tumor regression in xenograft models[132]. PSMA is also expressed in the vasculature of solid tumors, expanding the therapeutic scope of A10-based targeting strategies.

Aptamers offer several advantages: they are composed entirely of nucleic acids, making them inexpensive to synthesize, easy to modify, and generally non-immunogenic. However, they are still subject to many of the same delivery limitations as other nucleic acid therapeutics, including poor tissue penetration and susceptibility to degradation[72].

1.2.5 Conjugates for targeted activation

While much of the development in nucleic acid therapeutics has focused on improving tissue-specific delivery, another compelling strategy involves conditional activation—where a nucleic acid drug remains inactive during systemic circulation, and is selectively activated only at the intended target site[133,134]. This approach aims to minimize off-target effects and systemic toxicity, thereby increasing therapeutic precision and efficacy.

Targeted activation can be achieved either via internal stimuli, such as specific enzymes or pH levels, or through external triggers like light. Although internal triggers (for example, acidic tumor microenvironments or redox gradients) are commonly exploited in non-covalent delivery systems like nanoparticles[135,136], their specificity is often limited because similar conditions exist in non-target compartments (for

example, endosomes)[137,138].

One elegant solution involves enzyme-responsive conjugates. For example, antisense oligonucleotides have been cyclized through a cathepsin B-cleavable peptide linker. In the presence of this tumor-associated protease, the linker is cleaved, linearizing the ASO and restoring its activity. This strategy has shown promising tumor reduction in a prostate cancer model[139].

Externally triggered activation by light, offers unmatched spatiotemporal control. Photo-caging involves attaching light-sensitive groups to ASOs or siRNAs that suppress their activity until removed by illumination. Coumarin- or nitrobenzyl-based photocages have been used to block ASO activity, which can then be reactivated with UV light[140,141]. This technique has been applied in various systems, including zebrafish and Xenopus embryos, using morpholino-based photo-caged oligonucleotides to control the expression of developmental genes[142,96] (Figure 1.19). Further refinement of this technology allows orthogonal control—for example, two different ASOs activated by distinct light wavelengths (UV and blue)[143].

However, one major limitation of photo-caging strategies is that ultraviolet light has limited tissue penetration, making deep tissue activation difficult[144]. To address this, near-infrared (NIR) light-responsive systems have been developed. These longer-wavelength systems offer better penetration and are being explored for subdermal and internal organ nucleic acid delivery applications[145].

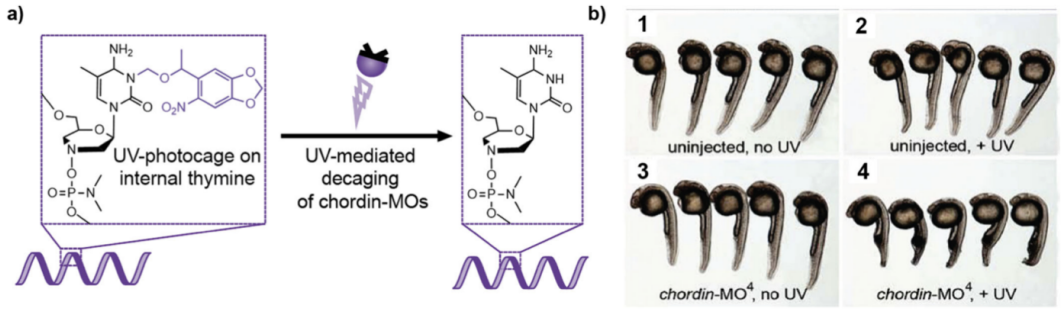

Figure 1.19: Light-responsive chemical modifications for targeted ASO activation. (a) A nitrobenzyl–photocage was used to inhibit activity of a PMO–based ASO. Activation of the chordin PMO was achieved using ultraviolet (UV) light. (b) UV–irradiation resulted in active chordin PMO that disrupted endogenous levels of chordin, resulting in deformity (4) compared to controls (1–3). *Figure adapted from "Nucleic Acid Conjugates: Unlocking Therapeutic Potential" by Kashyap et al., under CC BY-SA 4.0.*

1.2.6 Conjugates for expanding functionality

ASOs represent the most prominent class among clinically approved nucleic acid therapeutics. However, their mechanisms of action are largely confined to two modes: RNase H-mediated degradation and splice modulation[64]. Splice-switching ASOs act within the nucleus on pre-mRNA, which is sequestered behind the nuclear envelope, while RNase H-active ASOs target mature cytoplasmic mRNAs. One of the principal challenges in enhancing ASO performance is efficient subcellular localization: only a small fraction of ASOs reach their intended compartment. Quantitative studies have reported that less than 0.3% of GalNAc-siRNAs and roughly 1% of ASOs successfully escape the endosome[146,147], representing a key feature of therapeutic efficacy.

Given this, improving the intracellular partitioning of ASOs—particularly into the

nucleus, could significantly boost functional potency. For instance, conjugating ASOs to Hoechst dyes has been shown to dramatically improve nuclear localization and, as a result, target knockdown. Hoechst molecules bind the minor groove of double-stranded DNA with nanomolar affinities (1–10 nM), thus facilitating ASO retention in nuclear compartments[148]. Hoechst-ASO conjugates achieved greater knockdown of the nuclear long non-coding RNA MALAT1 than their unconjugated LNA-gapmer counterparts.

Beyond improving localization, ASO conjugates can also unlock entirely new biological pathways. One such example involves exploiting the RNase L antiviral defense system. RNase L is a cytoplasmic endoribonuclease activated by 2′-5′-linked oligoadenylates (2-5A) synthesized in response to double-stranded RNA by the OAS enzyme family[149]. By covalently linking ASOs to a synthetic 2-5A4 ligand, researchers have developed bi-functional constructs that not only hybridize to target RNAs but also activate RNase L to degrade them.

This strategy has been applied in infectious disease models. In one study, a 2′-OMe ASO targeting the SARS-CoV-2 spike RNA was conjugated to 2-5A4[150]. The conjugate induced significantly greater knockdown than either the ASO or 2-5A4 alone, reducing viral titers in a luciferase-reporter pseudovirus assay. Similarly, a 2-5A4-ASO targeting the RSV transcription elongation factor led to a threefold reduction in viral RNA compared to the unconjugated control[151] (Figure 1.20). These studies illustrate how chemical conjugation can not only enhance delivery

but also re-purpose innate cellular pathways to enhance oligonucleotide activity.

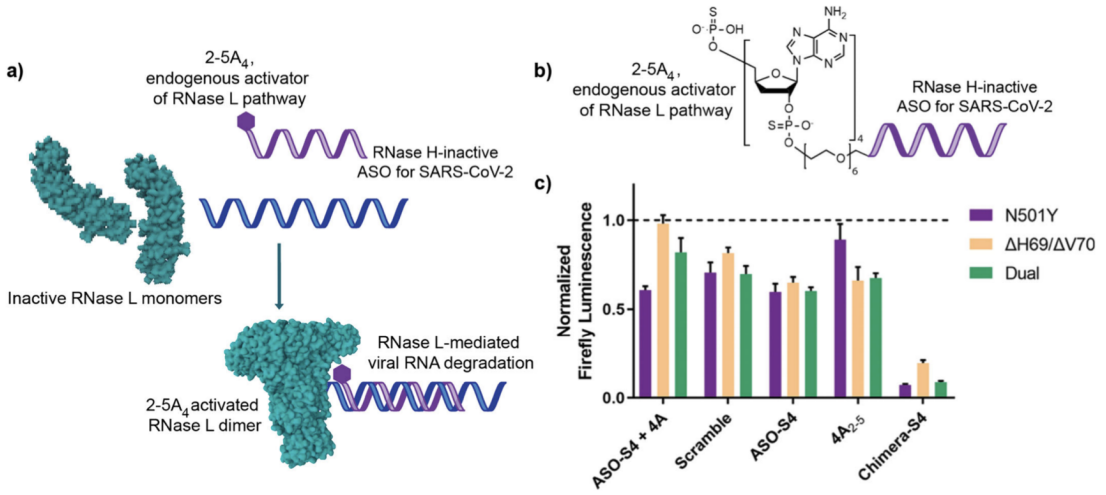

Figure 1.20: RNase L-mediated degradation of target RNA via antisense oligonucleotide-RNase L activator conjugate. (a) Proposed mechanism of 2′-5′poly(A)4 (2–5A4) mediated activation of RNase L for targeted viral RNA degradation.; b) Chemistry of the 2–5A4–ASO conjugate for targeting SARS–CoV–2 RNA.; c) Reduction in viral titer upon treatment with 2–5A4–ASO conjugate, measured using a luciferase infection model *Figure adapted from "Nucleic Acid Conjugates: Unlocking Therapeutic Potential" by Kashyap et al., under CC BY-SA 4.0.*

The toolbox of nucleic acid therapeutics continues to expand, driven by the convergence of chemical biology and drug delivery innovation. One of the most exciting frontiers lies in the conjugation of oligonucleotides with bio-active small molecules (Figure 1.21). These conjugates enable tunable pharmacokinetics, programmable sub-cellular trafficking, and even novel mechanisms of action. Researchers are increasingly exploring ligand-oligonucleotide conjugates. These include a wide range of chemical compounds, from receptor-targeting moieties to immuno-modulators and enzyme co-factors. As a result, we are witnessing the emergence of highly tailored, conditionally active therapies that offer remarkable therapeutic precision.

Despite challenges in endosomal escape, tissue specificity, and enzymatic degradation, nucleic acid therapeutics have consistently demonstrated clinical success in targeting genetic drivers of disease with minimal off-target toxicity. However, the field continues to evolve, with growing interest not only in refining delivery strategies but also in expanding the functional scope of oligonucleotides through chemical conjugation.

The rise of heterobifunctional small molecules such as PROTACs (proteolysis-targeting chimeras) exemplifies this transition. These molecules operate by simultaneously engaging a target protein and an E3 ubiquitin ligase, leading to selective proteasomal degradation. Over 20 PROTAC drugs have entered clinical trials as of 2022, underscoring the translational potential of bifunctional design[152]. Inspired by this model, nucleic acid analogs have begun to incorporate similar activity. Oligo-TRAFTACs, for instance, combine a DNA or RNA motif that binds transcription factors with an E3 ligase-recruiting ligand, resulting in proteasomal degradation of oncogenic TFs like c-Myc and brachyury[153] Similarly, RNA-PROTACs—engineered RNAs that recruit E3 ligases—have been developed to degrade RBPs such as LIN28 and RBFOX1[154]. These proof-of-concept studies highlight the need for precise linker tuning and structure-activity relationship (SAR) optimization to achieve consistent efficacy.

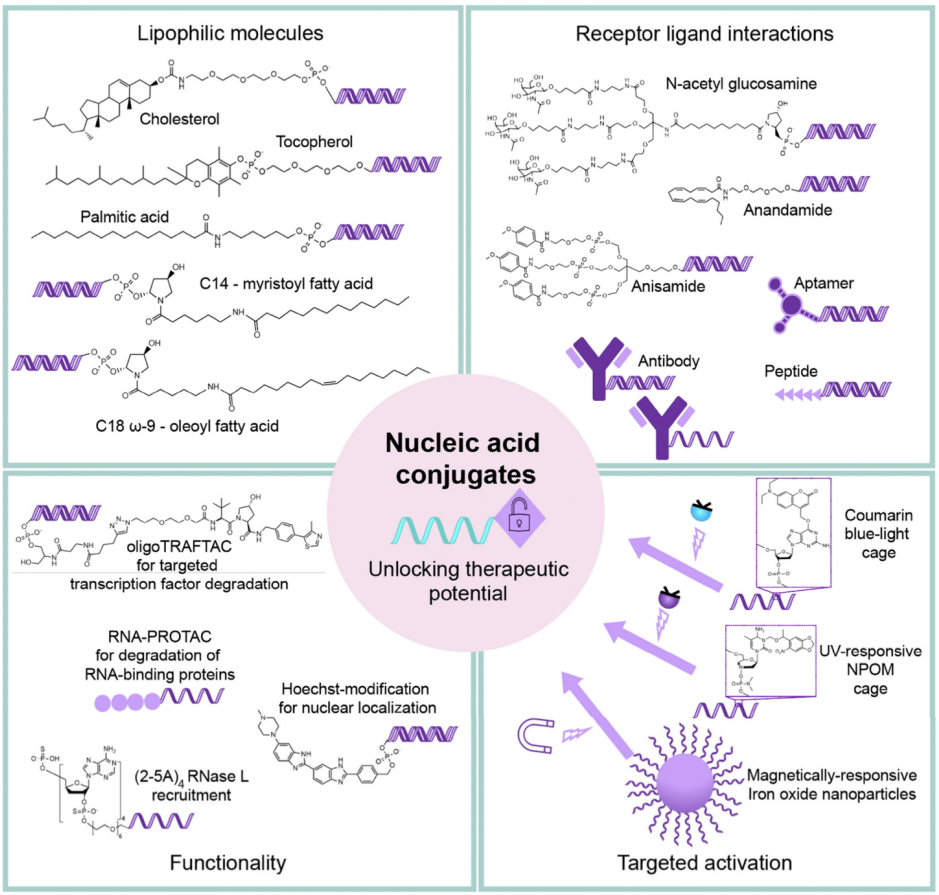

Figure 1.21: Next–generation therapeutic nucleic–acid conjugates can be broadly characterized into lipophilic conjugates, conjugates for receptor–ligand interactions, conjugates with new functionalities, and conjugates with targeted activation properties. *Figure adapted from "Nucleic Acid Conjugates: Unlocking Therapeutic Potential" by Kashyap et al., under CC BY-SA 4.0.*

1.3 Part I: Research Aims

This conceptual framework sets the stage for this body of research. Part I of this DPhil work explored the following directions:

◇ First, a strategy to improve the nuclear localization of ASOs by conjugating them to ligands that engage nuclear import machinery. The nucleus remains a key site

of action for splice-switching and RNase H-active oligonucleotides. However, passive diffusion across the nuclear envelope is inefficient, and existing delivery systems rarely optimize for subcellular nuclear localisation. By directing ASOs through nuclear trafficking pathways, we aimed to significantly enhance nuclear concentrations, thereby boost the efficiency of splicing correction and RNase H-mediated knockdown.

- Second, establishing a novel biochemical mechanism for cytoplasmic ASO knockdown, distinct from canonical RNase H or RISC-based pathways. This involved conjugating ASOs to small molecules to recruit the following cytoplasmic biochemical pathways: lysosomal trafficking and anti-viral RNase L-mediated RNA knockdown. Such a system could overcome the limitations of current ASO chemistries in non-nuclear compartments. Moreover, it can also provide a new mechanism of action for targeting mRNAs and non-coding RNAs implicated in disease.

Part I of this DPhil work was aimed at advancing the clinical potential of nucleic acid therapeutics. This focus of this research was on developing new modes of intracellular engagement and expanding the functional repertoire of antisense oligonucleotides. Through this work, the goal was to explore how chemical modifications can enable broader and more versatile therapeutic applications of antisense oligonucleotides.

Chapter 2

Altering the subcellular localization of ASOs to improve their therapeutic engagement and efficacy

2.1 Introduction

Nucleic acid drugs have emerged as a powerful class of therapeutics with the potential to revolutionize the treatment of a wide range of diseases[63]. Among these, antisense oligonucleotides or ASOs have attracted considerable attention because of their ability to provide precise control over gene expression at the RNA level (see subsection 1.2.1). ASOs function through multiple mechanisms: RNase H-mediated degradation of target mRNA bound to complementary DNA-based ASOs, modulation of pre-mRNA splicing, or steric hindrance of ribosome binding, thus preventing translation[64]. This precise RNA-level intervention allows for targeted correction of gene dysregulation associated with various pathological conditions—offering a highly specific and effective therapeutic strategy.

One of the most critical determinants of ASO efficacy is sub-cellular compartmentalisation. In particular, their ability to localize within the nucleus[64]. ASOs exert

their biological effects predominantly within the nucleus, particularly through mechanisms such as pre-mRNA splicing modulation and RNase H-mediated degradation of nuclear-retained transcripts. However, achieving efficient nuclear accumulation remains a major challenge because of the inherent physicochemical properties of ASOs such as their polyanionic nature. Current ASO therapeutics are shuttled in and out of the nucleus: an inherently inefficient process with only a fraction of administered ASOs accumulating within the nucleus[102]. This inefficient nuclear import limits their therapeutic efficacy, making strategies to enhance nuclear delivery an important area of research (Figure 2.1).

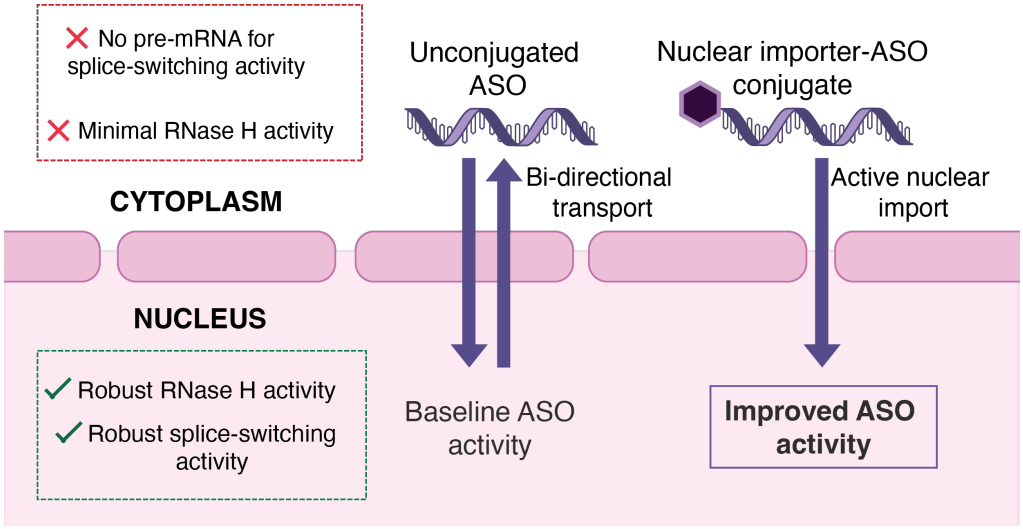

Figure 2.1: Schematic highlighting the rationale for the improved activity of nuclear-targeting ASO conjugates over unconjugated ASOs. Modification with nuclear-targeting moieties should enhance ASO activity in principle. *Figure re-produced from "Harnessing BET-Bromodomain Assisted Nuclear Import for Targeted Subcellular Localization and Enhanced Efficacy of Antisense Oligonucleotides" by Kashyap et al., under CC-BY 4.0.*

Enhancing the nuclear import and accumulation of ASOs has been postulated to significantly improve their target engagement and, consequently, their therapeutic

efficacy[155]. Previous work to improve nuclear delivery has employed nucleic acid conjugates with small molecules[105], aptamers[72], and peptides[156]. Conjugates generated with the double-stranded DNA-binding dye Hoechst have been explored as a strategy to enhance the nuclear accumulation of ASOs[148]. Hoechst dyes exhibit a strong affinity for the minor groove of DNA and are known to accumulate within the nucleus[157]. However, when conjugated to ASOs, these modifications resulted in minimal and inconsistent improvements in gene-knockdown efficacy. Specifically, targets degraded via the same mechanism of action were silenced to varying levels of efficacy suggesting that the Hoechst modification does not provide a reliable or predictable means of improving nuclear accumulation. Furthermore, the use of Hoechst derivatives in a therapeutic may be limited by concerns over cytotoxicity, as these dyes are known to interfere with DNA integrity, eliciting genotoxic stress and disrupting cellular homeostasis[158]. Thus, while Hoechst-based ASO conjugates offer an elegant small molecule-based approach to nuclear targeting, their practical use remains limited by efficacy and safety issues.

Another strategy that has been investigated for improving ASO nuclear localization involves conjugation to nuclear protein-binding aptamers such as AS411 for nucleolin[131]. Nucleolin is a ubiquitously expressed nucleolar phosphoprotein that plays a critical role in ribosomal biogenesis, RNA metabolism, and nucleocytoplasmic transport[159]. AS411 is a well-characterized nucleolin aptamer, has been conjugated to splice-switching oligonucleotides in order to enhance nuclear accumulation (Fig-

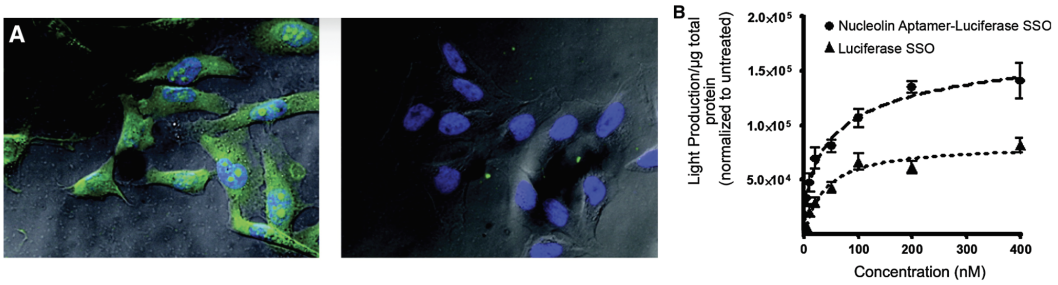

Figure 2.2: AS411 allows for enhanced nuclear delivery.(a) Fluorescent microscopy images upon treatment with Alexa488-nucleolin aptamer or Alexa488-control aptamer at a concentration of 100nM for 1h.(b)Dose response comparing the effects of nucleolin aptamer–SSO chimera and the SSO alone. *Figure adapted from "Aptamer-mediated delivery of splice-switching oligonucleotides to the nuclei of cancer cells" by Kotula et. al, under license 6007581355259.*

ure 2.2). However, this approach has demonstrated only modest improvements in splice-switching efficiency. The limited efficacy of this strategy may stem from several factors, including insufficient nucleolin-mediated transport, sub-optimal binding affinity, or inadequate endosomal escape following cellular uptake. Furthermore, concerns regarding the stability and pharmacokinetics of nucleolin-targeting aptamers present additional challenges to their potential use as nuclear-targeting moieties.

Peptide-based nuclear-targeting moieties such as nuclear localization signal (NLS) peptides have been extensively explored for facilitating ASO transport into the nucleus. NLS peptides are short amino acid sequences recognized by importin proteins, which mediate active nuclear import through the nuclear pore complex.[160,161]. The clinical use of NLS-ASO conjugates has been hindered by several critical limitations. First, peptide-conjugated ASOs often display poor intracellular uptake,

as their relatively large size and strong positive charge cause them to interact with the negatively charged plasma membrane rather than efficiently cross it[162]. Second, NLS motifs have been associated with increased cytotoxicity and potential immunogenicity, calling for the exploration of more diverse sequences[163]. This has resulted in a push for the exploration of more charge-balanced chemical designs and diverse sequences.

These studies highlight the challenges associated with current approaches to enhancing nuclear localization of ASOs. While small-molecule, aptamer-based, and peptide-based conjugates have demonstrated some degree of nuclear enrichment, their inconsistent efficacy, potential toxicity, and delivery constraints necessitate the development of alternative strategies. A more effective approach would require a balance between efficient nuclear targeting, high cellular uptake, and minimal off-target toxicity. The design of novel ASO conjugates incorporating ligands capable of engaging endogenous nuclear transport pathways while preserving ASO therapeutic activity represents a promising approach in the area.

A recent study demonstrated the potential of a bi-functional compound containing the small molecule (+)-JQ1 warhead to induce the nuclear localization of cytoplasmic proteins (Figure 2.3)[164]. (+)-JQ1 is a well-characterized and potent binder of the bromodomain and extra-terminal (BET) family of proteins, which play key roles in chromatin regulation and transcription[165]. These proteins, including BRD2, BRD3, BRD4, and BRDT, are primarily nuclear, where they act as epigenetic read-

ers, recognizing acetylated lysine residues on histones to regulate gene expression programs.[166,167] However, several studies have highlighted their secondary functions in the cytoplasm, particularly in cellular signaling pathways and stress responses.[168,169] This differential localisation of BET proteins functional pathways suggests that they exhibit an intermediary shuttling state between the nucleus and cytoplasm, a property that has been leveraged for nuclear delivery of a target protein. We set out to establish whether this nuclear targeting mechanism could be expanded to ASOs.

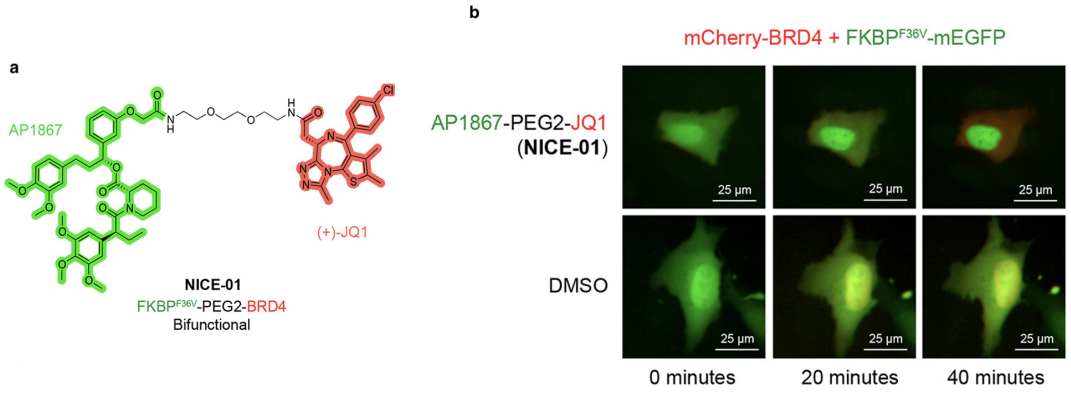

Figure 2.3: Rapid import of GFP into the nucleus by bi-functional small molecule, NICE-01. (a) Schematic for nuclear import of cytosolic protein. (b) Chemical structure of NICE-01. (c) U2OS cells co-transfected with mCherry-BRD4 and FKBPF36V-mEGFP, treated with NICE-01 (200 nM) or DMSO. *Figure adapted from "Bifunctional Small Molecules That Induce Nuclear Localization and Targeted Transcriptional Regulation" by Gibson et. al, under CC-BY-NC-ND 4.0.*

In this work, a series of novel covalent (+)-JQ1-ASO conjugates were synthesised. This work aimed at enhancing the active nuclear import of ASOs. This approach involves modifying ASOs with a single covalent (+)-JQ1 ligand, exploiting its affinity

for BET bromodomain proteins to facilitate nuclear enrichment. By taking advantage of the dynamic shuttling of BET proteins between the nucleus and cytoplasm, it was hypothesized that these (+)-JQ1-ASO conjugates would show increased ASO localization to the nucleus, thereby enhancing their efficacy.

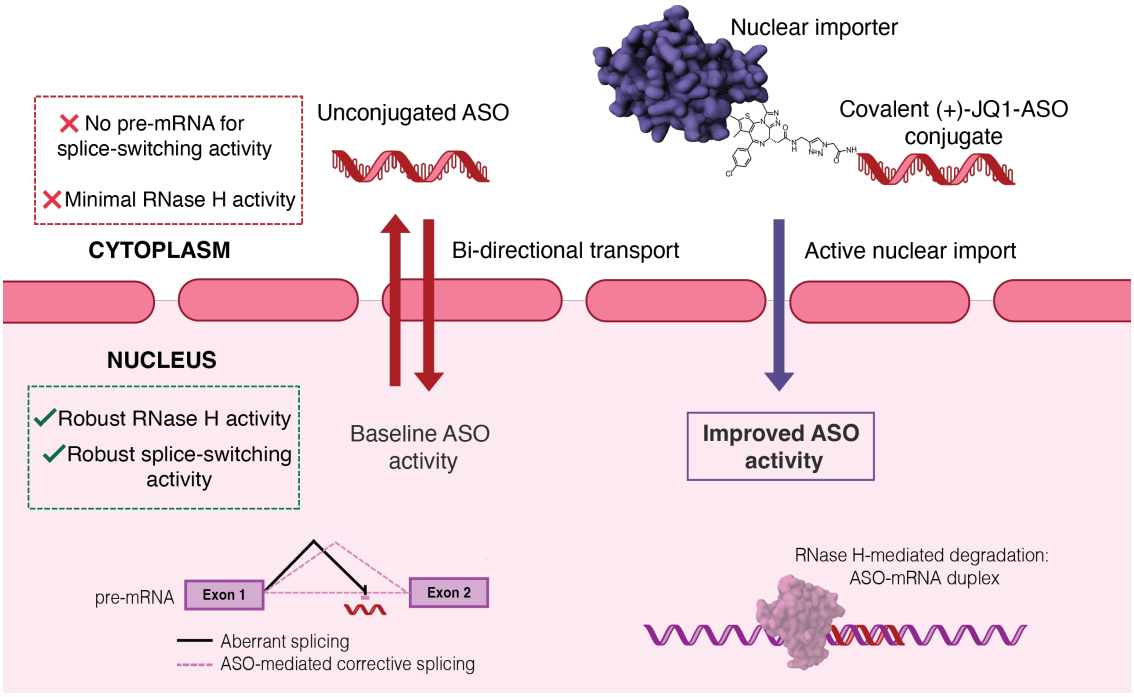

Figure 2.4: Schematic demonstrating the improved activity of (+)-JQ1-ASO conjugates over unconjugated ASOs. *(+)-JQ1-ASO conjugates improve splice-modulation and RNase H-mediated knockdown through increased nuclear accumulation. Figure re-produced from "Harnessing BET-Bromodomain Assisted Nuclear Import for Targeted Subcellular Localization and Enhanced Efficacy of Antisense Oligonucleotides" by Kashyap et al., under CC-BY 4.0.*

2.2 Aims

In this work, a series of novel covalent (+)-JQ1–ASO conjugates were synthesised with the aim of enhancing the active nuclear import of ASOs. The approach in-

volved modifying ASOs with a single covalent (+)-JQ1 ligand, exploiting its affinity for BET bromodomain proteins to facilitate nuclear enrichment. By taking advantage of the dynamic shuttling of BET proteins between the nucleus and cytoplasm, it was hypothesised that these conjugates would exhibit increased ASO localization to the nucleus, thereby improving their efficacy.

The strategy was intended to be tested across both mRNA knockdown and splice-switching mechanisms, as well as in multiple cell types relevant to approved nucleic acid drugs, in order to evaluate its general applicability to different ASO modalities and disease models. Mechanistic investigations were also planned to determine whether any enhancement in efficacy could be attributed to greater nuclear localization, and to establish whether the effect was dependent on BET bromodomain protein interactions. To further assess therapeutic relevance, studies were designed around a (+)-JQ1–Oblimersen conjugate, in which Oblimersen—a BCL-2–targeting ASO previously evaluated in clinical trials—was tested in the context of acute myeloid leukemia (AML).

More broadly, this line of investigation sought to establish a strategy for manipulating ASO subcellular localization through a defined protein interaction, offering a potential avenue for the development of next-generation ASO therapeutics. Current delivery approaches often rely on passive uptake mechanisms, which are inherently inefficient and frequently result in suboptimal nuclear concentrations. Conjugation of ASOs to (+)-JQ1 was therefore pursued as a means of actively promoting

nuclear accumulation while maintaining minimal toxicity, a critical parameter for translational application.

Overall, the study was directed toward assessing the feasibility of using small-molecule ligands such as (+)-JQ1 to guide ASOs to the nucleus, thereby exploring a chemically controlled approach to improving ASO efficacy. This strategy was envisaged as a way to broaden the applicability of ASO therapeutics, particularly for targets requiring nuclear engagement, and as a concept that could ultimately be extended to other nucleic acid-based modalities.

The objectives of this chapter were as follows:

- ◇ Synthesis and characterisation of high-yield high-purity covalent (+)-JQ1-ASO conjugates
- ◇ Functional validation of the activity of (+)-JQ1-ASO conjugates in various biologically relevant cell lines
- ◇ Mechanistic validation of (+)-JQ1-ASO conjugate activity
- ◇ Profiling selectivity and off-target effects of (+)-JQ1-ASO conjugate treatment

2.3 Results

2.3.1 Synthesis of JQ1-ASO conjugates

For this work, published ASO sequences were selected that had previously been validated with mismatch and scrambled controls. Since these sequences had been shown to specifically target their respective mRNAs, the primary comparative controls in our experimental validation of (+)-JQ1-ASO conjugates were ASOs without the (+)-JQ1 modification. These included both RNase H–active gapmers, which induce mRNA degradation, and splice-switching oligonucleotides (SSOs), which modulate pre-mRNA splicing.

To synthesise the covalent (+)-JQ1-ASO conjugate, copper-catalysed click chemistry was used. Alkyne-modified (+)-JQ1 and 5′-azide-modified ASOs were synthesised.

Synthesis of JQ1-alkyne

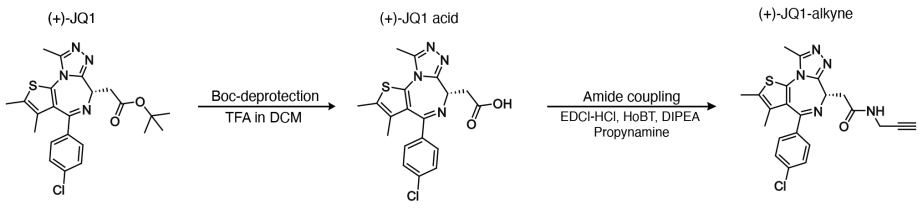

Figure 2.5: Synthesis scheme for (+)-JQ1-alkyne.

Alkyne-modified (+)-JQ1 was synthesised in two steps, starting from the commer-

cially available (+)-JQ1 ligand. First, the boc group of (+)-JQ1 was deprotected to yield the (+)-JQ1 acid[170]. This was followed by a hydroxybenzotriazole (HoBT) and (3-dimethylamino-propyl)-ethyl-carbodiimide hydrochloride (EDC-HCl)-mediated coupling with propargylamine, resulting in the formation of (+)-JQ1-alkyne[171] (Figure 2.5).

Synthesis of Azide-ASO

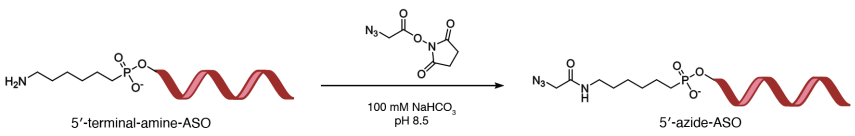

Figure 2.6: Synthesis scheme for 5′-azido-functionalised ASO.

5′-azide-ASO was prepared through an azidoacetic acid-N-hydroxysuccinimide (NHS) ester functionalisation of commercially available 5′-terminally amine-modified ASO under basic conditions (Figure 2.6).

General bioconjugation strategy

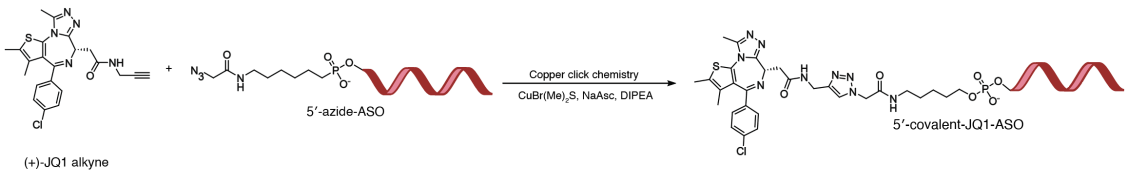

Figure 2.7: Synthesis scheme for 5′-(+)-JQ1-functionalised ASO.

All (+)-JQ1-ASO conjugate were prepared using copper-catalysed click conjugation of the (+)-JQ1-alkyne with the 5′-azide-ASO (Figure 2.7). $>$ 90% yields was

achieved for all bioconjugation reactions performed and > 95% purity following HPLC purification.

2.3.2 Synthesis of JQ1-SSO conjugate

The final (+)-JQ1-SSO conjugate was prepared using copper-catalysed click conjugation of the (+)-JQ1-alkyne with the 5′- azide-SSO (Appendix Figure A.15, Figure A.16). > 90% yields were achieved for all bioconjugation reactions performed and > 95% purity following HPLC purification.

2.3.3 JQ1-SSO outperforms unmodified SSO for splice switching efficacy

To evaluate the activity of (+)-JQ1-ASO conjugates, a splice-switching oligonucleotide (SSO) was selected for preliminary studies. The 18-mer SSO employed in our experiments had a fully phosphorothioated (PS) backbone, with all ribose sugars modified at the 2′-position with a methyl group, the 2′-OMe modification (Figure 2.8a). This gold standard SSO sequence was designed for the HeLa pLuc/705 cell line, which expresses a luciferase gene interrupted by a mutated β-globin intron[172]. The mutation introduces a 5′-splice site that activates a cryptic 3′-splice site, leading to incorrect mRNA splicing and the production of non-functional luciferase (Figure 2.8b). The SSO binds to the mutant 5′-splice site, promoting the exclusion of the aberrant intron and restoring proper pre-mRNA splicing to gener-

ate functional luciferase. Luminescence is thus used as a proxy for splice-switching efficacy.

To assess the activity of our (+)-JQ1-SSO conjugates in the HeLa pLuc/705 cell line, their efficacy was compared to the well-characterized SSO lacking the 5′-(+)-JQ1 modification and the intermediate azido-modified SSO. Cells were transfected with varying concentrations (25, 50, 100, and 200 nM) of either SSO (unconjugated, azido-modified, and (+)-JQ1 modified) for 24 hours and analyzed by luminometry, which served as a measure of splice correction and SSO efficacy. The (+)-JQ1-SSO conjugate exhibited 2.0-, 1.8-, 1.9-, and 1.7-fold higher splice-switching activity compared to the unconjugated and azido-modified SSO at 25, 50, 100, and 200 nM, respectively (Figure 2.8c). To evaluate activity in a more physiologically relevant context, gymnotic delivery of the (+)-JQ1-SSO conjugate was performed, alongside its unconjugated and azido-modified counterparts, at 5, 10, and 20 µM, with luminescence quantification as described above. Gymnotic delivery refers to oligonucleotide delivery without transfection reagents, providing a more physiologically and clinically relevant assessment of activity.

The gymnotically delivered (+)-JQ1-SSO showed significantly enhanced splice switching at 10 and 20 µM (Figure 2.8d). For both delivery methods, the unmodified and azido-SSOs exhibited identical fold changes in luminescence, as anticipated (Figure 2.9), with values lower than those seen for the (+)-JQ1-modified SSO, indicating that the observed improvement could be attributed to the (+)-JQ1 modification.

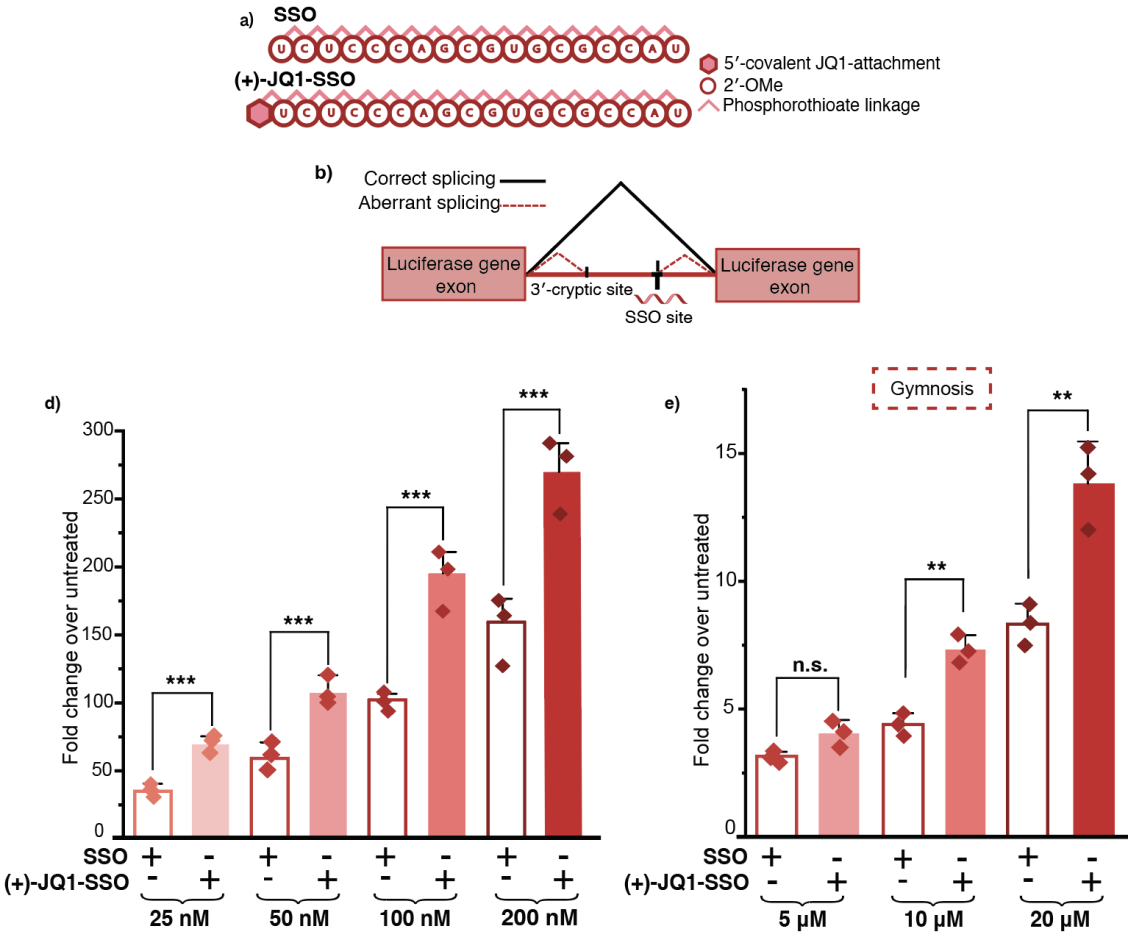

Figure 2.8: Covalent (+)-JQ1-SSO modification enhances slice-switching activity. (a) Sequence and chemical modifications for SSO used in the HeLa pLuc 705 cell line. (b) Splice-switching mechanism in HeLa pLuc 705 cells. (c) Luminescence values for SSO and (+)-JQ1-SSO activity, transfected with LLipofectamine 2000, at 24 hours at concentrations indicated. In all cases, luciferase activity was measured and normalised to untreated cells. (d) Luminescence values for SSO and (+)-JQ1-SSO activity, using gymnotic delivery, at 96 hours at concentrations indicated. In all cases, luciferase activity was measured and normalised to untreated cells. The vertical bars represent the mean and the error bars the standard deviation. ** represents $p<0.05$, *** represents $p<0.01$, n.s. represents p values that are not significant. *Figure adapted from "Harnessing BET-Bromodomain Assisted Nuclear Import for Targeted Subcellular Localization and Enhanced Efficacy of Antisense Oligonucleotides" by Kashyap et al., under CC-BY 4.0.*

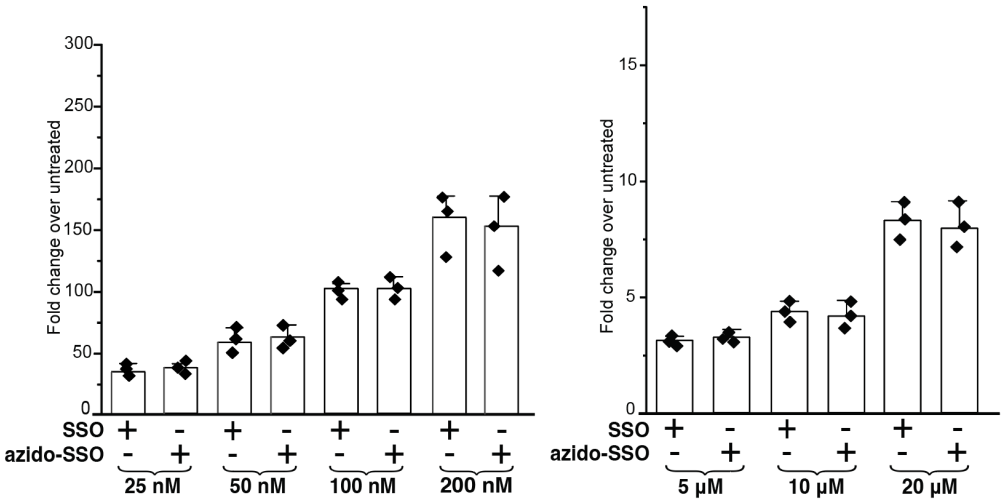

Figure 2.9: Luminescence values for SSO and azido-SSO activity for (a) transfection with lipofectamine 2000, at 24 hours, (b) gymnotic uptake at 96 hours at concentrations indicated. In all cases, luciferase activity was measured and normalised to untreated cells. The vertical bars represent the mean and the error bars the standard deviation. ** represents $p<0.05$, *** represents $p<0.01$, n.s. represents p values that are not significant. *Figure re-produced from supplementary information of "Harnessing BET-Bromodomain Assisted Nuclear Import for Targeted Subcellular Localization and Enhanced Efficacy of Antisense Oligonucleotides" by Kashyap et al., under CC-BY 4.0.*

Since covalent conjugation with small molecules can alter the cytotoxicity of oligonucleotide therapeutics[173], an assessment was performed to determine whether the attachment of (+)-JQ1 affected the baseline toxicity profile of the SSO. Moreover, (+)-JQ1 has been shown to inhibit cell proliferation significantly in a dose- and time-dependent manner in HeLa cells[174]. However, covalent addition of (+)-JQ1 resulted in little to no increase in the toxicity of the SSO at any concentration, relative to its unconjugated form in this HeLa model – assessed through total protein production quantified by BCA (Figure 2.10a) and CellTiter-Glo (Figure 2.10b).

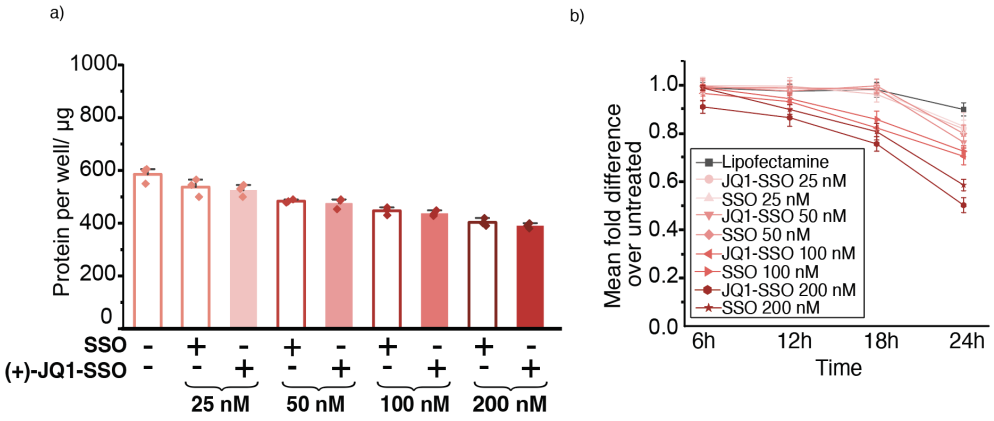

Figure 2.10: Covalent addition of (+)-JQ1 resulted in little to no increase in the toxicity of the SSO. (a) Cell protein production for indicated SSO treatment over 24h lipofectamine 2000 transfection quantified by BCA. (b) Viability of the HEK293T upon SSO and JQ1-SSO treatment evaluated by Cell-Titer Glo. The vertical bars represent the mean and the error bars the standard deviation. ** represents $p<0.05$, *** represents $p<0.01$, n.s. represents p values that are not significant. *Figure adapted from supplementary information of"Harnessing BET-Bromodomain Assisted Nuclear Import for Targeted Subcellular Localization and Enhanced Efficacy of Antisense Oligonucleotides" by Kashyap et al., under CC-BY 4.0.*

2.3.4 Enhanced JQ1-SSO conjugate activity is dependant upon specific interactions with BET bromodomain proteins

To confirm that the improved splice switching was driven by BET protein-mediated nuclear import rather than non-specific binding to cellular proteins, a blockade assay was conducted using excess small molecule (+)-JQ1. This assay was based on the hypothesis that excess (+)-JQ1 would saturate BET bromodomain binding sites, thereby blocking (+)-JQ1-SSO conjugate binding and resulting in a loss of activity. At low concentrations of (+)-JQ1 (5 nM), the activity of the unmodified

SSO remained unchanged, but the enhanced activity of the (+)-JQ1-SSO conjugate at 25 and 50 nM was effectively inhibited (Figure 2.11a). Consistent with the understanding that the (+)-JQ1-ASO conjugate functions via interaction with BET proteins, even higher concentrations of 200 nM (+)-JQ1 were required to inhibit the enhanced activity of the (+)-JQ1-SSO at 100 nM and 200 nM (Figure 2.11b). This trend was also observed across a broader range of SSO concentrations (Figure 2.12).

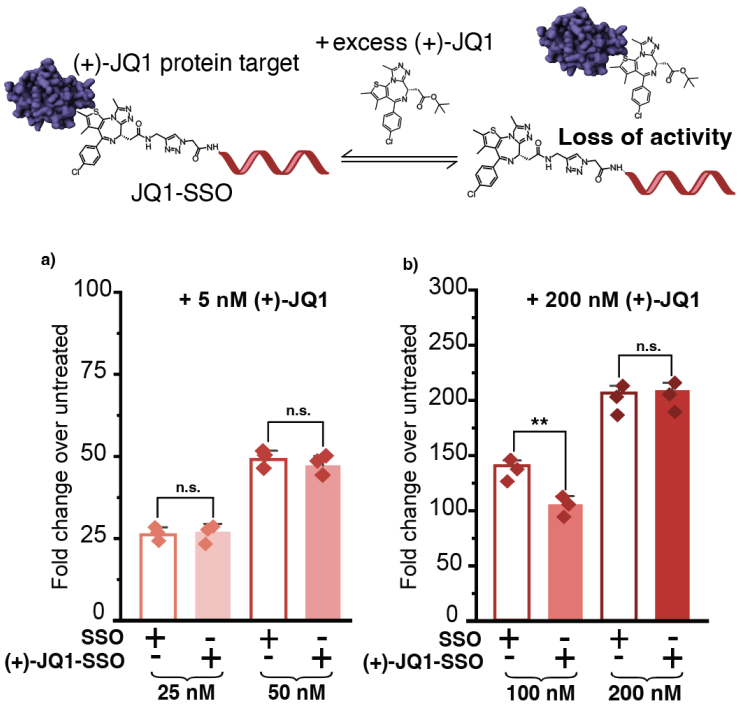

Figure 2.11: (+)-JQ1-SSO conjugate relies upon BET-protein engagement for enhancement of splice switching activity. Competition assay between (+)-JQ1-ASO conjugate and excess small molecule, (+)-JQ1 at a) 5nM and b) 200 nM results in loss of enhanced knockdown, assayed by RT-qPCR. Three biological replicates are shown as diamonds for each condition (each from three technical replicates). The vertical bars represent the mean and the error bars the standard deviation. ** represents $p<0.05$, *** represents $p<0.01$, n.s. represents p values that are not significant. *Figure adapted from "Harnessing BET-Bromodomain Assisted Nuclear Import for Targeted Subcellular Localization and Enhanced Efficacy of Antisense Oligonucleotides" by Kashyap et al., under CC-BY 4.0.*

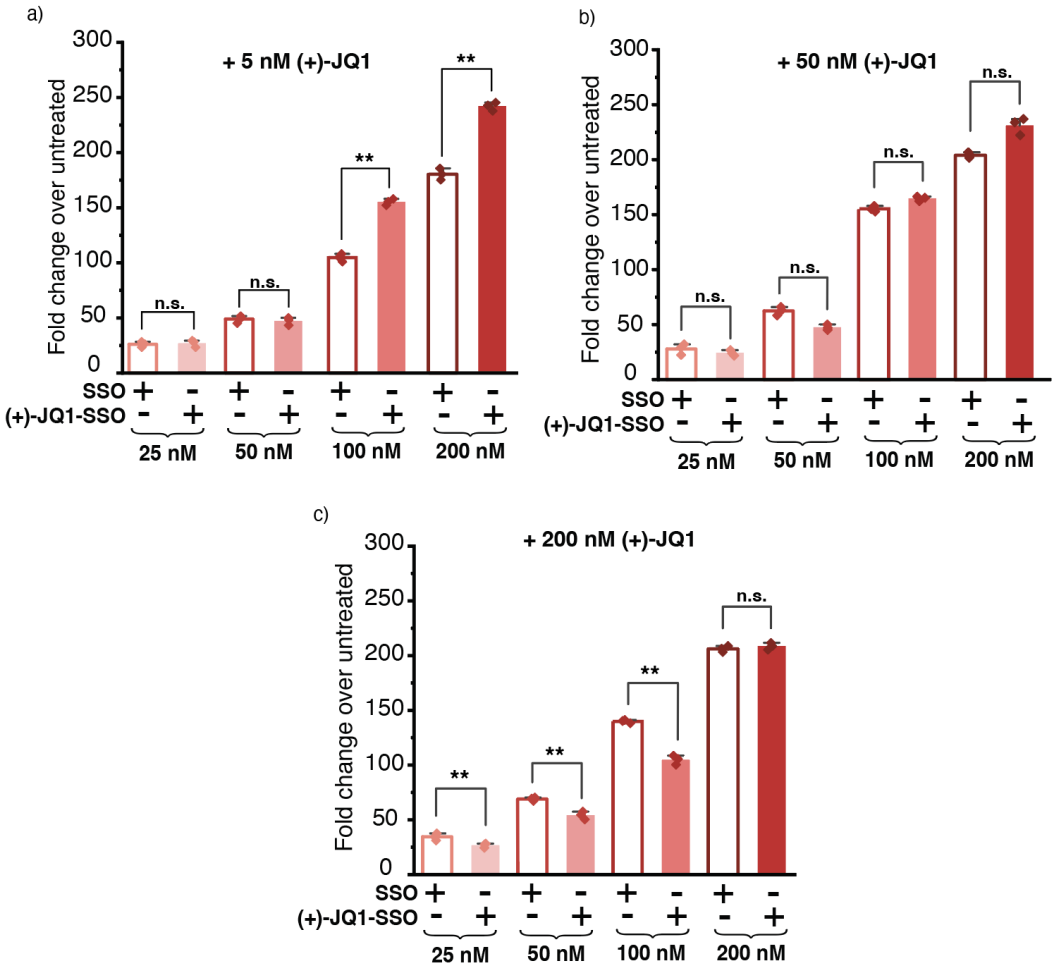

Figure 2.12: (+)-JQ1-SSO conjugate relies upon BET-protein engagement for enhancement of splice switching activity over wide range of concentrations. Competition assay between (+)-JQ1-ASO conjugate and excess small molecule, (+)-JQ1 at (a) 5nM, (b) 50 nM, and (c) 200 nM. Three biological replicates are shown as diamonds for each condition (each from three technical replicates). The vertical bars represent the mean and the error bars the standard deviation. ** represents $p<0.05$, *** represents $p<0.01$, n.s. represents p values that are not significant. *Figure re-produced from supplementary information from "Harnessing BET-Bromodomain Assisted Nuclear Import for Targeted Subcellular Localization and Enhanced Efficacy of Antisense Oligonucleotides" by Kashyap et al., under CC-BY 4.0.*

Thus, this demonstrated that splice-switching ASO activity can be doubled via a specific interaction with the BET proteins for enhanced nuclear import.

2.3.5 Synthesis of JQ1-MALAT1 gapmer ASO conjugate

After achieving an improvement in splice-switching activity, the potential to extend this approach to RNase H–mediated gene knockdown was tested. Our test system was a 20-mer ASO targeting the gold-standard knockdown target metastasis-associated lung adenocarcinoma transcript 1 (*MALAT1*), a nuclear-enriched long non-coding RNA (lncRNA)[100]. *MALAT1* plays critical roles in gene regulation and metastasis in cancer and is primarily retained in the nucleus[175,176]. This nuclear-localized target was selected to evaluate knockdown activity specifically within the nucleus.

In line with the current state-of-the-art for ASO design, the MALAT1-ASO used was designed as a 'gapmer', featuring a fully PS backbone with terminal wings consisting of five 2′-methoxy-ethyl (MOE) sugar modifications (Figure 2.13a,b). In this 'gapmer' design, the central region of DNA oligonucleotides is recognized by RNase H, while the flanks of 2′-modified sugars are RNase H-inactive but enhance nuclease stability and target binding[177].

The final (+)-JQ1-MALAT1 gapmer conjugate was prepared using copper-catalysed click conjugation of the (+)-JQ1-alkyne with the 5′-azide-MALAT1 gapmer (Appendix Figure A.17, Figure A.18). $>90\%$ yields were achieved for all bioconjugation reactions performed and $>95\%$ purity following HPLC purification.

2.3.6 JQ1-MALAT1 gapmer ASO outperforms unmodified MALAT1 gapmer ASO for RNase H-mediated mRNA knockdown

To evaluate the activity of the (+)-JQ1-MALAT1 gapmer RNase H-active conjugate (Figure 2.13a,b), *MALAT1* transcript levels were measured using reverse transcription-quantitative reverse transcription polymerase chain reaction (RT-qPCR) at 24 hours, comparing the knockdown to the unconjugated and azido-modified MALAT1 gapmer, normalized to the housekeeping gene GAPDH. Similar to the SSO conjugate, the (+)-JQ1-MALAT1 gapmer conjugate outperformed the unconjugated and azido-modified MALAT1 gapmer at all tested concentrations. The knockdown potency was improved, resulting in 20.1% 30.2% 56.8% and 54% less transcript with the (+)-JQ1 modified gapmer treatment compared to the unmodified gapmer at 5, 50, 100, and 200 nM, respectively (Figure 2.13c). *MALAT1* degradation was tracked over time by assessing transcript levels through RT-qPCR at 6, 12, and 24 hours following treatment. A significant reduction in *MALAT1* transcript levels was observed upon treatment with the (+)-JQ1-MALAT1 gapmer compared to the unmodified gapmer at all time points tested (Figure 2.13d).

To assess uptake in a more clinically relevant manner, gymnotic delivery was conducted with the (+)-JQ1-MALAT1 gapmer conjugate, comparing it to its unconjugated and azido-modified counterparts, at 5, 10, and 20 µM, quantified using

RT-qPCR as above. The gymnotically delivered (+)-JQ1-MALAT1 gapmer demonstrated a significant increase in *MALAT1* knockdown at all tested concentrations (Figure 2.13f). For both delivery methods, the unmodified MALAT1 gapmer and the azido-MALAT1 gapmer exhibited the same *MALAT1* knockdown, as expected (Figure 2.14), with values lower than those observed with the (+)-JQ1-modified MALAT1 gapmer, indicating that the enhanced knockdown was due to the presence of the (+)-JQ1 modification.

It was particularly notable that such a straightforward chemical modification could enhance the efficacy of an RNase H–mediated mechanism of action, beyond splice-switching, and that this effect was observed for a nuclear-enriched target where canonical knockdown strategies, like siRNA or shRNA[178], often display reduced efficiency.

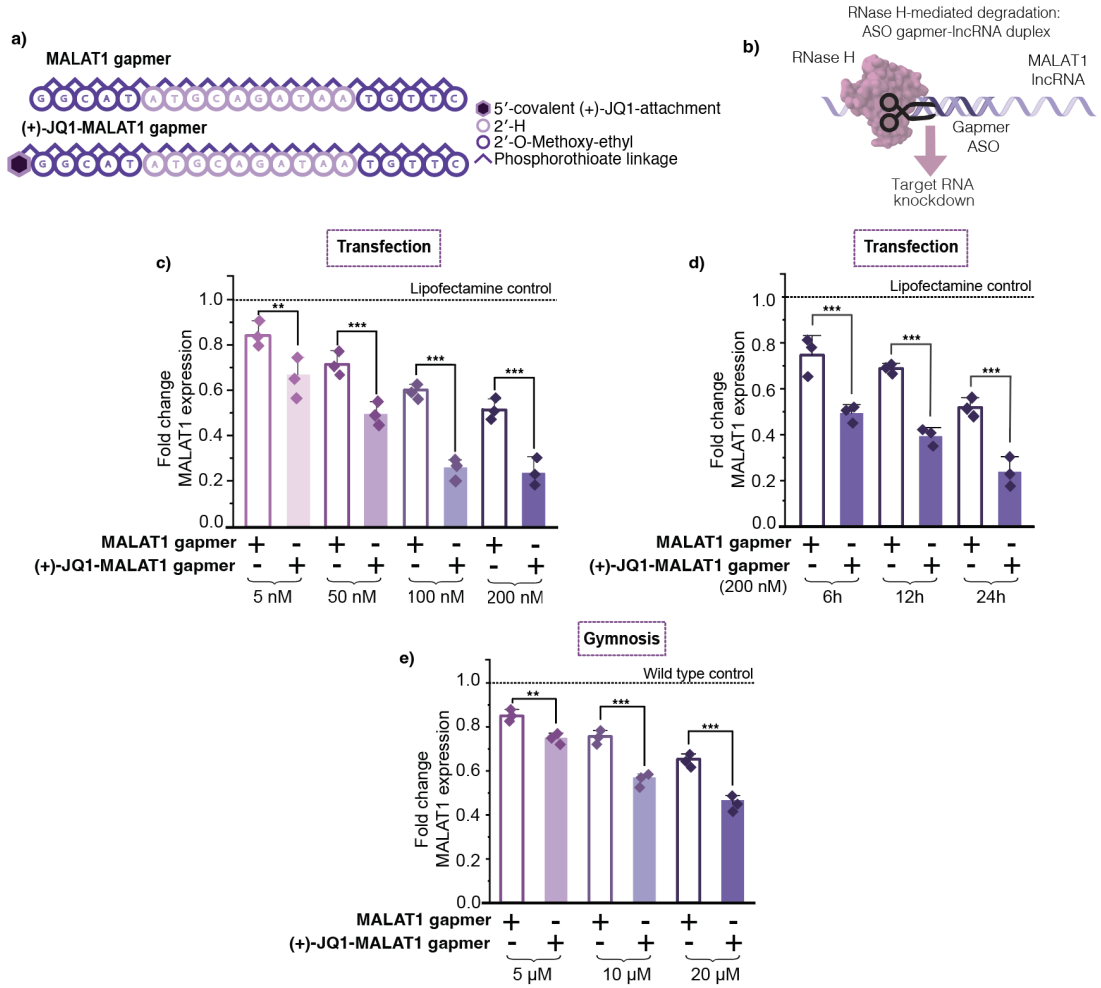

Figure 2.13: Covalent-(+)-JQ1 modification of an ASO enhances RNase H-mediated knockdown. (a) Sequence and chemical modifications for the MALAT1 gapmers used. (b) Mechanism of RNase H-mediated degradation of the lncRNA *MALAT1* by gapmer ASO. RT-qPCR data for *MALAT1* knockdown upon lipofectamine transfection of (+)-JQ1- and unconjugated-gapmer in HEK293T cells for (c) 24 hours at concentrations indicated, (d) a concentration of 200 nM for 6, 12, and 24 hours. (e) RT-qPCR data for *MALAT1* knockdown upon gymnosis of (+)-JQ1- and unconjugated-gapmer in HEK293T cells for 96 hours at concentrations indicated. For all RT-qPCR, three biological replicates are shown as diamonds for each condition (each from three technical replicates). The vertical bars represent the mean and the error bars the standard deviation. ** represents $p<0.05$, *** represents $p<0.01$, n.s. represents p values that are not significant. *Figure re-produced from "Harnessing BET-Bromodomain Assisted Nuclear Import for Targeted Subcellular Localization and Enhanced Efficacy of Antisense Oligonucleotides" by Kashyap et al., under CC-BY 4.0.*

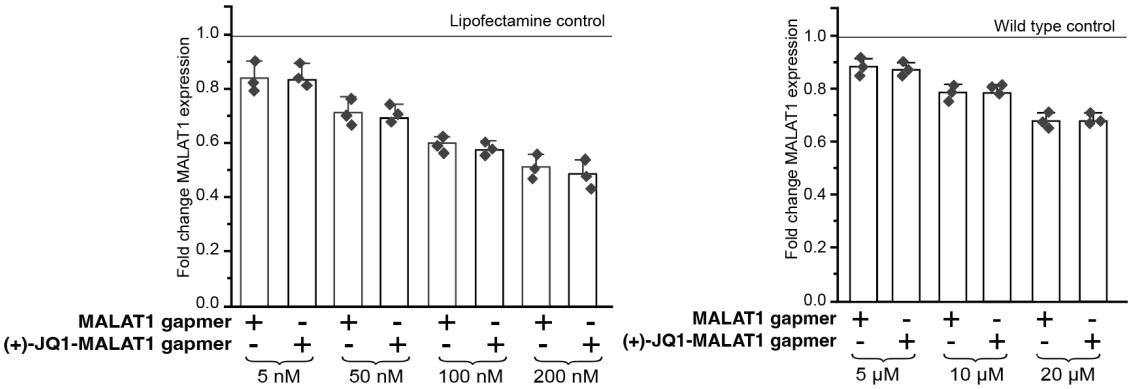

Figure 2.14: RT-qPCR data for *MALAT1* knockdown upon (a) lipofectamine transfection of unconjugated-MALAT1 gapmer and azido-MALAT1 gapmer in HEK293T cells for 24 hours at concentrations indicated, and (b) upon gymnosis of unconjugated-MALAT1 gapmer and azido-MALAT1 gapmer in HEK293T cells for 96 hours at concentrations indicated. Three biological replicates are shown as diamonds for each condition (each from three technical replicates). The vertical bars represent the mean and the error bars the standard deviation. ** represents $p<0.05$, *** represents $p<0.01$, n.s. represents p values that are not significant. *Figure reproduced from supplementary information of "Harnessing BET-Bromodomain Assisted Nuclear Import for Targeted Subcellular Localization and Enhanced Efficacy of Antisense Oligonucleotides" by Kashyap et al., under CC-BY 4.0.*

2.3.7 Improved JQ1-MALAT1 gapmer conjugate activity relies upon BET bromodomain protein-engagement

As with the SSO, it was investigated whether the enhanced activity of the (+)-JQ1–MALAT1 gapmer depended on specific (+)-JQ1–BET bromodomain protein interactions. The improvement in knockdown was found to rely on these interactions, as it was lost in the presence of excess amount of small molecule (+)-JQ1 (Figure 2.15). At a dose of 200 nM (+)-JQ1, the activity of the unmodified ASO remained unaffected but the enhanced activity of the (+)-JQ1-MALAT1 gapmer at

50, 100, and 200 nM was completely inhibited.

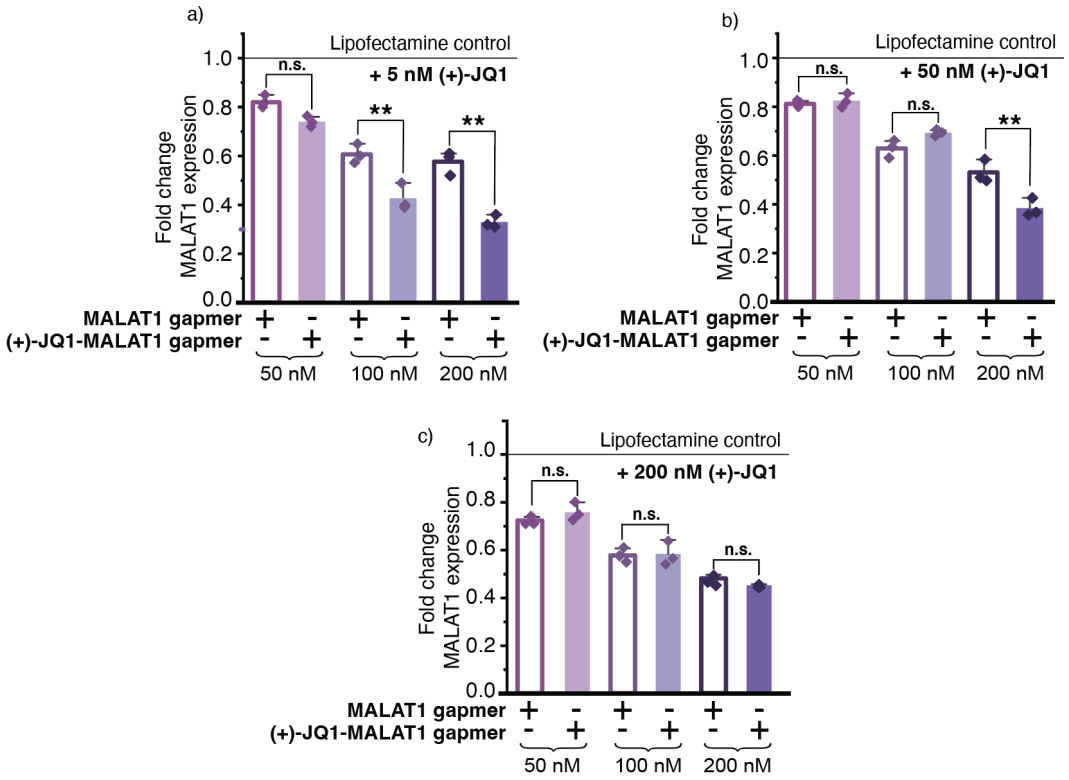

Figure 2.15: JQ1-MALAT1 gapmer enhanced activity dependant on BET-protein engagement. Competition assay between JQ1-MALAT1 gapmer and excess small molecule, (+)-JQ1 at (a) 5nM, (b) 50 nM, and (c) 200 nM. Error bars represent standard deviation. ** represents $p<0.05$, *** represents $p<0.01$, n.s. represents p value not significant. *Figure re-produced from supplementary information of "Harnessing BET-Bromodomain Assisted Nuclear Import for Targeted Subcellular Localization and Enhanced Efficacy of Antisense Oligonucleotides" by Kashyap et al., under CC-BY 4.0.*

Moreover, little to no increase in toxicity was observed for the (+)-JQ1-MALAT1 gapmer conjugate compared to the unconjugated MALAT1 gapmer at all concentrations (Figure 2.16). Functional testing was also extended to A549 cells, a clinically relevant lung adenocarcinoma model (Figure 2.17), observing a similar trend where the (+)-JQ1-modified ASO consistently outperformed its unmodified counterpart.

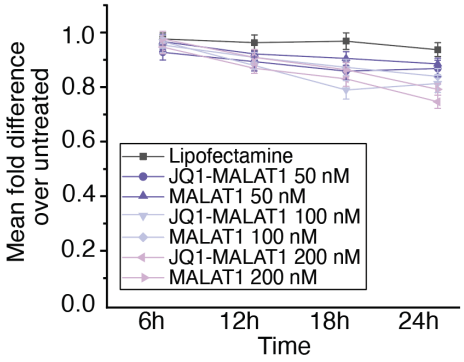

Figure 2.16: Viability of the HEK293T upon MALAT1 gapmer and JQ1-MALAT1 gapmer treatment evaluated by Cell-Titer Glo. *Figure re-produced from supplementary information of "Harnessing BET-Bromodomain Assisted Nuclear Import for Targeted Subcellular Localization and Enhanced Efficacy of Antisense Oligonucleotides" by Kashyap et al., under CC-BY 4.0.*

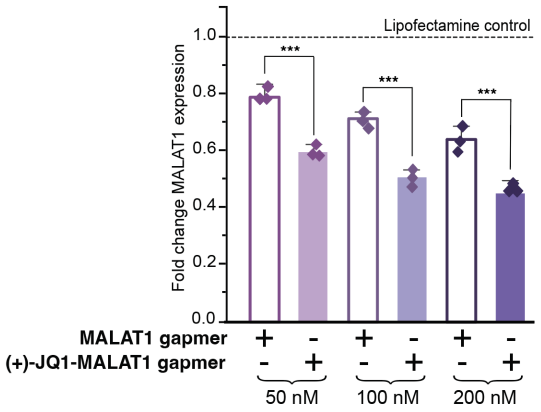

Figure 2.17: RT-qPCR data for *MALAT1* knockdown upon lipofectamine transfection of unconjugated-MALAT1 gapmer and azido-MALAT1 gapmer in A549 cells for 24 hours at concentrations indicated. *Figure re-produced from supplementary information of "Harnessing BET-Bromodomain Assisted Nuclear Import for Targeted Subcellular Localization and Enhanced Efficacy of Antisense Oligonucleotides" by Kashyap et al., under CC-BY 4.0.*

2.3.8 Enhancement in JQ1-MALAT1 gapmer conjugate activity due to increased nuclear concentration

Experiments performed by Martina Caddedu, MRC Nucleic Acid Therapy Accelerator

Next, to assess whether the addition of the (+)-JQ1-modification increased the nuclear localization of the conjugated ASO, immunocytochemistry was performed using an antibody raised against the PS backbone modification[179]. HEK293 cells were transfected with either the unmodified MALAT1 gapmer or the (+)-JQ1-MALAT1 gapmer at 200 nM and 500 nM for 24 hours, followed by immunostaining. Cells transfected with the unmodified ASO showed localization primarily in the perinuclear regions, as previously described for gapmers of this chemical composition[64]. In contrast, cells transfected with (+)-JQ1-*MALAT1* exhibited a significantly higher anti-PS signal within Hoechst-stained nuclei compared to those treated with the unmodified ASO (Figure 2.18a,b, Appendix Figure A.62), indicating enhanced nuclear localization of the JQ1-conjugated ASO. Specificity of the anti-PS immunostaining was confirmed by the absence of signal in Lipofectamine 2000-only treated cells (Figure 2.18a, Appendix Figure A.62).

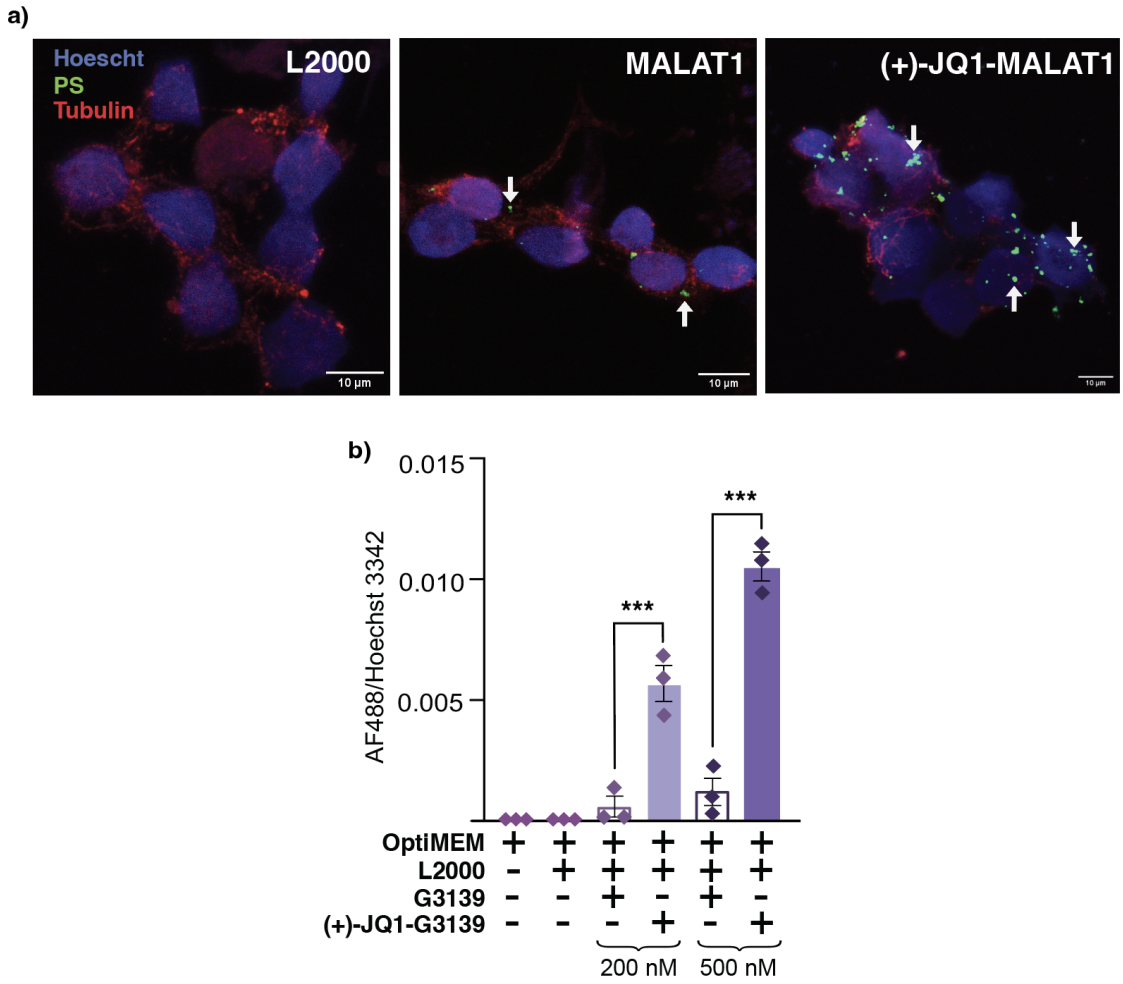

Figure 2.18: (+)-JQ1 modification increases concentration of ASO in the nucleus. (a) Representative immunocyochemistry of HEK293 cells transfected with 200 nM of the ASOs indicated for 24-hours using antibodies against the PS modifications (green) and a/b-tubulin (red). Arrows indicate ASO-containing puncta. Images are maximum intensity projections generated from Z-stacks; magnification 63x, scale bars as indicated. (b) Quantification of the fluorescent signal ratio between the PS immunopositive signal (AF488) within Hoechst-stained nuclei from HEK293T cells treated with the ASO concentrations as shown. Biological replicates represent random fields of view per condition. Data are shown as the mean +/- SEM. *Figure adapted from "Harnessing BET-Bromodomain Assisted Nuclear Import for Targeted Subcellular Localization and Enhanced Efficacy of Antisense Oligonucleotides" by Kashyap et al., under CC-BY 4.0. This data was generated by M. Caddedu, MRC NATA*

Together, these data demonstrate that (+)-JQ1 conjugation can significantly en-

hance both the splice-switching and gene-knockdown activity of ASOs across multiple cell lines. These functional improvements are dependent on BET protein interactions and consistent with previously reported (+)-JQ1-mediated nuclear transport of cytosolic proteins[164]. Furthermore, the increase in activity correlates with enhanced nuclear accumulation of the conjugated ASOs, as demonstrated by immunocytochemistry.

2.3.9 Synthesis of JQ1-Oblimersen

While MALAT1-targeting antisense oligonucleotides (ASOs) are currently being evaluated for therapeutic applications, Oblimersen (G3139) is a more advanced clinical candidate. G3139 is a first-generation 18-mer ASO with a fully PS backbone, designed to target the anti-apoptotic factor *BCL-2*. It has progressed to multiple phase III clinical trials (Figure 2.19a,b). *BCL-2* is a critical inhibitor of apoptosis that is overexpressed in various cancers[180]. Despite promising phase I-II results as a sensitizer for chemotherapy, G3139 failed to show efficacy in phase III trials[181]. Given that G3139 was well-tolerated by patients, the limiting factor was likely thought to be sub-cellular compartmentalisation, target engagement and efficacy[182]. Since G3139 functions as an RNase H–active ASO, similar to the MALAT1 gapmer, it was examined whether a (+)-JQ1–G3139 conjugate could result in a more potent drug molecule.

The (+)-JQ1-G3139 conjugate was synthesised using the same copper-catalysed

click methodology as the previous ASOs. The 5′-azide-G3139 was synthesised from the commercially-obtained 5′-amine G3139 PS ASO using azidoacetic acid-NHS ester functionalisation, and the (+)-JQ1 conjugate was synthesised through a copper-catalysed click reaction with the (+)-JQ1-alkyne (Appendix Figure A.19, Figure A.20).

To assess the specificity of the (+)-JQ1 conjugate-mediated activity and evaluate any potential effects of the (+)-JQ1 moiety when conjugated to an oligonucleotide, a (+)-JQ1-conjugated non-targeting phosphorothioate ASO ((+)-JQ1-NTC-ASO) control was included in our experimental design. The (+)-JQ1-NTC-ASO was synthesized following the same approach described above (Appendix Figure A.21).

2.3.10 JQ1-Oblimersen conjugate outperforms unmodified Oblimersen at both target mRNA and protein level reduction

The fully PS, RNase H-active G3139, azido-G3139, (+)-JQ1-NTC ASO, and (+)-JQ1-G3139 (Figure 2.19a,b) were transfected into HEK293T cells and *BCL-2* transcript and protein levels were measured using RT-qPCR and western blotting respectively after 24 hours. The (+)-JQ1-G3139 conjugate dramatically outperformed the unconjugated G3139, azido-G3139, and (+)-JQ1-NTC-ASO at all tested concentrations. On-target activity was improved by 43.9% 51.3% 50.9% and 64.5% with the conjugated (+)-JQ1-G3139 compared to the unconjugated G3139 at 50,

100, 200, and 500 nM, respectively (Figure 2.19c). A significant reduction in comparative protein levels was also observed, particularly at lower ASO concentrations (Figure 2.19d, Appendix Figure A.45).

A time-course study was conducted to profile the kinetics of *BCL-2* degradation by assessing transcript levels via RT-qPCR at 6, 12, and 24 hours following treatment. A significant reduction in *BCL-2* transcript levels was observed with the (+)-JQ1-G3139 conjugate compared to the unconjugated G3139 at all time points tested.

To assess cellular uptake in a more clinically relevant manner, gymnotic delivery of the (+)-JQ1-G3139 conjugate was performed, comparing activity to its unconjugated and azido-modified counterparts and the (+)-JQ1-NTC-ASO, at 5, 10, and 20 µM, quantified using RT-qPCR as described. Gymnotically delivered (+)-JQ1-G3139 ASO showed a significant increase in knockdown compared to unmodified G3139 at all tested concentrations at the RNA level.

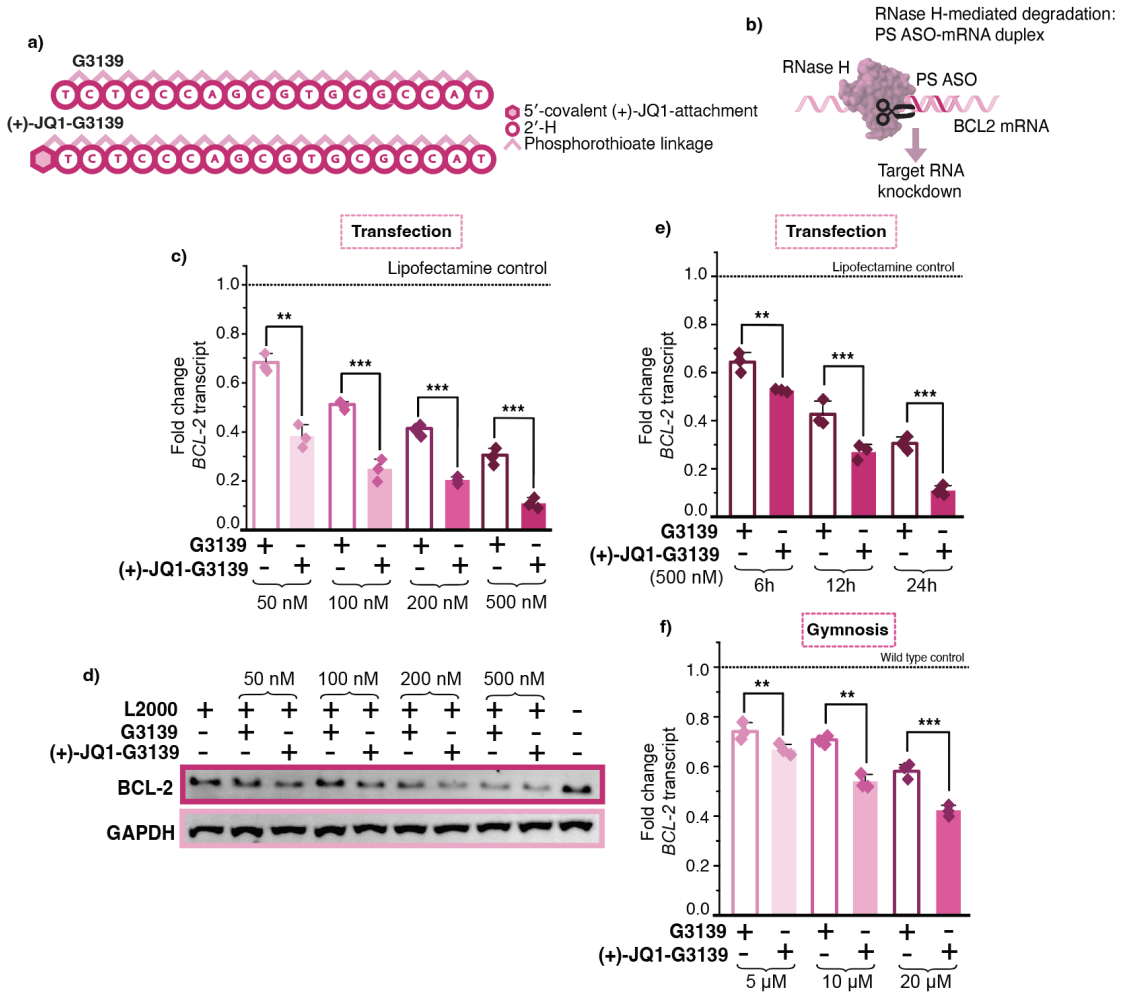

Figure 2.19: (+)-JQ1-G3139 outperformed the unconjugated G3139, a late-stage clinical ASO. (a) Sequence and chemical modifications for Oblimersen (G3139) used. (b) Mechanism of RNase H-mediated degradation of *BCL-2* mRNA by a gapmer ASO. (c) RT-qPCR data of *BCL-2* knockdown upon (+)-JQ1-G3139 and unconjugated-G3139 Lipofectamine transfection in HEK293Ts for 24 hours at concentrations indicated. (d) RT-qPCR data of *BCL-2* knockdown upon (+)-JQ1-G3139 and unconjugated-G3139 Lipofectamine transfection in HEK293Ts at 500 nM at 6, 12, and 24 hours. (e) RT-qPCR data of *BCL-2* knockdown upon (+)-JQ1-G3139 and unconjugated-G3139 Lipofectamine upon gymnotic delivery in HEK293Ts at 96 hours at the concentrations indicated. (f) Western blot of *BCL-2* levels upon treatment with G3139 and (+)-JQ1-G3139 upon transfection with Lipofectamine at 24 hours at concentrations indicated. Normalised to GAPDH expression levels. *Figure adapted from "Harnessing BET-Bromodomain Assisted Nuclear Import for Targeted Subcellular Localization and Enhanced Efficacy of Antisense Oligonucleotides" by Kashyap et al., under CC-BY 4.0.*

In comparison, for delivery by both transfection (Figure 2.20a) and gymnosis (Figure 2.20b), azido-G3139 showed no significant increase in *BCL-2* knockdown compared to unmodified G3139, demonstrating that the observed effect was specific to the covalent (+)-JQ1 modification of G3139. Additionally, the (+)-JQ1-NTC-ASO showed no significant effect on *BCL-2* transcript levels, confirming that the (+)-JQ1 small molecule conjugated to an oligonucleotide alone does not affect activity.

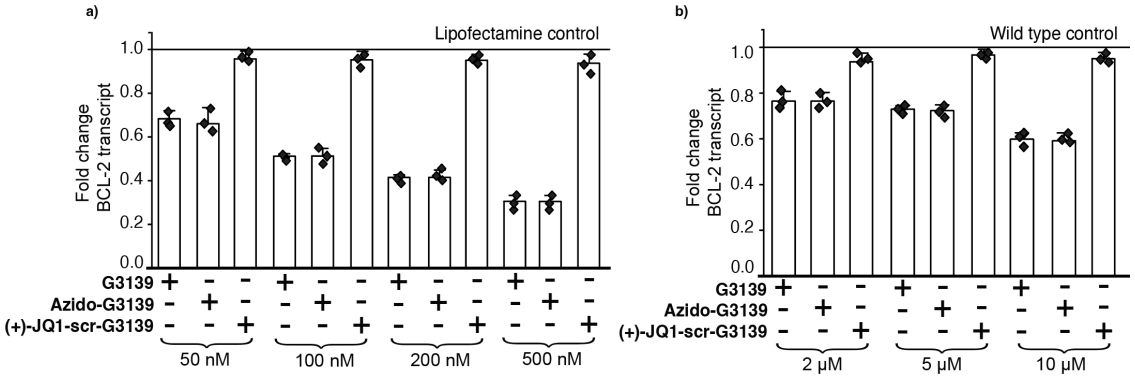

Figure 2.20: RT-qPCR data of *BCL-2* knockdown upon unconjugated-G3139, azido-G3139, and (+)-JQ1-NTC-ASO (a) transfection for 24 hours, (b) gymnosis for 96 hours in HEK293Tsat concentrations indicated. *Figure re-produced from supplementary information of "Harnessing BET-Bromodomain Assisted Nuclear Import for Targeted Subcellular Localization and Enhanced Efficacy of Antisense Oligonucleotides" by Kashyap et al., under CC-BY 4.0.*

2.3.11 Improved JQ1-Oblimersen activity relies upon BET bromodomain protein-engagement

A blockade assay was conducted using excess small molecule (+)-JQ1, similar to the approach used with the other conjugates to assess the mechanism of enhanced (+)-JQ1-G3139 activity. As expected, at both the 5 and 200 nM doses of small molecule (+)-JQ1, the activity of unmodified G3139 was unaffected. However,

at 5 nM (+)-JQ1, the enhanced activity of (+)-JQ1-G3139 at 100 nM showed a significant reduction, and at 200 nM (+)-JQ1, the enhanced activity of (+)-JQ1-G3139 at 100 nM was fully inhibited (Figure 2.21). As observed with previous (+)-JQ1 conjugates, little to no increase in cellular toxicity was observed for (+)-JQ1-G3139 compared to the unconjugated ASO (Figure 2.22).

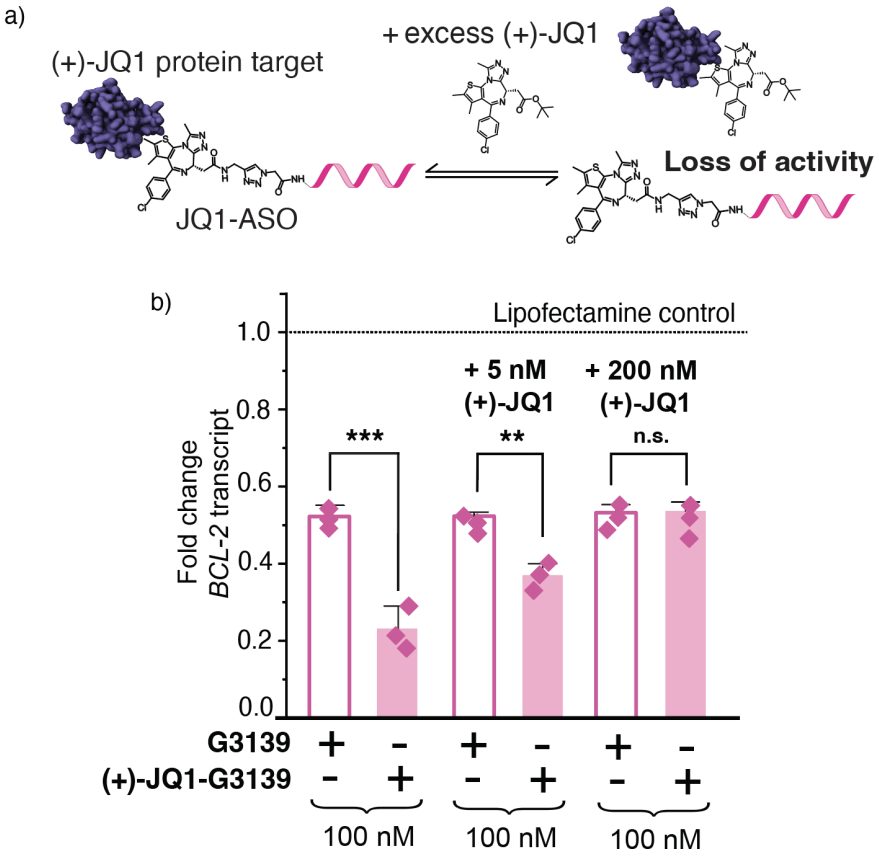

Figure 2.21: Reduction of enhanced *BCL-2* knockdown observed in competition assay in the presence of 5 nM and 200 nM (+)-JQ1. *Figure re-produced from "Harnessing BET-Bromodomain Assisted Nuclear Import for Targeted Subcellular Localization and Enhanced Efficacy of Antisense Oligonucleotides" by Kashyap et al., under CC-BY 4.0.*

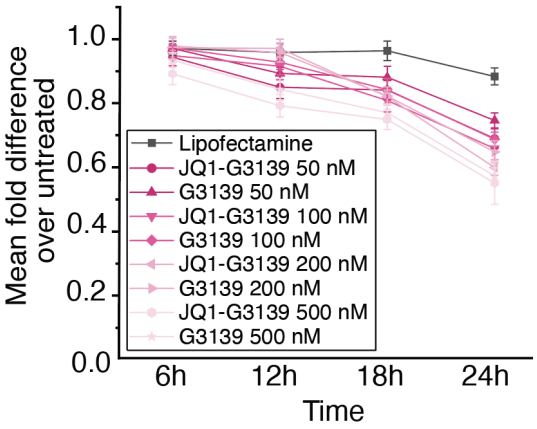

Figure 2.22: Viability of the HEK293T upon G3139 and JQ1-G3139 treatment evaluated by Cell-Titer Glo. *Figure re-produced from "Harnessing BET-Bromodomain Assisted Nuclear Import for Targeted Subcellular Localization and Enhanced Efficacy of Antisense Oligonucleotides" by Kashyap et al., under CC-BY 4.0.*

2.3.12 Enhancement in JQ1-G3139 conjugate activity is a result of increased nuclear concentration

To confirm that the enhanced ASO activity resulted from increased nuclear accumulation, the levels of G3139 and the (+)-JQ1-G3139 conjugate within the nucleus and cytoplasm were quantified using sub-cellular fractionation. To enable simple fluorescence-based detection of ASO localization, a (+)-JQ1-G3139-Cy3 conjugate was synthesised. The (+)-JQ1-G3139-Cy3 conjugate was synthesized as described above, from the commercially available 5′-terminal amine- and 3′-terminal Cy3-modified G3139 PS ASO. A 5′-azide was installed using azidoacetic acid-NHS ester functionalization, and the final (+)-JQ1-G3139-Cy3 conjugate was synthesized through a copper-catalyzed click reaction of the 5′-azide-G3139-3′-Cy3 with the (+)-JQ1-alkyne (Appendix Figure A.22, Figure A.23).

RT-qPCR was first used to confirm that addition of a Cy3 moiety at the 3′ end of G3139 or (+)-JQ1–G3139 did not affect the knockdown activity observed previously (Figure 2.23a). The cells were then transfected with either G3139-Cy3 or (+)-JQ1-G3139-Cy3 for 6, 12, and 24 hours, followed by sub-cellular fractionation (Figure 2.23b). The fluorescence intensity of the cytoplasmic and nuclear fractions was measured using a plate reader.

A significant increase in the nuclear accumulation of the (+)-JQ1-G3139-Cy3 conjugate was observed compared to its unmodified counterpart, at both 200 nM and 500 nM, for all time points. This indicates that the enhanced nuclear accumulation was driven by the covalent (+)-JQ1 modification (Figure 2.24). Furthermore, the nuclear and cytoplasmic distribution of G3139 and (+)-JQ1-G3139 at 200 nM and 500 nM was consistent with the activity trends observed at the protein and RNA levels.

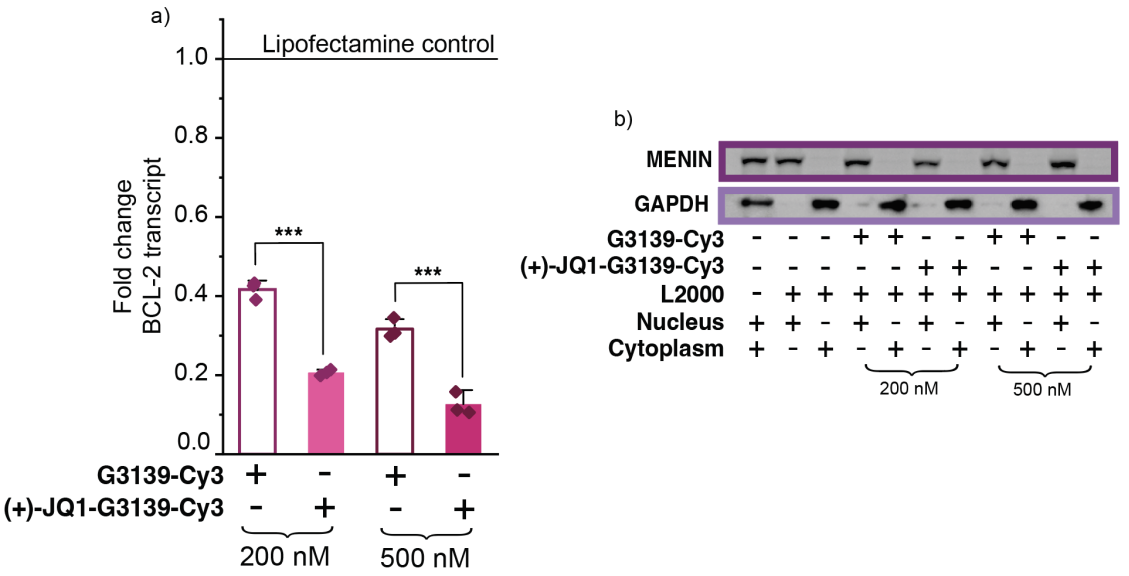

Figure 2.23: Addition of Cy3 moiety has no effect on JQ1-ASO activity. (a) RT-qPCR data of BCL-2 knockdown upon G3139-Cy3 and (+)-JQ1-G3139-Cy3 lipofectamine transfection in HEK293Ts for 24 hours at concentrations indicated; (b) Western blot for verification of successful cytoplasmic (GAPDH) and nuclear (MENIN) fractionation upon G3139-Cy3 and (+)-JQ1-G3139-Cy3 lipofectamine transfection in HEK293Ts for 24 hours at concentrations indicated. *Figure reproduced from supplementary information of "Harnessing BET-Bromodomain Assisted Nuclear Import for Targeted Subcellular Localization and Enhanced Efficacy of Antisense Oligonucleotides" by Kashyap et al., under CC-BY 4.0.*

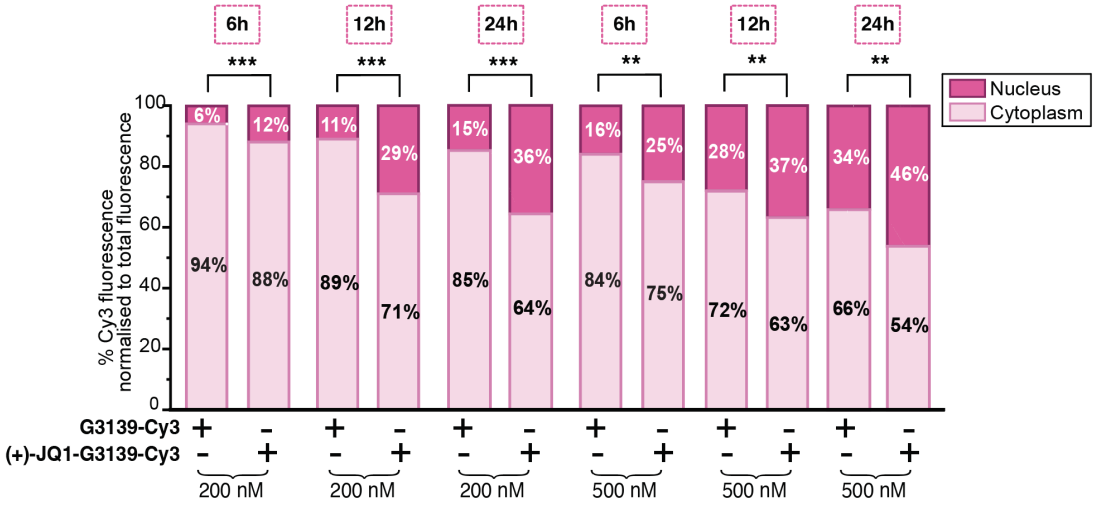

Figure 2.24: Enhanced (+)-JQ1-G3139 knockdown activity observed in presence of increased ASO concentration in the nucleus: percent Cy3 fluorescence normalised to total fluorescence in nuclear or cytoplasmic fraction upon (+)-JQ1-G3139 and unconjugated-G3139 lipofectamine transfection in HEK293Ts for 6, 12, and 24 hours at concentrations indicated. *Figure adapted from "Harnessing BET-Bromodomain Assisted Nuclear Import for Targeted Subcellular Localization and Enhanced Efficacy of Antisense Oligonucleotides" by Kashyap et al., under CC-BY 4.0.*

Experiment performed by Martina Caddedu, MRC Nucleic Acid Therapy Accelerator

To corroborate these findings, which were based on fluorescently labeled ASOs, anti-PS immunocytochemistry was performed using (+)-JQ1-G3139 and unconjugated G3139 without fluorescent tags following a 24-hour transfection at 200 nM and 500 nM. In line with the results from *MALAT1*-targeted staining, a significant increase in the nuclear-localised signal was observed for the (+)-JQ1-G3139 conjugate compared to the unconjugated G3139 ASO (Figure 2.25, Appendix Figure A.63). As previously shown, the specificity of the anti-PS immunostaining was confirmed by the absence of signal in lipofectamine 2000-treated cells.

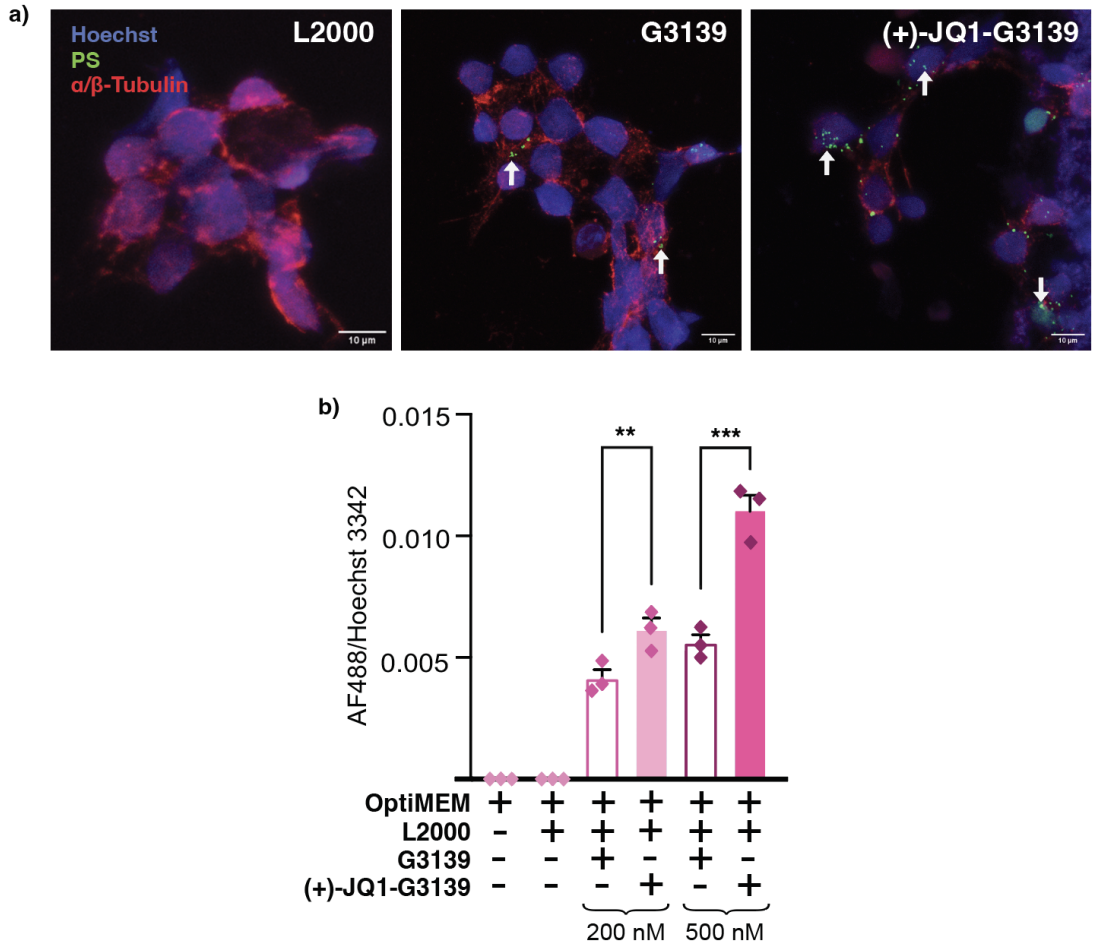

Figure 2.25: (+)-JQ1-modification increases the nuclear concentrations of G3139. (a) Representative immunocyochemistry of HEK293 cells transfected with 500 nM of unconjugated and (+)-JQ1-modified G3139 for 24 hours using antibodies against the PS modifications (green) and a/b-tubulin (red). Arrows indicate ASO-containing puncta. Images are maximum intensity projections generated from Z-stacks; magnification 63x, scale bars as indicated. (b) Quantification of the fluorescent signal ratio between the PS immunopositive signal (AF488) within Hoechst-stained nuclei from HEK293 cells treated with the ASO concentrations as shown. Biological replicates represent random fields of view per condition. The vertical bars represent the mean and the error bars the standard deviation. ** represents $p<0.05$, *** represents $p<0.01$. *Figure re-produced from "Harnessing BET-Bromodomain Assisted Nuclear Import for Targeted Subcellular Localization and Enhanced Efficacy of Antisense Oligonucleotides" by Kashyap et al., under CC-BY 4.0. This data was generated by M. Caddedu, MRC NATA*

2.3.13 JQ1-Oblimersen shows enhanced knockdown in clinically relevant leukemia cell line

To test our nuclear localization strategy in a more clinically relevant model, the activity of the (+)-JQ1-G3139 conjugate was evaluated in THP-1 cells, an acute myeloid leukemia (AML) cell line. G3139 had previously progressed to phase III clinical trials as a chemosensitiser (chemotherapy sensitisation) in AML for cytarabine-dosing regimens[182,183], highlighting its therapeutic potential. Testing the conjugate in this context allowed us to assess the feasibility of JQ1-mediated ASO nuclear transport in a disease-relevant setting (Figure 2.26a).

G3139, azido-G3139, (+)-JQ1-G3139, and (+)-JQ1-NTC-ASO were delivered into THP-1 cells using electroporation and *BCL-2* transcript levels were measured via RT-qPCR after 48 hours. The (+)-JQ1-G3139 conjugate significantly outperformed the unconjugated G3139 at all concentrations tested. The modified (+)-JQ1-G3139 showed 23.6% 35.8% and 48.3% less transcript compared to the unconjugated G3139 at 200 nM, 500 nM, and 1 µM, respectively (Figure 2.26b). Protein-level knockdown was then confirmed by measuring *BCL-2* protein levels after a second round of electroporation and western blotting at 96 hours. A marked reduction in protein levels was observed at all tested concentrations, in line with the trend observed at the RNA level (Figure 2.26c, Appendix Figure A.46, Figure A.47).

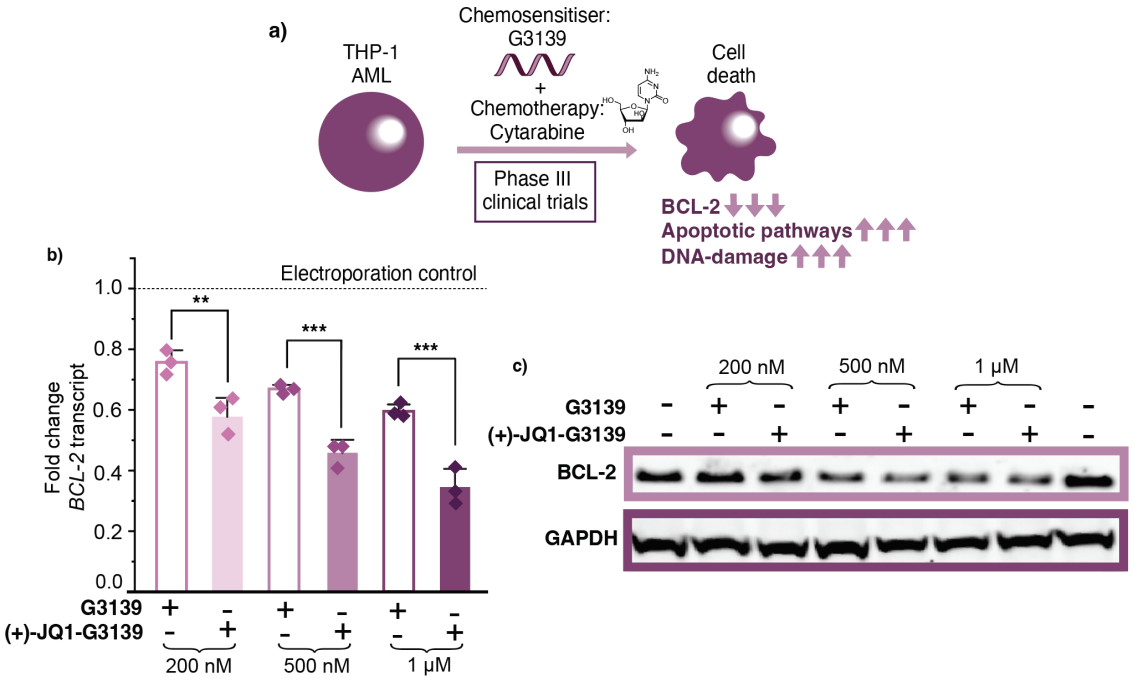

Figure 2.26: (+)-JQ1-G3139 shows enhanced knockdown and chemosensitisation in THP-1 cells, a clinically relevant model for AML. (a) Schematic for G3139 mechanism of action in the THP-1 AML cell line. (b) RT-qPCR data of BCL-2 knockdown upon (+)-JQ1-G3139 and unconjugated-G3139 upon electroporation for 48 hours at concentrations indicated. (c) Western blot of BCL-2 levels following treatment with G3139 and (+)-JQ1-G3139 upon two rounds of electroporation at 96 hours at concentrations indicated. Normalised to GAPDH expression levels. For RT-qPCR, three biological replicates are shown as diamonds for each condition (each from three technical replicates). The vertical bars represent the mean and the error bars the standard deviation. ** represents $p<0.05$, *** represents $p<0.01$, n.s. represents p values that are not significant. *Figure re-produced from "Harnessing BET-Bromodomain Assisted Nuclear Import for Targeted Subcellular Localization and Enhanced Efficacy of Antisense Oligonucleotides" by Kashyap et al., under CC-BY 4.0.*

As observed previously, azido-G3139 showed no significant difference in *BCL-2* knockdown compared to the unconjugated G3139, and the (+)-JQ1-NTC-ASO showed little to no effect on *BCL-2* transcript levels. This further confirms that the increased efficacy of *BCL-2* knockdown was attributed to the covalent (+)-JQ1

modification (Figure 2.27).

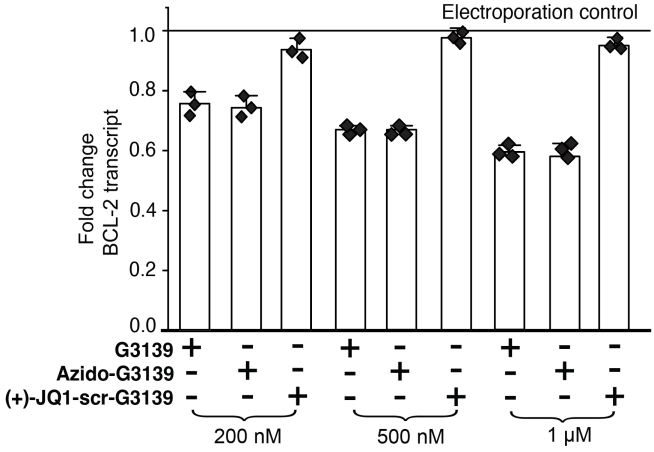

Figure 2.27: RT-qPCR data of BCL-2 knockdown upon unconjugated-G3139, azido-G3139, and (+)-JQ1-NTC-ASO electroporation in THP-1s for 48 hours at concentrations indicated. Three biological replicates are shown as diamonds for each condition (each from three technical replicates). The vertical bars represent the mean and the error bars the standard deviation. ** represents $p<0.05$, *** represents $p<0.01$, n.s. represents p values that are not significant. *Figure re-produced from supplementary information of "Harnessing BET-Bromodomain Assisted Nuclear Import for Targeted Subcellular Localization and Enhanced Efficacy of Antisense Oligonucleotides" by Kashyap et al., under CC-BY 4.0.*

A blockade assay was conducted next using excess small molecule (+)-JQ1, following the same approach used with G3139 in HEK293Ts. This was done to ascertain whether the same mechanism could be extended to THP-1 cells. The results were similar to those observed earlier. At both the 5 and 200 nM doses of (+)-JQ1, the activity of unmodified G3139 was unaffected. However, at 5 nM (+)-JQ1, the enhanced activity of (+)-JQ1-G3139 at 1 µM showed a significant reduction, and at 200 nM (+)-JQ1, the enhanced activity of (+)-JQ1-G3139 was completely lost (Figure 2.28a). This confirmed that the mechanism of action for the (+)-JQ1-mediated ASO nuclear transport could be extended to THP-1 cells.

Finally, to evaluate the chemosensitizing potential of (+)-JQ1-G3139, a CellTiter-Glo assay was performed. THP-1 cells were treated with G3139 alone and in combination with cytarabine to establish a baseline response, followed by treatment with (+)-JQ1-G3139 alone and in combination with cytarabine (Figure 2.28b). Notably, treatment with (+)-JQ1-G3139 resulted in a significantly greater reduction in cell viability compared to the unconjugated G3139, both as a single agent and in combination with cytarabine.

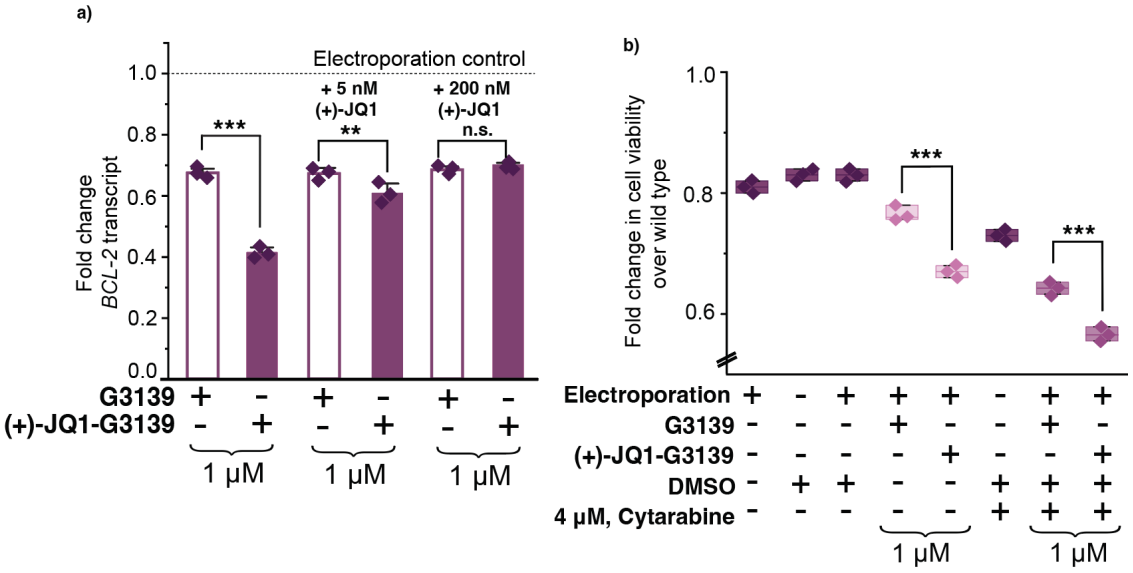

Figure 2.28: (+)-JQ1-G3139 shows enhanced knockdown and chemosensitisation in THP-1 cells. (a)Reduction of enhanced BCL-2 knockdown observed in competition assay in the presence of 5 nM and 200 nM (+)-JQ1 assayed by RT-qPCR. (b) Cell viability upon treatment with G3139 and (+)-JQ1-G3139 via electroporation for 48 hours as single agents or in combination with cytarabine, at concentrations indicated. For RT-qPCR, three biological replicates are shown as diamonds for each condition (each from three technical replicates). The vertical bars represent the mean and the error bars the standard deviation. ** represents $p<0.05$, *** represents $p<0.01$, n.s. represents p values that are not significant. *Figure adapted from "Harnessing BET-Bromodomain Assisted Nuclear Import for Targeted Subcellular Localization and Enhanced Efficacy of Antisense Oligonucleotides" by Kashyap et al., under CC-BY 4.0.*

2.3.14 RNA-seq profiling on the specificity and selectivity of JQ1-Oblimersen in an acute myeloid leukemia model

To investigate the transcriptional effects of the (+)-JQ1-ASO conjugates, RNA-seq profiling was conducted in THP-1 cells after a 48-hour treatment with G3139 and (+)-JQ1-G3139, using NTC-ASO and (+)-JQ1-NTC-ASO as the respective controls. RNA-seq profiling was considered essential, as (+)-JQ1 is known to broadly modulate transcriptional programs in THP-1 cells[184], and this approach enabled the differentiation of the effects of G3139-mediated knockdown, JQ1-mediated transcriptional changes, and any synergistic interactions from each other.

RNA-seq data was processed by **Catherine Chahrour** with the Seqnado pipeline developed by Catherine Chahrour and Alastair Smith, Milne lab.

Transcriptional signature of (+)-JQ1-G3139 draws from both G3139 and (+)-JQ1-NTC-ASO

Hierarchical clustering demonstrated that JQ1-G3139 induces a global gene expression pattern more closely aligned with G3139 than with the JQ1-NTC-ASO control. Heatmap of the top 50 up- and down-regulated genes highlighted this similarity, suggesting that the G3139 ASO component contributes substantially to the transcriptional signature of the conjugate (Figure 2.29).

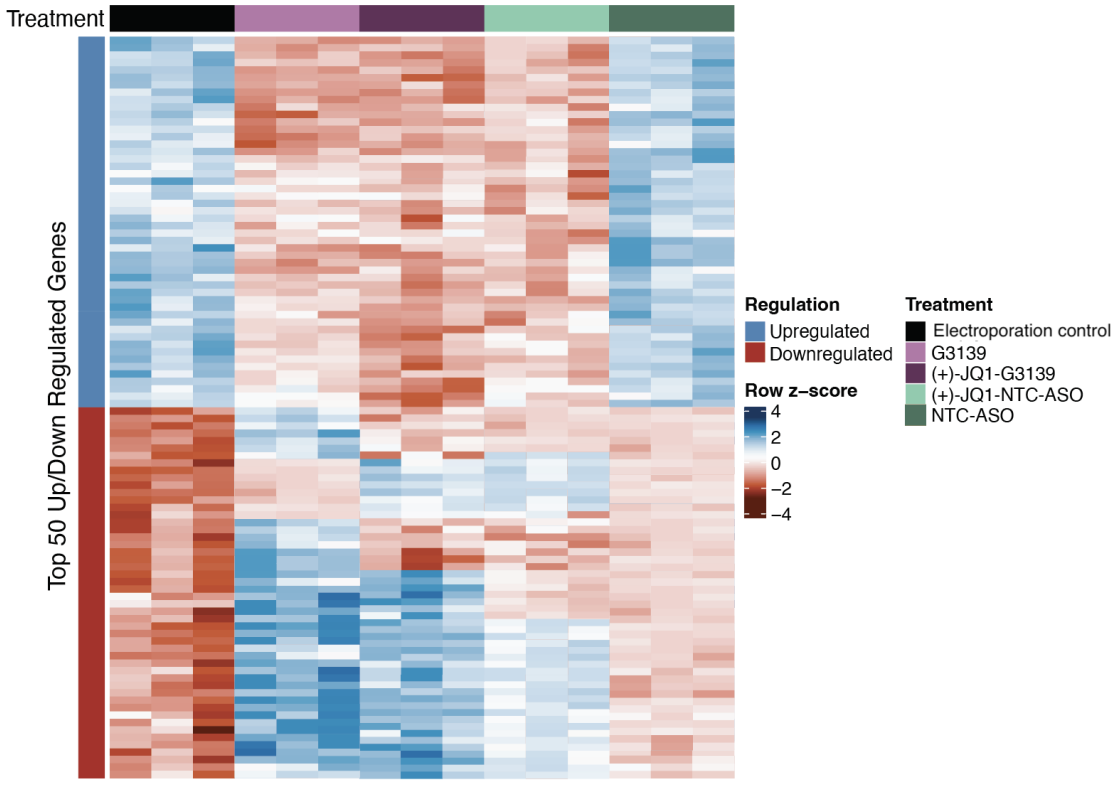

Figure 2.29: (+)-JQ1-G3139 induces a transcriptional program more closely aligned with G3139 than with (+)-JQ1-NTC-ASO. Global transcriptomic changes across treatment groups, electroporation control, (+)-JQ1-G3139, G3139, NTC-ASO, and (+)-JQ1-NTC-ASO in THP-1 cells. Heatmap displaying the top 50 upregulated and top 50 downregulated genes (ranked by absolute ($\log_2$(FoldChange)) relative to electroporation control) across all treatment groups in THP-1 cells. Gene expression values are row-wise Z-scores of normalized expression.

Lipid metabolism suppression unique to (+)-JQ1-G3139

To investigate transcriptional programs uniquely suppressed by the (+)-JQ1-G3139 conjugate, significantly downregulated genes unique to this treatment group were identified. Hierarchical clustering of these genes revealed a prominent enrichment for regulators of lipid metabolism (Figure 2.30a), including SCD, FASN, INSIG1, HMGCS1, and multiple genes involved in cholesterol and fatty acid biosynthesis.

Importantly, this suppression was not observed in the G3139 or (+)-JQ1-NTC-ASO treatments, indicating a synergistic effect of G3139-mediated *BCL-2* knockdown and (+)-JQ1-mediated BRD4 inhibition.

Expression of master lipid metabolic regulators SREBF1 and SREBF2, as well as their transcriptional targets SCD and FASN, was significantly reduced only in the (+)-JQ1-G3139 group (Figure 2.31a), despite minimal change in MYC expression. Many of these lipid metabolism genes are known targets of the transcription factors SREBF1 and SREBF2, which are regulated downstream of MYC[185]. Interestingly, although MYC mRNA levels were not significantly reduced, coordinated suppression of SREBP target genes suggests a functional disruption of this regulatory axis. Thus, BRD4 inhibition (via (+)-JQ1-moiety) may cooperate with G3139-mediated *BCL-2* knockdown to functionally repress the MYC–SREBP axis activity without directly lowering MYC mRNA levels. Other possibilities include transient or post-transcriptional MYC suppression or MYC-independent mechanisms.

Gene set enrichment analysis (GSEA) confirmed selective repression of hallmark pathways including "Fatty Acid Metabolism," "Cholesterol Homeostasis," "MYC Targets," and "mTORC1 Signaling" (Figure 2.31b), further supporting a broad transcriptional reprogramming of lipid metabolic gene networks specifically in response to the conjugate. These findings show the potential of combinatorial targeting strategies to disrupt lipid homeostasis in a context-specific manner—combining G3139-mediated *BCL-2* knockdown and (+)-JQ1-mediated BRD4 inhibition.

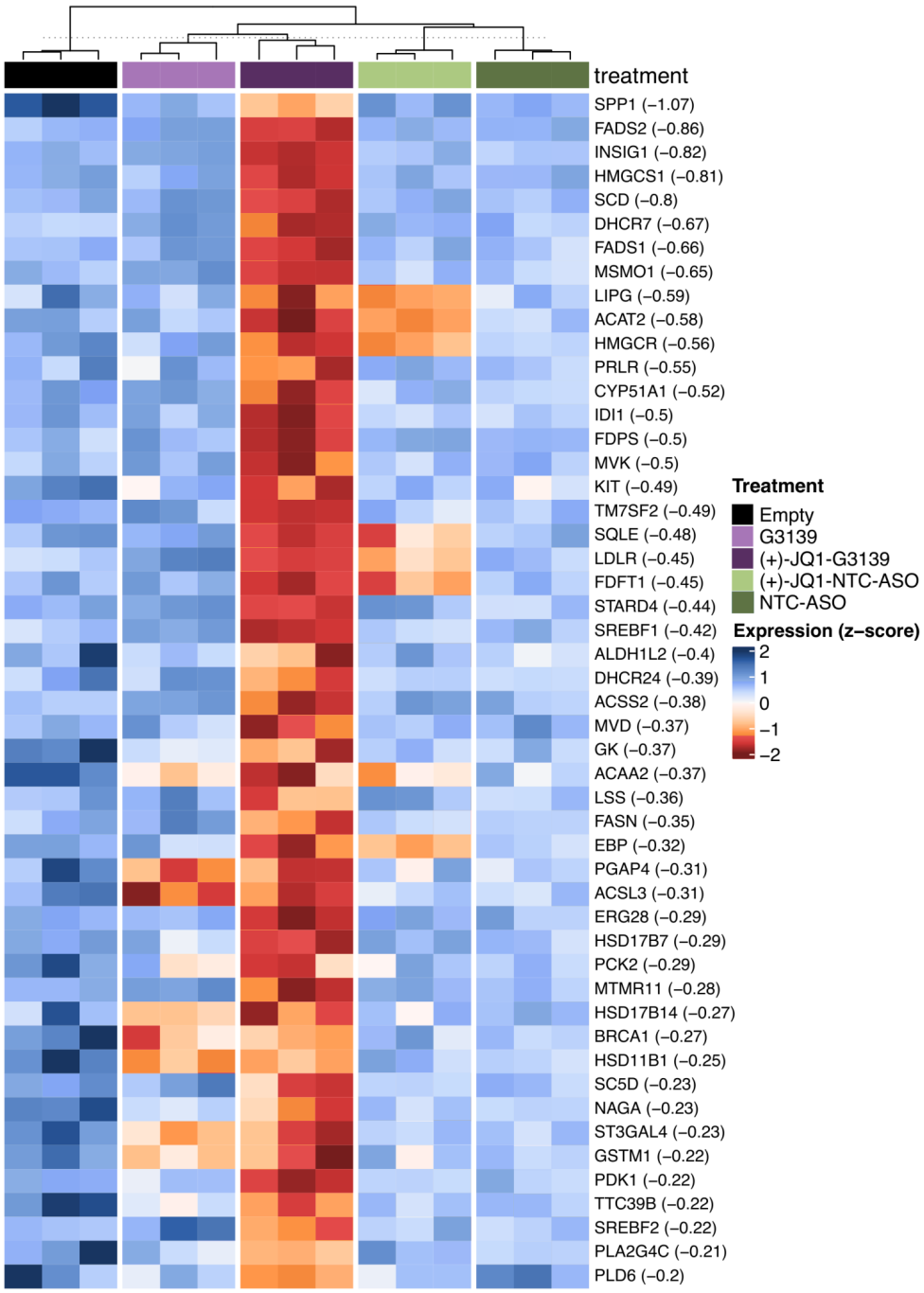

Figure 2.30: (+)-JQ1-G3139 selectively downregulates lipid metabolism genes and MYC–SREBP target programs. Heatmap showing hierarchical clustering of genes significantly downregulated only in the (+)-JQ1-G3139 treatment group. Many genes are involved in fatty acid and cholesterol biosynthesis, including targets of SREBF1/2. Values are Z-score normalized expression.

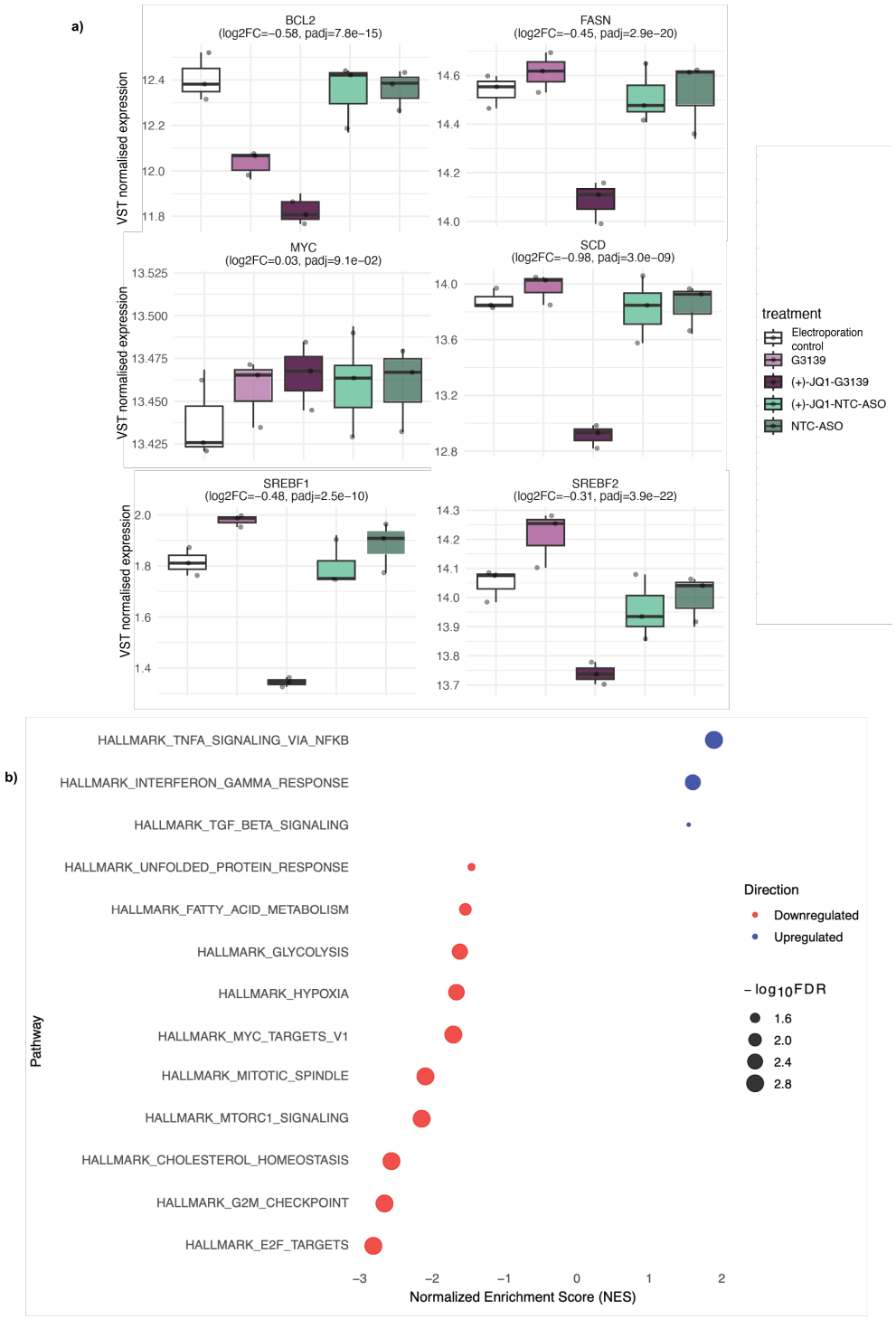

Figure 2.31: (+)-JQ1-G3139 selectively downregulates lipid metabolism genes and MYC–SREBP target programs. (a) VST-normalized expression of selected genes, including key lipid metabolic enzymes (SCD, FASN), transcriptional regulators (SREBF1, SREBF2), and MYC. Only (+)-JQ1-G3139 induced significant repression of these targets. (b) Gene set enrichment analysis (GSEA) of differentially expressed genes in the (+)-JQ1-G3139 group. Pathways related to lipid metabolism, MYC signaling, and mTORC1 signaling were selectively downregulated. Dot size reflects statistical significance ($(-\log_{10}(\text{FDR}))$); NES indicates direction and magnitude of enrichment.

Convergence of BRD4 inhibition targets for (+)-JQ1-G3139 and (+)-JQ1-NTC-ASO

(+)–JQ1–G3139 and JQ1–NTC–ASO shared a core set of downregulated genes that reflected hallmark features of BRD4 inhibition, particularly the suppression of MYC-driven transcriptional programs and cell cycle regulators. Functional annotation of these genes revealed coordinated repression across multiple BRD4-regulated transcriptional axes, including TP53- and SMAD-mediated transcription, RNA polymerase II activity, and FOXO-regulated cell cycle control (Figure 2.32a). Additionally, there was a broad silencing of chromatin remodeling and epigenetic regulatory programs, such as those involving SWI/SNF complexes, SUMOylation, and ATP-dependent chromatin remodelers. Suppression of RUNX-, AP1/2-, and SMAD-family transcription factors further suggested disruption of key developmental and differentiation-associated transcription networks (Figure 2.32a). This broad repression of chromatin- and transcription-associated pathways is consistent with the known role of BRD4 in orchestrating enhancer–driven gene expression.

Both conjugates also downregulated a conserved set of canonical MYC targets, cell cycle regulators, and DNA replication factors, such as E2F2, TOP2A, AURKA, CDK1, and MCM2/4. Genes in metabolic reprogramming such as HK2, LDHA, and SLC2A1 were also suppressed (Figure 2.32b). This shared signature reinforces that the BRD4 blockade was functionally retained—thus, despite conjugation to an ASO, (+)-JQ1 moiety is able to preserve its transcriptional silencing activity.

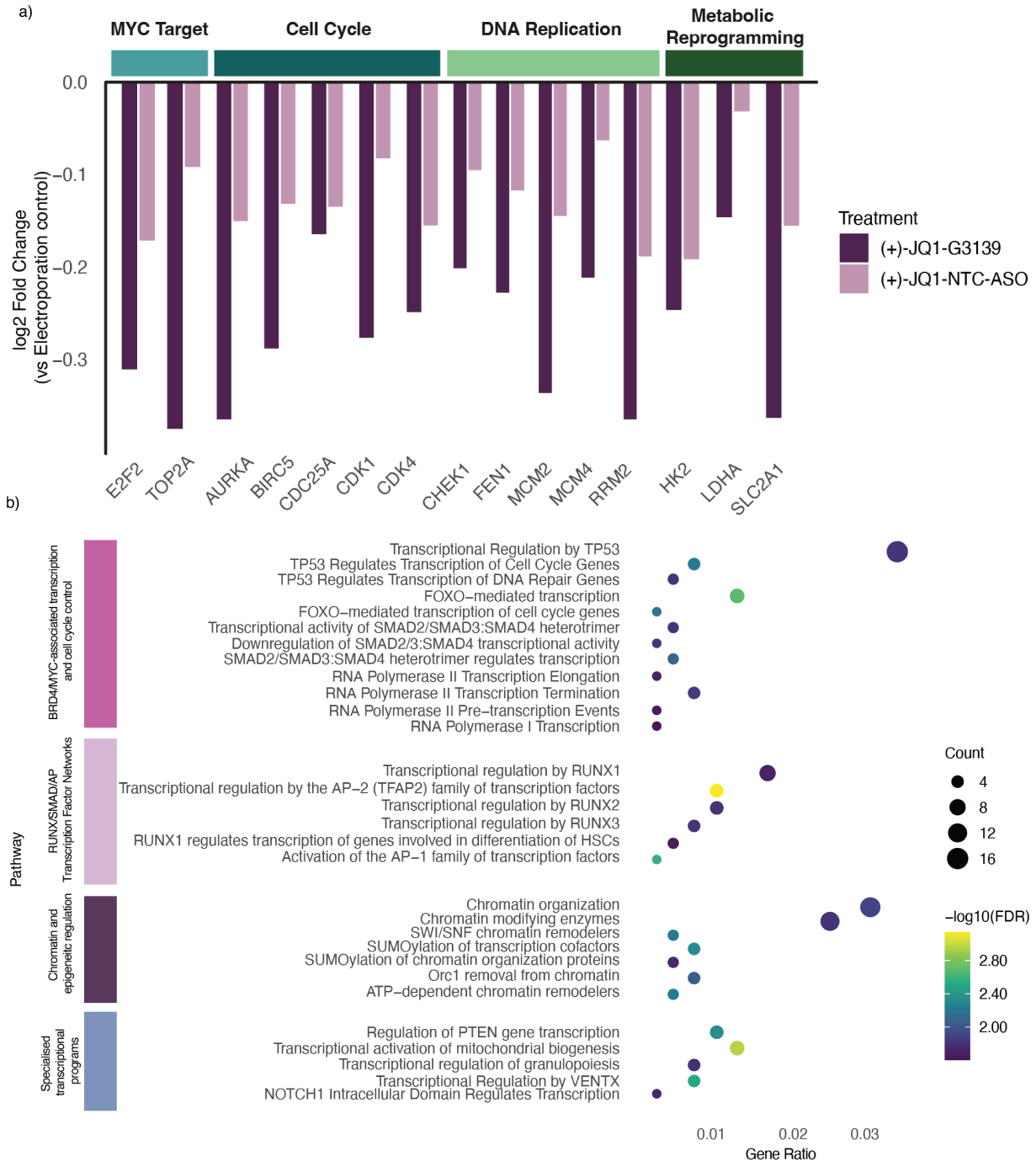

Figure 2.32: BRD4 inhibition and transcriptional repression retained across both (+)-JQ1-conjugated ASOs. (a) Downregulation of BRD4-regulated genes in MYC, cell cycle, DNA replication, and metabolic programs. Bar plot showing $-\log_2$(Foldchange) (vs. electroporation control) for selected genes significantly downregulated by both (+)-JQ1–G3139 and JQ1–NTC–ASO. Genes are grouped by functional annotation. (b) Functional categories of transcriptional programs downregulated by (+)-JQ1–G3139 and JQ1–NTC–ASO. Shared downregulated genes span BRD4-regulated transcriptional modules, including TP53-, SMAD-, and FOXO-mediated transcription, chromatin remodeling (SWI/SNF, SUMOylation), and RNA polymerase II-dependent gene expression.

Induction of apoptosis by *BCL-2* knockdown observed in both G3139 and (+)-JQ1-G3139

Gene expression analysis also revealed that both the (+)-JQ1-G3139 and G3139 conjugate show consistent induction of apoptosis- and differentiation-associated transcriptional programs. Both treatments downregulated anti-apoptotic genes (for example, BCL2, BIRC5) (Figure 2.33a), and increased expression of pro-apoptotic effectors (for example, CASP3, CASP8), consistent with engagement of the intrinsic apoptotic pathway. Moreover, genes linked to monocyte/macrophage differentiation (for example, CD14, CSF1R, CEBPB, S100A8/A9) were strongly upregulated, particularly in the (+)-JQ1-G3139 condition.

Pathway enrichment analysis of the differentially expressed genes confirmed significant over-representation of gene sets associated with apoptosis, including "Intrinsic Pathway for Apoptosis" and "Regulation of Apoptosis," as well as "Defective Intrinsic Pathway for Apoptosis" (Figure 2.33b). Together, these data support the conclusion that the G3139 sequence retains biological activity in the context of the (+)-JQ1-G3139 conjugate, promoting both apoptotic and differentiation pathways. Such transcriptional programs are considered therapeutically desirable in AML models like THP-1, where loss of self-renewal and terminal differentiation are associated with anti-leukemic efficacy.

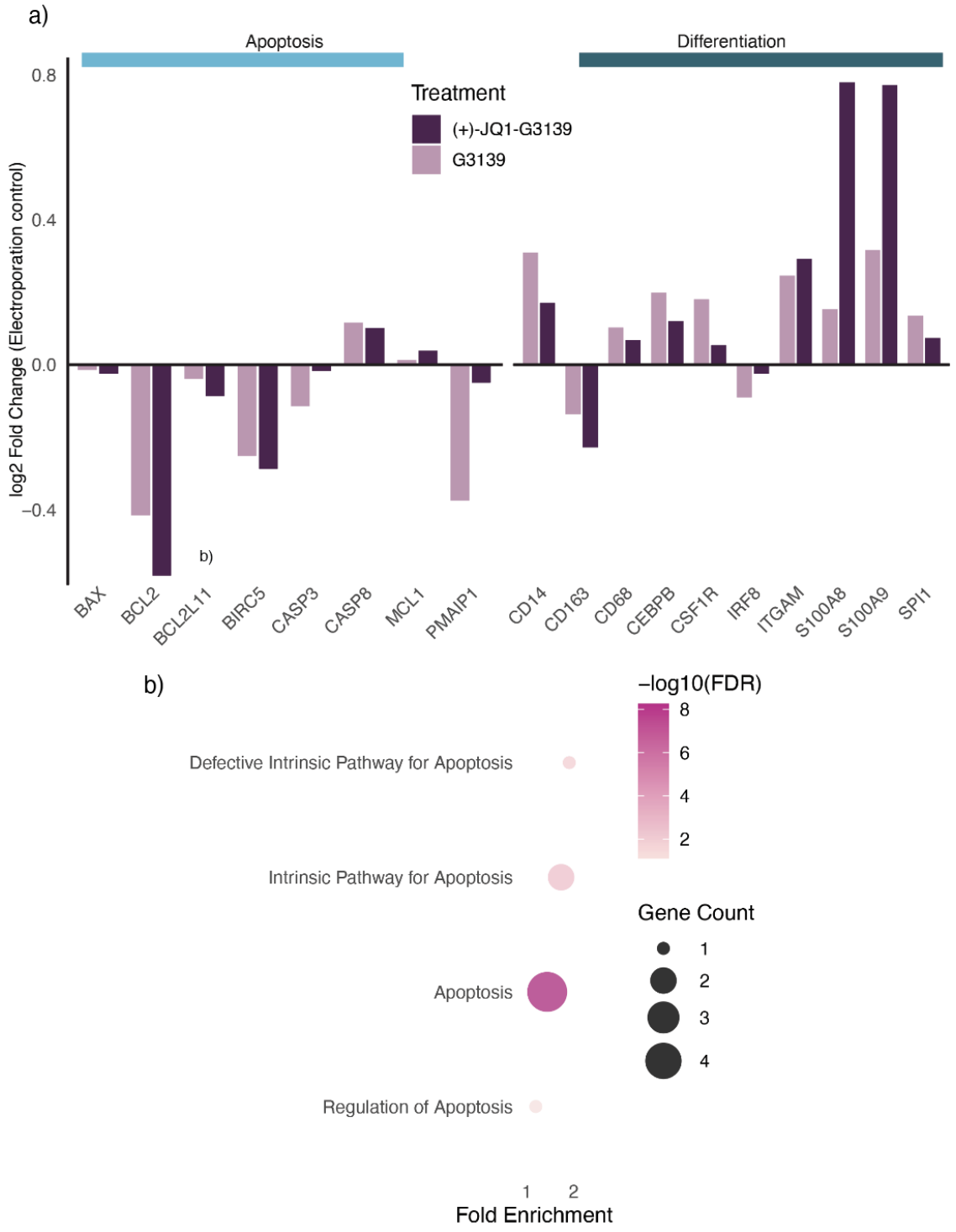

Figure 2.33: (+)-JQ1-G3139 and G3139 activate apoptotic and differentiation gene expression programs in THP-1 cells. (a) ($-\log_2$(FoldChange)) fold changes in gene expression (relative to electroporation control) for genes involved in apoptosis and myeloid differentiation following treatment with G3139 or (+)-JQ1-G3139. Color bars above indicate functional categories. (b) Reactome pathway analysis for enrichment for apoptosis-related pathways among upregulated genes in both treatments. Dot size represents gene count per pathway; color intensity reflects statistical significance ($-\log_{10}$(FDR)), and x-axis indicates fold enrichment.

2.4 Discussion

We present a novel, straightforward, and widely applicable chemical strategy to enhance the nuclear localization and potency of antisense oligonucleotides (ASOs) through covalent conjugation with the small-molecule BET-bromodomain ligand, (+)-JQ1. This modular approach markedly improves ASO efficacy across a range of targets, diverse backbone chemistries, both transfection-based and gymnotic delivery methods, and the two primary ASO mechanisms of action—RNase H-mediated degradation and splice modulation. The ASO chemistries and mechanisms featured here are utilized in multiple clinically approved nucleic acid therapeutics, highlighting the translational relevance of this work.

By showing that conjugation to (+)-JQ1 promotes nuclear accumulation of ASOs in a BET bromodomain-dependent manner, we expand upon existing literature that positions (+)-JQ1 as a nuclear importer. Our results highlight the critical importance of directing therapeutic agents to their intended site of action. Enhancing ASO nuclear localisation has led to improved therapeutic efficacy. In doing so, we establish that nuclear localization is essential for maximizing ASO activity in both splice modulation and RNase H-driven knockdown contexts.

Notably, we apply our strategy to Oblimersen, a well-characterized ASO targeting BCL-2, which has reached Phase III clinical trials but failed to demonstrate strong efficacy. Through covalent conjugation with (+)-JQ1, we substantially enhance

Oblimersen's nuclear localization, BCL-2 knockdown efficiency, and chemosensitization potency in a clinically relevant AML model. Our approach may similarly enable other under-performing ASO drugs to become more potent therapeutics.

The modular nature of this technology opens exciting possibilities for future applications. By demonstrating that small molecules can be potent effectors of ASO subcellular compartmentalization and thus, functionality, we pave the way for the development of advanced therapeutic strategies through small molecule conjugation. The integration of small molecules to manipulate cellular environments and target sites offers a promising approach to enhance therapeutic outcomes of nucleic acid-based therapeutics.

While this work focuses on the proof-of-concept application of (+)-JQ1 as a nuclear localization enhancer, BET bromodomain ligands like JQ1 can have broader transcriptomic effects due to their role as epigenetic modulators. Future work must explore alternative ligands or delivery strategies to minimize off-target transcriptional consequences while retaining nuclear targeting efficiency. Additionally, it will be important to elucidate the precise mechanism of nuclear accumulation, including whether it occurs via active transport or passive retention. Linker architecture may also impact cellular uptake, nuclear import, or conjugate orientation. In this conjugate design, a minimal azido-acetic acid linker is employed for its simplicity and high-yielding conjugation, but future iterations will explore linker length, polarity, and flexibility to further optimize intracellular trafficking and nuclear localization.

This work contributes to the rapidly advancing field of bi-functional molecules, which combines multiple distinct functionalities into a single entity[186]. This convergence allows our approach to be situated within a broader framework of therapeutic innovation, capitalizing on the synergy between small-molecule ligands and nucleic acid-based modalities.

In conclusion, this work offers a compelling demonstration of how small molecules can be used to enhance ASO activity through improved nuclear localization, spanning multiple targets and mechanisms. The modularity of this platform, along with its compatibility with emerging bi-functional therapeutic strategies, positions it as a powerful tool for future nucleic acid-drug development.

Chapter 3

Exploring RNase L recruitment via an Activator-ASO conjugate for knockdown of the MLL-AF4 fusion oncogene

3.1 Introduction

Genetic factors contribute to the pathogenesis of all diseases, with variable penetrance. Nucleic acids are thus poised to be a powerful therapeutic modality—simple base-pair complementarity allows for targeting of a variety of pathologically relevant proteins, without prior knowledge of structure, function, or cellular location[187,63]. Antisense oligonucleotides, one such class of nucleic acid therapeutics, are short, synthetic single-stranded DNAs that alter protein expression at the transcriptional level by binding to mRNA[188]. ASOs lead the race as clinically viable candidates with nine approved drugs on the market, targeting mainly Duchenne Muscular Dystrophy and Spinal Muscular Atrophy[187]. ASOs have also been employed as highly

personalised "n-of-1" therapies, such as Milasen, designed specifically for a patient with Batten disease[189].

Although initially considered poor drug candidates, ASOs have undergone extensive optimization to yield favorable pharmacological and pharmacokinetic properties[190]. Chemical modifications of the backbone, sugar, and nucleobase have improved stability and cellular delivery while maintaining efficacy[191]. ASOs can be broadly divided into two classes based on their mechanism of action: RNase H-active and steric-blocking. RNase H-active ASOs rely on recruitment of RNase H to the DNA-RNA duplex to degrade the RNA transcript[188]. These ASOs have negatively charged backbones that can pose toxicity issues and limit cell delivery. Furthermore, RNase H is localized in the nucleus, where mature mRNAs are largely absent.

In contrast, steric-blocking ASOs, such as phosphorodiamidate morpholino oligomers (PMOs) or fully modified 2′- OMe sugars cannot recruit RNases and instead block specific mRNA functions, such as splicing[187]. While five PMO drugs are currently on the market, they are not catalytic and require high, stoichiometric doses for efficacy.

A key aim of this chapter is to harness an alternate biochemical pathway for catalytic mRNA degradation: the potent cytoplasmic RNase L response. By conjugating RNase L recruiters to RNase-inactive ASOs into catalytically active drugs,

leading to improved target engagement and lower drug doses. Moreover, activating a cytoplasmic endoribonuclease may also improve access to mature mRNAs, potentially outperforming conventional RNase H-active ASOs.

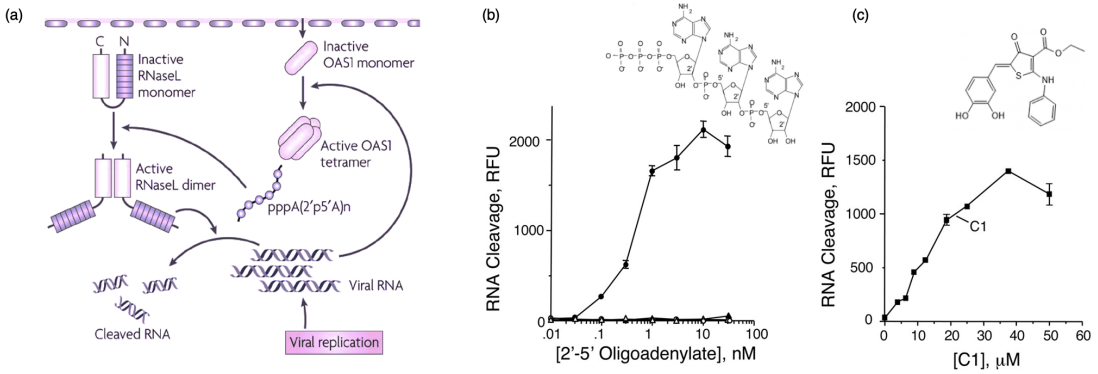

Figure 3.1: Anti-viral RNase L pathway: different modes of activation. (a) Biochemical activation of RNase L pathway is directed by the presence of 2′-5′ linked oligoadenylates that trigger dimerization and bring about RNase activity. *Figure adapted from "Interferon-inducible antiviral effectors" by Sadler et al., reproduced with permission from Springer Nature.* (b) Activation (EC50) of RNase L in response to endogenous activator, 2′-5′ linked triadenylate. (c) Activation (EC50) of RNase L in response to small molecule, thiophenaniline. *Figure adapted from "Small-molecule activators of RNase L with broad-spectrum antiviral activity" by Thakur et al., under CC BY-NC-ND 4.0.*

The interferon-inducible 2′-5′-Oligoadenylate Synthetase (OAS)/RNase L system is a well-characterized antiviral pathway activated by double-stranded RNA[192,193]. Interferons induce expression of OAS enzymes, which, upon activation by viral dsRNA, synthesize 5′-triphosphorylated, 2′,5′ - linked oligoadenylates (2-5A). These activate RNase L, leading to cleavage of both viral and host RNAs, suppression of replication, and apoptosis of infected cells (Figure 3.1a).

The endogenous activator 2-5A has been conjugated to ASOs to achieve RNase L-

mediated degradation of viral transcripts, including the SARS-CoV-2 spike protein and RSV transcription elongation factor[194] (Figure 3.1b). Bifunctional molecules such as RIBOTACs (RIBOnuclease TArgeting Chimeras), which combine 2-5A with RNA-binding moieties, have also been shown to recruit RNase L for degradation of structured RNA targets like microRNA precursors[195,196]. However, the use of small-molecule–ASO conjugates to engage RNase L for targeted mRNA degradation has not yet been explored.

3.2 Aims

In this chapter, a small molecule activator of RNase L, based on an anilinothiophene carboxylate core[197] was used instead of established 2-5A ligand to recruit RNase L for ASO-mediated mRNA degradation. While this compound has moderate activity ($EC_{50} \sim 25\,\mu M$), its lower activation potential may allow selective mRNA degradation without triggering broad cytotoxic responses (Figure 3.1c). This scaffold has been applied to RIBOTAC designs targeting microRNAs, but it has not yet been conjugated to ASOs (for mammalian targets). This chapter was aimed at the synthesis and evaluation RNase L-ASO conjugates for targeted mRNA knockdown.

As a proof of concept, it was aimed to demonstrate that these ASO–RNase recruiter conjugates could be used to knock down the MLL-AF4 fusion protein that drives a form of acute lymphoblastic leukemia (ALL), one of the most common childhood and infant cancers. Most childhood ALL is curable, but a subset of ALLs caused by

a chromosomal translocation of the Mixed lineage leukemia gene, more prevalent in infant patients, remains incurable. The translocation event leads to the rearrangement of the MLL gene (MLL/KMT2A), giving rise to MLL-rearranged leukemias (MLL-r)[198]. MLL rearrangements fuse the gene in frame to a large number of different fusion partners (MLL-FP), the most common of which is AF4 (Figure 3.2a)[199]. AF4 is a member of the Super Elongation Complex, a complex of proteins that serve as a checkpoint for transcriptional elongation[200,201]. While wild type MLL is responsible for the expression of key developmental HOX genes in normal hematopoietic stem/progenitor cells for proliferation, survival and differentiation, the MLL-AF4 fusion protein has the ability to transform hematopoietic cells at different developmental stages into leukemic cells possessing stem-like properties[202,203]. This is generally attributed to the chromatin-modifying activities of the MLL-FP protein that drives aberrant gene expression – binding at promoters of several key oncogenes and upregulating expression by recruiting elongation-associated factors. This unique fusion protein has a unique mRNA sequence (Figure 3.2b), absent in healthy cells, that provides an excellent opportunity for nucleic-acid based approaches (Figure 3.2c) —moving beyond the current therapeutic landscape that aims at targeting transcription factors/binding partners.

siRNA sequences have been developed that successfully knock down MLL-AF4, thereby reversing the leukemia phenotype[204]. In this work, a drug-like ASO with comparable activity was first established and subsequently designed for conjugation

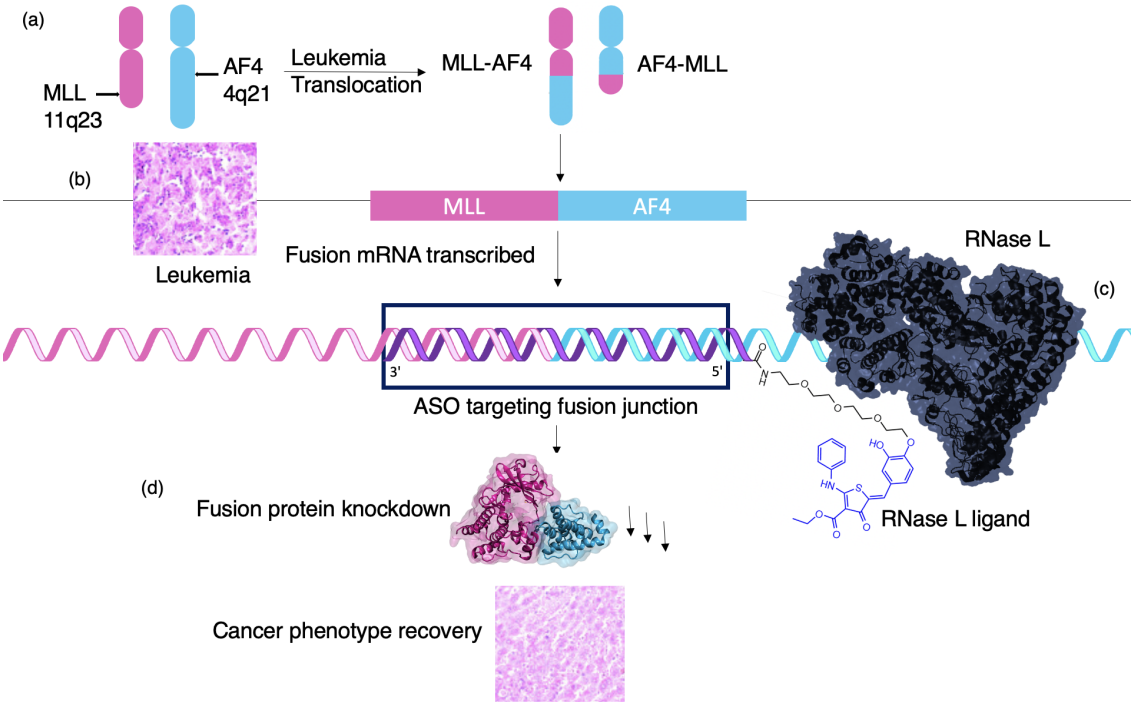

Figure 3.2: RNase L recruiter-ASO conjugate for *MLL-AF4* leukemias.(a) A subset of incurable acute lymphoid leukemias is caused by the chromosomal translocations of the Mixed lineage leukemia, MLL (11q23) gene. The most common fusion partner of such MLL-rearrangement leukemias is AF4 (4q21). (b) The MLL-AF4 fusion mRNA is a unique sequence that has the potential of being targeted by ASOs. (c) Activating the cytoplasmic RNase L pathway, the RNase L recruiter-ASO conjugates may allow for selective degradation of the fusion mRNA. (d) Knockdown of the fusion mRNA leads to a knockdown of the MLL-AF4 protein, rescuing the cancer phenotype.

to the RNase L recruiter in order to assess knockdown efficacy (Figure 3.2c,d). A comparative analysis with the unmodified parent ASO was planned to evaluate whether RNase L–ASO conjugates could enhance target knockdown, reduce dosage requirements, and achieve a greater degree of phenotypic rescue.

The objectives of this chapter were as follows:

◇ Design and *in vitro* validation of ASOs that selectively knockdown the MLL-AF4 fusion transcript

◇ Synthesis and characterisation of high purity RNase L-ASO conjugates

◇ Biological testing of RNase L-ASO conjugates in MLL-AF4 leukemia cells

3.3 Results

3.3.1 Generation of truncated *MLL-AF4*, *MLL*, and *AF4* for ASO design

Full length sequences for the *MLL-AF4* fusion transcript, *MLL* (KMT2A), and *AF4* were obtained from GenBank. The fusion junction for MLL-AF4 oncogene was identified in the SEM cell line (established from a specific patient[205]) through sequence alignment, and used to define the target region for ASO optimisation studies.

To identify regions suitable for ASO binding, a range of RNA fragments (0.5–5 kb) centered around the fusion breakpoint were evaluated for secondary structure using RNA secondary structure prediction software, Forna[206]. Based on structural accessibility and targeting by ASOs, fragment lengths of 1500 nt for *MLL-AF4*, 1450 nucleotides (nt) for *MLL*, and 1550 nt for *AF4* were selected for further experiments (Appendix Table A.1).

To generate templates for generating RNA fragments via in vitro transcription (IVT), the selected fragments were cloned into a plasmid backbone derived from

the DHFR control plasmid supplied with the NEB PURExpress *In Vitro* Protein Synthesis Kit. The DHFR backbone was PCR-amplified, and used for all constructs to ensure consistency.

The *MLL* and *AF4* inserts were PCR-amplified from a previously prepared *hMLL-AF4* plasmid[207]. The *MLL-AF4* insert corresponding to the SEM cell line fusion transcript was obtained as a 1498 nt synthetic gene block. All constructs were assembled via homologous recombination and sequence-verified prior to use.

3.3.2 Designed ASOs show effective MLL-AF4 knockdown efficacy and little-to-no off-target effects in *in vitro* RNase H assay

Each construct was used as a template for IVT to generate RNA transcripts for *MLL-AF4*, *MLL*, and *AF4*. Transcripts were then purified and incubated with a panel of fusion junction-targeting ASOs (Figure 3.3a) in the presence of RNase H (Figure 3.3b). Reactions were analyzed by denaturing polyacrylamide gel electrophoresis to assess target RNA degradation.

The RNase H assay revealed robust and selective degradation of the *MLL-AF4* fusion transcript by all ASOs tested (Figure 3.3c). In particular, the wild-type *MLL* and *AF4* RNAs were not degraded under identical conditions, indicating no off-target activity. These results demonstrate that the selected 1500 nt region

around the fusion breakpoint is a suitable and specific target for ASO-mediated RNase H cleavage. This high specificity of the ASO against *MLL-AF4* establishes a solid foundation for downstream conjugate development and functional testing.

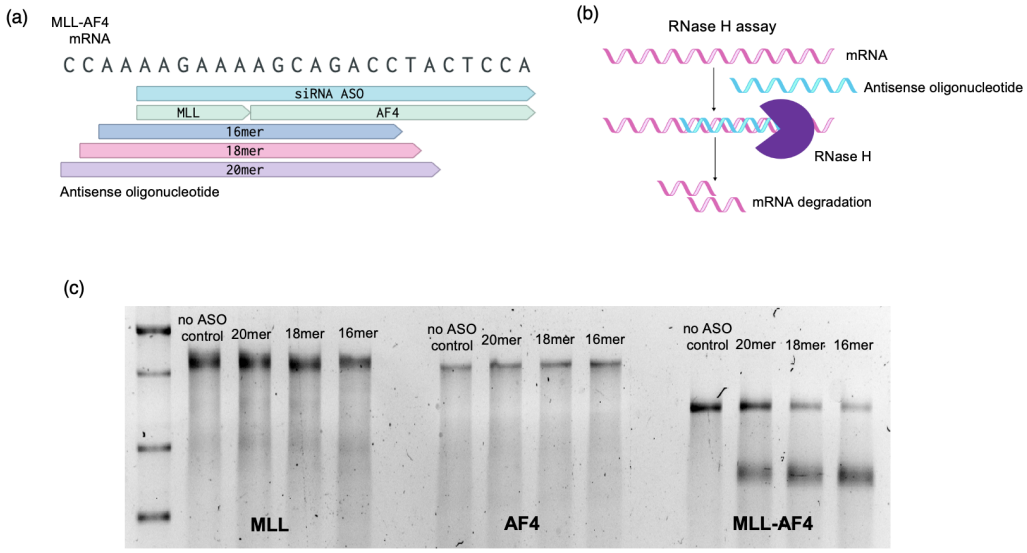

Figure 3.3: RNase H-based optimisation or ASO sequence for targeting the MLL-AF4 fusion transcript. (a) Sequence of MLL-AF4 fusion mRNA targeted by ASOs and the positioning of various ASOs around the fusion junction. (b) Principle of the RNase H assay: RNase H degrades ASO-mRNA (DNA-RNA) duplex. (c) RNase H assay for the identification of promising sequences, 16mer, 18mer, 20mer that degrade MLL-AF4 RNA but not MLL or AF4 RNA.

3.3.3 Designed ASOs show effective MLL-AF4 knockdown efficacy in MLL-AF4 leukemia model, SEM cell line

Initial ASO sequence optimisation via RNase H assay yielded promising candidates that were subjected to initial functional validation in SEM[208] cells. SEM cells were electroporated with the designed ASOs at a concentration of 250 nM—along with

the previous developed siRNA[204]. siMA6 at the same concentration as the positive control. Cutting-edge ASO chemistries were tested in addition to the standard PS linkages (Figure 3.4a), ie. a 16mer LNA gapmer containing 3-base pair (bp) wings containing the ribose sugar with 2′, 4′- methylene bridge was tested along with a 20mer MOE gapmer containing containing 5-bp wings of 2′-methoxyl-ethyl ribose sugar. Transcript levels for *MLL*, *AF4*, and *MLL-AF4* were assayed by RT-qPCR at 48 hours after the cells had recovered from electroporation.

The LNA gapmer sequence proved to be the most promising candidate—with the highest levels of *MLL-AF4* knockdown and negligible *MLL* and *AF4* knockdown (Figure 3.4b). As previous reported in the literature, although siMA6 showed the most potent *MLL-AF4* knockdown, significant *MLL* and *AF4* knockdown was also observed[204]. The other PS ASOs and the MOE-modified ASO also showed moderate knockdown of MLL-AF4, but lacked the favorable specificity and potency profile of the LNA gapmer. Overall, the data highlight the superior balance of potency and selectivity offered by the LNA gapmer in targeting the MLL-AF4 fusion transcripts even compared to the siMA6 siRNA.

3.3.4 Synthesis of high purity RNase L-ASO conjugates

The small-molecule RNase L activator has previously been synthesised and functionalised for conjugation to small molecules. Similar chemistry was used for nucleic acid bioconjugation[195]. The synthesis for the functionalised RNase L recruiter is

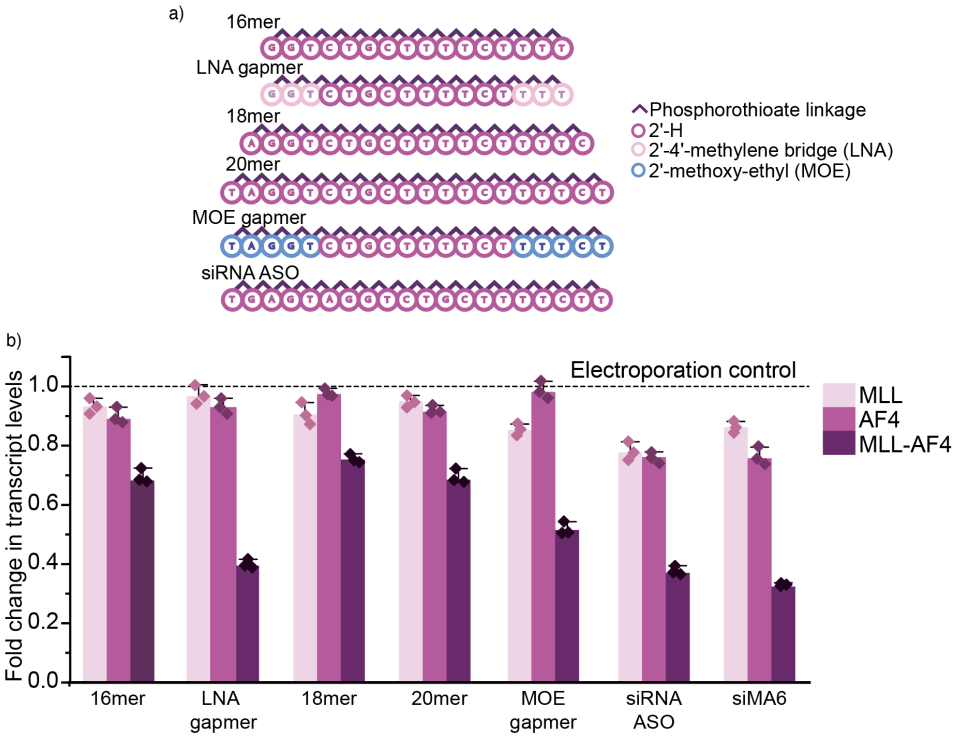

Figure 3.4: Designed ASOs show selective *MLL-AF4* knockdown in SEM cell line. (a) Sequence and chemistry for panel of ASOs designed for cell testing. (b) RT-qPCR data for knockdown of *MLL-AF4*, *MLL*, and *AF4* at 48 hours upon 250 nM ASO treatment via electroporation.

as follows (following literature procedure[195]): first step, involves the formation of a substituted anilinothiophene core via condensation of ethyl acetoacetate, phenyl isothiocyanate, and a diester chloride under basic conditions. The second step involves an etherification reaction between the catechol and the tosylated PEG-alcohol under basic conditions in N,N - dimethylformamide at 90°C overnight. The resulting ether derivative is then subjected to microwave-assisted Knoevenagel condensation with the anilinothiophene core to afford the PEG-linker functionalised RNase L recruiter.

We diverged from literature procedure by further functionalisation of the PEG-

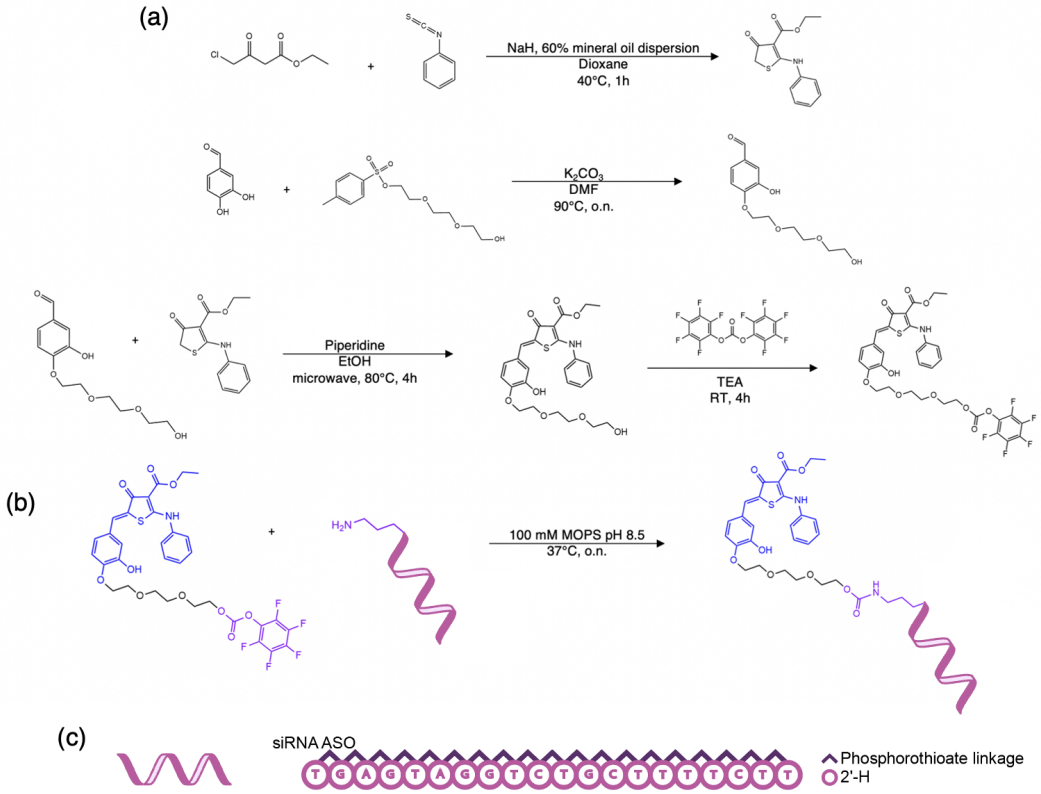

Figure 3.5: Synthesis scheme for RNase L recruiter-ASO conjugate. (a) Synthesis scheme for RNase L recruiter and its chemical functionalisation for nucleic acid bioconjugation. (b) Conditions used for nucleic acid bioconjugation – using pentafluorophenyl carbonate end group on RNase L ligand and 5′-terminal amine on ASO. (c) Sequence of ASO used for nucleic acid bioconjugation, same as antisense strand of siMA6, previously developed siRNA[204].

linker of RNase L recruiter into a PFP carbonate-ester to allow formation of a carbamate linkage—with the commercially available, 5′-terminal amine-functionalised PS-modified ASO. Thus, the PEG-linker was activated by formation of a pentafluorophenyl (PFP) ester—introduced under mild conditions using triethylamine at room temperature, for downstream nucleic acid bioconjugation (Figure 3.5a,b). Initial reaction optimisation was performed with unmodified sugars, and a fully PS backbone with a sequence identical to the antisense strand of the siRNA previously

shown to knockdown *MLL-AF4* (Figure 3.5c).

Prior to proceeding with the bioconjugation, confirmation was obtained that the correct regioisomer (para-isomer) was isolated from the etherification in the second step. This represented a key bottleneck in the overall synthesis, as only the desired regioisomer could be carried forward. Modification with the PEG-linker at the meta position yielded the inactive RNase L ligand, making correct regioisomer isolation essential for downstream biological activity. 2D-NMR spectroscopy, specifically NOESY (Nuclear Overhauser Effect Spectroscopy), was performed to determine regioisomeric composition of the etherification reaction (Figure 3.6a). This analysis verified the substitution pattern on the catechol ring, ensuring the desired regioisomer was obtained (Figure 3.6b).

The bioconjugation reaction was optimised at an oligonucleotide concentration of $\sim$10μM (approximately 700ng scale), using a large excess of the small molecule (12.5mM). This resulted in a reaction conversion of approximately 80% and excellent purity. Importantly, this bioconjugation strategy is independent of both oligonucleotide sequence and backbone chemistry. The modified ASOs were subsequently purified via high-performance liquid chromatography (HPLC) (Figure 3.7) and characterised via denaturing PAGE (Figure 3.8a) and mass spectrometry (Figure 3.8b,c). However, subsequent attempts to scale-up the reaction led to $< 60\%$ conversion and poor separation/purity unfit for *in vitro* testing. The intrinsic instability of the ligand was a key limitation: potentially, the exo-cyclic double bond was

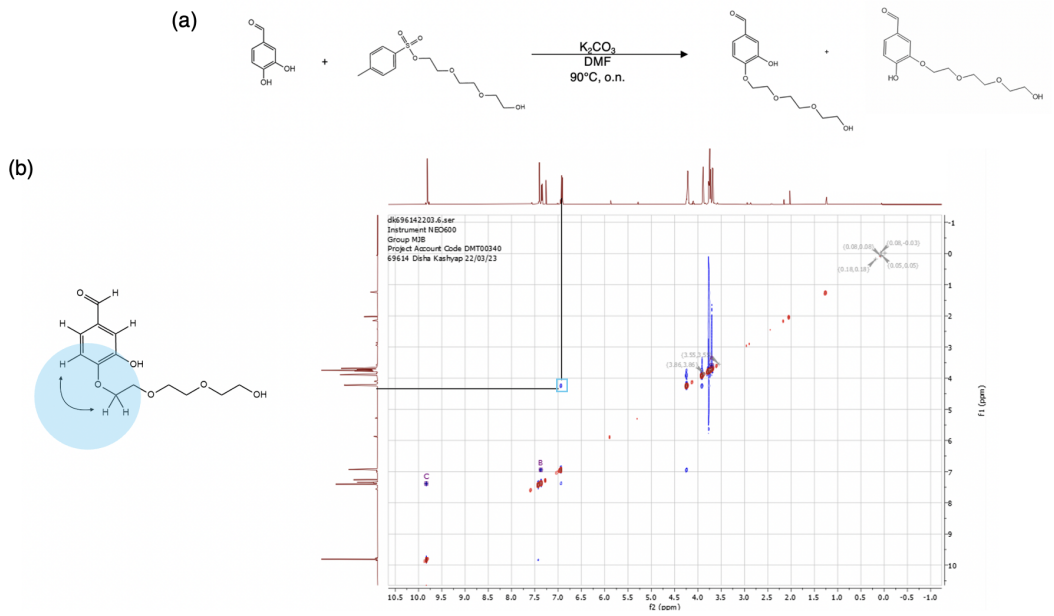

Figure 3.6: 2D-NMR characterisation of regioisomers of key intermediate compound for RNase recruiter synthesis. (a) Reaction scheme for PEG-tosylate addition to catechol at both m- and p- positions of benzaldehyde ring, resulting in regioisomers. (b) NOESY showing proton-coupling through space — interaction between benzaldehyde CHAr and CH2 of PEG-tosylate showing the right regioisomer is isolated.

prone to side reactions, which produced additional side products and contributed to incomplete conversion. This was observed both during the basic reaction and purification conditions. These issues were further exacerbated by solubility constraints, which impeded both the reaction and downstream purification. Importantly, such challenges became pronounced only upon scale-up, as smaller-scale reactions had not revealed the same degree of instability or inefficiency. The overall process was thus economically untenable.

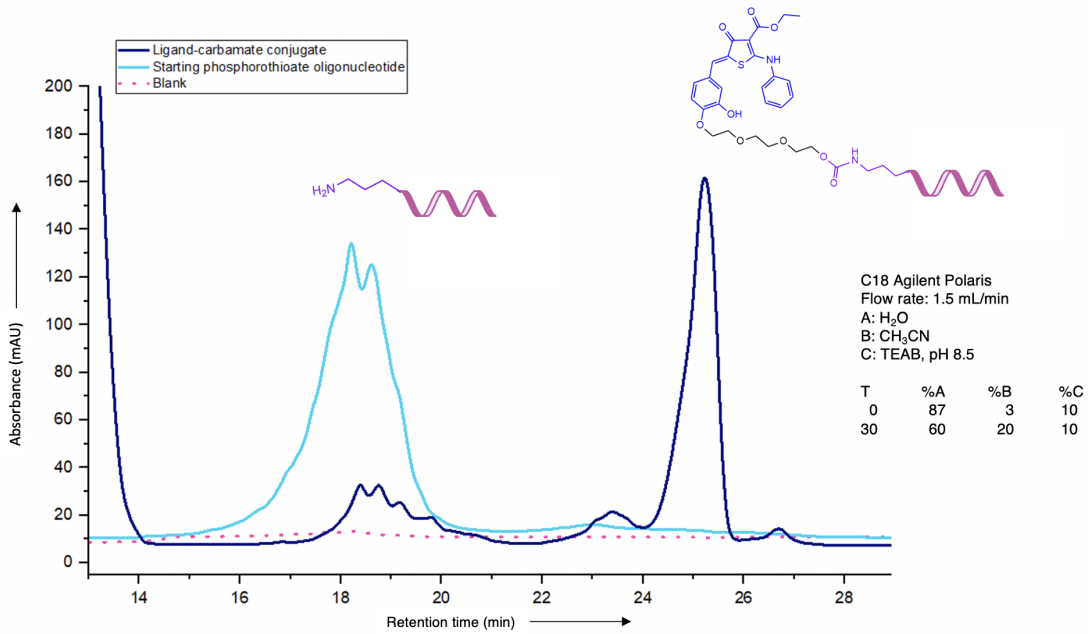

Figure 3.7: Purification of RNase L recruiter-ASO conjugate. (a) HPLC trace (at 260 nm) for purification of the RNase L recruiter-ASO bioconjugation reaction, reaction conversion of ~80%. Purification method, stationary and mobile phases used for HPLC purification noted in figure.

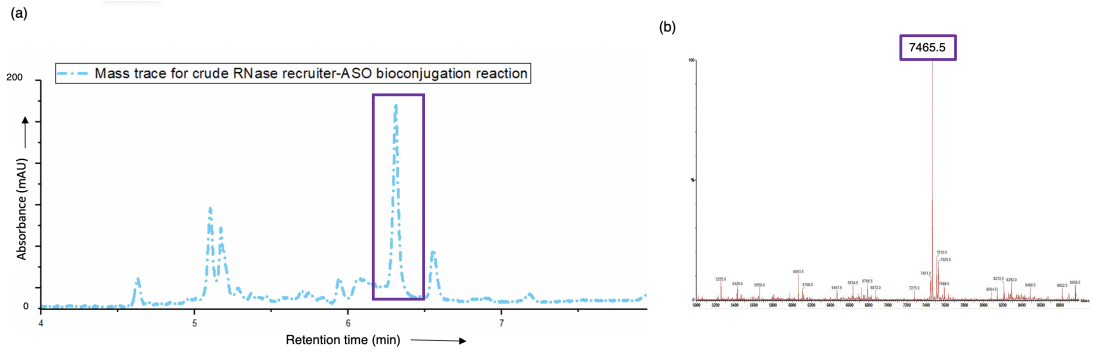

Figure 3.8: Characterisation and optimisation of RNase recruiter-ASO bioconjugation reaction. (a) Mass spectrometer trace for the crude bioconjugation reaction, peak at t=6.41 corresponds to RNase L recruiter-ASO conjugate. (b) Deconvoluted mass for peak, t=6.41 corresponds to predicted mass for RNase L recruiter-ASO conjugate.

3.4 Discussion

This chapter aimed to establish the design and synthesis of RNase L recruiter-ASO conjugates for the selective knockdown of the leukemogenic *MLL-AF4* fusion transcript. This work explored the design of antisense oligonucleotides (ASOs) that specifically target the unique fusion junction of *MLL-AF4*. In parallel, this work also explored the chemical feasibility of synthesising RNase L activator-ASO conjugates to harness RNase L as a novel mechanism for targeted mRNA degradation. This strategy extends beyond traditional RNase H- or RNAi-based approaches and offers a new paradigm for cytoplasmic mRNA knockdown.

A key strength of this approach lies in the specificity and selectivity of the designed ASOs for *MLL-AF4* knockdown. In vitro RNase H assays confirmed potent and selective degradation of the *MLL-AF4* fusion transcript without observable off-target cleavage of wild-type *MLL* or *AF4* mRNAs. This specificity was retained in cellular assays, with LNA-modified gapmers showing the most robust knockdown of the fusion transcript and negligible suppression of endogenous *MLL* or *AF4*. Compared to the benchmark siRNA siMA6, the LNA gapmer offered comparable potency with markedly improved specificity—mitigating the undesirable off-target *MLL* or *AF4* knockdown observed with siMA6.

The chemical synthesis of the RNase L recruiter was adapted from prior work on small-molecule RNase L activators[195] and was further tailored for nucleic acid conju-

gation via a pentafluorophenyl carbonate-activated PEG linker. Through 2D-NMR (NOESY) characterization, the correct regioisomer for PEG conjugation was verified, ensuring stereochemical fidelity for downstream applications. Bioconjugation to a 5′-amine-modified PS-ASO was efficient (∼80% conversion) under mild aqueous conditions, and the resulting conjugates were successfully purified by reverse-phase HPLC and confirmed by mass spectrometry. Notably, the bioconjugation chemistry is both sequence- and backbone-independent, allowing for broad adaptability across different ASO platforms.

However, scale-up attempts of the bioconjugation reaction resulted in diminished yields and low purity, highlighting a current bottleneck in the translational potential of this platform. In particular, the RNase L recruiter ligand showed high instability: potentially, its exo-cyclic double bond was highly susceptible to side reactions such as hydrolysis, leading to the wrong conjugation products and incomplete conversion. These effects, compounded by poor solubility, interfered with both the reaction and downstream purification. While smaller-scale reactions had appeared manageable, these limitations became pronounced during scale-up, rendering the process inefficient and economically impractical. Thus, optimization of reaction stoichiometry, HPLC purification protocols, and the solubility and stability of the hydrophobic recruiter ligand may be required to support larger-scale synthesis suitable for *in vitro* and *in vivo* functional validation. Future work should also aim to improve linker strategies or establish alternative conjugation chemistries to ensure robust

scalability.

While the RNase L recruiter-ASO conjugates were not functionally validated in cells due to scale-up limitations, the chemical validation establishes a solid foundation for future functional evaluation. Future work must focus on the chemical optimisation and *in vitro* validation of the conjugates in SEM cells. Furthermore, transcriptome-wide off-target profiling and cytotoxicity assays will also be essential to determine the selectivity and safety profile of the developed conjugates. It is worth noting that the recruiter itself demonstrated only modest potency, further undermining its suitability as a lead candidate in light of these synthetic and purification challenges. Additional analogues in the literature[209] were not explored further, as their potency was within a similar range and their efficacy in the oligonucleotide context was considered doubtful. Future iterations must thus explore SAR-guided optimisation of the RNase L recruiter to enhance its potency while minimising non-specific RNase L-mediated global RNA decay.

In conclusion, this work establishes promising ASO candidates for the knockdown of *MLL-AF4* fusion transcripts in the SEM leukemia model. It also lays the foundation for a chemical strategy to enable the synthesis of RNase L recruiter-ASO conjugates, with a clear scope to improve conjugation chemistry. The strategy of combining steric-blocking ASOs (with favourable safety and biodistribution properties) and RNase L recruitment (for catalytic mRNA degradation in the cytoplasm) represents a conceptually powerful therapeutic mechanism.

Chapter 4

Designing small-molecule ASO conjugates to harness the lysosome for targeted mRNA degradation

4.1 Introduction

Nucleic acid therapeutics represent a promising class of drugs because of their exceptional specificity in targeting genetic pathways[63]. One such class of therapeutics: ASOs are short, synthetic DNA strands that regulate gene expression by binding to RNA through sequence complementarity. Approved ASO drugs function via two principal mechanisms: they either modulate pre-mRNA splicing or induce RNA degradation through RNase H activation[210]. Despite notable clinical success, most approved ASOs are limited in scope: both in the range of diseases they address and in their primary mechanisms, which predominantly occur within the nucleus.

Splice-modulating ASOs must operate within the nucleus through specialised mechanisms, where pre-mRNA resides[211]. These ASOs bind to pre-mRNA transcripts

to influence their splicing into mature mRNA, offering a potent therapeutic strategy for genetic disorders caused by aberrant splicing. In contrast, gene knockdown strategies that rely on RNase H activity face challenges due to a mismatch between the effector and molecular target: RNase H is primarily nuclear, while mature mRNAs are typically found in the cytoplasm[212]. Furthermore, RNase H recruitment is unreliable as its expression levels vary not only with cellular localisation but also with cell and tissue type[213].

A viable strategy to enhance the efficacy of ASO-mediated mRNA knockdown involves overcoming this spatial separation between the RNA target and its effector enzyme. Covalent modification of ASOs with nuclear importers has been shown to boost the performance of both splice switching and RNase H-competent ASOs (see Chapter 2)[214]. However, directing ASOs to the nucleus may not be suitable for all mRNA targets. Alternatively, selective cytoplasmic degradation through the antiviral RNase L enzyme can be achieved by attaching ASOs to RNase L recruiters (see Chapter 3)[151,150]. However, RNase L activity must be tightly controlled; unchecked activation can lead to global protein synthesis shutdown, cellular stress amplification, and apoptosis[215,216]. This demonstrates the need to develop new methods to harness a selective cytoplasmic ASO pathway for targeted degradation of mRNA.

Lysosomes serve as the primary degradation compartment of cells, with the ability to degrade a wide range of biomolecules[217,218,219]. This degradation capacity has been exploited for targeted protein degradation[220] using systems like LYTACs

(lysosome-targeting chimeras)[221,222] (Figure 4.1), bispecific aptamer conjugates[223], and small-molecule-based strategies like MrTACs (methylarginine-targeting chimeras)[224]. These approaches use tags or ligands to direct target proteins to lysosomes for destruction. Inspired by such technologies, we explored whether lysosomal trafficking could also be harnessed for ASO-mediated mRNA degradation.

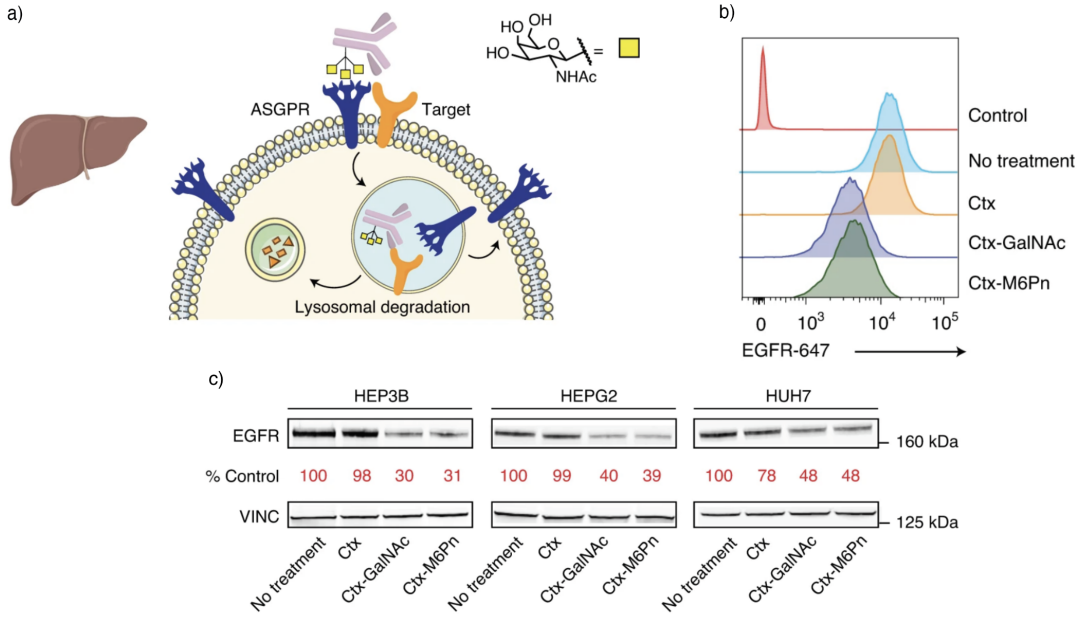

Figure 4.1: Lysosome-targeting chimeras that (a) engage the asialoglycoprotein receptor (ASGPR), a liver-specific lysosome-targeting receptor, to degrade extracellular proteins in a cell-type-specific manner. (b) Cetuximab (Ctx)-LyTAC conjugates show higher degradation of cell surface EGFR in HEP3B cells determined by live-cell flow cytometry following 48 hours of treatment (Cetuximab (Ctx) is an FDA-approved blocking antibody against EGFR for colorectal cancer and head and neck cancer). Western blot analysis of total EGFR levels in HEP3B, HEPG2 and HUH7 cells after treatment with Ctx-LYTAC shows same trend. *Reproduced with permission from Springer Nature.*

4.2 Aims

Autophagy and lysosomal trafficking represent powerful cellular quality-control pathways. Recent advances have demonstrated that they can be harnessed pharmacologically for targeted protein degradation. Building on these developments, this chapter sought to investigate whether a similar strategy could be applied to antisense oligonucleotide (ASO)-mediated mRNA degradation.

To this end, the small molecule, ispinesib, was employed. Ispinesib is a small molecule initially developed as an Eg5 kinesin inhibitor for cancer therapy[225,226]. Ispinesib has also served as a warhead in bifunctional molecules that drive protein degradation via lysosomal pathways[227]. These compounds are thought to bind LC3 localised within autophagosomes, which then fuse with lysosomes to complete the degradation process. Their activity depends on intact autophagy and lysosomal trafficking, and compounds using this mechanism are classified as autophagosome-tethering compounds (ATTECs)[228].

Building on this concept, the design of lysosomal trafficking antisense oligonucleotides (LyTONs) was explored — by covalently linking ispinesib to ASOs. The aim was to design RNase H-inactive LyTONs that could induce mRNA knockdown through lysosomal degradation (Figure 4.2). It was hypothesized that inhibition of lysosomal acidification, for example via bafilomycin, would impair LyTON activity, thereby demonstrating that mRNA transport to the lysosome was required for

knockdown. Similarly, it was reasoned that lysosomal membrane permeabilisation by chloroquine would disrupt activity, suggesting that intact lysosomal function would be essential. To explore potential clinical applications of this approach, the development of LyTONs targeting Menin (MEN1), a transcriptional regulator implicated in leukemia[229], was attempted.

More broadly, the goal with this lysosomal targeting strategy was to enable efficient mRNA degradation without disrupting endogenous cellular mechanisms or inducing widespread toxicity. Unlike traditional nucleic acid-based knockdown methods, which rely on DNA or RNA backbones to recruit endogenous enzymes, LyTONs were envisioned as constructs that could be built from alternative oligonucleotide chemistries (which possess superior potency and pharmacokinetic properties).

The objectives of this chapter were as follows:

◇ Synthesis and characterisation of high-yield high-purity covalent ispinesib-ASO 'LyTON' conjugates

◇ Functional validation of the activity of LyTON conjugates in various relevant cell lines

◇ Mechanistic validation of LyTON conjugate activity

◇ Demonstration of the clinical potential of LyTONs in treating AML

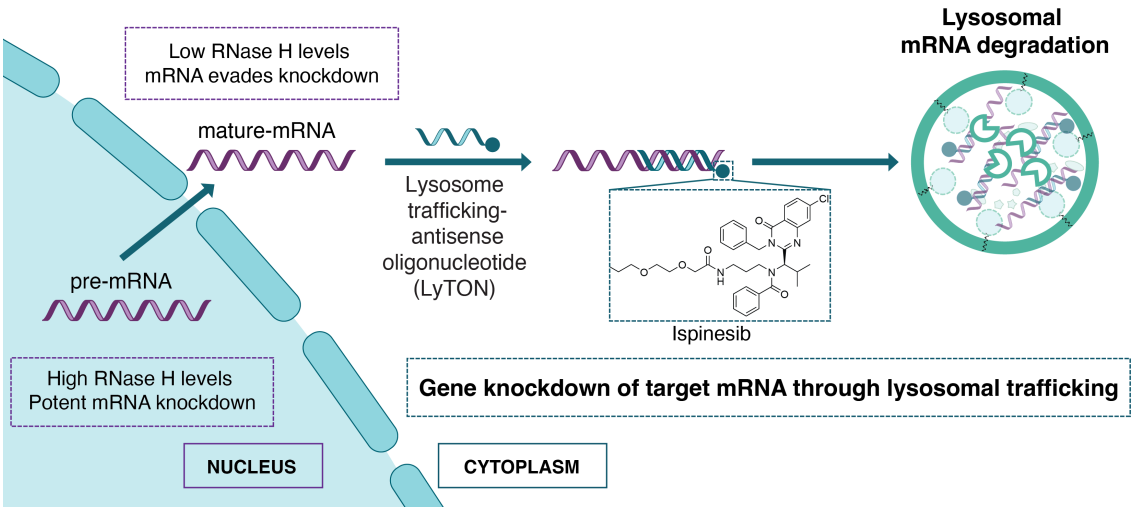

Figure 4.2: Ispinesib-ASO conjugates act as lysosomal trafficking antisense oligonucleotides (LyTONs), enabling targeted mRNA degradation in the lysosome. *Figure re-produced from "Engineering antisense oligonucleotides for targeted mRNA degradation through lysosomal trafficking" by Kashyap et al., under CC-BY 3.0.*

4.3 Results

4.3.1 Synthesis of Ispinesib-ASO conjugates

For this chapter, published ASO sequences were selected that had previously been validated using mismatch and scrambled controls. Since these sequences had been shown to specifically target their corresponding mRNA, the key comparative controls in our experimental validation of the ispinesib-ASO conjugates were ASOs without the ispinesib modification.

To synthesise the covalent ispinesib-ASO conjugate, copper-free click chemistry was used: with azide-modified ispinesib and 5′-dibenzocyclooctyne (DBCO)-modified ASOs.

Synthesis of DBCO-modified ASOs

A 5′-DBCO-ASO was synthesised by reacting a 5′-terminally modified-amine ASO with excess DBCO-NHS ester under basic conditions—in 60% N,N-dimethyl formamide (DMF) to aid to DBCO-solubilisation (Figure 4.3).

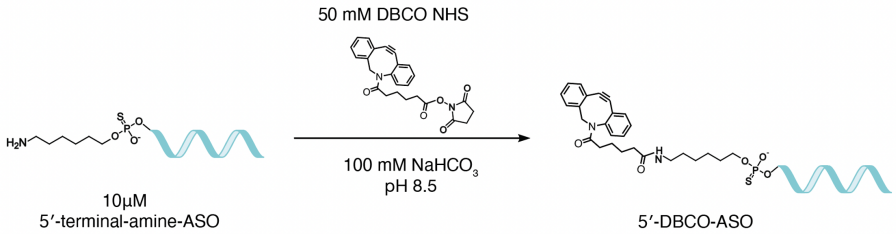

Figure 4.3: Synthesis scheme for 5′-terminally modified-DBCO ASO.

General bioconjugation strategy

Subsequently, strain-promoted azide-alkyne click (SPAAC) chemistry was used[230] to couple commercially available ispinesib-azide to the 5′- DBCO ASO, in 1XPBS and 60% DMF. We achieved >90% yields for all bioconjugation reactions performed and >95% purity post HPLC purification (Figure 4.4).

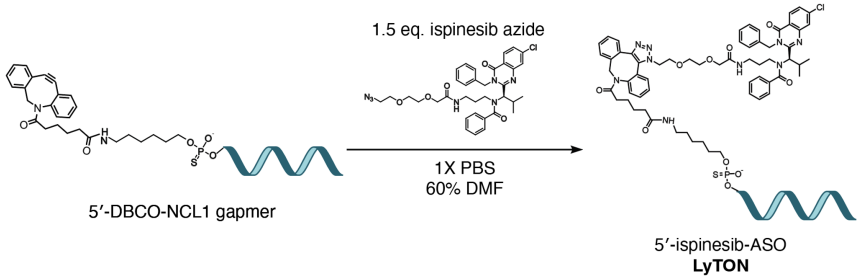

Figure 4.4: Synthesis scheme for 5′-ispinesib-ASO.

4.3.2 Synthesis of Ispinesib-NCL1 RNase H-inactive conjugate

The final Ispinesib-NCL1 RNase H-inactive ASO conjugate (chemistry: 2′-OMe) was prepared using SPAAC chemistry of the Ispinesib-azide with the 5′-DBCO NCL1 2′-OMe ASO (Appendix Figure A.24, Figure A.25). > 90% yields were achieved for all bioconjugation reactions performed and > 95% purity following HPLC purification. This conjugate is hereafter mentioned as the NCL1 2′-OMe LyTON.

Additionally, to assess any off-target effects of the ispinesib moiety itself, a non-targeting control phosphorothioate ASO without ispinesib (ispinesib-NTC-ASO) was synthesised[100] (Figure A.26). To minimize potential non-specific interactions, one-step copper-catalyzed chemistry was employed to ensure minimal linker effects in the ispinesib-NTC-ASO.

4.3.3 NCL1 2′-OMe LyTON outperforms unmodified parent ASO for mRNA knockdown

To investigate whether the ATTEC-warhead ispinesib could facilitate lysosomal trafficking and subsequent lysosomal degradation of target mRNA (Figure 4.5a), the fully 2′-O-Methyl (2′-OMe) sugar-modified ASO backbone was chosen. This chemistry is known to be RNase H-inactive, allowing us to evaluate the ispinesib-

ASO without interference from RNase H-mediated degradation (Figure 4.5b). A previously validated ASO sequence designed to target cytoplasmic NCL1 mRNA[100] was chosen with the 5′-terminal modified with ispinesib via SPAAC, as described earlier.

NCL1 transcript levels were measured using RT-qPCR in HEK293T, A549, and HeLa cells following lipofectamine transfection at 24 hours, all normalized to the housekeeping gene GAPDH. NCL1 transcript levels were compared after treatment with NCL1 2′-OMe LyTON, NCL1 2′-OMe ASO, and 5′-DBCO-modified NCL1 2′-OMe ASO. The DBCO-modified ASO served as a control to account for any effects of modifying the ASO with a hydrophobic end group. The NCL1 2′-OMe LyTON significantly outperformed its unconjugated counterpart at all concentrations tested and across all cell lines (Figure 4.5b,c,d), while the unmodified NCL1 2′-OMe ASO and DBCO-modified counterpart exhibited similarly poor knockdown, as they only block the target mRNA sterically (Figure 4.6). The ispinesib-NTC-ASO showed little to no reduction in NCL1 transcript levels (Figure 4.6).

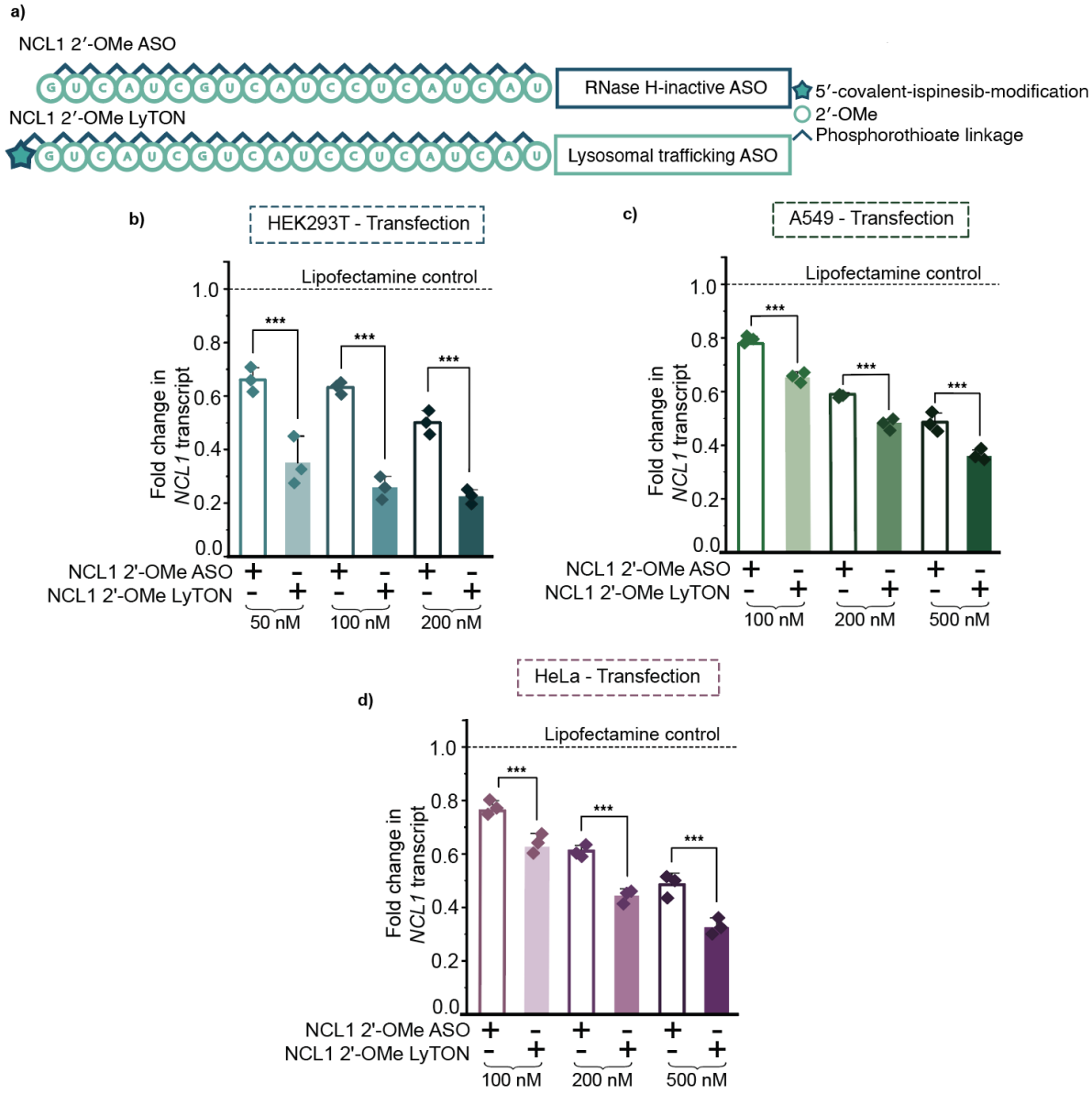

Figure 4.5: Covalent ispinesib modification of RNase H-inactive 2′- OMe ASO enables potent knockdown of target mRNA. (a) Sequence and chemical modifications of NCL1 ASOs used. (b)-(d) RT-qPCR data for NCL1 knockdown upon lipofectamine transfection for 24 hours) NCL1 2′-OMe LyTON and unconjugated-NCL1 2′-OMe ASO in HEK293T (b), A549 (c), or HeLa (d) cells at concentrations indicated. Three biological replicates are shown as diamonds for each condition (each from three technical replicates). The vertical bars represent the mean and the error bars the standard deviation. ** represents $p<0.05$, *** represents $p<0.01$, n.s. represents p values that are not significant.*Figure re-produced from "Engineering antisense oligonucleotides for targeted mRNA degradation through lysosomal trafficking" by Kashyap et al., under CC-BY 3.0.*

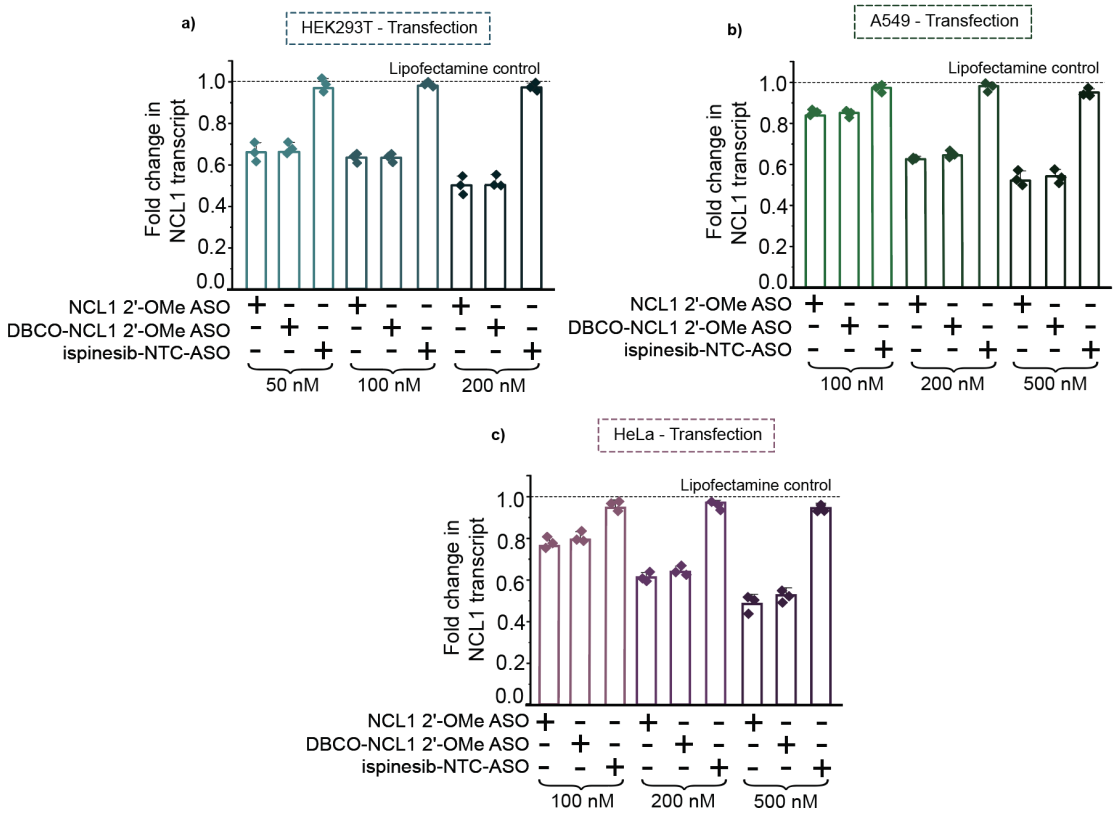

Figure 4.6: RT-qPCR data of NCL1 knockdown upon unmodified NCL1 2′-OMe ASO, DBCO-modified NCL1 2′-OMe ASO and ispinesib-NTC-ASO lipofectamine transfection in (a) HEK293Ts, (b) A549, (c) HeLa for 24 hours at concentrations indicated. Three biological replicates are shown as diamonds for each condition (each from three technical replicates). The vertical bars represent the mean and the error bars the standard deviation. ** represents $p<0.05$, *** represents $p<0.01$, n.s. represents p values that are not significant. *Figure re-produced from supplementary information of "Engineering antisense oligonucleotides for targeted mRNA degradation through lysosomal trafficking" by Kashyap et al., under CC-BY 3.0.*

Furthermore, little to no differences was observed in the toxicity profiles of the unconjugated and ispinesib-conjugated ASOs, assessed by Cell Titer Glo (Figure 4.7a,b,c) and RNA transcript levels of key housekeeping genes (Figure 4.8). These results align with our initial expectations, as our treatments were within the sub-micromolar range, far below concentrations that would cause toxicity associated

with kinesin spindle protein (Eg5) inhibition, the canonical target of ispinesib.

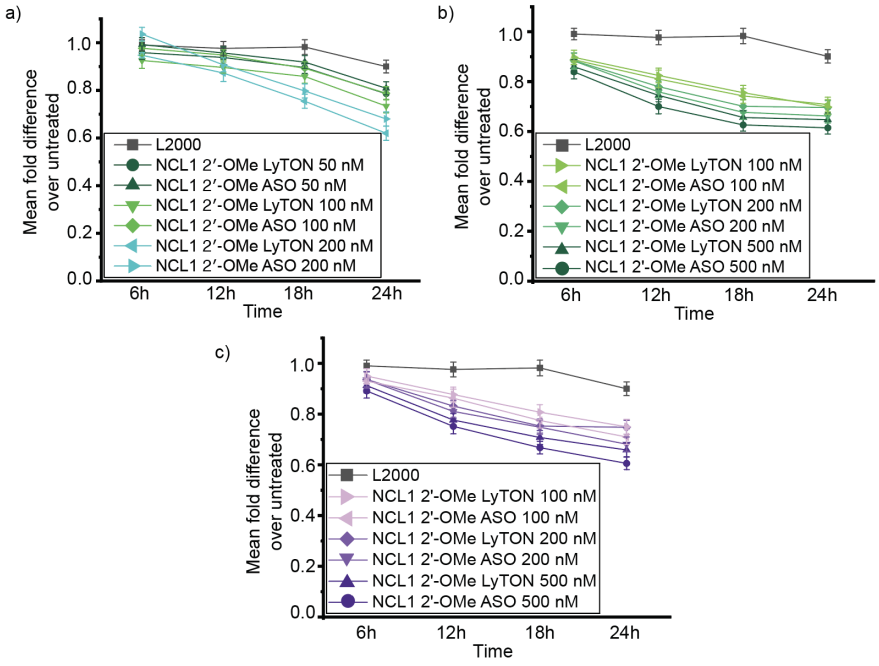

Figure 4.7: Cell viability of the (a) HEK293T, (b) A549, (c) HeLa upon NCL1 2′-OMe ASO and NCL1 2′-OMe LyTON treatment evaluated by Cell-Titer Glo. *Figure re-produced from supplementary information of "Engineering antisense oligonucleotides for targeted mRNA degradation through lysosomal trafficking" by Kashyap et al., under CC-BY 3.0.*

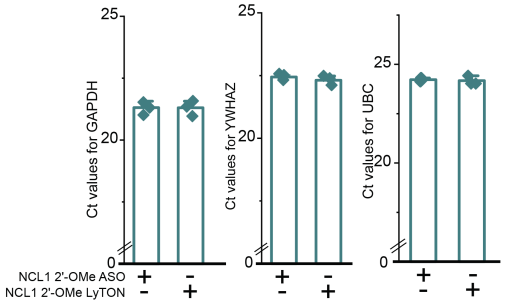

Figure 4.8: Ct values for key housekeeping genes upon NCL1 2′- OMe ASO and NCL1 2′- OMe LyTON treatment at 200 nM in HEK293T. *Figure re-produced from supplementary information of "Engineering antisense oligonucleotides for targeted mRNA degradation through lysosomal trafficking" by Kashyap et al., under CC-BY 3.0.*

Using SPAAC chemistry, two regioisomeric NCL1 2′-OMe LyTON products (Fig-

ure 4.9) were obtained. Both regioisomers exhibited comparable activity, suggesting that the configuration of ispinesib around the DBCO linkage does not influence the functional activity of the conjugate (Figure 4.9). All subsequent experiments were performed using a combination of both regioisomers.

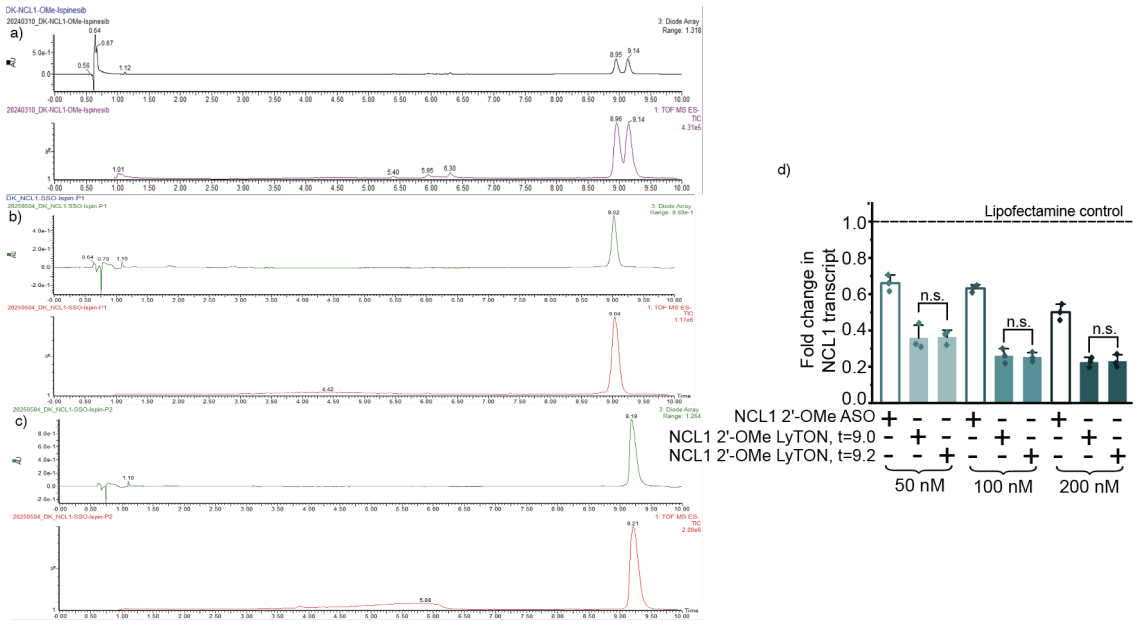

Figure 4.9: LC-MS characterisation and RT-qPCR for regioisomers for ispinesib modification of NCL1 2′-OMe ASO. (a) LC-MS trace for HPLC-purified NCL1 2′-OMe LyTON regioisomer mixture . (b) LC-MS trace for HPLC-purified NCL1 2′-OMe LyTON regioisomer, t=9.0. (c) LC-MS trace for HPLC-purified NCL1 2′-OMe LyTON regioisomer, t=9.2. (d) RT-qPCR data for NCL1 transcript levels upon lipofectamine transfection with purified regioisomers of NCL1 2′-OMe LyTON at 24 hours at concentrations indicated.*Figure re-produced from "Engineering antisense oligonucleotides for targeted mRNA degradation through lysosomal trafficking" by Kashyap et al., under CC-BY 3.0.*

After establishing improved knockdown efficiency under transfection conditions, the next objective was to evaluate the activity of the LyTON conjugate by employing gymnotic delivery. Gymnotic delivery refers to oligonucleotide delivery without transfection reagents, providing a more physiologically and clinically relevant as-

sessment of activity.

To this end, the LyTON was compared with its unconjugated and 5′-DBCO–modified counterparts, as well as with an ispinesib–NTC–ASO control, at concentrations of 5, 10, and 20 µM over a 96-hour period, with transcript levels quantified by RT-qPCR as before. Consistent with expectations, the ispinesib–NTC–ASO exhibited negligible knockdown activity, confirming that the effects observed with LyTONs were sequence-dependent rather than arising from nonspecific contributions of the small-molecule cargo. Similarly, the DBCO-modified NCL1-2′-OMe ASO produced results nearly identical to those of the unconjugated ASO, indicating that the simple addition of a reactive handle does not enhance efficacy (Figure 4.10). In contrast, the ispinesib-conjugated LyTON demonstrated a striking and consistent increase in knockdown across all tested concentrations and cell types, far exceeding the activity of the unconjugated NCL1-2′-OMe ASO (Figure 4.11a–c).

Taken together, these findings suggest that ispinesib conjugation specifically enhances the potency of RNase H–inactive ASOs, while avoiding sequence-independent or off-target effects. This highlights the potential utility of LyTONs as a generalizable strategy for improving the performance of chemically modified ASOs under clinically relevant delivery conditions.

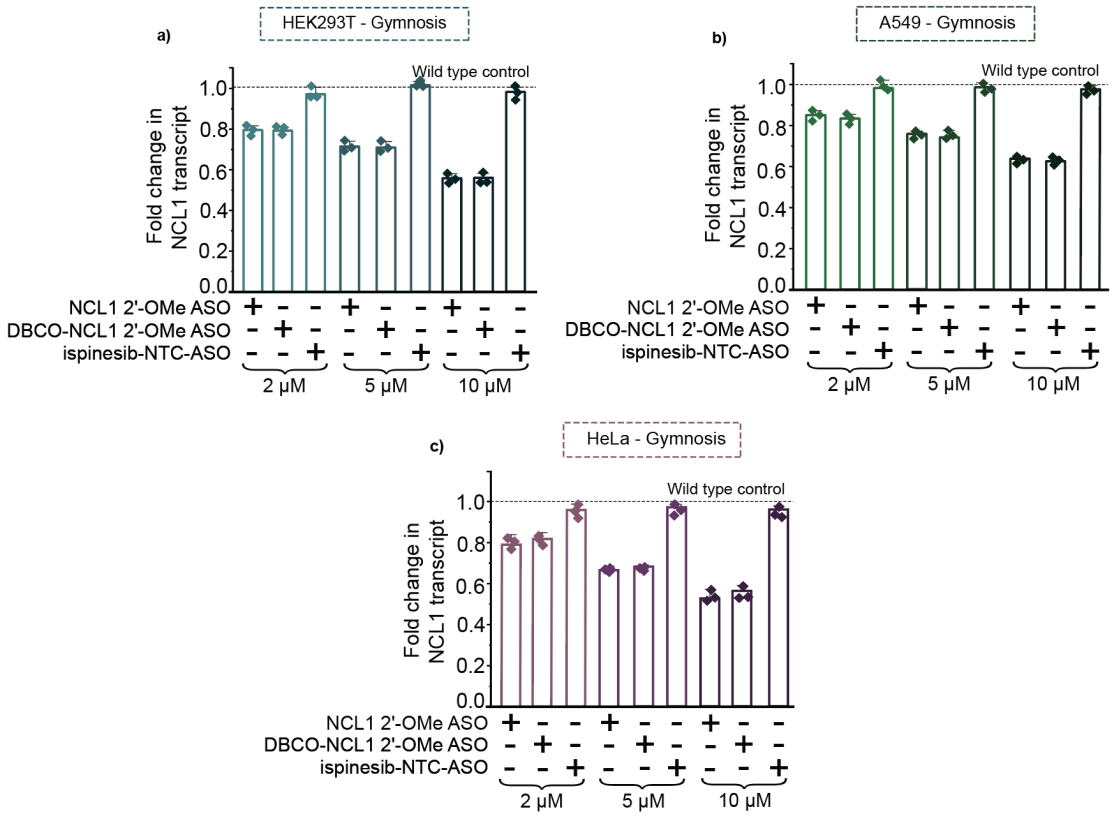

Figure 4.10: RT-qPCR data of NCL1 knockdown upon unmodified NCL1 2′-OMe ASO, DBCO-modified NCL1 2′-OMe ASO and ispinesib-NTC-ASO gymnosis in (a) HEK293T, (b) A549, (c) HeLa for 96 hours at concentrations indicated. Three biological replicates shown as diamonds for each condition (each from three technical replicates). The vertical bars represent the mean and the error bars the standard deviation. ** represents $p<0.05$, *** represents $p<0.01$, n.s. represents p values that are not significant. *Figure re-produced from supplementary information of "Engineering antisense oligonucleotides for targeted mRNA degradation through lysosomal trafficking" by Kashyap et al., under CC-BY 3.0.*

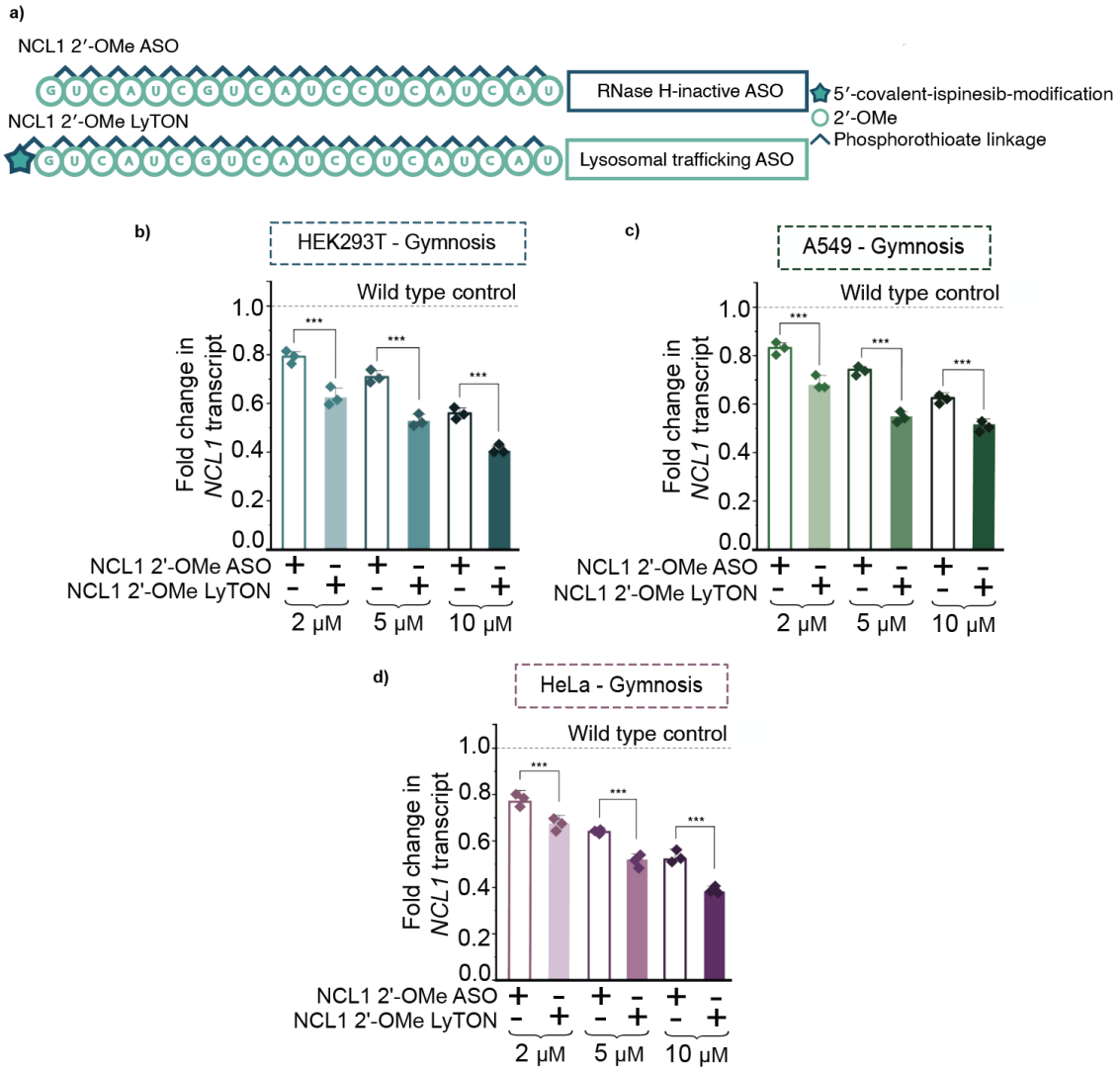

Figure 4.11: Covalent ispinesib modification of RNase H-inactive 2′- OMe ASO enables potent knockdown of target mRNA via gymnosis. (a) Sequence and chemical modifications of NCL1 ASOs used. (b)-(d) RT-qPCR data for NCL1 knockdown upon gymnosis for 96 hours NCL1 2′- OMe LyTON and unconjugated-NCL1 2′-OMe ASO in HEK293T (b), A549 (c), or HeLa (d) cells at concentrations indicated. Three biological replicates are shown as diamonds for each condition (each from three technical replicates). The vertical bars represent the mean and the error bars the standard deviation. ** represents $p<0.05$, *** represents $p<0.01$, n.s. represents p values that are not significant. *Figure re-produced from "Engineering antisense oligonucleotides for targeted mRNA degradation through lysosomal trafficking" by Kashyap et al., under CC-BY 3.0.*

4.3.4 Synthesis of Ispinesib-NCL1 RNase H-active conjugate

The NCL1 ASO sequence used was originally designed for RNase H-mediated knockdown as a 'gapmer'. The cutting-edge ASO chemistry 'gapmer' design comprises wings of five bases containing 2′-MOE sugars and a central DNA region[231]. It was then assessed whether the covalent ispinesib modification of the NCL1 'gapmer' ASO could enhance its efficacy. Synthesis was carried out as previously described, starting with a 5′-amine-modified gapmer (Appendix Figure A.27, Figure A.28).

4.3.5 Ispinesib-modification compatible with ASO gapmer knockdown chemistry and enhances knockdown efficacy

The dual activity' conjugate was synthesised by linking ispinesib to the NCL1 gapmer, combining RNase H-mediated degradation with lysosomal trafficking (Figure 4.12a,b). The NCL1 gapmer LyTON, along with unconjugated and 5′-DBCO-modified controls, was transfected into HEK293T, A549, and HeLa cells using lipofectamine 2000, and NCL1 transcript levels were measured at 24 hours by RT-qPCR. Across all tested cell lines, the dual activity' LyTON outperformed controls at middle and lower concentrations, while at higher concentrations activity improved in A549 but plateaued in HEK293T and HeLa (Figure 4.12c–e).

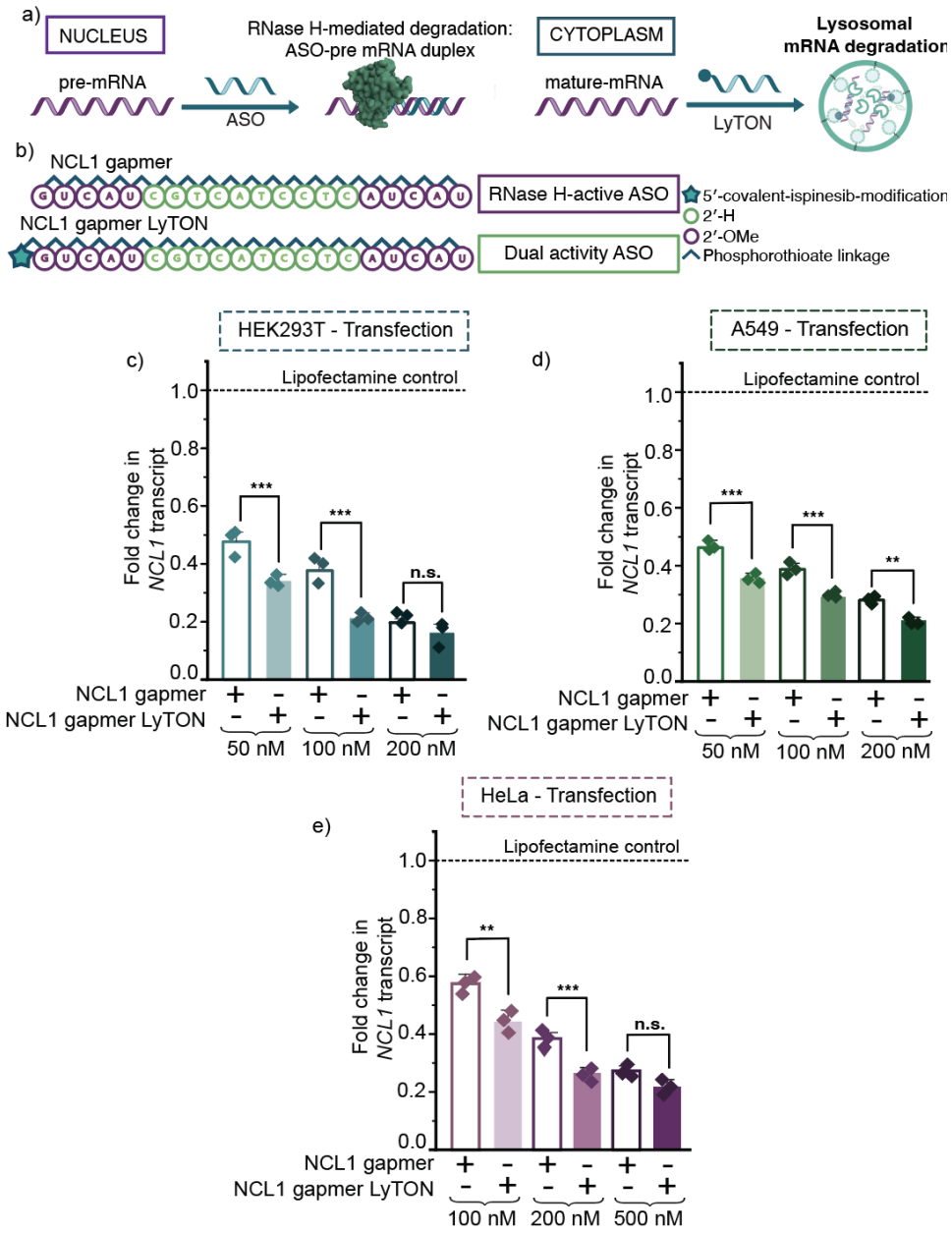

Figure 4.12: Covalent ispinesib modification of RNase H-active gapmer ASO yields a "dual activity" conjugate with enhanced knockdown capacity of target mRNA. (a) Proposed mechanism of action for the lysosome trafficking-ispinesib ASO (LyTON) conjugates for mRNA knockdown, in contrast to the established RNase H mechanism for mRNA knockdown of ASOs. (b) Sequence and chemical modifications of NCL1 gapmer ASOs used. RT-qPCR data for NCL1 knockdown upon lipofectamine transfection of NCL1 gapmer LyTON and unconjugated-NCL1 gapmer ASO in HEK293T (c), A549 (d), or HeLa (e) cells at concentrations indicated for 24 hours. Three biological replicates are shown as diamonds for each condition (each from three technical replicates). The vertical bars represent the mean and the error bars the standard deviation. ** represents $p<0.05$, *** represents $p<0.01$, n.s. represents p values that are not significant. *Figure re-produced from "Engineering antisense oligonucleotides for targeted mRNA degradation through lysosomal trafficking" by Kashyap et al., under CC-BY 3.0.*

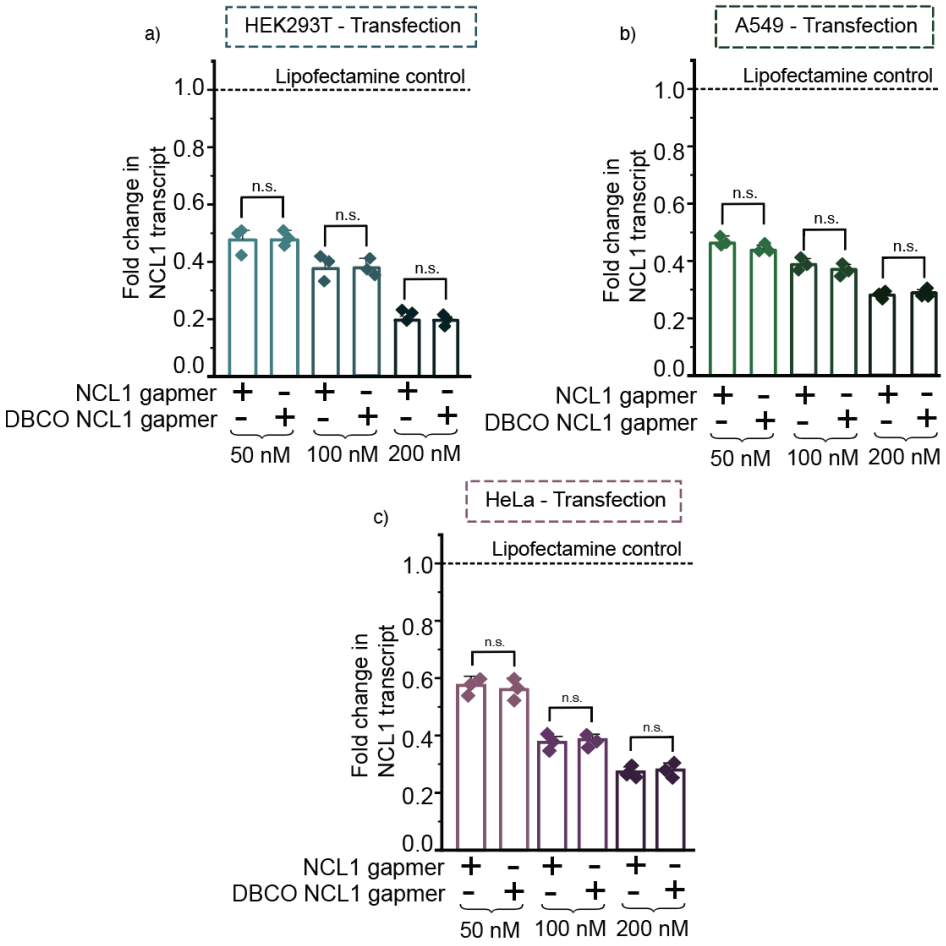

Figure 4.13: RT-qPCR data of NCL1 knockdown upon unmodified and DBCO-modified NCL1 gapmer lipofectamine transfection in (a) HEK293T, (b) A549, (c) HeLa for 24 hours at concentrations indicated. Three biological replicates shown as diamonds for each condition (each from three technical replicates). The vertical bars represent the mean and the error bars the standard deviation. ** represents $p<0.05$, *** represents $p<0.01$, n.s. represents p values that are not significant. *Figure re-produced from supplementary information of "Engineering antisense oligonucleotides for targeted mRNA degradation through lysosomal trafficking" by Kashyap et al., under CC-BY 3.0.*

Knockdown efficacy was further evaluated under conditions of gymnotic uptake, in which oligonucleotides are delivered without transfection reagents, providing a more physiologically and clinically relevant assessment of activity. The performance of the

NCL1 gapmer LyTON was compared directly to both the unmodified NCL1 gapmer and the 5′-DBCO–modified gapmer, thereby establishing whether the conjugation strategy could confer a measurable advantage in the absence of facilitated delivery.

Consistent with the results obtained using lipofectamine-mediated transfection, gymnotic delivery produced a marked enhancement in the knockdown activity of the 'dual activity' NCL1 gapmer LyTON. Across all cell types tested and at nearly all concentration ranges, the LyTON outperformed the unmodified NCL1 gapmer, with the exception of the highest concentrations, where activity reached a plateau (Figure 4.14). Importantly, both the unmodified and the DBCO-modified controls displayed comparable levels of activity, which were consistently and significantly lower than those of the ispinesib-conjugated LyTON (Figure 4.15).

These findings highlight that the observed improvements in efficacy can be attributed specifically to the ispinesib modification, highlighting the potential of this conjugation strategy to enhance therapeutic performance under clinically relevant conditions.

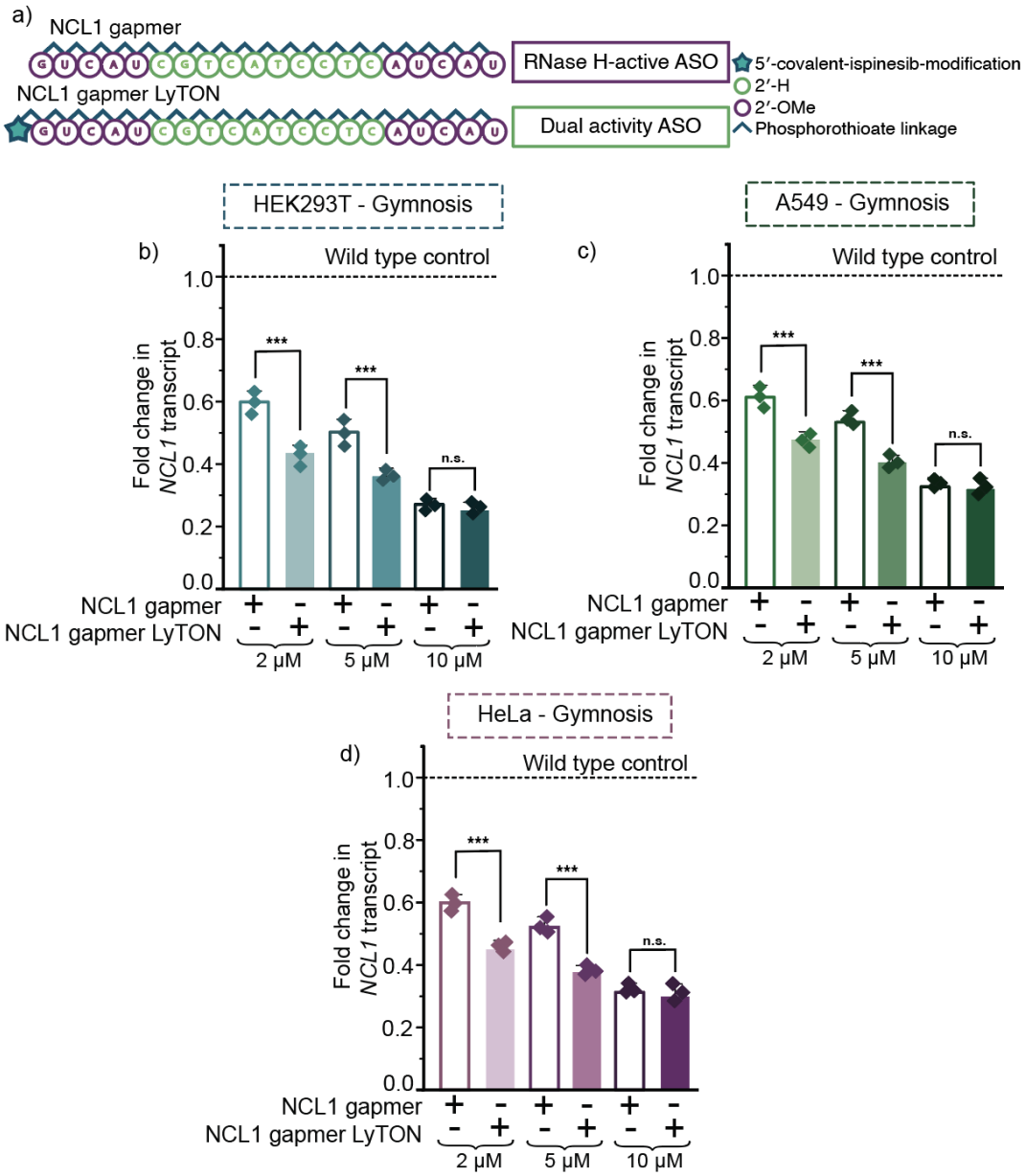

Figure 4.14: Covalent ispinesib modification of RNase H-active gapmer ASO yields a "dual activity" conjugate with enhanced knockdown capacity of target mRNA via gymnosis. (a) Sequence and chemical modifications of NCL1 gapmer ASOs used. (b)-(d) RT-qPCR data for NCL1 knockdown upon gymnosis of NCL1 gapmer LyTON and unconjugated-NCL1 gapmer ASO in HEK293T (b), A549 (c), or HeLa (d) cells at concentrations indicated for 96 hours. Three biological replicates are shown as diamonds for each condition (each from three technical replicates). The vertical bars represent the mean and the error bars the standard deviation. ** represents $p<0.05$, *** represents $p<0.01$, n.s. represents p values that are not significant.*Figure re-produced from "Engineering antisense oligonucleotides for targeted mRNA degradation through lysosomal trafficking" by Kashyap et al., under CC-BY 3.0.*

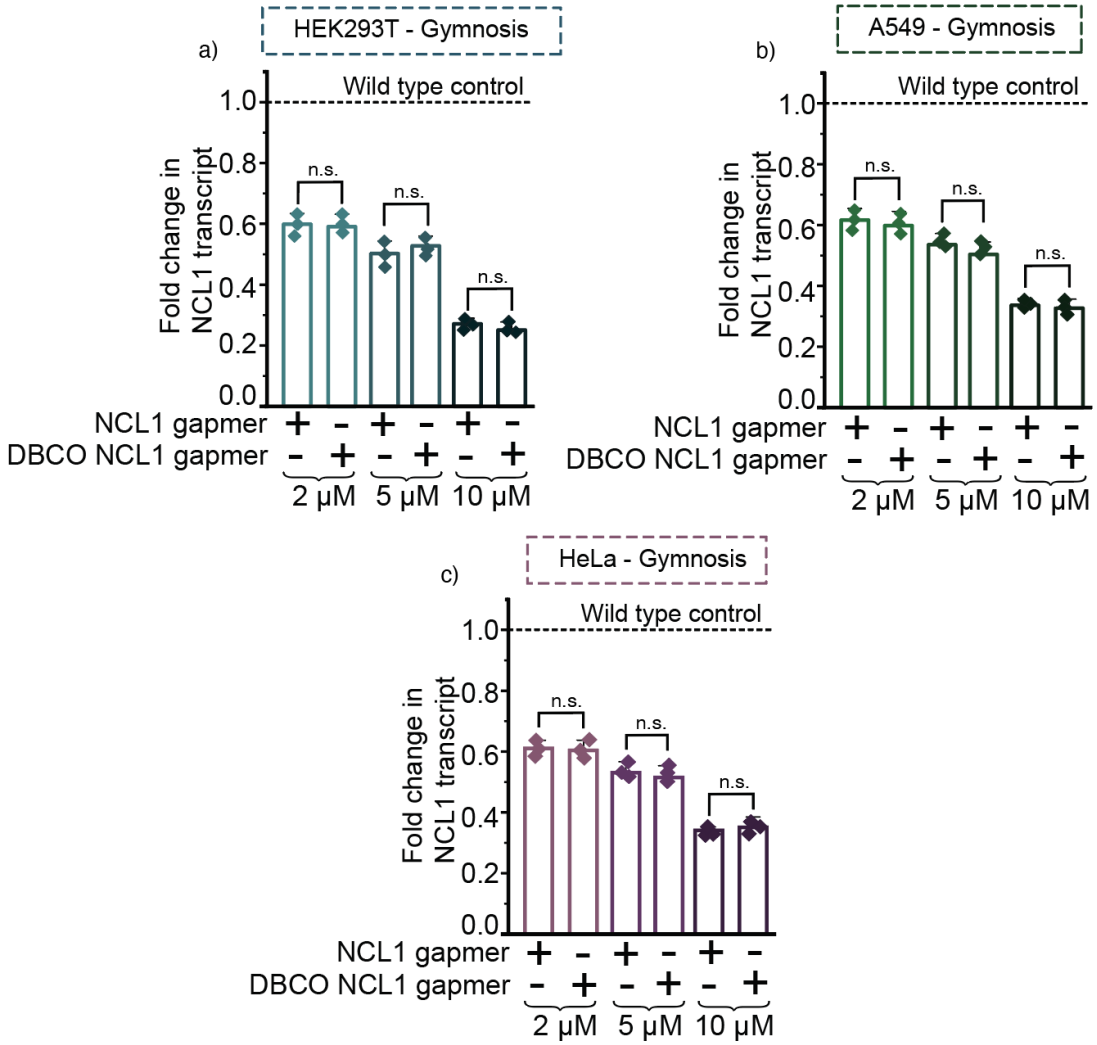

Figure 4.15: RT-qPCR data of NCL1 knockdown upon unmodified and DBCO-modified NCL1 gapmer gymnosis in (a) HEK293T, (b) A549, (c) HeLa for 96 hours at concentrations indicated. Three biological replicates are shown as diamonds for each condition (each from three technical replicates). The vertical bars represent the mean and the error bars the standard deviation. ** represents $p<0.05$, *** represents $p<0.01$, n.s. represents p values that are not significant. *Figure re-produced from supplementary information of "Engineering antisense oligonucleotides for targeted mRNA degradation through lysosomal trafficking" by Kashyap et al., under CC-BY 3.0.*

4.3.6 Mechanism of action for NCL1 2′-OMe LyTON is selective: loss of activity upon bafilomycin and chloroquine treatment

These results thus far demonstrate that the conjugation of ispinesib to NCL1 RNase H-inactive or RNase H-active ASOs results in a significant increase in target mRNA reduction. Next, the aim was to confirm whether the mechanism of mRNA degradation involved the lysosome by using inhibitors of various aspects of lysosomal function: bafilomycin and chloroquine.

Bafilomycin is a well-characterized inhibitor of lysosomal activity[232,233] (Figure 4.16a). Bafilomycin inhibits vacuolar (V)-ATPase, preventing lysosomal acidification and disrupting basal lysosomal flux. If the LyTONs were trafficking the target mRNA to the lysosome, treatment with bafilomycin would result in a loss of knockdown activity.

HEK293T cells were first treated with bafilomycin for 24 hours and lysosomal inhibition was confirmed by observing an increase in LC3-II levels (Figure 4.16b, Appendix Figure A.48). Since 100 nM bafilomycin caused cell toxicity, which could lead to inaccurate ASO efficacy assessments, a lower 10 nM concentration (which did not affect cell viability) was used for further studies (Figure 4.16c).

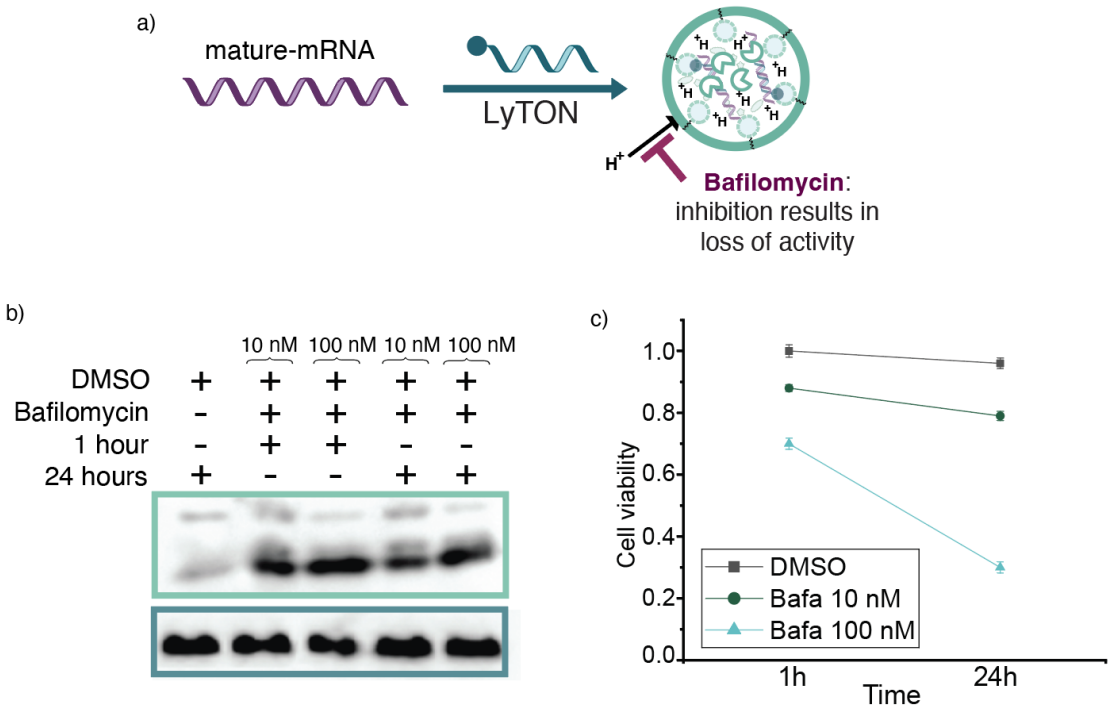

Figure 4.16: Biological characterisation for Bafilomycin inhibition and toxicity evaluation. (a) Mechanism of bafilomycin-mediated lysosomal inhibition in relation to LyTON activity. (b) Uncropped western blot of LC3-I and LC3-II levels upon treatment with bafilomycin at indicated concentrations and time points in HEK293Ts. (c) Cell viability upon bafilomycin (Bafa) treatment in HEK293Ts assayed by dye exclusion on hemocytometer. *Figure re-produced from "Engineering antisense oligonucleotides for targeted mRNA degradation through lysosomal trafficking" by Kashyap et al., under CC-BY 3.0.*

NCL1 transcript knockdown was then measured after transfection with the NCL1 2′-OMe ASO, NCL1 2′-OMe LyTON, NCL1 gapmer, and NCL1 gapmer LyTON in the presence or absence of bafilomycin in HEK293T cells (Figure 4.17a). As expected, bafilomycin treatment did not affect the activity of the NCL1 2′-OMe ASO or NCL1 gapmer. However, the enhanced mRNA knockdown activity of both the NCL1 2′-OMe LyTON and NCL1 gapmer LyTON was completely lost in the presence of bafilomycin, resulting in comparable activity to the unmodified NCL1

2′-OMe ASO or NCL1 gapmer. The same trend was observed in A549 (Figure 4.17b) and HeLa cells (Figure 4.17c).

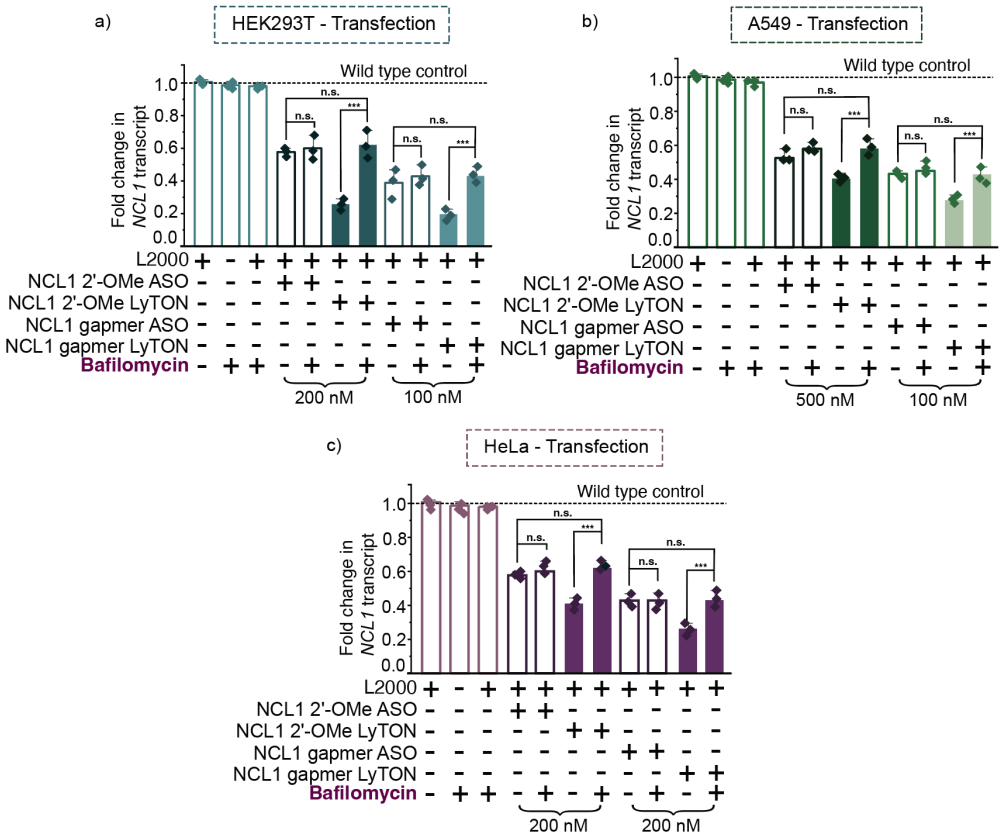

Figure 4.17: LyTON-warhead ispinesib unlocks a new mechanism of ASO-mediated mRNA degradation via lysosomal trafficking, validated using bafilomycin. RT-qPCR data for NCL1 knockdown upon lipofectamine transfection of NCL1 gapmer ASO, NCL1 gapmer LyTON, NCL1 2′-OMe ASO, and NCL1 2′-OMe LyTON in the presence or absence of 10 nM bafilomycin, at the concentrations indicated, in (a) HEK293T, (b) A549, (c) HeLa cells. Three biological replicates are shown as diamonds for each condition (each from three technical replicates). The vertical bars represent the mean and the error bars the standard deviation. ** represents $p<0.05$, *** represents $p<0.01$, n.s. represents p values that are not significant. *Figure re-produced from "Engineering antisense oligonucleotides for targeted mRNA degradation through lysosomal trafficking" by Kashyap et al., under CC-BY 3.0.*

To eliminate potential confounding effects of lipofectamine-mediated transfection, the bafilomycin inhibition assay was repeated using gymnotic delivery of NCL1

2′-OMe ASO, NCL1 2′-OMe LyTON, NCL1 gapmer, and NCL1 gapmer LyTON (Figure 4.18). The same trend was observed: bafilomycin treatment did not affect the activity of the NCL1 2′-OMe ASO or NCL1 gapmer upon gymnotic delivery. However, the increased mRNA knockdown activity of both the NCL1 2′-OMe LyTON and NCL1 gapmer LyTON, when delivered gymnotically, was completely lost in the presence of bafilomycin, with activity restored to the parent unmodified NCL1 2′-OMe ASO or NCL1 gapmer. This confirmed that LyTONs rely on lysosomal degradation for activity and that inhibition of normal lysosomal flux reduced them to conventional ASOs.

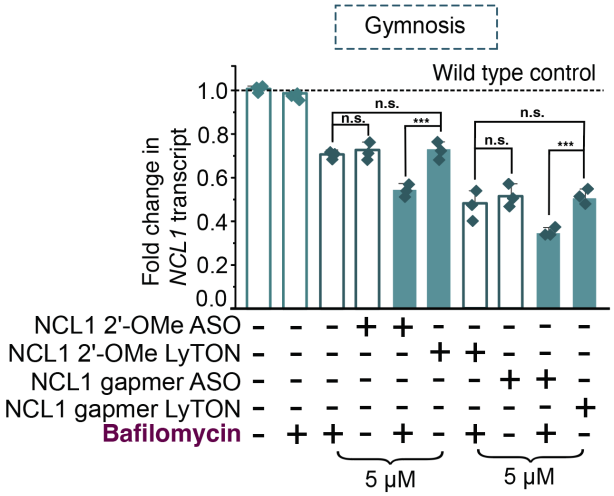

Figure 4.18: LyTON-warhead ispinesib unlocks a new mechanism of ASO-mediated mRNA degradation via lysosomal trafficking, validated using bafilomycin—via gymnosis. RT-qPCR data for NCL1 knockdown upon gymnosis of NCL1 gapmer ASO, NCL1 gapmer LyTON, NCL1 2′-OMe ASO, and NCL1 2′-OMe LyTON in the presence or absence of 10 nM bafilomycin, at the concentrations indicated HEK293T cells. Three biological replicates are shown as diamonds for each condition (each from three technical replicates). The vertical bars represent the mean and the error bars the standard deviation. ** represents $p<0.05$, *** represents $p<0.01$, n.s. represents p values that are not significant. *Figure re-produced from "Engineering antisense oligonucleotides for targeted mRNA degradation through lysosomal trafficking" by Kashyap et al., under CC-BY 3.0.*

Chloroquine is another well-characterized lysosomal inhibitor— known to accumulate in the lysosome due to its weakly basic nature. This raises intra-lysosomal pH and causes lysosomal membrane permeabilization, leading to partial leakage of lysosomal contents into the cytosol (Figure 4.19a)[234]. Chloroquine is commonly used to enhance the endosomal/lysosomal escape of ASOs, improving their activity within cells.

First, a chloroquine dose titration was conducted, as excessive chloroquine can cause broad lysosomal dysfunction and cytotoxicity, which may obscure or reduce ASO activity (Figure 4.19b). Next, the NCL1 gapmer and NCL1 2′-OMe ASO were transfected in HEK293T cells in the presence and absence of 30 µM chloroquine and, as expected, a significant improvement in the activity of both conventional ASOs (Figure 4.19c) was observed. In contrast, chloroquine treatment inhibited the activity of both the NCL1 2′-OMe LyTON and NCL1 gapmer LyTON (Figure 4.19c). This confirmed that functional lysosomal integrity is necessary for the LyTON mechanism of action.

These findings highlight a key distinction in the intracellular processing pathways between unconjugated ASOs, which may benefit from disrupted lysosomal barriers, and LyTON conjugates, which require intact lysosomal processing machinery for activity.

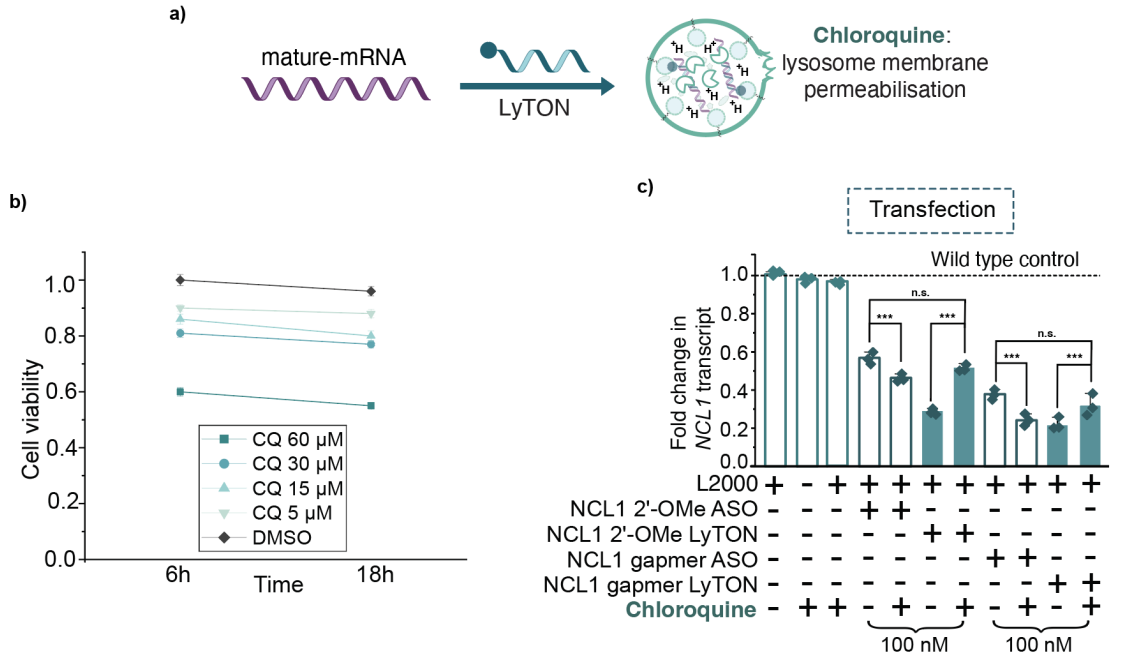

Figure 4.19: LyTON-warhead ispinesib unlocks a new mechanism of ASO-mediated mRNA degradation via lysosomal trafficking, validated using chloroquine. RT-qPCR data for NCL1 knockdown upon lipofectamine transfection of NCL1 gapmer ASO, NCL1 gapmer LyTON, NCL1 2′-OMe ASO, and NCL1 2′-OMe LyTON in HEK293T cells in the presence or absence of 30 µM chloroquine, at the concentrations indicated. Three biological replicates are shown as diamonds for each condition (each from three technical replicates). The vertical bars represent the mean and the error bars the standard deviation. ** represents $p<0.05$, *** represents $p<0.01$, n.s. represents p values that are not significant. *Figure re-produced from "Engineering antisense oligonucleotides for targeted mRNA degradation through lysosomal trafficking" by Kashyap et al., under CC-BY 3.0.*

4.3.7 Synthesis of Ispinesib-MEN1 RNase H-inactive conjugate

After establishing the chemistry and mechanism of action of LyTONs, the next goal was to target a therapeutically relevant gene of interest: the MEN1 gene, which encodes the protein Menin. Menin plays a crucial role in MLL-rearranged

leukemias[229]. A well-established MEN1 ASO sequence was selected, which contains all 2′-OMe-modified sugars (RNase H-inactive)[235]. As with the NCL1 LyTONs, ispinesib was conjugated to the 5′-terminus of the MEN1 2′-OMe ASO using SPAAC chemistry.

4.3.8 MEN1 2′-OMe LyTON conjugate outperforms unmodified MEN1 2′-OMe ASO for both target mRNA knockdown and protein degradation

Menin is an important oncogenic cofactor in MLL-rearranged and KRAS-driven cancers, making it an attractive therapeutic target. Menin serves as a scaffold for oncogenic MLL fusion proteins, driving transcriptional activation programs that promote leukemic cell survival and growth[236]. It also plays a key role in KRAS-driven cancers[237]. Inhibition of Menin has been shown to disrupt these cancer-sustaining pathways, resulting in reduced cell proliferation and increased apoptosis[238,239].

While small-molecule Menin inhibitors have shown early clinical promise, recent studies have reported emerging resistance and patient relapse due to somatic mutations in MEN1[240]. These mutations occur in a critical region of the inhibitor-binding pocket, which is essential for stabilizing Menin-inhibitor binding but not for the Menin-MLL interaction. These challenges in small molecule drug resistance could potentially be circumvented by targeting MEN1 mRNA with ASOs. Thus,

the MEN1 2′-OMe LyTON was investigated as a alternative (Figure 4.20a).

MEN1 transcript levels were measured after transfection of the MEN1 2′-OMe LyTON using RT-qPCR in HEK293T cells at 24 hours, comparing the knockdown to the unconjugated and 5′-DBCO-modified MEN1 2′-OMe ASO, and the ispinesib-NTC-ASO, all normalized to the housekeeping gene GAPDH. The MEN1 2′-OMe LyTON significantly outperformed the unmodified MEN1 2′-OMe ASO at all tested concentrations (Figure 4.20b). A marked reduction in Menin protein levels was also observed upon MEN1 2′-OMe LyTON treatment, compared to the unconjugated ASO, in a concentration-dependent manner (Figure 4.20c, Appendix Figure A.49). Similar trends were observed in A549 and HeLa cells (Figure 4.21a,b) at all tested concentrations.

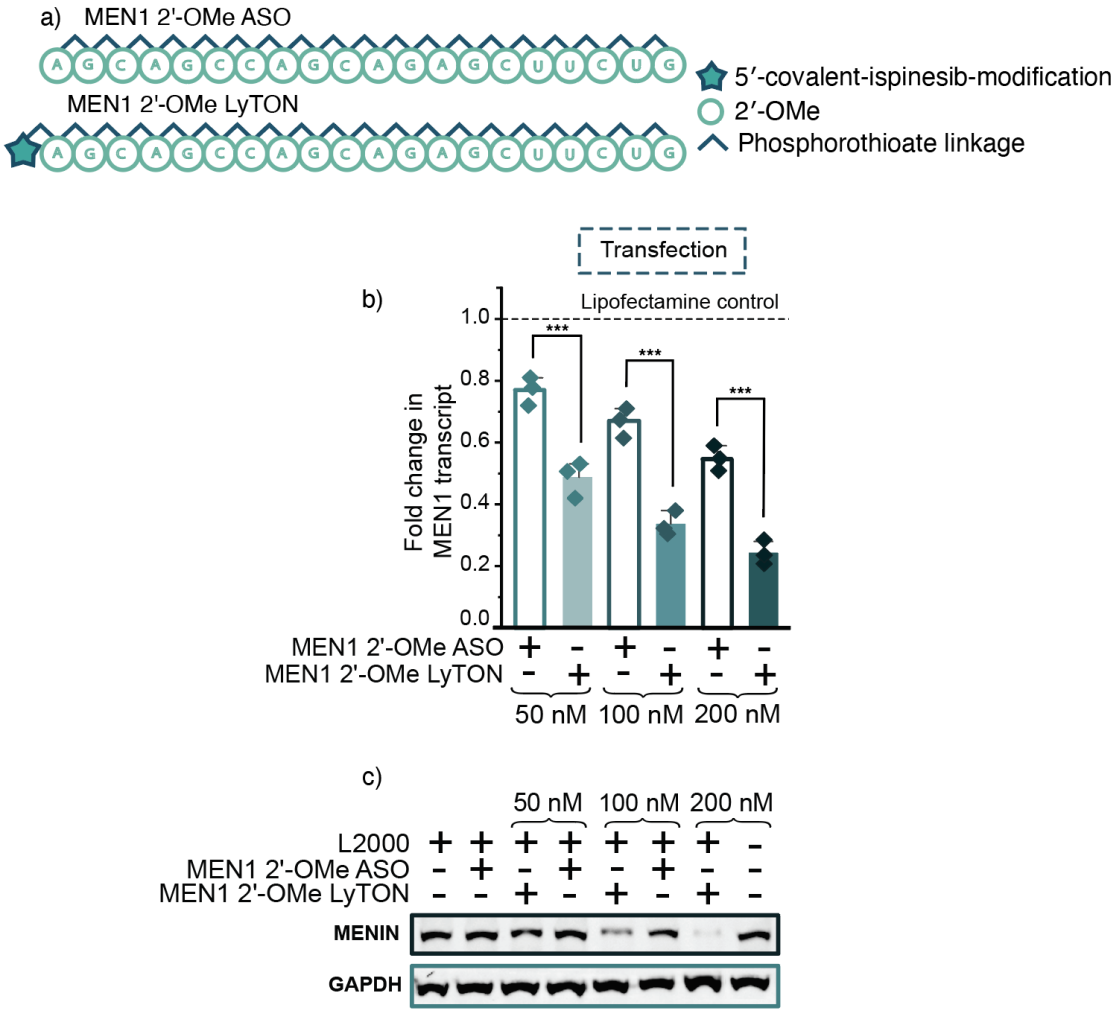

Figure 4.20: MEN1 2′-OMe LyTON treatment results in significant knockdown of MEN1 mRNA and protein. (a) Sequence and chemical modifications of ASOs used to target MEN1. (b) RT-qPCR data and (c) Western blot for MEN1/Menin knockdown upon lipofectamine transfection of MEN1 2′-OMe ASO and MEN1 2′-OMe LyTON ASO in HEK293T cells at concentrations indicated. Three biological replicates are shown as diamonds for each condition (each from three technical replicates). The vertical bars represent the mean and the error bars the standard deviation. ** represents $p<0.05$, *** represents $p<0.01$, n.s. represents p values that are not significant. *Figure re-produced from "Engineering antisense oligonucleotides for targeted mRNA degradation through lysosomal trafficking" by Kashyap et al., under CC-BY 3.0.*

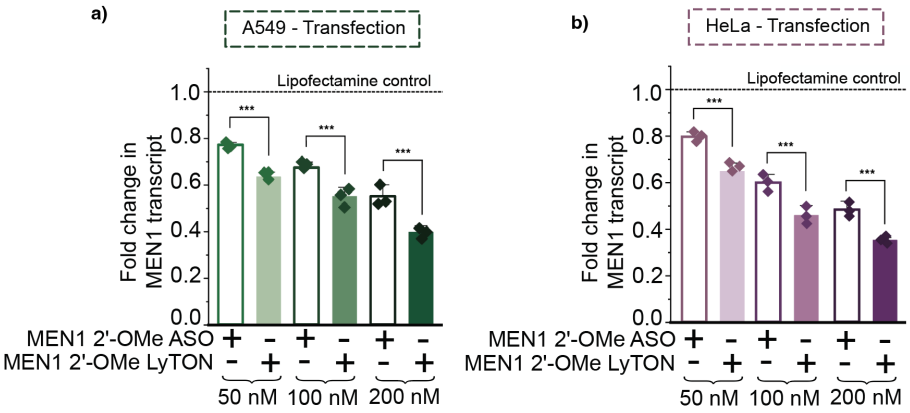

Figure 4.21: RT-qPCR data for MEN1 knockdown upon lipofectamine transfection of unmodified MEN1 2′- OMe ASO and MEN1 2′- OMe LyTON ASO in (a) A549, (b) HeLa at the concentrations indicated for 24 hours. Three biological replicates are shown as diamonds for each condition (each from three technical replicates). The vertical bars represent the mean and the error bars the standard deviation. ** represents $p<0.05$, *** represents $p<0.01$, n.s. represents p values that are not significant. *Figure re-produced from supplementary information of "Engineering antisense oligonucleotides for targeted mRNA degradation through lysosomal trafficking" by Kashyap et al., under CC-BY 3.0.*

The ispinesib–NTC–ASO exhibited little to no knockdown activity, consistent with its design as a non-targeting control and confirming that the presence of the ispinesib moiety alone is insufficient to elicit degradation in the absence of a complementary sequence. Likewise, the DBCO-modified MEN1 2′-OMe ASO produced results nearly identical to those of the unconjugated MEN1 2′-OMe ASO across all tested cell lines, indicating that the addition of a reactive handle does not alter the intrinsic activity of the ASO (Figure 4.22).

Thus, these findings establish that the activity is sequence- and conjugation-specific, rather than arising from non-specific chemical modification of the oligonucleotide.

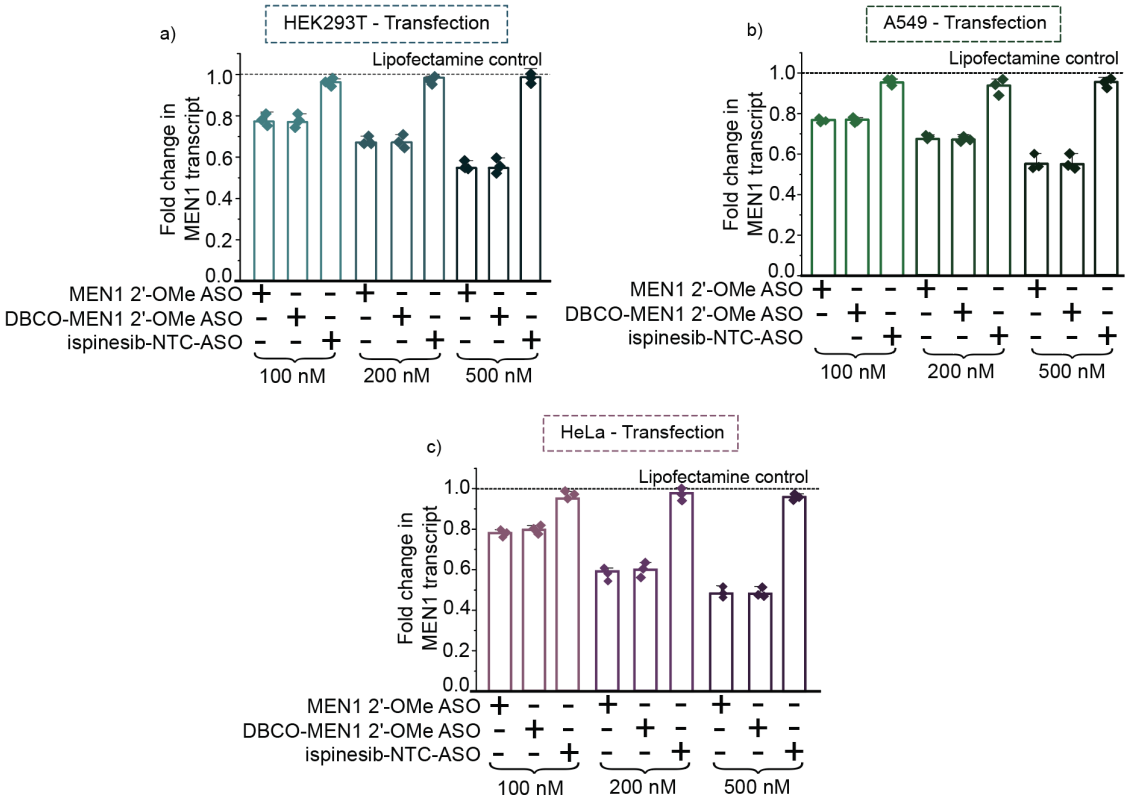

Figure 4.22: RT-qPCR data of MEN1 knockdown upon unmodified MEN1 2′- OMe ASO, DBCO-modified MEN1 2′- OMe ASO and ispinesib-NTC-ASO lipofectamine transfection in (a) HEK293T, (b) A549, (c) HeLa for 24 hours at concentrations indicated. Three biological replicates are shown as diamonds for each condition (each from three technical replicates). The vertical bars represent the mean and the error bars the standard deviation. ** represents $p<0.05$, *** represents $p<0.01$, n.s. represents p values that are not significant. *Figure re-produced from supplementary information of "Engineering antisense oligonucleotides for targeted mRNA degradation through lysosomal trafficking" by Kashyap et al., under CC-BY 3.0.*

The MEN1 2′-OMe LyTON also showed improved knockdown under gymnotic delivery. This effect was consistent across all tested concentrations in HEK293T cells after 96 hours, as measured by RT-qPCR (Figure 4.23a), and the same trend of higher efficacy compared to the unconjugated and DBCO-modified ASOs was observed in A549 and HeLa cells (Figure 4.23b,c). In contrast, both the unmodified and DBCO-

modified MEN1 2′-OMe ASOs displayed similarly poor knockdown, reflecting their ability only to sterically block the target mRNA, while the ispinesib–NTC–ASO showed little to no reduction in MEN1 transcript levels (Figure 4.24).

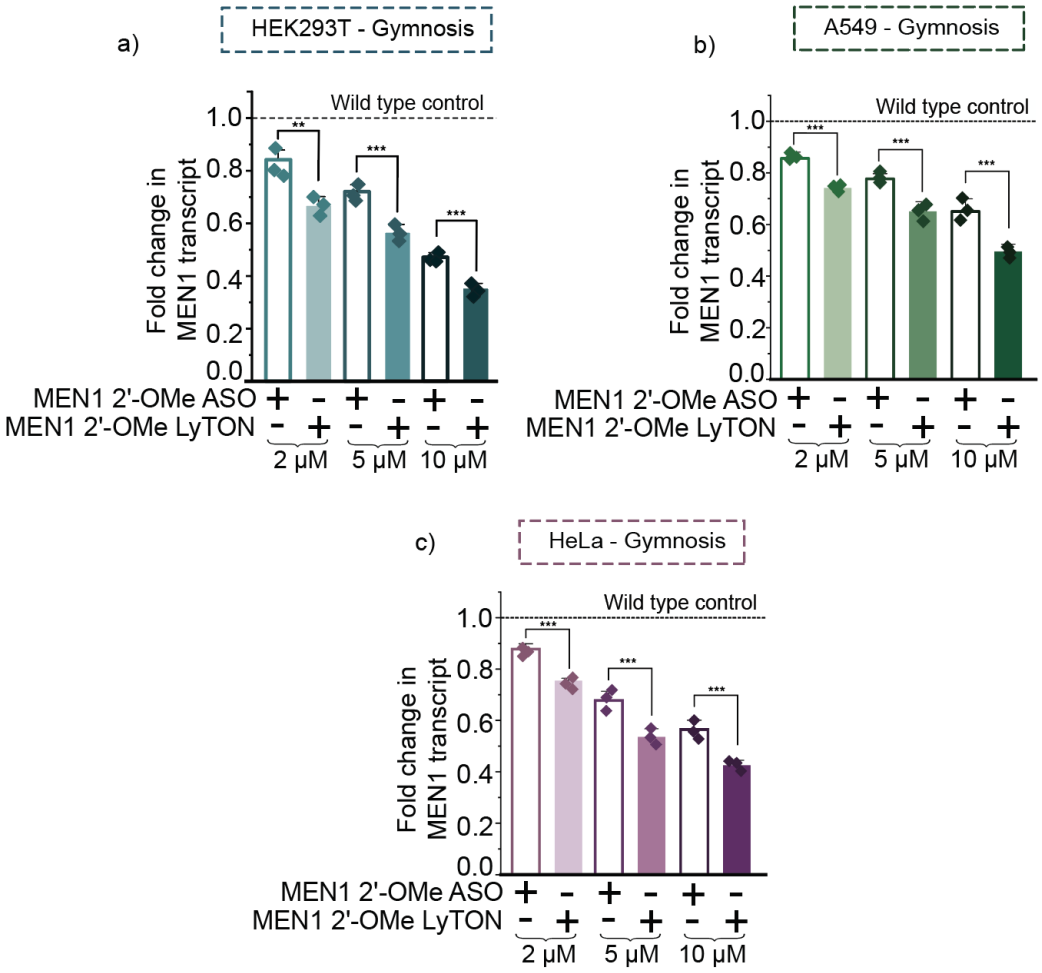

Figure 4.23: MEN1 2′- OMe LyTON treatment results in significant knockdown of MEN1 mRNA via gymnosis. RT-qPCR data for MEN1/Menin knockdown upon gymnosis of MEN1 2′- OMe ASO and MEN1 2′- OMe LyTON ASO in (a) HEK293T, (b) A549, (c) HeLa cells at the concentrations indicated for 96 hours. The vertical bars represent the mean and the error bars the standard deviation. ** represents $p<0.05$, *** represents $p<0.01$, n.s. represents p values that are not significant. *Figure re-produced from "Engineering antisense oligonucleotides for targeted mRNA degradation through lysosomal trafficking" by Kashyap et al., under CC-BY 3.0.*

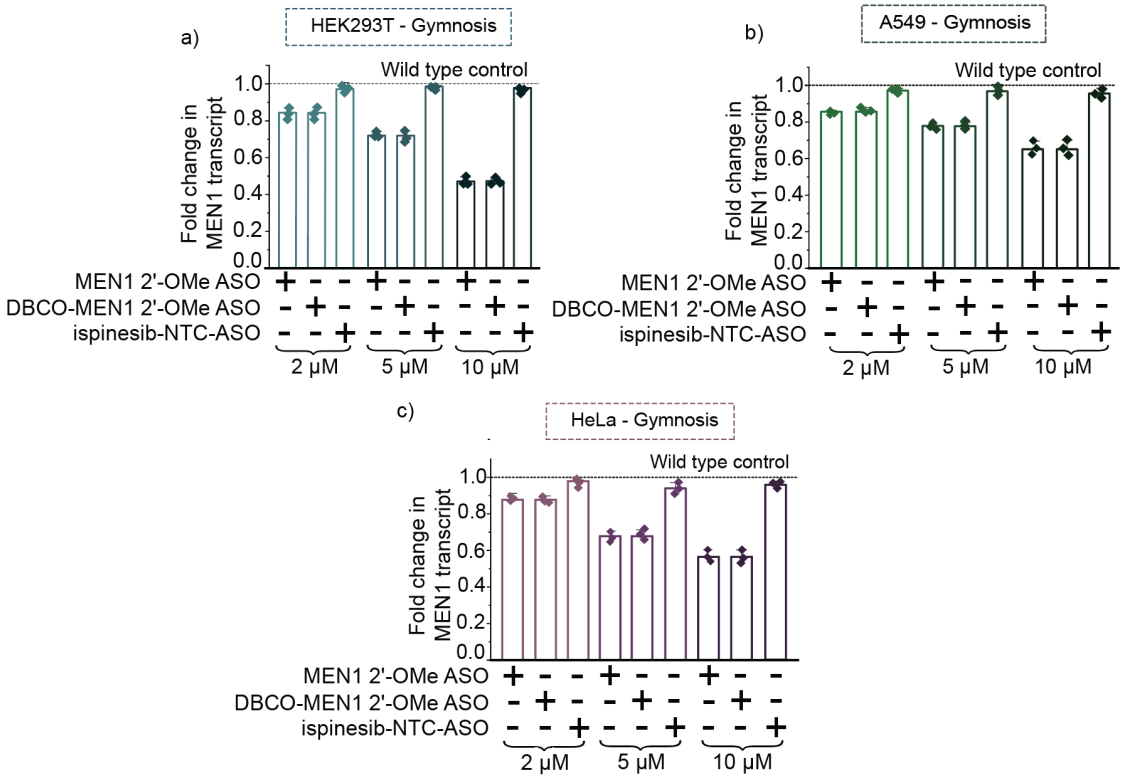

Figure 4.24: RT-qPCR data of MEN1 knockdown upon unmodified MEN1 2′-ASO, DBCO-modified MEN1 2′-OMe ASO and ispinesib-NTC-ASO gymnosis in (a) HEK293T, (b) A549, (c) HeLa for 96 hours at concentrations indicated. The vertical bars represent the mean and the error bars the standard deviation. ** represents $p<0.05$, *** represents $p<0.01$, n.s. represents p values that are not significant. *Figure re-produced from supplementary information of "Engineering antisense oligonucleotides for targeted mRNA degradation through lysosomal trafficking" by Kashyap et al., under CC-BY 3.0.*

Furthermore, little to no differences was observed in the toxicity profiles of the unconjugated and ispinesib-conjugated MEN1 ASOs, assessed by Cell Titer Glo (Figure 4.25a,b,c) and RNA transcript levels of key housekeeping genes (Figure 4.26). Again these results align with our initial expectations, as our treatments were within the sub-micromolar range, far below concentrations that would cause toxicity due to Eg5 inhibition.

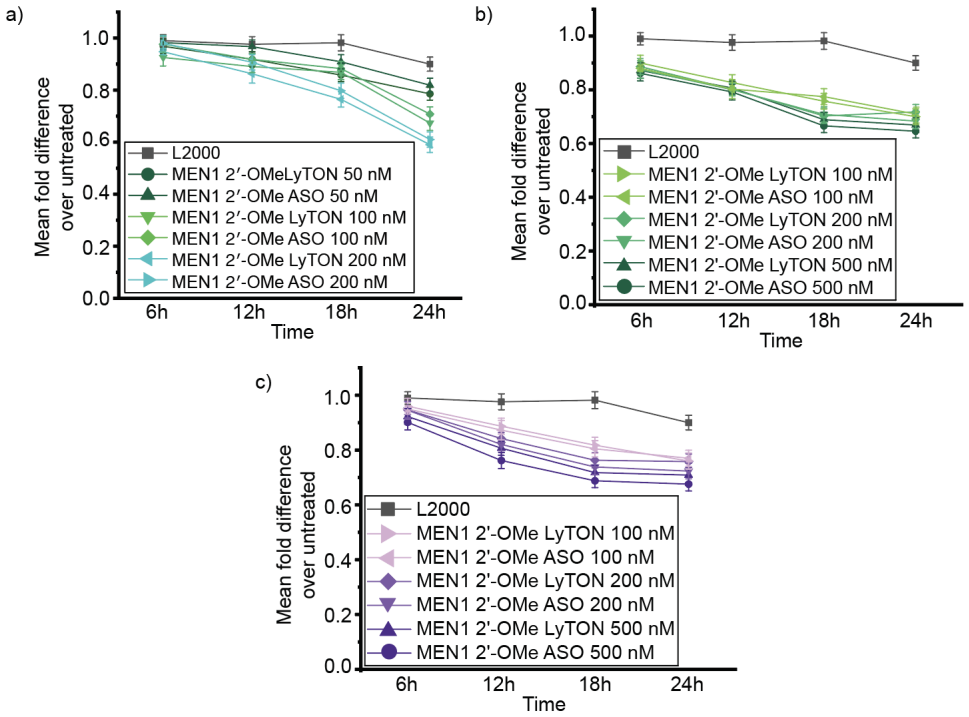

Figure 4.25: Cell viability of the (a) HEK293T, (b) A549, (c) HeLa upon MEN1 2′-OMe ASO and MEN1 2′-OMe LyTON treatment evaluated by Cell-Titer Glo. *Figure re-produced from supplementary information of "Engineering antisense oligonucleotides for targeted mRNA degradation through lysosomal trafficking" by Kashyap et al., under CC-BY 3.0.*

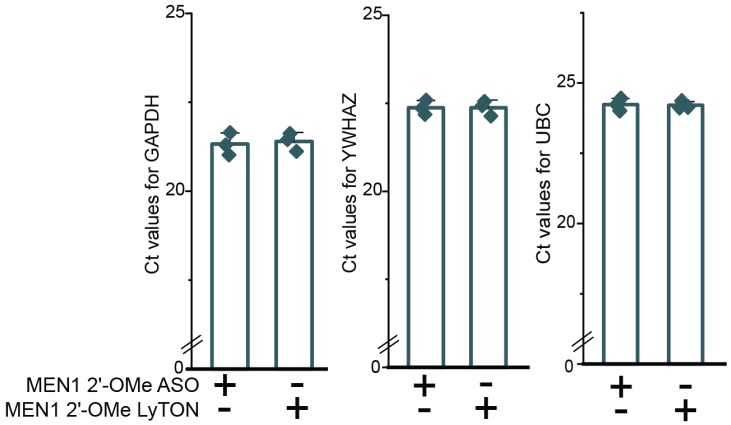

Figure 4.26: Ct values for key housekeeping genes upon MEN1 2′- OMe ASO and MEN1 2′-OMe LyTON treatment at 200 nM in HEK293T. *Figure re-produced from supplementary information of "Engineering antisense oligonucleotides for targeted mRNA degradation through lysosomal trafficking" by Kashyap et al., under CC-BY 3.0.*

4.3.9 Mechanism of action for conserved for MEN1 2′- OMe LyTON: loss of activity upon bafilomycin treatment

Next, the goal was to confirm the mechanism of action of the ispinesib–MEN1 ASO conjugates through pharmacological inhibition of lysosomal activity using bafilomycin treatment. As observed previously with the NCL1 LyTON, treatment with bafilomycin completely abolished the enhanced mRNA knockdown activity of the MEN1 2′-OMe LyTON (Figure 4.27a). Under these conditions, only baseline steric blocking activity, comparable to that of the unconjugated MEN1 2′-OMe ASO, was detected.

This effect was not restricted to transcript levels; loss of activity upon bafilomycin treatment was also clearly evident at the protein level (Figure 4.27b). Together, these findings support a lysosome-dependent mechanism of action for the MEN1 LyTON and reinforce that the enhanced knockdown arises from targeted lysosomal trafficking rather than conventional steric blocking.

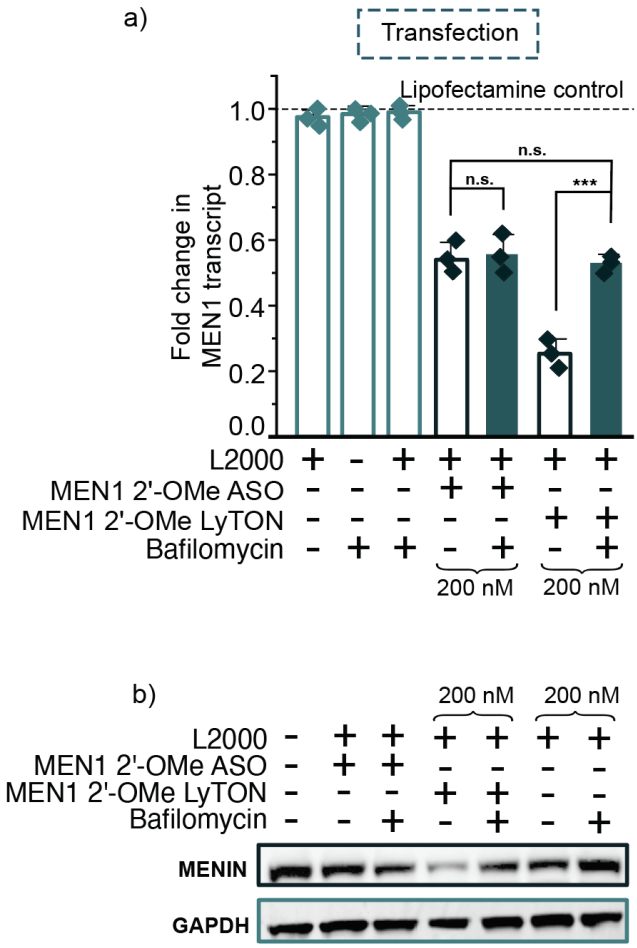

Figure 4.27: MEN1 2′-OMe LyTON-mediated mRNA knockdown occurs via the lysosome — validated by bafilomycin inhibition. (a) RT-qPCR data and (b) Western blot for MEN1/Menin knockdown upon lipofectamine transfection of MEN1 2′-OMe ASO and MEN1 2′-OMe LyTON ASO in HEK293T cells in the presence or absence of 10 nM bafilomycin, at the concentrations indicated. Three biological replicates are shown as diamonds for each condition (each from three technical replicates). The vertical bars represent the mean and the error bars the standard deviation. ** represents $p<0.05$, *** represents $p<0.01$, n.s. represents p values that are not significant. *Figure re-produced from "Engineering antisense oligonucleotides for targeted mRNA degradation through lysosomal trafficking" by Kashyap et al., under CC-BY 3.0.*

4.4 Discussion

Targeted mRNA degradation is a powerful strategy for therapeutic intervention: it enables the targeting of previously "undruggable" genes, facilitates personalized "n-of-1" medicine, and has the potential to overcome traditional mechanisms of small molecule drug resistance. Currently, mRNA knockdown can only be achieved through RNase H recognition of DNA-based ASOs or RISC formation with siRNA. In this work, an alternative mechanism for targeted mRNA degradation was introduced. By conjugating ispinesib, an ATTEC warhead, to ASOs, target mRNA was directed to the lysosome for subsequent degradation. These lysosomal trafficking antisense oligonucleotides (LyTONs) were designed to be modular and versatile, generated through simple post-synthetic modification chemistry with high purity and yield. LyTONs demonstrated improved knockdown efficacy across multiple molecular targets and cell lines, using both lipofectamine-mediated and gymnotic delivery. Furthermore, by combining lysosomal trafficking with RNase H activity, LyTONs enhanced the performance of state-of-the-art gapmer ASOs. The therapeutic potential of LyTONs was exemplified by their application to Menin, an important target in cancer medicine, where effective protein-level knockdown was achieved.

RNase H-competent ASOs primarily function in the nucleus, where effective RNase H concentration is the highest. However, mRNA is exported to the cytoplasm for

translation. While siRNAs mediate cytoplasmic degradation of mRNA, their cellular delivery remains more challenging than that of ASOs. This approach harnesses lysosomal degradation to improve mRNA target engagement, thereby enhancing the potential for ASO-based therapeutic modulation of clinically relevant genes. The LyTON platform enables a re-imagining of gene-silencing oligonucleotide design. Since it does not require DNA-based sequences for RNase H activity or RNA-based sequences for RISC loading, this approach allows exploration of alternative oligonucleotide chemistries. These may offer superior chemical stability, enhanced binding affinity, and improved delivery properties for gene silencing.

A concern in the induced-proximity field is whether certain reported ATTEC binders truly function via direct lysosomal engagement or instead act through canonical PROTAC-like mechanisms[241,242,243,244]. While ATTECs are generally defined as small molecules that tether targets to the autophagy–lysosome pathway, several compounds initially described as ATTECs have later been reclassified as functioning through ubiquitin–proteasome–mediated degradation[245]. This has blurred the mechanistic distinction between these two degrader classes. This raises the question of whether ispinesib, when incorporated into LyTONs, engages a bona fide lysosomal trafficking partner or whether additional, proteasome-related mechanisms could contribute.

Importantly, in the case of LyTONs, knockdown activity was clearly abolished upon lysosomal inhibition, and protein-level effects were lost under conditions that

disrupt lysosomal function. These findings strongly support a lysosome-dependent mechanism in this context, even while the broader debate regarding ispinesib's binding partner and degradation pathway remains unresolved. Resolving this ambiguity will be essential for fully understanding LyTON activity and for guiding the rational design of next-generation conjugates. Understanding this interaction will support the rational design of next-generation LyTONs with enhanced capabilities.

In conclusion, this work represents a major advance in targeted mRNA degradation. By utilizing lysosomal trafficking via a bifunctional ispinesib–ASO conjugate, a novel and potent strategy for selective gene silencing has been developed. This platform holds significant promise for precision medicine, particularly in expanding the chemical space for oligonucleotide therapeutics. With its modular design and capacity for future advancements, this technology could emerge as a powerful platform for the development of next-generation nucleic acid-based treatments.

Part II

Chapter 5

Introduction

5.1 DNA-nanotechnology for tunable targeted protein degradation

5.1.1 DNA-nanotechnology principles

DNA nanotechnology leverages the predictable base-pairing rules of nucleic acids to construct nanoscale structures and functional devices with high spatial precision. Unlike classical molecular biology, which views DNA primarily as a genetic material, DNA nanotechnology re-purposes it as a structural and dynamic material for nanoscale engineering[246]. This field bridges the gap between molecular biology, synthetic chemistry, and nanomedicine, offering programmable tools for diagnostics, therapeutics, and synthetic biology.

At its core, DNA nanotechnology exploits Watson–Crick base-pairing to create pre-

dictable, programmable interactions between nucleic acid polymer strands. These interactions are used to design and assemble precise nanostructures such as DNA tiles, origami, and walkers, as well as dynamic systems like molecular switches and circuits. The primary design strategy involves "sticky ends", which are single-stranded overhangs that allow controlled self-assembly and sequence-specific hybridization that confers spatial precision (Figure 5.1a).

There are two broad categories of DNA nanotechnology: structural DNA nanotechnology and dynamic DNA nanotechnology.

◇ Structural DNA nanotechnology focuses on constructing static architectures such as DNA origami, where a long single-stranded DNA (scaffold) is folded into the desired shape using short synthetic "staple" strands.

◇ Dynamic DNA nanotechnology involves the construction of systems that change conformation or function in response to stimuli (for example, pH, enzymes, microRNA (miRNA)). This branch is central to bio-sensing and responsive therapeutic delivery, for example.

5.1.2 Structural DNA Nanotechnology

◇ Extended lattices: The earliest architectural motifs in structural DNA nanotechnology centered around periodic lattices. DX tiles, composed of two DNA double helices linked by crossovers, could self-assemble into 2D crystalline arrays

using complementary sticky ends[247] (Figure 5.1b). These allowed modular, programmable assembly and laid the foundation for aperiodic tiling schemes capable of simulating computational logic in molecular form[248]. 3D periodic crystals were later realized using tensegrity triangle motifs—rigid triangular units capable of packing into extended 3D lattices with atomic-level precision[249]. These developments not only demonstrated that DNA could form well-ordered materials, but also expanded its applications in materials science and molecular computing.

◇ Discrete polyhedral assemblies: Beyond lattices, discrete polyhedral structures have also been synthesised from DNA. These constructs, such as tetrahedra, icosahedra, and buckyball analogs, are composed of edge-sharing DNA helices and junctions. For example, a truncated octahedron comprising 12 helical edges was built using a "one-pot" assembly of multiple oligonucleotides[250]. Such closed 3D shapes offer encapsulation capabilities, important for targeted delivery of drugs or imaging agents. These polyhedra are programmable in both geometry and chemical functionality. Modifications at specific positions along the DNA enable the tethering of functional modules like fluorophores or aptamers, allow for biomedical applications of such tetrahedra.

◇ DNA origami and nanoscale folding: A major leap in nanoscale design came with the advent of DNA origami[251]. In this method, a long single-stranded scaffold (first examples use the M13 bacteriophage genome) is folded into arbitrary 2D or 3D shapes by hundreds of short "staple" strands. This enables single-nanometre-

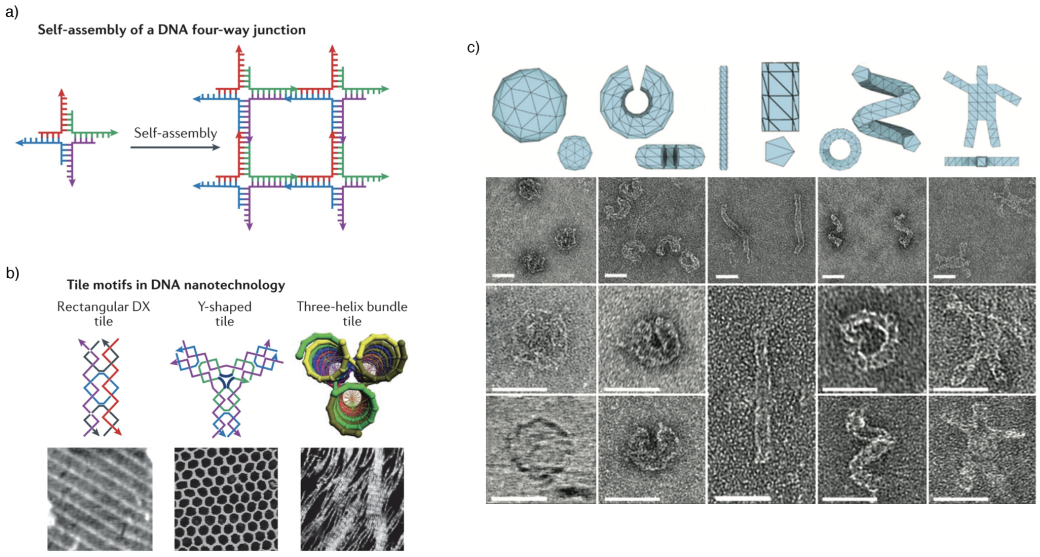

Figure 5.1: (a) A DNA four-way junction with self-complementary, single-stranded ends ('sticky ends') self-assembles into a quadrilateral shape. (b) DNA nanotechnology motifs. The top panels show tile motifs in DNA nanotechnology, and the bottom panels show atomic force microscopy images of their assemblies into lattices. The left panels show an example of a double-crossover (DX) tile; the middle panels show an example of Y-shaped DNA motif self-assembly into hexagonal 2D lattices; and the right panels show an example of three-helix bundles. (c) Wireframe DNA origami structure. Scale bars are 50 nm. *Figure adapted from "DNA nanotechnology" by Semen et al. Reproduced with permission from Springer Nature.*

scale precision in constructing sophisticated geometries like smiley faces, maps, and even nanoboxes (Figure 5.1c). DNA origami simplifies structural design, improves folding yields, and increases robustness. Software tools such as caDNAno allow rapid design of arbitrary structures. DNA origami has been used to make reconfigurable boxes that can open in response to molecular cues, and nanocages capable of drug encapsulation and triggered release[252].

5.1.3 Dynamic and responsive DNA systems

The DNA-nanotechnology field has matured from static structures to dynamic, stimuli-responsive devices. These systems undergo conformational changes in response to environmental triggers such as pH, small molecules, or nucleic acids. A central mechanism here is toehold-mediated strand displacement, wherein an invading DNA strand displaces a pre-hybridized strand via binding to a single-stranded overhang (toehold)[253].

DNA-based nanomachines include:

- DNA walkers, which move stepwise on a track via sequential strand displacement[254]
- Nanorobots, such as an origami device that opens in response to antigen recognition to release thrombin and induce cell death[255]. Switchable tweezers and aptamer gates, used for logic circuits and molecular computation[256] also as dynamic processors and actuators in molecular-scale devices.

These systems exemplify how DNA nanostructures can function not only as scaffolds but also as dynamic processors and actuators in molecular-scale devices.

5.1.4 Biomedical applications of DNA nanotechnology

Drug delivery and theranostics: DNA origami devices have been loaded with doxorubicin and targeted to cancer cells using aptamer modifications. These

nanostructures improve pharmacokinetics, reduce off-target toxicity, and allow triggered release in response to intracellular cues such as pH or miRNA presence[257]. The high addressability of DNA scaffolds allows multi-drug loading and co-delivery strategies.

Diagnostics and super-resolution imaging: DNA-based sensors offer high specificity and sensitivity in detecting nucleic acid biomarkers. Moreover, DNA-PAINT (Points Accumulation for Imaging in Nanoscale Topography) uses transient binding of fluorescent DNA strands for super-resolution imaging, enabling spatial resolution beyond the diffraction limit[258].

Delivery for gene therapy and vaccines: Spherical nucleic acids (SNAs)—nanoparticles coated with a dense shell of DNA—exhibit high cellular uptake and resistance to nuclease degradation. SNAs have been used to deliver short interfering RNA (siRNA), messenger RNA (mRNA), and immunostimulatory oligonucleotides in clinical trials[259]. Their modular design and intrinsic biocompatibility make them strong candidates for personalized medicine (Figure 5.2).

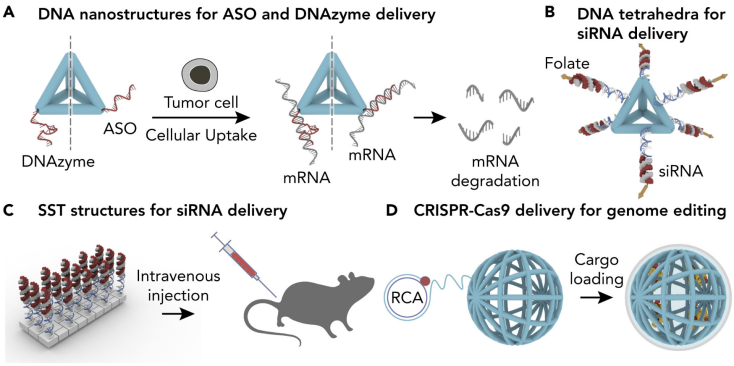

Figure 5.2: DNA-based delivery vehicles for nucleic acid therapeutics delivery. (a) Non-viral delivery of ASO and DNAzyme by a DNA tetrahedron for post-transcriptional gene silencing. DNA nanocarriers enhance the cellular uptake of ASO and DNAzyme. (b) Folate-modified DNA tetrahedra were used for the targeted delivery of siRNA to xenograft tumors *in vivo*.(c) siRNA delivery by SST carriers for *BCL-2* depletion *in vivo*. (d) CRISPR-Cas9 delivery by using PEI-coated DNA nanoclews for genome editing. *Figure adapted from "Designer DNA nanostructures for therapeutics" by Jiang et al. Reproduced with permission from Springer Nature.*

Orthogonal interactions and logic-gated systems: One of DNA nanotechnology's most powerful features is its capacity for orthogonality—the design of independent, non-interacting sub-systems within a framework. This enables parallel processing of multiple molecular inputs using logic circuits built from strand displacement reactions. For example, DNA-based logic gates (AND, OR, NOT) that operate in response to inputs such as disease-specific miRNAs. These logic gates have been used to control DNA nanorobot activity in live cells resulting in the release of therapeutics only when specific combinations of biomarkers are detected[260]. Logic-gated nanodevices can thus integrate molecular information and execute intelligent behaviors at the cellular level, laying the groundwork for autonomous molecular therapeutics.

Thus, all these principles provide a platform for the building of biomolecular tools that interact with cellular machinery in novel ways. Among emerging applications, DNA-guided targeted protein degradation stands out as a promising area where the information-coding and programmable nature of DNA can be combined with small-molecule pharmacology.

5.2 Targeted protein degradation technologies

Targeted protein degradation has emerged as a transformative approach in small-molecule drug discovery, offering a fundamentally distinct mechanism from conventional enzyme inhibition. Unlike classical small-molecule inhibitors that require sustained occupancy of a protein's active or allosteric site to suppress function, degraders eliminate the protein altogether—thereby decoupling pharmacological activity from occupancy. Among the most promising tools in this field are proteolysis-targeting chimeras.

5.2.1 PROTAC small molecules

Proteolysis-targeting chimeras or PROTACs represent a paradigm shift in small-molecule pharmacology by enabling the selective degradation of intracellular proteins via the ubiquitin–proteasome system (UPS). PROTACs function catalytically: once a PROTAC binds its protein target facilitating its ubiquitination, the target protein is eliminated, and the PROTAC is recycled to engage another target[261].

PROTACs are heterobifunctional molecules composed of two ligands tethered by a linker:

- ◇ One ligand binds the protein of interest (POI), such as a kinase, transcription factor, or epigenetic regulator
- ◇ The other recruits an E3 ubiquitin ligase, such as cereblon (CRBN), von Hippel–Lindau (VHL), or MDM2
- ◇ The linker provides the right spatial orientation to facilitate ternary complex formation between POI, PROTAC, and E3 ligase

Upon formation of the ternary complex, the POI is poly-ubiquitinated and subsequently degraded by the 26S proteasome (Figure 5.3a). Since the process is not reliant on inhibition of the protein target, PROTACs can act on proteins previously considered "undruggable"[262,263].

The first generation of PROTACs, developed in the early 2000s, utilized peptide-based E3 ligase ligands and exhibited low cellular permeability[264]. Subsequent iterations incorporated small-molecule ligands, notably thalidomide derivatives for CRBN and VH032 for VHL, significantly improving pharmacokinetics and bioavailability[265].

PROTACs have now entered trials for diseases such as prostate cancer (ARV-110, targeting androgen receptor) and breast cancer (ARV-471, targeting estrogen re-

ceptor)[266] (Figure 5.3b). The versatility of the platform also extends to immune modulation, neurodegeneration, and viral infections.

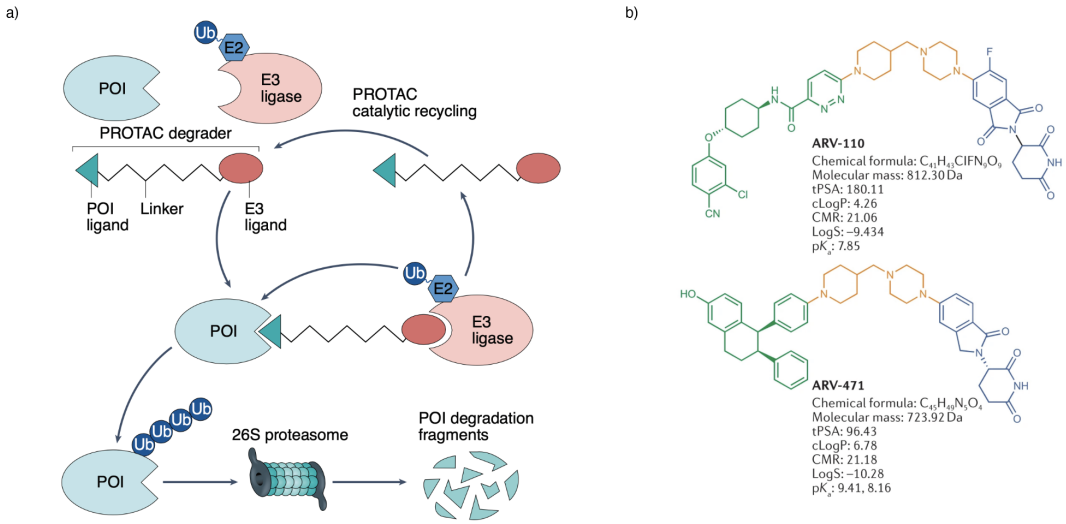

Figure 5.3: (a) PROTAC mechanism of action: A POI can be degraded by the ubiquitin (Ub)–proteasome system in a process mediated by a PROTAC, a catalytic molecule consisting of a POI ligand connected to an E3 ligand via a linker. *Figure adapted from "The PROTAC gold rush" by Garber, K. Reproduced with permission from Springer Nature.* (b) Structure and properties of two proteolysis-targeting chimeras (PROTACs) that have entered clinical trials, ARV-110 and ARV-471. PROTACs are composed of a target-binding moiety (green), a linker (orange) and an E3 ligase-binding moiety (blue). *Figure adapted from "PROTAC targeted protein degraders: the past is prologue" by Békés et al. Reproduced with permission from Springer Nature.*

However, key limitations persist:

◇ Molecular weight often exceeds 800 Da, complicating drug-like properties

◇ Linker optimization remains entirely empirical, and thus, time-consuming

◇ Precise spatio-temporal control of degradation is lacking

These challenges have motivated exploration of modular, programmable frameworks—

such as integration with DNA nanotechnology.

5.2.2 DNA-linkers for PROTACs

The linker is a crucial determinant of PROTAC efficacy, influencing cell permeability, ternary complex formation, and degradation kinetics. Traditionally, linkers are composed of polyethylene glycol (PEG), alkyl chains, or triazoles[267]. These provide tunable length and flexibility, but offer limited programmability or stimulus-responsiveness.

In contrast, DNA strands can serve as structural, dynamic, and stimuli-responsive linkers between two functional ligands. This modularity opens up several advantages:

- ◇ Precise length and geometry: Duplex DNA helices offer nm-scale control of spatial distance and orientation
- ◇ Programmable hybridization: Complementary sequences can mediate conditional assembly or disassembly of PROTAC units
- ◇ Responsive Behavior: DNA can be engineered to fold, unfold, or react via strand displacement in response to environmental triggers

A recent advancement in the area is the design of DNA-framework-based PROTACs (DbTACs): using rigid DNA tetrahedra to precisely control ligand orientation and

spacing for optimized degradation[268]. This approach improves structural control, supports bispecific degrader formats, and enables high-throughput scaffold design.

Another study has developed a miR-21-responsive pre-PROTAC system using DNA hairpins labeled with JQ1 and pomalidomide that assemble via a hybridization chain reaction[269]. This design enabled tumor-selective BRD4 degradation with optional light-controlled activation.

DNA-based PROTACs also enable novel delivery strategies. For example, DNA linkers can be appended with aptamers to promote cell-specific uptake or embedded within DNA origami carriers for encapsulation and co-delivery with nucleic acid therapeutics[270].

However, challenges remain:

- ◇ Chemically unmodified-DNA is susceptible to nuclease degradation *in vivo*
- ◇ Large nucleic acid scaffolds may impair cell permeability and lead to poor delivery
- ◇ Conjugation chemistry between DNA and small molecules must be optimized for scalability and yield—moreover, assembly into complex shapes is not readily achievable or scalable

Despite these challenges, the integration of PROTAC and DNA nanotechnology offers a powerful framework for constructing programmable, logic-responsive protein degraders with enhanced specificity.

5.3 Part II: Research Aims

The following chapter features work that aimed to address the aforementioned limitations on PROTAC activity. This chapter attempted to develop tunable, chemically stable PROTAC–DNA conjugates (OligoPROTACs) that incorporate programmable oligonucleotide elements into the molecular design.

Our aim was to exploit the inherent programmability and structural predictability of DNA to establish a system capable of offering greater external control over PROTAC activity. In contrast to conventional small-molecule PROTACs, which are constitutively active once delivered into the cellular environment, OligoPROTACs were envisioned as constructs that could be selectively switched "OFF" through rationally engineered, sequence-specific strand-displacement reactions.

Chapter 6

Tunable control over PROTAC Activity via DNA Hybridization and Strand Displacement

6.1 Introduction

Targeted protein degradation has rapidly emerged as a game-changing strategy in modern drug discovery[271]. Unlike conventional protein inhibition, which requires continuous occupancy of active or functional domains, degradation eliminates the protein altogether—resulting in several distinct therapeutic advantages. These include prolonged effects due to the complete removal of the target protein, reduced drug dosage requirements, and an expanded range of potential targets within the proteome. Since degradation doesn't rely on the presence of catalytic sites or functional motifs, it bypasses many of the constraints that limit traditional inhibition approaches. Among the most promising tools for inducing targeted protein degradation are proteolysis-targeting chimeras (PROTACs)[264,272]. These are heterobifunctional, catalytic small molecules that simultaneous bind a protein of interest

(POI) and an E3 ubiquitin ligase[273]. This induced proximity enables E3 ligase-mediated ubiquitination of the POI, flagging it for degradation. This allows for the hijacking of a core mechanism of cellular protein turnover for therapeutic purposes.

Despite their enormous potential, the broader application of PROTACs has been limited by concerns over specificity and toxicity[274]. PROTACs have been successfully developed to degrade clinically important proteins such as the androgen receptor[275] and estrogen receptor[276], and several candidates are currently undergoing clinical evaluation. Nonetheless, the potent catalytic nature of PROTACs raises challenges in regulating their activity across tissues[277]. Uncontrolled degradation of the POI in both diseased and healthy cells may lead to significant toxicity. For instance, while BET bromodomain inhibition is tolerable, complete loss of proteins like BRD2 and BRD4 is lethal, narrowing the therapeutic index of PROTACs such as dBET1, which targets these proteins[278,265]. Additionally, the chemical scaffolds commonly used in PROTAC development can be promiscuous, causing off-target degradation and systemic side effects[279]. This underscores the urgent need for next-generation PROTACs with tunable activity to enhance control over protein degradation and reduce unintended proteome-wide consequences.

To address these limitations, previous approaches have attempted to use stimuli-responsive strategies for controlling PROTAC activation. Typically, these systems remain inactive until triggered by an internal or external cue, allowing spatially and temporally restricted activation. One such approach involves click-formed

proteolysis-targeting chimeras (CLIPTACs), which are generated intracellularly via bioorthogonal click chemistry between two separately delivered precursors[280]. However, issues with mismatched pharmacokinetics and low in situ assembly efficiency limit clinical viability. Internal triggers such as hypoxia[281,282] or reactive oxygen species (ROS)[283] have also been exploited to activate PROTACs, though such cues are often distributed across multiple tissues, increasing the risk of unintended activation or "leaky" off-states. Photocaging has been applied to activate PROTACs using light[284], but poor tissue penetration of light hinders therapeutic application. In contrast, mechanisms for inactivating PROTACs post-activation remain scarce. To date, only one reversible strategy has been described[285], utilizing photoswitches to toggle degradation on and off with UV/visible light. However, this too is limited by the inherent drawbacks of light-dependent activation. As a result, a clinically viable method to switch PROTAC activity "off", a key feature for temporal precision and safety, has yet to be developed.

In this work, we introduce a DNA nanotechnology-based method to inactivate PROTACs on demand. DNA nanostructures are exceptionally well-suited for this purpose due to their predictable base-pairing, tunable chemistry, and versatile 3D architectures[286]. These attributes have enabled the design of programmable DNA constructs for diverse biomedical applications, including targeted drug delivery[286], bio-sensing, and molecular diagnostics[287,288]. Recent advances in chemical modifications for improved nuclease resistance and delivery have accelerated the develop-

ment of nucleic acid therapeutics, with over 23 approved drugs currently in clinical use[63]. Emerging work has explored incorporating DNA into PROTAC designs for enhanced programmability and target selectivity[289]. For example, E3 ligase ligands have been conjugated to sequence-specific oligonucleotides, such as aptamers[290] or transcription factor binding motifs[153], enabling selective degradation of nucleic acid-binding proteins. However, previous attempts to use DNA nanostructures for PROTAC control have faced practical challenges: attaching PROTAC warheads to large DNA tetrahedra is synthetically demanding and difficult to scale up[268], while DNA-based hybridization chain reactions require dual strand delivery and complex assembly in cells[269].

6.2 Aims

The goal of this chapter was to establish the design of oligonucleotide-linked PROTACs (OligoPROTACs)—modular, double-stranded oligonucleotide constructs assembled by the hybridisation of two short DNA strands: one modified at the 3′-end with a POI-binding ligand and the other at the 5′-end with an E3 ligase ligand. The aim was to investigate whether the introduction of various non-complementary arms into the double-stranded DNA (dsDNA) linker could optimise the spatial configuration of the ligands to support efficient protein degradation. A toehold sequence was also incorporated to enable reversible inactivation via strand displacement. In this envisioned mechanism, the addition of a third, complementary “inhibitor” strand

was anticipated to trigger toehold-mediated strand exchange, thereby disrupting the duplex and separating the warheads, effectively switching "off" protein degradation activity. As this control element was encoded at the sequence level, it was expected to offer a generalisable and programmable strategy for the dynamic regulation of PROTAC function.

Consideration was also given to how the clinical translation of OligoPROTACs might be facilitated by their design: short, double-stranded, chemically stabilised oligonucleotides, structurally similar to small interfering RNAs (siRNAs), several of which have already been approved as drugs for diverse indications by the FDA. By leveraging the unique capabilities of DNA nanotechnology and incorporating a simple, sequence-based off-switch, a framework was sought for enhancing the precision and safety of PROTAC therapies. Taken together, the work in this chapter was directed toward laying the foundation for future "smart" degraders that could combine the power of protein degradation with programmable control using nucleic acid scaffolds.

The objectives of this chapter were as follows:

- ◇ Synthesis and characterisation of high-yield high-purity oligonucleotide-linked proteolysis targeting chimeras (OligoPROTACs)
- ◇ Functional and mechanistic validation of the activity of OligoPROTACs

◇ Leveraging the presence of the DNA linker to establish temporal control over PROTAC-mediated protein degradation

6.3 Results

6.3.1 Synthesis of OligoPROTACs

The small molecule PROTAC AZ1[291] was chosen as the chemical scaffold to inspire OligoPROTAC design. AT1 is known to selectively degrade BRD4, a member of the BET bromodomain protein family, and effectively inhibits tumor growth in AML[292]. Structurally, AT1 comprises the well-characterised BET bromodomain inhibitor (+)-JQ1[293] as the POI-targeting ligand, and VH032 as the E3 ligase recruiter for the VHL complex[294]. For the OligoPROTAC, VH032 was conjugated to the 5′-end of one DNA strand and (+)-JQ1 to the 3′-end of the complementary strand. Upon hybridisation, both ligands would be brought into spatial proximity at one end of the dsDNA (Figure 6.1a).

To avoid biological activity from the DNA itself, a previously established non-targeting control ASO sequence and its reverse complement were chosen[100]. All oligonucleotides were contained phosphorothioate modified backbones to ensure resistance to nucleases within cells.

6.3.2 Synthesis of VH032-ssDNA conjugates with varying linker lengths

The 5′- VH032 OligoPROTAC strand was synthesised from a commercial 5′- hexynl-modified PS DNA with a commercially-sourced VH032-azide, through copper-catalysed click chemistry (Figure 6.1b).

6.3.3 Synthesis of JQ1-ssDNA conjugates with varying linker lengths

The 3′- (+)-JQ1 OligoPROTAC strand was synthesised from a commercial 3′- azide-modified PS DNA with (+)-JQ1 alkyne, through copper-catalysed click chemistry (Figure 6.1c). The (+)-JQ1 alkyne was synthesised in two steps: first, the Boc group of (+)-JQ1 was deprotected to yield the (+)-JQ1 acid[170]; followed by a hydroxybenzotriazole (HoBT) and (3-Dimethylamino-propyl)-ethyl-carbodiimide hydrochloride (EDC-HCl)-mediated coupling with propargylamine, resulting in the formation of (+)-JQ1-alkyne[171].

6.3.4 General annealing strategy for assembly for oligoPROTACs

Both modified-DNA strands were purified using HPLC and analysed by LC-MS, with yields >90% and purity >95% . The complementary strands were subse-

quently combined in equimolar concentrations and annealed under high-salt conditions with rapid thermal cycling. This procedure was chosen to promote efficient hybridisation and minimise the formation of secondary structures or incomplete duplexes. Through this process, the intended OligoPROTAC constructs were reliably assembled (Figure 6.1d).

Given the well-established importance of linker length in determining the efficacy of small-molecule PROTACs, the spatial separation of the ligands in OligoPROTACs was deliberately modulated in an analogous manner. To achieve systematic variation in linker length and spatial positioning, non-complementary thymine "arms" were incorporated into the constructs at defined positions flanking the ligands. By adjusting the number of these flexible spacer residues [n = 0, 1, 2, 3, 5, 10], a panel of OligoPROTACs was generated with tunable inter-ligand distances. This design strategy was intended to probe how fine adjustments in spatial orientation influence proximity-induced ubiquitination, and subsequent degradation. This was done to mirror one of the key optimisation parameters in conventional PROTAC development. Thus, these additional bases serve as tunable spacers between the ligands and the duplex region (Appendix Figure A.31, Figure A.32, Figure A.33, Figure A.34, Figure A.35, Figure A.36, Figure A.37, Figure A.38, Figure A.39, Figure A.40, Figure A.41, Figure A.42).

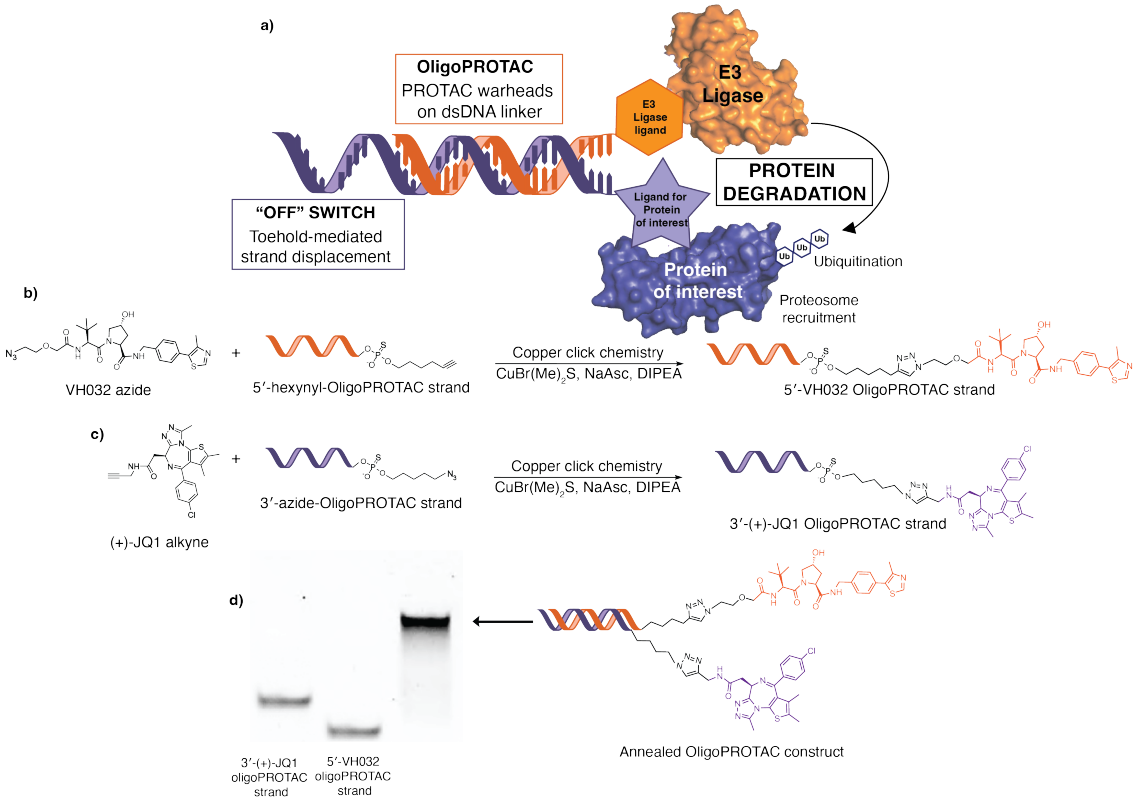

Figure 6.1: Chemical synthesis of oligoPROTACs. (a) OligoPROTACs utilize a double-stranded DNA linker to present PROTAC warheads, which recruit an E3 ligase to induce ubiquitination and subsequent degradation of a target protein. The system includes a toehold sequence to facilitate a toehold-mediated strand displacement mechanism as an "off" switch for controlled activation. (b) Reaction scheme for copper click conjugation of VH032 azide with 5'-alkyne modified PS DNA. (c) Reaction scheme for copper click conjugation of (+)-JQ1 alkyne with 3'-azide modified PS DNA. (d) Native PAGE gel showing assembly of dsDNA oligoPROTAC. *Figure re-produced from "DNA-programmable Protein Degradation: Dynamic Control of PROTAC Activity via DNA Hybridization and Strand Displacement' by Kashyap et al., under CC-BY 4.0.*

6.3.5 Linkerology: varying oligoPROTAC linker lengths for optimising efficacy

HEK293T cells were transfected with OligoPROTAC designs featuring different linker lengths (Figure 6.2a), and BRD4 degradation was assessed via western blotting after 12 hours. A clear distance-dependent pattern was observed (Figure 6.2b): constructs with [n = 0] arms displayed minimal degradation, which improved as linker length increased, peaking at [n = 3], where BRD4 degradation matched that of the parent small-molecule PROTAC AT1. Further increasing linker length [n = 5, 10] diminished activity, with no degradation seen for [n = 10]. A similar relationship was observed in HeLa (Figure 6.2c) and A549 (Figure 6.2d) cells, again with [n = 3] yielding the most effective degradation.

To confirm that activity was contingent upon precise ligand positioning, control constructs were generated. These included partial OligoPROTACs with only one ligand (3′-(+)-JQ1 or 5′-VH032 paired with a non-modified complement) (Figure 6.2f,g) and an asymmetric construct with ligands on opposite ends (5′-VH032 and 5′-(+)-JQ1) (Figure 6.2h, Appendix Figure A.43). None of these controls induced BRD4 degradation in any cell line, confirming that activity required both ligands being correctly oriented on the same end of the duplex (Figure 6.2b–h).

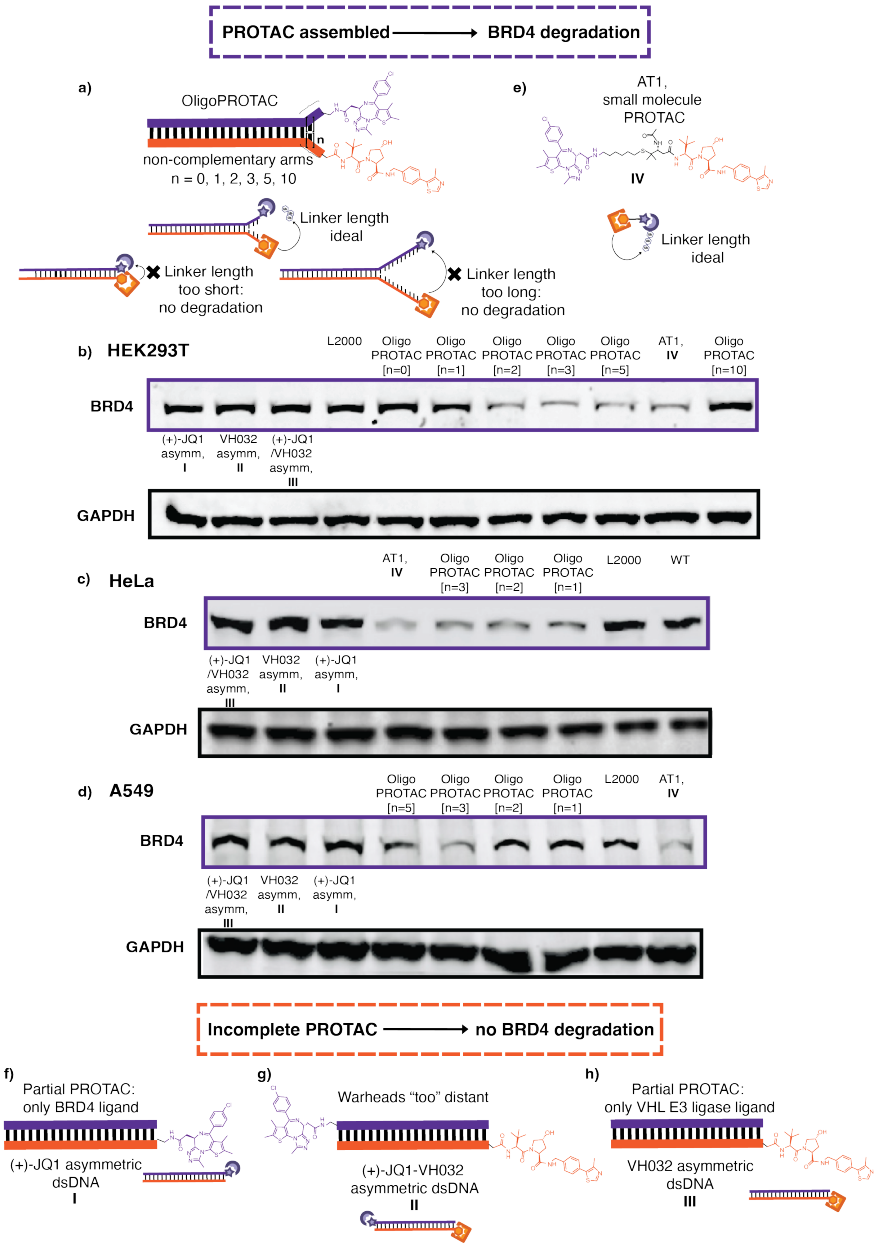

Figure 6.2: Screening of oligoPROTAC dsDNA linker length. (a) Assembled dsDNA oligoPROTAC with non-complementary thymine arms of varying lengths, [n= 0, 1, 2, 3, 5, 10]. (b) Western blot for BRD4 levels following treatment with oligoPROTACs of varying dsDNA linker length, upon Lipofectamine 2000 transfection in (a) HEK293T, (b) HeLa, (c) A549 cells at 12 hours. Normalised to GAPDH levels. (e) Chemical structure of small molecule PROTAC, AT1. (f) Structure for (+)-JQ1 partial construct comprising of 3′-(+)-JQ1 oligoPROTAC strand annealed to a non-modified complementary strand. (g) Structure for VH032 partial construct comprising of 3′-(+)-JQ1 oligoPROTAC strand annealed to a non-modified complementary strand. h) Structure for (+)-JQ1/VH032 asymm. construct, the asymmetric oligoPROTAC, where the ligands are on opposite ends of the dsDNA (5′-VH032 and 5′-(+)-JQ1). *Figure re-produced from "DNA-programmable Protein Degradation: Dynamic Control of PROTAC Activity via DNA Hybridization and Strand Displacement' by Kashyap et al., under CC-BY 4.0.*

6.3.6 OligoPROTAC JQ1-VH032 shares mechanistic similarity to small molecule PROTAC, AT1

The most potent construct, OligoPROTAC [n = 3], was benchmarked against the parent small-molecule degrader AT1 to assess relative performance and mechanistic similarities. BRD4 protein levels were assayed over a 12-hour time course across a range of concentrations, providing a detailed view of concentration dependence. OligoPROTAC [n = 3] displayed degradation profiles closely paralleling those of AT1 (Figure 6.3a), and time-course experiments at 1 µM further confirmed highly comparable kinetics of BRD4 depletion (Figure 6.3b).

Downstream effects were also evident: MYC protein and transcript levels were markedly reduced, consistent with AT1 activity (Figure 6.3c,d). Phenotypic consequences of cytotoxic stress—including cell rounding, reduced confluency, and impaired proliferation—were observed (Figure 6.3e), and cell viability assays confirmed comparable cytotoxicity between OligoPROTAC [n = 3] and AT1 (Figure 6.3f). Together, these findings demonstrated that the optimised OligoPROTAC reproduced both molecular and phenotypic responses of AT1, validating DNA as a viable linker for PROTAC design.

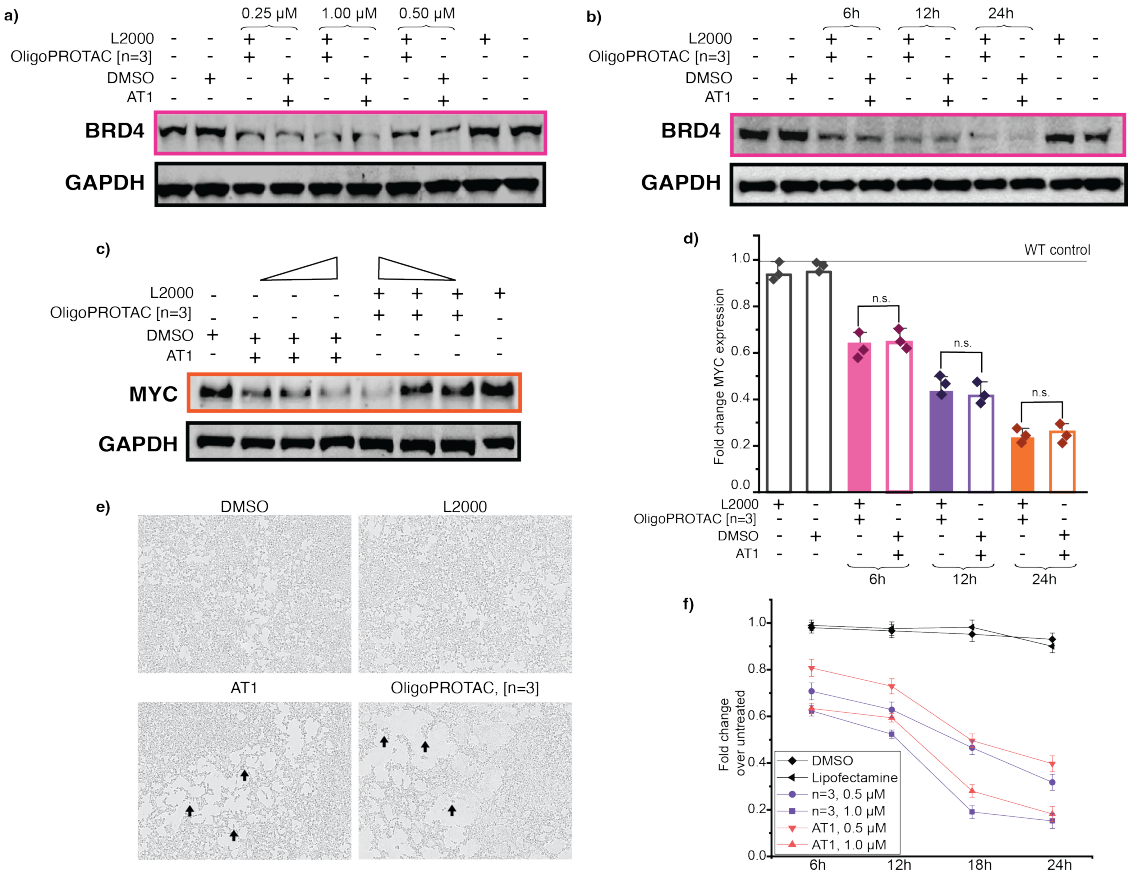

Figure 6.3: Evaluation of efficacy and mechanistic characterisation of oligoPROTAC [n=3] compared to small molecule, AT1. (a) Western blot for BRD4 levels upon treatment with oligoPROTAC [n=3] or small molecule PROTAC, AT1, at concentrations indicated, upon Lipofectamine 2000 transfection/DMSO treatment in HEK293T cells at 12 hours. Normalised to GAPDH levels. (b) Western blot for BRD4 levels upon treatment with oligoPROTAC [n=3] or small molecule PROTAC, AT1, at 1 μM over 6, 12, and 24 hours, upon Lipofectamine 2000 transfection/DMSO treatment in HEK293T cells. Normalised to GAPDH levels. (c) Western blot for MYC levels upon treatment with oligoPROTAC [n=3] or small molecule PROTAC, AT1, at concentrations (0.25, 0.50, and 1.00 μM) upon Lipofectamine 2000 transfection/DMSO treatment in HEK293T cells at 12 hours. Normalised to GAPDH levels. (d) RT-qPCR data for MYC expression upon lipofectamine transfection of oligoPROTAC [n=3] or AT1 incubation in HEK293T cells at 1.00 μM over 6 hours, 12 hours, and 24 hours. (e) Phase contrast images captured on the Incucyte of HEK293T cells treated with oligoPROTAC [n=3] or small molecule PROTAC at 1.00 μM for 12 hours. Arrows indicate cells with rounded morphology. (f) Cell viability upon treatment with oligoPROTAC [n=3] or small molecule PROTAC at concentration indicated over a 24-hour time period assessed by CellTiter Glo. *Figure re-produced from "DNA-programmable Protein Degradation: Dynamic Control of PROTAC Activity via DNA Hybridization and Strand Displacement' by Kashyap et al., under CC-BY 4.0.*

Experiments by Dr. Shozeb Haider, UCL School of Pharmacy

The structural arrangement of the ternary complex was explored to assess whether the DNA helix of OligoPROTAC [n = 3] could be accommodated within the framework of the BRD4–VHL crystal structure. Using ICM-Pro modelling based on the MZ1 structure (PDB: 5T35), it was found that the duplex could be positioned without steric clashes, and a plausible model of the ternary complex was successfully constructed (Figure 6.4).

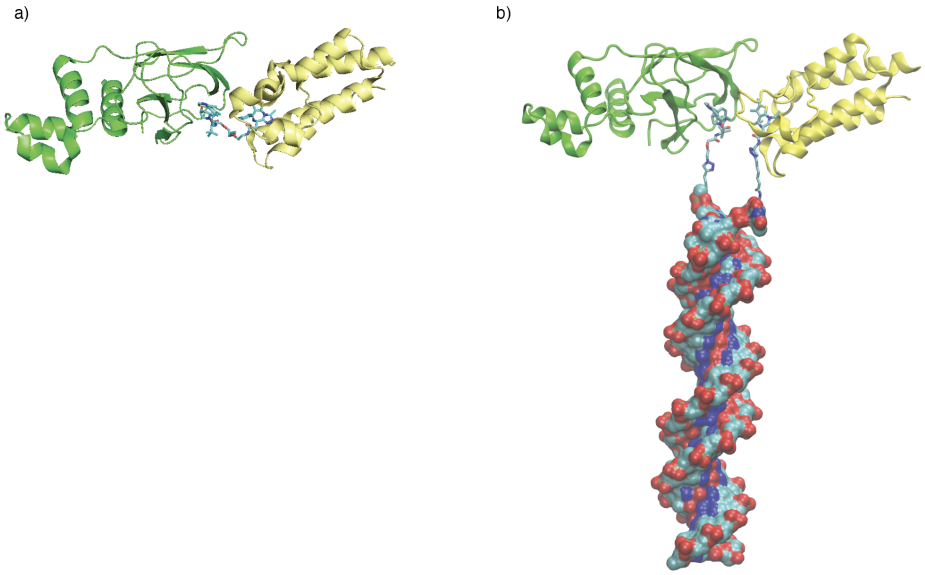

Figure 6.4: Molecular model of OligoPROTAC, (n=3) compared to small molecular PROTAC, MZ1. (a) Crystal structure, 5T353, modified to show MZ1, PROTAC warheads, VH032 and (+)-JQ1 in complex with BRD4: BD2 (yellow) and pVHL (green). (b) Molecular model of OligoPROTAC, (n=3) with VH032 and (+)-JQ1 warheads in complex with BRD4:BD2 (yellow) and pVHL (green). The 23-bp duplex DNA stem is illustrated as a space fill model. *Figure re-produced from the supplementary information of"DNA-programmable Protein Degradation: Dynamic Control of PROTAC Activity via DNA Hybridization and Strand Displacement' by Kashyap et al., under CC-BY 4.0. Data generated by prof. Shozeb Haider.*

Together, this data showed that the OligoPROTACS achieve comparable degra-

dation efficacy to small molecule PROTACs in the case of both the dose-response profile and BRD4 degradation kinetics. Moreover, the shared mechanistic features such as downstream molecular targets and cytotoxicity of the OligoPROTAC and small molecule PROTAC highlight that the DNA linker may allow control over activity without affecting either potency or mechanism.

6.3.7 Tunable "on" and "off" oligoPROTAC states: toehold-mediated strand displacement

To exploit the programmability of the DNA linker, a toehold-mediated strand displacement reaction—widely employed in DNA nanotechnology—was integrated into the OligoPROTAC design as a means of deactivating the construct on demand (Figure 6.5a). The most effective design, OligoPROTAC [n = 3], was selected as the scaffold for this strategy. A series of 3′-(+)-JQ1 ssDNA strands lacking the JQ1 modification and bearing 5′-toehold extensions of 7–10 nucleotides were annealed to complementary 5′-VH032 strands (without the VH032 modification), producing duplexes with a single-stranded toehold on one end and [n = 3] thymine arms on the other (Figure 6.5b). Addition of a complementary anti-toehold strand triggered strand displacement for all tested lengths, as confirmed by gel electrophoresis, demonstrating feasibility *in vitro*.

Based on prior in-cell validation[295], the 8-base toehold was selected for further experiments. To implement this in the functional degrader, the full-length 3′-(+)-JQ1

strand with the 8-base toehold (Appendix Figure A.44) was synthesised and annealed to the 5′-VH032 strand, generating a construct with a toehold at one end and the PROTAC ligands positioned on [n = 3] thymine arms at the other—establishing a programmable off-switch within the OligoPROTAC architecture.

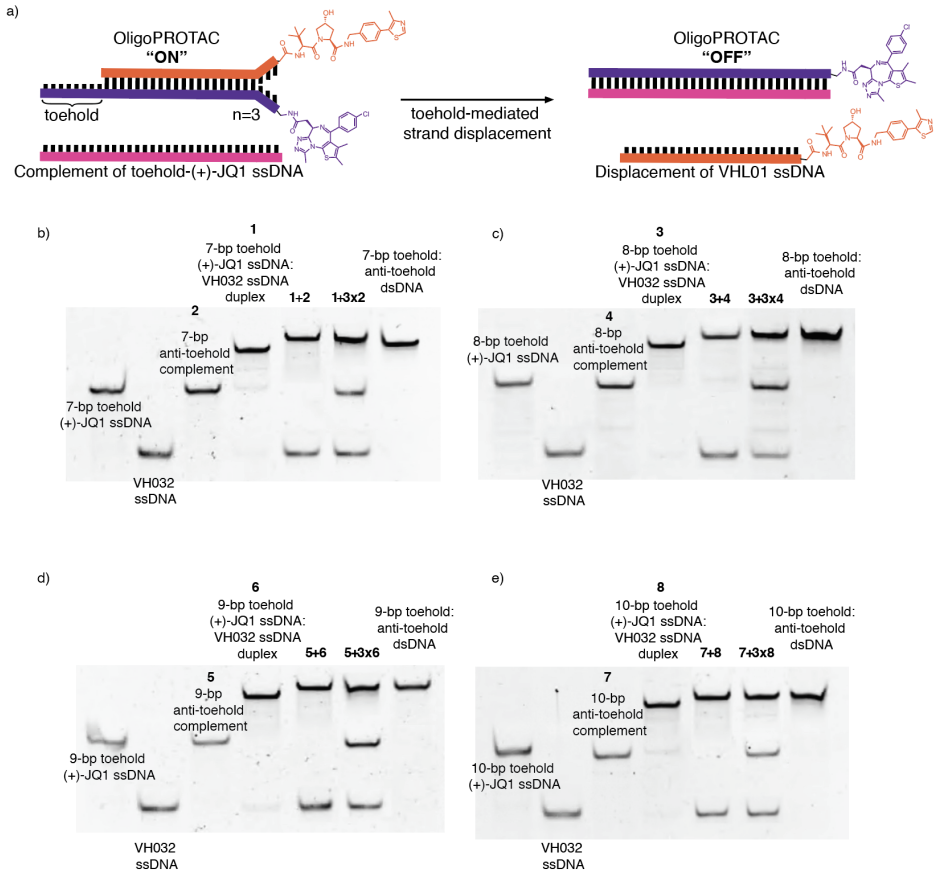

Figure 6.5: (a) Schematic for the toehold mediated strand displacement reaction between the toehold oligoPROTAC [n=3] with the anti-toehold complement, resulting in disruption of dsDNA oligoPROTAC duplex and loss of activity. (b) Native PAGE gel for screening toehold sequences (7, 9, 10-base pair toehold, sequences in Supplementary Table 1) for toehold mediated strand displacement "off" switch for OligoPROTAC construct. *Figure re-produced from "DNA-programmable Protein Degradation: Dynamic Control of PROTAC Activity via DNA Hybridization and Strand Displacement' by Kashyap et al., under CC-BY 4.0.*

The "toehold"-containing construct was transfected into HEK293T cells, and BRD4

degradation was assessed after 12 hours. The presence of the toehold did not impair efficacy, with degradation levels comparable to the original OligoPROTAC [n = 3] (Figure 6.6a,b). To deactivate the construct in cells, Lipofectamine 2000–complexed toehold OligoPROTAC [n = 3] was co-transfected with anti-toehold strands at 1:1 and 1:3 molar ratios, delivered using separate complexes to ensure displacement occurred only intracellularly. In both conditions, BRD4 degradation was abolished (Figure 6.6b), whereas co-transfection with a scrambled strand failed to inhibit degradation.

To determine whether BRD4 degradation could be reversed dynamically, sequential transfections were performed. Cells were first transfected with toehold OligoPROTAC [n = 3] for 12 hours to induce degradation, followed by transfection with either the anti-toehold or a scrambled control strand for an additional 12 hours. After 24 hours, restoration of BRD4 protein levels was observed only in cells receiving the anti-toehold complement, as confirmed by western blotting (Figure 6.6c). These results demonstrated that the “off” switch operated via a sequence-specific strand displacement mechanism occurring intracellularly, representing the first design of a programmable sequence-encoded switch for controlling PROTAC activity.

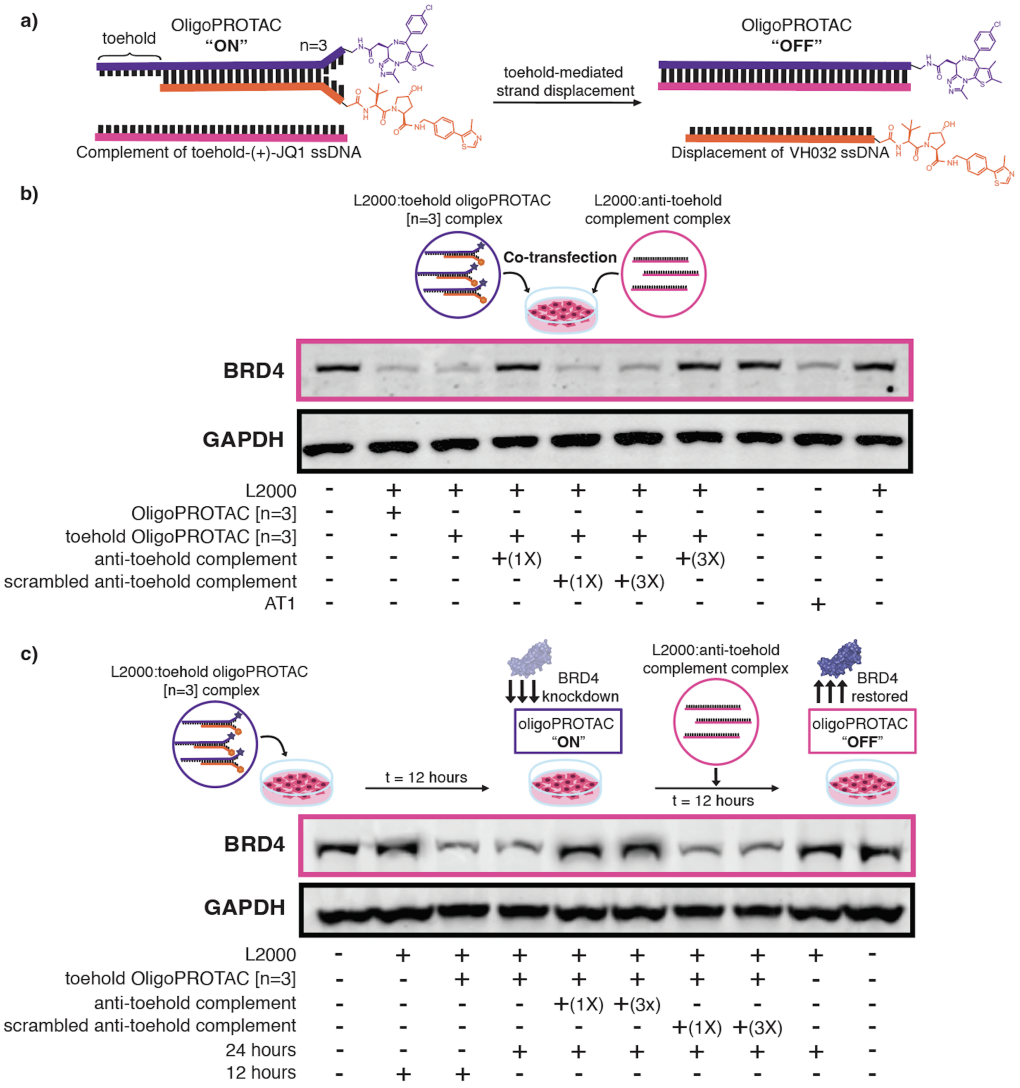

Figure 6.6: Dynamic "off" switch introduced into the oligoPROTAC through toehold-mediated strand displacement. (a) Schematic for the toehold mediated strand displacement reaction between the toehold oligoPROTAC [n=3] with the anti-toehold complement, resulting in disruption of dsDNA oligoPROTAC duplex and loss of activity. (b) Western blot of BRD4 levels upon co-transfection with toehold oligoPROTAC [n=3], along with anti-toehold complement and scrambled anti-toehold complement. Separate Lipofectamine 2000 nanoparticles were produced for the oligoPROTAC and anti-toehold sequences, prior to transfection in HEK293T cells. Normalised to GAPDH levels. (c) Western blot of BRD4 levels upon treatment with toehold oligoPROTAC [n=3] for 12 hours, followed by anti-toehold complement and scrambled anti-toehold complement and harvest at 24 hours. HEK293T cells were treated with the toehold oligoPROTAC [n=3] for 12 hours and activity was then turned "off" with a second transfection with the anti-toehold complement. Normalised to GAPDH levels. *Figure re-produced from "DNA-programmable Protein Degradation: Dynamic Control of PROTAC Activity via DNA Hybridization and Strand Displacement' by Kashyap et al., under CC-BY 4.0.*

6.4 Discussion

PROTACs represent a promising class of targeted protein degradation technologies; however, their clinical applications have been constrained by off-target effects and associated toxicity. Consequently, strategies to fine-tune PROTAC activity are required. To address this, OligoPROTACs were developed, comprising PROTAC warheads positioned in space by a short dsDNA linker. These constructs achieved proximity-dependent protein degradation that could be switched "off" through the addition of a third inhibitor strand. The inhibitor strand separated the duplex linker, and thereby the PROTAC warheads, via toehold-mediated strand displacement. As this control mechanism was independent of the warheads employed, it offered a generalisable approach for regulating the activity of PROTACs or other heterobifunctional molecules.

This study demonstrated that DNA-based systems can be rationally designed to minimise off-target effects and improve control over PROTAC function. OligoPROTAC activity was validated across multiple cell lines, including HEK293T, HeLa, and A549, representing diverse tissue types and biological contexts. These results highlighted the broad applicability and robustness of the platform in both non-cancerous and cancerous cellular environments.

The programmability of DNA further enabled precise tuning of OligoPROTAC structures, including linker length, sequence, and binding affinities. While phos-

phorothioate modifications were incorporated to enhance nuclease stability, the platform readily accommodates additional chemical modifications to improve pharmacokinetic and pharmacodynamic properties. Crucially, activity did not rely on enzymatic recognition of the nucleic acid scaffold[296]. Moreover, OligoPROTACs closely resembled clinically approved short, double-stranded nucleic acid therapeutics such as siRNAs, both in structure and composition. Their duplex architecture and phosphorothioate-modified backbones render them compatible with established siRNA delivery strategies, including lipid nanoparticles and conjugation to targeting ligands such as lipids, sugars, peptides, or antibodies[119]. While the present study focused on in vitro validation, the clinical success of siRNA therapeutics provides a strong precedent for the future in vivo development and translation of OligoPROTACs.

The implications of this work extend beyond enhancing the safety and clinical utility of PROTAC therapies. By integrating DNA nanotechnology into protein degradation strategies, a pathway is opened toward the development of "smart" therapeutics capable of adaptive responses to biological cues. For example, OligoPROTACs could be engineered to respond selectively to disease-specific biomarkers, ensuring that activity is restricted to pathological conditions. Furthermore, the modularity of DNA nanotechnology offers opportunities for multiplexed targeting, enabling the coordinated degradation of multiple proteins simultaneously.

In conclusion, OligoPROTACs represent a significant step forward in the develop-

ment of precision-protein degraders. By harnessing the programmability and versatility of DNA nanotechnology, this approach provides a new layer of control over therapeutic activity, paving the way for safer, "smarter", and thus, more effective protein degradation therapies.

Chapter 7

Future work

This section outlines prospective directions and opportunities for extending the work presented in this thesis. Future work is organized by chapter to reflect the structure and focus of each component of the project.

Chapter 2: Altering the subcellular localization of ASOs to improve their therapeutic engagement and efficacy

The work presented in this chapter establishes a novel platform for enhancing the nuclear delivery and thereby, the therapeutic efficacy of ASOs via covalent conjugation to the small-molecule BET inhibitor, (+)-JQ1. This approach enables improved nuclear accumulation and efficacy across multiple ASO chemistries, molecular targets, and mechanisms of action, including RNase H-mediated knockdown

and splice-switching. The strategy demonstrates broad applicability across various cell lines, including clinically relevant models such as the THP-1, for acute myeloid leukemias. These promising results open several avenues for further optimisation and expanding the applications of this technology.

7.0.1 Mechanistic Elucidation of BET-Mediated Nuclear Import

While the data supports a model in which (+)-JQ1-ASO conjugates directly engage BET proteins to facilitate nuclear import, the precise trafficking mechanism remains undefined. It is unclear whether the conjugates are co-transported through active nuclear import pathways, retained within the nucleus following passive diffusion, or trafficked via a BET protein-dependent shuttling mechanism. The best insight we have to understand the mechanism at present comes from previous work that demonstrate cytoplasmic-to-nuclear shuttling of cytosolic proteins, via BET protein-dependent mechanisms, using hetero-bifunctional small molecules[164]. In this study, the authors showed that a protein present in the cytosol can be rapidly (within 1 hour) transferred to the nucleus by treatment with the small molecule (Main text figures 1c and 2d). This short timeframe along with the shuttling of a specifically cytosolic proteins, indicate an active transport mechanism. However, further studies are necessary to elucidate the underlying dynamics and directional trafficking involved with our oligonucleotide version.

To delineate this, future work should incorporate real-time imaging approaches such as live-cell single-particle tracking of fluorescently labeled ASOs to visualise exact trafficking mechanisms. In parallel, proximity labelling-based approaches coupled with mass spectrometry may help identify nuclear transport factors or trafficking intermediates associated with the conjugates. These efforts will enable the understanding of the precise mechanism of nuclear accumulation, including whether it occurs via active transport or passive retention.

7.0.2 Alternative ligands for nuclear delivery and minimising off-target transcriptional perturbation

Although (+)-JQ1 demonstrates clear utility as a nuclear-targeting ligand, its established role as a transcriptional modulator raises potential concerns regarding off-target gene expression changes, especially in a therapeutic context. Transcriptomic profiling revealed BRD4-inhibition mediated downstream effects in both targeting and non-targeting (+)-JQ1-conjugated ASOs. Moreover, (+)-JQ1 conjugation induced secondary transcriptional programs, including suppression of lipid metabolism and cell cycle genes. Future work should refine the balance between efficient nuclear delivery and unintended transcriptional modulation. Thus, a priority for future work is the identification and validation of alternative small molecule ligands that preserve nuclear targeting capability while minimizing global transcriptional effects.

Now that this work has demonstrated the utility of BET bromodomain proteins in enhancing ASO nuclear accumulation, future efforts can explore both orthosteric inhibitors and allosteric modulators for this class of proteins. Promising alternatives may include small molecules that target nuclear-restricted proteins with limited chromatin-modifying activity, such as nuclear transport receptors, splicing regulators, or nucleolar proteins, offering more selective nuclear delivery with reduced transcriptional perturbation. A high-throughput screening pipeline comprising nuclear-targeting ligand libraries conjugated to ASOs could identify promising alternatives. This could also involve incorporating shorter-lived or cleavable (+)-JQ1 analogues, limiting BET engagement duration. Alternatively, approaches such as inducible or stimuli-responsive conjugates could allow for temporal control of nuclear targeting. In parallel, single-cell RNA-seq could uncover cell-type specific sensitivities to the conjugates guiding therapeutic window design.

7.0.3 Linker architecture and conjugation chemistry

In this work, a minimal azidoacetic acid-based linker was employed to conjugate (+)-JQ1 to the ASO via copper-catalyzed click chemistry. While effective and high-yielding, the linker design could influence intracellular trafficking, conjugate flexibility, BET binding affinity, and even endosomal escape. Systematic exploration of linker length, polarity, rigidity, and biodegradability will be important to optimize intracellular trafficking and minimize steric hindrance or entropic penalties that might impact protein interactions. Incorporating cleavable or pH-responsive linkers

could also allow for nuclear-specific release of the ASO, potentially uncoupling the delivery moiety from off-target activity post-import.

7.0.4 Expanding the nuclear-targeting platform to include other nucleic acid drugs

While this study focused on conventional ASO chemistries, including 2′-OMe splice-switching oligonucleotides and MOE gapmers, this nuclear-targeting strategy could be extended to a broader class of nucleic acid-based agents. These include double-stranded siRNAs that target nuclear-retained RNAs, antisense components of CRISPR systems (for example, synthetic sgRNAs), or decoy oligonucleotides that sequester nuclear-localized RNA-binding proteins. Additionally, nuclear-retained RNAs such as NEAT1 and XIST[297], enriched in the nucleus and implicated in cancer or neurological disease, represent attractive therapeutic targets. Testing (+)-JQ1-conjugated ASOs in these contexts may uncover new applications for gene regulation and mechanistic dissection of nuclear RNA biology.

7.0.5 *In vivo* evaluation in pre-clinical disease models

To establish translational potential, *in vivo* evaluation of (+)-JQ1-ASO conjugates will be a critical next step. Pharmacokinetic and biodistribution studies should assess tissue penetration, nuclear localization, and conjugate stability. Importantly, therapeutic efficacy should be tested in xenograft or syngeneic models of diseases

relevant to the targets studied, such as *BCL-2*–driven leukemias (for G3139) or solid tumors expressing *MALAT1* (for the MALAT1 gapmer). Moreover, AML mouse models could be used to test whether (+)-JQ1-G3139 improves chemosensitization to cytarabine *in vivo*. Additionally, toxicology profiling in animal models will help establish safety margins and off-target effects associated with prolonged exposure to the (+)-JQ1 conjugates. Fluorescence or radiolabeling may assist in quantifying *in vivo* nuclear delivery and retention.

7.0.6 Integration with emerging hetero-bifunctional therapeutic strategies

The modularity of the (+)-JQ1-ASO design lends itself well to integration with emerging bifunctional drug platforms. Inspired by proteolysis-targeting chimeras (PROTACs) and molecular glues, future constructs could incorporate dual-targeting elements. For example, coupling nuclear-targeting with endosomal escape agents or aptamers. Similarly, combining the ASO payload with small molecules that simultaneously modulate epigenetic or splicing regulators may yield synergistic effects in disease contexts with complex regulatory networks. The ability to fine-tune cellular localization and target engagement through chemical design will be a powerful asset in next-generation therapeutic development.

In summary, the (+)-JQ1-ASO conjugation platform presents a promising strategy for enhancing the nuclear delivery and efficacy of oligonucleotide therapeutics.

Building upon the proof-of-concept studies presented here, future work should focus on refining molecular designs, expanding target scope, minimizing transcriptional side effects, and validating therapeutic efficacy *in vivo*.

Chapter 3: Exploring RNase L recruitment via an Activator-ASO conjugate for knockdown of the MLL-AF4 fusion oncogene

The work presented in this chapter establishes a proof-of-concept framework for targeted knockdown of the leukemogenic *MLL-AF4* fusion transcript using antisense oligonucleotides (ASOs) conjugated to small-molecule RNase L recruiters. While the results demonstrate specific and efficient *in vitro* activity of optimized ASOs and outline a robust synthetic route for bioconjugation, several avenues remain open for further investigation to develop this approach into a viable therapeutic strategy.

7.0.7 Structure-Activity Relationship studises for the design of RNase L activators

The current recruiter scaffold, an anilino-thiophene derivative, has low activity, poor selectivity, and an unstable chemical structure (due to the presence of an exocyclic double bond). Future work should explore SAR-based optimisation to improve RNase L potency while avoiding global RNA degradation. Modifications

to the aromatic core, linker composition, or PEG length could enhance engagement and fine-tune activity. In parallel, new RNase L-targeting ligands with improved pharmacokinetics or cell permeability should be explored.

7.0.8 Optimisation of RNase L ligand-ASO conjugate chemistry

Although high-yield and high-purity conjugates were obtained at small scale, scale-up efforts led to reduced reaction conversion and lower product purity possibly due to the instability of the ligand. Addressing this synthetic bottleneck will be a key priority. Future work should explore alternative linker chemistries that offer improved solubility, stability, and coupling efficiency. It is also important to develop sequence-independent and backbone-agnostic conjugation strategies for diverse ASO chemistries to confirm broad applicability.

7.0.9 Functional validation of RNase L activator-ASO Conjugates

The ultimate goal of this work is to achieve cytoplasmic, catalytic degradation of target mRNAs via RNase L activation. While the conjugates were synthesised, *in vitro* functional testing was not achieved due to scale up limitations. With improved synthesis, a key next step will be to evaluate these conjugates in the SEM leukemia cell line, assessing knockdown of *MLL-AF4* at both the mRNA and protein

levels. Comparisons to unconjugated ASOs and the previously established siRNA (siMA6[204]) will allow for the evaluation of potency and specificity improvements achieved by RNase L recruitment.

7.0.10 Mechanistic studies and RNase L recruitment

To confirm that enhanced activity arises specifically from RNase L activation, future experiments should incorporate RNase L inhibition or knockdown strategies (such as siRNA or CRISPR). Co-localisation studies using fluorescently labelled ASOs and immunostaining of RNase L could further elucidate intracellular recruitment and mechanism of action.

This strategy holds promise as a next-generation nucleic acid therapeutic platform that combines the catalytic power of cytoplasmic RNases with the sequence specificity of antisense oligonucleotides.

Chapter 4: Designing small-molecule ASO conjugates to harness the lysosome for targeted mRNA degradation

This chapter on the development of lysosome-targeting antisense oligonucleotides (LyTONs) represents a significant advance in the field of nucleic acid therapeutics,

establishing a third major mechanism for mRNA knockdown: lysosomal degradation. This approach, distinct from RNase H- and RISC-based methods, enables targeted mRNA degradation through conjugation of ASOs to the small-molecule lysosomal-importer, ispinesib. Our work demonstrates that the covalent ispinesib modification can enhance the efficacy of both RNase H-inactive and RNase H-active ASOs, with broad activity across multiple cell lines and modes of delivery. Future work should focus on mechanistic understanding, translational validation, and platform expansion.

7.0.11 Elucidating the molecular mechanism of LyTON trafficking

A critical next step is to define the molecular mechanism of LyTON-mediated lysosomal degradation of target mRNA. While ispinesib has been shown to engage LC3/GABARAP proteins as part of its ATTEC-like activity, the exact protein partners responsible for LyTON internalisation and delivery remain undefined[242,241]. Proteomic pull-down assays, co-immunoprecipitation, and LC3-binding site mutagenesis could identify the key adaptor proteins or chaperones that facilitate LyTON routing. Additionally, live-cell imaging using fluorescently labelled LyTONs, coupled with lysosome and autophagosome markers, could offer spatiotemporal resolution of intracellular trafficking pathways. These studies would help determine whether LyTONs access the lysosome via macroautophagy, microautophagy, endo-

cytosis, or a hybrid mechanism. Understanding these pathways will enable rational design of next-generation LyTON conjugates with enhanced trafficking efficiency.

7.0.12 Structure-Activity Relationship of Ispinesib-Based Warheads

Our current LyTON platform employs commercially available ispinesib–azide derivative conjugated via strain-promoted azide–alkyne click chemistry (SPAAC). Although this approach has proven to be effective, future work should prioritise mechanistic validation to identify direct protein binding partners and trafficking pathways. Such insights will enable a more rigorous SAR analysis of the ispinesib scaffold—for example, modifications to the ispinesib core, PEG linker, and electronic properties could be guided by lysosome reporter assays and LC3 recruitment readouts. Moreover, this understanding would also allow for the high throughput screening of alternative ligand scaffolds to achieve enhanced potency and selectivity for lysosomal targeting.

7.0.13 Expanding the scope of target genes and disease models

LyTONs have been tested *in vitro* against *NCL1* and *MEN1* transcripts in immortalised cell lines. Given the modularity of the platform, future studies should expand the range of gene targets and evaluate LyTONs in primary cells and disease-relevant

models. Furthermore, *in vivo* validation using xenograft or genetically engineered mouse models of MLL-rearranged leukemia (for *MEN1* targeting) would establish proof-of-concept efficacy. LyTONs could be evaluated for their impact on tumour volume, survival, proliferation, and differentiation phenotypes.

7.0.14 Toxicology and transcriptome-wide off-target profiling

Although LyTONs demonstrated minimal toxicity *in vitro* at sub-micromolar concentrations and no significant impact on housekeeping genes, further safety profiling is required. Long-term exposure studies should evaluate potential lysosomal overload, autophagic stress, or immune activation. RNA-seq in LyTON-treated versus wild type/ispinesib-modified NTC ASO treated cells will enable unbiased assessment of off-target transcriptional activity. Parallel proteomic profiling could reveal unintended effects on lysosomal or autophagy networks.

7.0.15 Understanding the dual-mechanism LyTON gapmers

One of the most promising observations in this work was the synergy between RNase H-mediated cleavage and lysosomal degradation observed in the NCL1 gapmer LyTON. These dual-mechanism constructs combine rapid enzymatic degradation with sustained lysosomal targeting. Future work should test the additive or redundant nature of these mechanisms across multiple sequences and chemistries. For exam-

ple, it is unclear whether gapmers targeting nuclear-localised versus cytoplasmic transcripts benefit equally from ispinesib conjugation.

7.0.16 Exploring alternative oligonucleotide chemistries

A major strength of the LyTON platform is its compatibility with RNase H-inactive backbones, such as 2′- OMe and MOE. This opens the possibility of using chemistries that are otherwise unsuitable for RNase H cleavage, but that offer superior stability, immuno-tolerance, or pharmacokinetics. Future studies could explore PNAs, LNAs, and PMOs as LyTON scaffolds. These backbones can be incompatible with knockdown mechanisms, but may find new utility when conjugated to lysosomal-importers.

In summary, the LyTON platform introduces a novel and modular therapeutic platform for cytoplasmic mRNA degradation. By leveraging lysosomal trafficking via small molecule-ASO conjugates, this strategy bypasses the limitations of nuclear localisation, RISC-dependence, and RNase H recruitment. Future work focused on mechanistic elucidation, chemical diversification, and *in vivo* validation will pave the way for LyTONs to become a generalizable and therapeutically valuable addition to the oligonucleotide toolkit.

Chapter 6: Tunable control over PROTAC Activity via DNA Hybridization and Strand Displacement

This work introduces OligoPROTACs, a novel class of double-stranded DNA-based proteolysis-targeting chimeras that enable programmable and reversible control over protein degradation. By conjugating E3 ligase ligands and protein-of-interest (POI) ligands to opposite ends of a tunable dsDNA linker, we achieved catalytic, proximity-driven protein degradation. Furthermore, we engineered a toehold-mediated strand displacement system that acts as a programmable "OFF" switch, enabling dynamic inactivation of OligoPROTAC function in cells. These findings offer a robust foundation for precision degraders that integrate the modularity of DNA nanotechnology with the potency of PROTAC pharmacology. Several future directions are possible to optimise, expand, and allow for clinical translation of this technology.

7.0.17 Tuning Degradation Potency via DNA Structure and Chemistry

One of the most significant findings in this work was the effect of "linker", determined by the number of non-complementary thymine bases—on BRD4 degradation

efficiency. Future studies should expand on various kinds of "linker" distances by systematically testing alternative non-complementary spacers (for example, abasic sites, PEG-modified bases) or rigid versus flexible spacers to alter DNA helical geometry. These structural modifications could modify the spatial orientation of the warheads in the ternary complex and potentially improve E3 ligase recruitment efficiency.

Likewise, incorporating chemically modified backbones (for example, LNA, 2′- O-methyl, 2′- fluoro, phosphorodiamidate morpholino oligomers (PMOs)) could increase intracellular stability, reduce immunogenicity, and improve pharmacokinetics.

7.0.18 Mechanistic elucidation: Kinetics and structural biology

While we have demonstrated that degradation is dependent on ligand positioning, further elucidation of ternary complex formation and kinetics is essential. Techniques such as fluorescence resonance energy transfer (FRET), surface plasmon resonance (SPR), and single-molecule tracking could quantify dissociation constants (K_d) and off-rates for ternary complex formation, assembly lifetime of the DNA-protein complexes, and the recruitment kinetics of the ubiquitin machinery.

Additionally, cryo-electron microscopy (cryo-EM) or X-ray crystallography of BRD4-

VHL complexes bound by the oligoPROTAC would provide structural insights into orientation, spacing, and flexibility requirements for efficient degradation. These data could inform rational linker design and model future constructs computationally.

7.0.19 Expanding the platform to include other protein targets and E3 ligases

This work focused on degradation of the well-studied BET bromodomain protein BRD4 using (+)-JQ1 and VHL ligand, VH032, as the PROTAC warheads. Future designs should test different POI ligands such as FKBP12, CDK9, BCL-XL, $KRAS^{G12D}$, or mutant p53 along with recruiting other E3 ligases such as CRBN, MDM2, RNF114, or cIAP.

We anticipate that linker flexibility, spatial constraints, and degradation efficiency will vary based on warhead pairing. The modular nature of DNA enables rapid generation of combinatorial libraries of OligoPROTACs to screen POI/E3 pairings and linker configurations in parallel. These could be evaluated using high-content imaging, proteomic profiling, or phenotypic assays in the relevant cell types.

7.0.20 Tissue-specific and stimuli-responsive OligoPROTACs

A key limitation of existing PROTACs is their constitutive activity, which may cause toxicity in healthy tissues. Our work provides the first instance of a DNA-based,

sequence-programmed “off” switch via toehold-mediated strand displacement. Future improvements could extend this system to “on” switches and logic-gated control, including miRNA-responsive degradation activity and strand displacement cascades triggered by specific intracellular redox or pH environments.

This would allow for precise spatiotemporal control of degradation and enable Boolean logic operations over protein degradation (for example, AND, NOT, OR gates). The potential for conditional activation of PROTAC degraders via the OligoPROTAC design opens new avenues in cell type-specific therapeutics.

7.0.21 *In vivo* translation of OligoPROTACs

OligoPROTACs resemble short double-stranded nucleic acids such as siRNA or antagomiRs in structure and size. This similarity supports direct clinical translation with existing delivery platforms such as LNPs used in siRNA drugs or GalNAc conjugates for liver-specific delivery or AOCs for tissue-targeted therapies.

Building on this, the next steps toward translational development would include pharmacokinetic, biodistribution, and serum stability studies in mice using fluorescently labelled or radiolabelled OligoPROTACs. Pilot efficacy trials in xenograft tumour models (for example, AML models with BRD4/MYC dependency) would demonstrate therapeutic relevance. Additionally, immunogenicity screening and off-target transcriptome analysis (RNA-seq, proteomics) would be essential for clinical advancement.

7.0.22 Multimeric and multivalent systems for simultaneous targeting of multiple proteins

Another promising direction is to expand from monomeric constructs to multivalent OligoPROTACs capable of simultaneous degradation of multiple proteins, bivalent recruitment of the same POI for enhanced avidity or allosteric regulation of degrader efficacy.

DNA origami and tile systems could enable precise spatial arrangement of multiple warheads, while preserving programmability. Multivalent designs could exploit cooperativity for enhanced degradation, or logic-gated degradation for exquisite spatiotemporal conteol.

In conclusion, the OligoPROTAC framework merges the programmability of DNA nanotechnology with the catalytic efficiency of PROTACs, offering precise control over protein degradation. With tunable linker geometry and reversible strand-displacement switches, these constructs address current limitations in specificity, toxicity, and off-switch design. Continued development across chemistry, cell biology, and therapeutic delivery will enable OligoPROTACs to serve as a blueprint for the next generation of smart, modular, and logic-responsive protein-degrading biologics.

Chapter 8

Materials and methods

For clarity and ease of understanding, this section has been organized on a chapter-wise basis, with each chapter detailing the specific experimental procedures relevant to its corresponding results.

Chapter 2: Altering the subcellular localization of ASOs to improve their therapeutic engagement and efficacy

8.0.1 General synthesis

Reagents were purchased from commercial sources (Merck, Fluorochem, BLD Pharm and Alfa Aesar) and used without further purification. Solvents were used as supplied (analytical/HPLC-grade from Fisher or Sigma-Aldrich) or if dry solvents were required, taken from a solvent drying system (MBraun MB-SPS-5-Bench Top) un-

der nitrogen atmosphere (H_2O content < 20 ppm as determined by Karl Fischer titration).

Eluent mixtures are reported in volume:volume or percent volume. Column chromatography was carried out using Merck Geduran Silica Gel 60 or on an automated Biotage Selekt One purification machine with Biotage Sfär Silica D Duo flash chromatography cartridges. HPLC grade solvents were used for purifications, extractions, and work-ups. TLC was carried out on Merck silica gel 60 F254 Al plates visualized either under UV light (254 nm) or by staining with vanillin dye, phosphomolybdic acid or permanganate.

NMR spectroscopy measurements were recorded using a Bruker AVII400, AVII500 or AVIII600 instrument and peaks were referenced to the residual solvent peak. High Performance Liquid Chromatography (HPLC) was carried out on an Agilent Technologies 1260 Infinity Machine equipped with an Agilent Polaris C18-A column, 150x4.6 mm, 5µm particle size and 180Å pore size. Infrared Spectra (IR) were recorded on a Bruker Tensor 27 FT-IR. Melting points (mp) were determined using a Stuart SMP-40 automated melting point apparatus. Reversed-phase chromatography was performed on an ACQUITY I-Class PLUS UPLC System (Waters, Milford, MA, USA) coupled to an ACQUITY RDa mass spectrometer (Waters, Milford, MA, USA) equipped with an ESI probe, in positive ion mode.

8.0.2 (S)-2-(4-(4-Chlorophenyl)-2,3,9-trimethyl-6H-thieno[3,2-f][1,2,4] triazolo[4,3-a][1,4]diazepin-6-yl)acetic acid

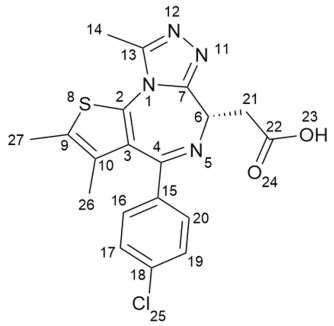

Following a literature procedure[170], to a stirred solution of (+)-JQ1 (90.0 mg, 0.2 mmol) in dichloromethane (4.0 mL) was added trifluoroacetic acid (0.5 mL). The reaction mixture was stirred at room temperature for 2 hours. The reaction mixture was concentrated under vacuum to give (+)-JQ1-acid, and used without purification. White solid, mp: 90–93 °C. ^{1}H NMR (600 MHz, $CDCl_3$) δ/ppm: 7.45 (d, J = 8.6 Hz, 2H, C(17)H + C(19)H), 7.36 (d, J = 8.6 Hz, 2H, C(18)H + C(20)H), 6.36 (s, 2H, C(3)H + C(4)H), 4.63 (t, J = 6.8 Hz, 1H, C(21)H), 3.81–3.55 (m, 2H, $C(6)H_2$), 2.74 (s, 3H, $C(27)CH_3$), 2.44 (s, 3H, C(26)CH), 1.72 (s, 3H, $C(13)CH_3$). ^{13}C NMR (101 MHz, $CDCl_3$) δ/ppm: 173.48, 164.25, 155.29, 150.01, 137.04, 136.27, 131.98, 131.25, 131.02, 130.53, 129.97, 128.78, 53.68, 36.74, 14.45, 13.16, 11.77. IR (film $CDCl_3$/cm^{-1}) 3260, 2500, 1715, 1680, 1600, 1505, 1295, 760. HR-LC MS (ESI, m/z): MS (ESI+) found 401.0835, [M+H]+. Characterisation data obtained was in agreement with the literature values.

8.0.3 (S)-2-(4-(4-chlorophenyl)-2,3,9-trimethyl-6H-thieno[3,2-f][1,2,4] triazolo[4,3-a][1,4]diazepin-6-yl)-N-(prop-2-yn-1-yl)acetamide

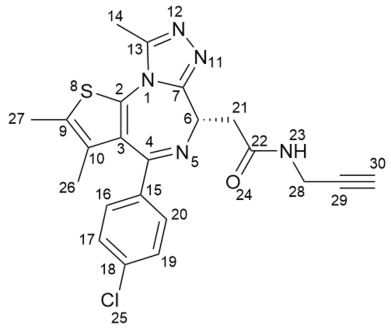

Following a patented procedure[171], to a solution of (+)-JQ1 acid (160 mg, 0.4 mmol), prop-2-yn-1-amine (26.4 mg; 0.5 mmol), EDCl-HCl (84.2 mg; 0.44 mmol), and HoBT (74.4 mmol; 0.44 mmol) in DMF (2 ml) was added DIPEA (181 mg; 1.4 mmol). The reaction mixture was stirred at room temperature overnight. The reaction mixture was subsequently diluted with water and extracted with ethyl acetate. The organic layer was washed with brine, dried over Na_2SO_4, and concentrated. The resulting residue was purified by normal phase column chromatography with (0 to 10% MeOH : DCM) to give JQ1-alkyne (159 mg; 87.8%). Off-white oil, bp: $>$ 205 °C. ^{1}H NMR (600 MHz, $CDCl_3$) δ/ppm: 7.42 (d, J = 8.1 Hz, 2H, C(17)H + C(19)H), 7.32 (d, J = 8.6 Hz, 2H, C(18)H + C(20)H), 6.93 (br s, 1H, C(23)NH), 4.63 (dd, J = 6.5, 6.5 Hz, 1H, C(21)H), 4.18 (ddd, J = 17.5, 5.6, 2.4 Hz, 1H, C(28)Ha), 3.97 (ddd, J = 17.5, 4.5, 2.3 Hz, 1H, C(28)Hb), 3.33 (dd, J = 14.0, 6.5 Hz, 1H,

C(6)H), 2.60 (s, 3H, C(27)CH_3), 2.33 (s, 3H, C(26)CH_3), 2.14 (t, J = 2.5 Hz, 1H, C(30)H), 1.60 (s, 3H, C(13)CH_3). ^{13}C NMR (101 MHz, $CDCl_3$) δ/ppm: 170.20, 164.32, 155.40, 150.16, 141.13, 137.05, 136.28, 131.72, 131.41, 131.10, 130.73, 129.91, 128.75, 128.57, 126.68, 125.86, 117.67, 110.94, 79.64, 71.47, 54.11, 53.43, 38.72, 29.7, 29.3. IR (film $CDCl_3$/cm^{-1}) 3290, 2116, 1692, 1658, 1602, 1578, 1510, 1332, 1296, 760. HR-LC MS (ESI, m/z): MS (ESI+) found 438.1141 [M+H]+. Characterisation data obtained was in agreement with the patent.

8.0.4 Antisense oligonucleotide sequences

All unmodified oligonucleotides were purchased from IDT as desalted and lyophilised products – resuspended in 10 mM Tris pH 8. Amine-containing oligonucleotides were purchased from IDT, HPLC-purified in lyophilised form and dissolved in 10 mM potassium phosphate buffer, pH 8.

Table 8.1: Antisense oligonucleotide sequences used for all transfection, electroporation, gymnosis experiments with 5′- terminal amine or azide modifiers for functionalisation chemistry
* denotes phosphorothioate linkages
__ denotes 2′-Methoxy-ethyl sugars
m denotes 2′- O-Methyl sugars

S.No.	**Name**	**Sequence (5′ – 3′)**
1	SSO	mC*mC*mU*mC*mU*mU*mA*mC*mC*mU*mC*mA*mG*mU*mU*mA*mC*mA
2	MALAT1 gapmer	G*G*C*A*T*A*T*G*C*A*G*A*T*A*A*T*G*T*T*C
3	Oblimersen, G3139	T*C*T*C*C*C*A*G*C*G*T*G*C*G*C*C*A*T
4	NTC-ASO	T*C*G*T*G*G*G*T*A*G*G*T*C*C*G*C*A*C*T*A

8.0.5 (+)-JQ1-ASO conjugates synthesis, purification and characterisation

Azidoacetic acid-NHS ester functionalisation

To a 0.5 mL Eppendorf DNA LoBind tube was added 1 µL of the PS-modified DNA (100 µM stock concentration), 1 µL of NaHCO3 pH 8.5 (1 M), 2 µL of H_2O, 5 µL of a 50 mM solution of azido-acetic acid NHS in dry DMF. The reaction was vortexed, spun down in a tabletop centrifuge and placed in a Thermomixer (Eppendorf) overnight, shaking at 800 rpm at 37 °C.

The excess hydrolysed small molecule was removed using Amicon 3K 0.5 mL spin columns, according to the manufacturer's instructions. Briefly, the reaction was

made up to a volume of 500 µL with H_2O and spun at 14,700g for 10 minutes. The eluent was removed and the above process was repeated for a total of three times. The column was then inverted, inserted into a fresh collection tube and spun at 14,700g for 1 minute.

HPLC purification method for azido-modification

The eluent obtained was then purified by HPLC on an Agilent Polaris C18 column (150 x 4.6 mm), column heated to 50 °C using a gradient of 3-30% CH3CN (indicated in appendix figures) over 20 minutes, flow rate of 1.5 mL/min, with 10 mM triethylammonium bicarbonate (TEAB) pH 8.5 as an ion-pairing buffer throughout.

(+)-JQ1-functionalisation with copper click chemistry

To a 0.5 mL Eppendorf DNA LoBind tube was added, listed in order of addition, 1 µL of the PS-modified DNA (1 mM stock concentration), 1.5 µL of 1 mM (+)-JQ1-alkyne (stock in DMF), 1 µL of 200 mM DIPEA, 5.5 µL of H_2O, 1 µL of 200 mM sodium ascorbate and finally, 1 µL of 200 mM copper (I) bromide-dimethyl sulphide (stock in DMSO). The reaction was vortexed, spun down in a tabletop centrifuge and placed in a Thermomixer (Eppendorf) overnight, shaking at 800 rpm at room temperature. An alternate protocol, listed in order of addition, used 1 µL of the PS-modified DNA (1 mM stock concentration), 1.5 µL of 1 mM (+)-JQ1-alkyne (stock in DMF), 0.4 µL of 100 mM sodium ascorbate, 1.6 µL of H_2O, and finally, 0.5 µL of 100 mM copper (I) sulphate pre-complexed with 100 mM

Tris(3-hydroxypropyltriazolylmethyl)amine (1:1, final concentration of both at 50 mM), shaking at 800 rpm overnight at room temperature.

The reaction was quenched with 250 µL of 0.5 M EDTA pH 8, made up to 500 µL with H_2O and first run through a Amicon 3K 0.5 mL column/tube as described above to chelate excess copper and remove it along with the unreacted small molecule. The final eluent collected after inversion.

HPLC purification method for (+)-JQ1 modification

The final eluent collected was then purified by HPLC on an Agilent Polaris C18 column (150 x 4.6 mm), column heated to 50°C using a gradient of 3-30% or 3-50% CH_3CN (indicated in Appendix Figures) over 20 minutes, flow rate of 1.5 mL/min, with 10 mM triethylammonium bicarbonate (TEAB) pH 8.5 as an ion-pairing buffer throughout.

Oligonucleotide MS characterisation

Oligonucleotide Mass Spectra were recorded on a Waters Xevo G2 QTOF ESI-UPLC-MS system. A gradient of MeOH in Et3N and hexafluoroisopropanol (HFIP) was used (buffer A, 8.6 mM Et3N, 200 mM HFIP in 5% MeOH/H_2O (v/v); buffer B, 20% buffer A in MeOH). Data was then deconvoluted using MassLynx software v4.1 and recorded in Table 8.2.

Table 8.2: Molecular weights of antisense oligonucleotide conjugates prepared via azide/(+)-JQ1 functionalisation chemistry.

S.No.	Name	Expected mass	Mass after deconvolution
1	Azide-SSO	6360.0	**6359.8**
2	JQ1-SSO	6799.0	**6797.8**
3	Azide-MALAT1 gapmer	7493.0	**7491.6**
4	JQ1-MALAT1 gapmer	7930.0	**7928.6**
5	Azide-G3139	5947.0	**5945.5**
6	JQ1-G3139	6385.0	**6383.6**
7	JQ1-NTC-ASO	7239.0	**7239.5**
8	Azide-G3139-Cy3	6588.0	**6590.0**
9	JQ1-G3139-Cy3	7034.0	**7030.0**

8.0.6 Cell culture

HeLa pLuc/705, HEK293T, A549 cells were both cultured in Dulbecco's Modified Eagle Medium (DMEM) supplemented with 1X GlutaMAX (Gibco) and 10% (v/v) Foetal Bovine Serum (FBS) (Gibco) and) at 37 °C in a humidified incubator with 5% CO2.

HEK293 cells were cultured in DMEM supplemented with 1X GlutaMAX (Gibco), 10% FBS (Gibco), 1% penicillin-streptomycin (Gibco), 1% HEPES (Gibco) and 1% sodium pyruvate (Gibco), and maintained at 37°C in a humidified incubator with

5% CO2.

THP-1 cells were cultured in Roswell Park Memorial Institute 1640 Medium supplemented with 1X GlutaMAX (Gibco) and 10% (v/v) FBS (Gibco) at 37 °C in a humidified incubator with 5% CO2.

8.0.7 Nucleic acid delivery: Lipid-based transfection, electroporation, gymnosis

Transfection

For **transfection** with lipofectamine 2000, HeLa pLuc/705 cells were seeded at a density of 1 × 104 cells/well in 100 µL of culture media in 96-well plates (Corning) for 16 hours before transfection to reach 70-80% cell confluency. For HEK293T A549 cells, 2.5 × 10^5 2.2 × 10^5 cells were plated in 1 mL of culture media in 24-well plates (Corning) 16 hours before transfection to reach 70-80% cell confluency. Prior to transfection, the culture media was replaced with OptiMEM, 100 µL for the 96-well plates and 1 mL for the 24-well plates. When using HEK293 cells for immunocytochemistry, cells were plated at a density of 5 × 10^4 cells/well in an 8-well chamber slide (Nunc, Thermo Fischer Scientific) in 400 µL of culture media 24 hours before transfection to reach 70-80% cell confluency. Prior to transfection, culture media was replaced with 180µL fresh complete media.

For the HeLa pLuc/705 cells, 5 µL of Lipofectamine 2000 (Invitrogen) was diluted

in 495 µL OptiMEM (Gibco) and incubated at room temperature for 5 minutes before mixing with 4 nmol of oligonucleotide dissolved in 500 µL of OptiMEM[298]. The resulting mixture was incubated at room temperature for 20 minutes allowing complexation to occur. The complexes were then added at the required concentrations to the cells (with total volume at 100 µL per well). The cells were then incubated at 37 °C in a 5% CO2 incubator. After 6 hours the media was replaced with 100 µL of culture media and the cells were returned to the incubator for a further 18 hours.

For the HEK293T A549 cells HEK293, 2 µL of Lipofectamine 2000 (Invitrogen) was added to 48 µL OptiMEM (Gibco) and incubated at room temperature for 5 minutes before mixing with 0.5 nmol of oligonucleotide dissolved in 50 µL of OptiMEM. The resulting mixture was incubated at room temperature for 20 minutes allowing complexation to occur. The complexes were then added to the cells at the required concentrations (with total volume of 1 mL per well). The cells were then incubated at 37 °C in a 5% CO2 incubator. After 6 hours the media was replaced with 1 mL of culture media and the cells were returned to the incubator for another 18 hours.

For HEK293, briefly, as above OptiMEM-Lipofectamine 2000 complexes were prepared by mixing the required volume of OptiMEM (Gibco) and the required volume of Lipofectamine 2000 (Invitrogen) and incubated at room temperature for 5 minutes. The required volumes of ASOs to achieve a 200nM or 500nM dose were added to the OptiMEM-Lipofectamine 2000, and the transfection mix was incubated for

20 minutes at room temperature to allow for ASO-Lipofectamine 2000 complex formation. 40µl of the transfection mix was added to the wells, and the cells were returned to the incubator for 24 hours.

Gymnosis

For **gymnosis**, HEK293T cells were seeded at a density of 5×10^4 cells/well in 1 mL of culture media in 24-well plates for 16 hours before transfection to reach 70-80% cell confluency. Prior to transfection, the culture media was replaced with OptiMEM and the ASO was added at the desired concentration. After 6 hours, OptiMEM was replaced with 1 mL of complete culture media and the cells were returned to the incubator for a further 90 hours (total time of 96 hours).

Electroporation

For **electroporation**, THP-1 cells were resuspended in complete media at a density of 10^8 cells/mL and the ASOs were added directly to the cell suspension at the desired final concentration. Cells were subjected to a 10 ms 330 V electroporation using a rectangle pulse EPI 2500 electroporator (Fischer, Heidelberg), after which they were diluted to 10^6 cells/mL. Cells were either harvested at 48h, or at this point, a second electroporation was performed, and cells were harvested after a further 48h for a 96h knockdown.

8.0.8 Luciferase assay

The culture media was removed from the well and the cells were washed with 200 µL of PBS. 100 µL of GloLysisTM buffer (Promega) was added to each well and the plate was incubated at room temperature on the orbital shaker for 10 minutes to lyse the cells. 50 µL of the cell lysate was added to 50 µL of Bright-GloTM luciferase reagent (Promega) in a white 96-well plate and the luminescence was measured using a CLARIOstar microplate reader (BMG Labtech). The luminescence values were normalised to the values for untreated cells.

8.0.9 BCA protein assay

25 µL of the cell lysate (as prepared above) was then used for protein quantification using a Pierce BCA protein assay according to the manufacturer's instructions, using the GloLysis buffer as a blank standard. Briefly, a working reagent (WR) was prepared by mixing 50 parts of BCA reagent A with 1 part of BCA reagent B. To 25 µL protein lysate of each sample in a 96-well plate, 200 µL WR was added. The plate was covered with foil and incubated for 1 hour at 37 °C in a 5% CO2 incubator. Absorbance values were corrected for the GloLysis buffer and titrated against known protein standards for quantification.

8.0.10 Competition assay

For all competition assays, cells were co-treated with the specified concentrations of (+)-JQ1 dissolved in DMSO and ASOs. Transfections were performed as described previously, and the cells were treated with (+)-JQ1 treatment concurrently with the addition of the lipofectamine-nucleic acid complexes. Luciferase assay was then performed as described above for the SSO and JQ1-SSO conjugate and qPCR was performed as described below for MALAT1 gapmer, JQ1-MALAT1, G3139 and JQ1-G3139.

8.0.11 CellTiter-Glo

Transfection experiments were carried out as outlined above. Cells were subjected to the CellTiter-Glo assay at the indicated time points following the manufacturer's guidelines. Briefly, 100 µL CellTiter-Glo Reagent was added to 100 µl of media containing cells in a white (Thermofischer Nunc MicroWell polystyrene, 236105) 96-well plate. Subsequently, the contents of the wells were mixed on an orbital shaker for 2 minutes to induce cell lysis. The plate was then incubated at room temperature for 10 minutes to stabilize the luminescent signal. The luminescence was measured using a CLARIOstar microplate reader (BMG Labtech). The luminescence values were normalised to the values for untreated cells.

8.0.12 RT-qPCR

RNA extraction

Total RNA was extracted and DNase I-treated from pellets with 1×10^6 cells using the RNeasy Mini kit (Qiagen) following the manufacturer's instructions. Briefly, cell pellets were lysed by dissolving in RLT buffer containing β-mercaptoethanol, followed by addition of 70% ethanol and transfer to a spin column. The columns were centrifuged at 12,000g, treated with DNase I (Qiagen), washed with RW1 and RPE buffers, and the RNA, thus obtained, was eluted in RNase-free water. RNA quality and concentration were assessed using NanoDrop (ThermoFisher Scientific).

Reverse transcription — cDNA synthesis

RNA was reverse-transcribed (RT) using SuperScript III (ThermoFisher Scientific) as follows. 1 µg of RNA in 8 µL total volume was incubated with 1 µL random hexamers (3µg/µl, 58875) and 1 µL of a mix of all four deoxynucleoside triphosphates (dNTPs, 10mM 18427-013) and nuclease-free H_2O at 65 °C for 5 minutes. The complementary DNA (cDNA) was synthesised from the above RNA-primer-dNTP solution with the cDNA synthesis reaction mix in Table 8.3 under the cDNA synthesis reaction conditions in Table 8.4.

Table 8.3: Composition of the cDNA synthesis reaction mix used for reverse transcription. The mix includes RNA, random hexamer primers, and dNTPs, followed by essential components for first-strand synthesis including buffer, DTT, RNase inhibitor, and SuperScript III reverse transcriptase.

S. No.	**Component**	**Volume (µL)**
1	RNA, random primers, dNTPs mix	8
2	5X First Strand Buffer	4
3	Nuclease-free H_2O	2
4	1,4-Dithiothreitol (DTT)	2
5	RNaseOUT (00000840)	1
6	SuperScript III (200 U/µL, 56575)	1

Table 8.4: Reaction conditions for the reverse transcription reaction using SuperScript III.

S. No.	**Temperature (°C)**	**Time (minutes:seconds)**
1	25	5:00
2	50	60:00
3	70	15:00

cDNA samples were diluted 10x for Reverse transcriptase quantitative polymerase chain reaction (RT-qPCR) analysis. The reaction mix in Table 8.5 was set up in individual wells of a 96-well PCR plate (MicroAmp Fast Optical 96-well Reaction Plate, 4346906, Applied Biosystems). SYBR green was used for quantification in in QuantStudio 3 Real-time PCR machine (qPCR primers listed in Table 8.6) using reaction conditions in Table 8.7. Gene expression was normalized to mature mRNA

levels of the housekeeping gene, GAPDH.

Table 8.5: Composition of the RT-qPCR reaction mix used for SYBR Green-based quantification. The reaction includes forward and reverse primers, SYBR Green master mix, nuclease-free water, and template cDNA.

S. No.	**Component**	**Volume (µL)**
1	10 µM Forward Primer	0.5
2	10 µM Reverse Primer	0.5
3	Fast SYBR Green Master Mix (4385612, Applied Biosystems)	10.0
4	Nuclease-Free Water	4.5
5	DNA	5.0

Table 8.6: Primer sequences used for SYBR Green-based RT-qPCR assays to quantify knockdown. FWD and REV refer to forward and reverse primer sequences respectively.

S. No.	**Name**	**Sequence ($5' - 3'$)**
1	GAPDH FWD	TTGGCTACAGCAACAGGGTG
2	GAPDH REV	GGGGAGATTCAGTGTGGTGG
3	MALAT1 FWD	GAAGGAAGGAGCGCTAACC
4	MALAT1 REV	TACCAACCACTCGCTTTCCC
5	BCL2 FWD	CCCTGTGGATGACTGAGTACCTG
6	BCL2 REV	CCAGCCTCCGTTATCCTGG

Table 8.7: Table B: Thermal cycling conditions used for SYBR Green-based RT-qPCR analysis. The protocol includes initial denaturation, repeated denaturation-annealing-extension cycles, and final extension.

S. No.	**Temperature (°C)**	**Time (minutes:seconds)**	**Cycles**
1	95	3:00	1
2	98	0:20	30
3	65	0:15	30
4	72	1:00	30
5	72	2:00	1

8.0.13 Western blotting

Salt-soluble proteins were extracted from 1×10^6 cells by incubating cells in a high-salt lysis buffer (20 mM Tris-HCl pH 8.0, 300 mM KCl, 5 mM EDTA, 20% glycerol, 0.5% IGEPAL CA-630, protease inhibitor cocktail (PIC)) for 30 minutes at 4 °C. Lysates were centrifuged at 16,000g for 10 minutes and 4 °C, and the supernatant was mixed with LDS sample buffer for running SDS-PAGE followed by western blotting. Protein extracts were then run on a NuPAGE 12% BisTris gels (Life Technologies) at 180V for 1 hour and blotted onto a polyvinylidene fluoride membrane (Immobilon) at 100V for 1 hour using a Tris-glycine blotting buffer[299] The blots were then probed with 1:10,000 dilution of primary antibody for BCL-2 (CST #4223, D55G8) and GAPDH (Bethyl, A300-641A) in 5% milk/TBS-tween at 4 °C overnight. BCL-2 / GAPDH blots were then probed with secondary antibody (ab216773, IRDye 800CW) for 2 hours at room temperature, followed by imaging

on the ChemiDoc MP system.

8.0.14 Subcellular fractionation — Cy3 quantification

1×10^6 cells were lysed in 1 mL Buffer A (10 mM HEPES pH 7.9, 10 mM KCl, 1.5 mM MgCl , 0.34 M sucrose, 10% glycerol) with 0.2% NP-40 and 1:200 PIC for 5 minutes on ice. Following a 5-minute centrifugation at 500g and 4 °C, the cytoplasmic fraction (supernatant) was removed, and intact nuclei (pellet) were washed once in Buffer A with PIC. Nuclei were then resuspended in 1 mL Nuclear lysis buffer (50 mM Tris-HCl, pH 8.0, 2 mM MgCl2, 150 mM NaCl) with 0.5% NP40 and 1:200 PIC for 1 hour on a rotating wheel at 4 °C. After centrifugation at 18,000g for 10 min and 4 °C, the supernatant containing the nuclear fraction was obtained. Equal proportions of each fraction were adjusted to 1x NuPage LDS sample buffer (ThermoFisher Scientific NP0008) for SDS-PAGE, followed by western blotting.

Whole cell lysate controls were prepared with lysis directly in BC300 buffer (50 mM Tris-HCl, pH 8.0, 300 mM KCl, 5 mM EDTA, 20% glycerol) with 0.5% NP40 and PIC for 30 minutes on ice. Lysates were centrifuged at 16,000g for 10 minutes and 4 °C, and the supernatant was mixed with LDS sample buffer for running SDS-PAGE followed by western blotting. To ensure successful fractionation was achieved, cytoplasmic protein, GAPDH (Bethyl, A300-641A) and nuclear-localised Menin (Bethyl A300-105A) were probed in respective fractions via western blotting.

Cy3 fluorescence readout was obtained by taking the respective cytoplasmic or

nuclear fractions in a white (Thermofischer Nunc MicroWell polystyrene, 236105) 96-well plate, and using the Cy3 settings (excitation peak at 554 nm, emission peak at 570 nm) for reading fluorescence using the CLARIOstar microplate reader (BMG Labtech). The fluorescence values were normalised to the values for the respective subcellular fractions for untreated cells.

8.0.15 Immunocytochemistry (ICC)

Experiments performed by Martina Caddedu (MRC NATA)

Nuclear stain was prepared by diluting Hoechst 3342 dye (Invitrogen) in PBS to obtain a 1:2000 dilution. Cell media post-transfection was removed, and 400 µL of nuclear stain was added followed by an incubation for 5 minutes at room temperature on a shaker with protection from light. The nuclear stain was then removed, and the cells were washed with PBS 3 times for 5 minutes each. Next, 4% paraformaldehyde (PFA) solution was prepared by diluting a 16% PFA stock (Thermo Scientific) in PBS. The PBS from the washes was removed, and 400 µL of 4% PFA was added to the cells followed by incubation for 10 minutes at room temperature on a shaker with protection from light. Then the PFA solution was removed, and the cells were washed 3 times with PBS for 5 minutes each. Next, the permeabilization buffer was prepared by diluting Triton-X (Bio-Rad) in PBS to obtain a 0.1% solution. The PBS from the washes was then removed and 400 µL of 0.1% permeabilization buffer was added followed by incubation for 10 min-

utes at room temperature on a shaker with protection from light. Blocking buffer was then prepared by diluting goat serum (Gibco) in permeabilization buffer to obtain a 5% solution. Thereafter, the permeabilization buffer was removed, 400 µl of 5% blocking buffer was added and incubated for 1 hour at room temperature on a shaker with protection from light. The primary antibody dilutions were prepared next. The primary antibodies PS03 (mouse) (Rockland Immunochemicals) and α/β-tubulin (rabbit) (Cell Signalling Technology) were diluted in blocking buffer to obtain 1:1000 and 1:500 dilutions respectively. The blocking buffer was removed and 400 µL of diluted antibodies was added followed by incubation for 1 hour at room temperature on a shaker with protection from light. Diluted primary antibodies were then removed, and the cells were washed 3 times with PBS for 5 minutes each. Thereafter, the secondary antibodies anti-mouse AF488 (Invitrogen) and anti-rabbit AF467 (Invitrogen) were diluted in blocking buffer to obtain 1:2000 dilutions each. The PBS from the washes was removed and 400 µL of the diluted secondary antibodies was added followed by incubation for 1 hour at room temperature on a shaker with protection from light. The cells were then washed 3 times with PBS for 5 minutes each for the final time. Slides were then mounted in Fluoromount-G mounting medium (Invitrogen).

8.0.16 Imaging and image processing

Experiments performed by Martina Caddedu (MRC NATA)

Imaging was performed on a Zeiss LSM 900 confocal microscope equipped with a 63x objective (immersion oil) (Carl Zeiss). 2-D images and 3-D Z-stack images were acquired on ZEN blue (Zeiss) software 3.7 with the following parameters: bidirectional scanning, 4x averaging, 16 bits per pixel, 10-20 slices with a range of 10-20 µm and interval of 1 µm. Images were processed and analysed using Zeiss ZEN software (Carl Zeiss) and Fiji (NIH). For each treatment, three randomly selected fields of view were used to generate 2-D images and Z-stacks. For each Z-stack image, maximum intensity projections were generated, and the areas of AF488 within the nuclei and Hoechst 3342 signals were measured. Statistical analysis was performed using the GraphPad Prism 10.4.1 software. Data are presented as mean ± standard error of the mean (SEM). Differences between groups were analysed using One-Way Analysis of Variance (ANOVA) followed by Šídák's multiple comparisons test.

8.0.17 RNA-seq

RNA extraction and polyA+ selection

Performed as outlined above in section Section 8.0.12. RNA concentration was measured using the Nanodrop (ThermoFisher Scientific) and RNA quality was assessed using RNA Screen Tape (Agilent 2200 TapeStation system). PolyA+ RNA was

separated from polyA- RNA using the NEBNext Poly(A) mRNA magnetic isolation module (E7490, NEB). Briefly, 1 µg of total RNA was incubated with oligo dT beads in 1X RNA binding buffer at 65 °C for 5 minutes and then cooled to 4 °C. Material not attached to the beads containing the polyA- was discarded. The beads were washed twice in wash buffer and resuspended in 50 µL Tris-HCl, followed by incubation at 80 °C for 2 minutes to elute the RNA. 1X RNA binding buffer was added to the beads again, and the RNA was allowed to re-bind the beads in a 5-minute incubation at room temperature.

Library preparation and sequencing

Next generation sequencing libraries of the polyA+ fraction were generated using the NEBNext Ultra II Directional RNA library preparation kit (E7760, NEB). Library quality was assessed using the DNA 1000 High Sensitivity Screen Tape (Agilent 2200 TapeStation system) and quantified by High Sensitivity dsDNA Qubit (Thermofischer Q32851) followed by 150-base pair paired-end Illumina sequencing by Azenta.

Bioinformatics analyses

Sequencing data were processed by Catherine Chahrour with the Seqnado pipeline developed by Catherine Chahrour and Alastair Smith in the Milne lab: `https://github.com/alsmith151/SeqNado`. Quality checking of FastQ files was performed using FastQC (v0.12.1)[300]. The reads were trimmed using Trim Galore (v0.6.10)[301].

STAR (v2.7.10b) was then used to map the trimmed reads to the hg38 reference genome[302]. Quantification of gene expression was performed using featureCounts (v2.0.3)[303]. Differential gene analysis was performed using DESeq2 (v1.40.2)[304]. Batch effect correction was carried out using RUVSeq (v1.36.0)[305].

Chapter 3: Exploring RNase L recruitment via an Activator-ASO conjugate for knockdown of the MLL-AF4 fusion oncogene

General synthesis

As outlined in Section 8.0.1, all synthetic procedures were conducted using commercially sourced reagents without further purification, and solvents were employed as supplied or dried under nitrogen when necessary. Standard purification and analytical techniques, including column chromatography, TLC, NMR, MS, LC-MS, HPLC, and IR spectroscopy, were used as described previously.

8.0.18 Ethyl 4-oxo-2-(phenylamino)-4,5-dihydrothiophene-3-carboxylate

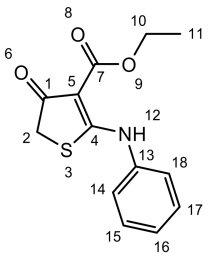

Following a literature procedure[195], to a solution of ethyl 4-chloroacetoacetate (2.9 mL, 21.4 mmol, 1 eq.) in dioxane (17.4 mL) was treated with sodium hydride (0.98 g, 0.097 mol of NaH, 60 % dispersion in oil) at 30°C. Once the evolution of hydrogen ceased, a solution of phenyl isothiocyanate (2.5 mL, 17.3 mmol, 97 mmol) in dioxane (25 ml) was added at 25-30°C. The temperature was allowed to reach 40°C, and after stirring for 1 hour, the thick slurry so formed was added to water and the solid formed was collected, washed with water and recrystallised using ethanol (13.3 g, 87%). Pale-yellow coloured solid, mp: 135–140 °C. ^{1}H NMR (400 MHz, $CDCl_3$) δ/ppm: 11.50 (s, 1H, N(12)H), 7.46 (t, J = 7.7 Hz, 2H, C(15)H + C(17)H), 7.40–7.31 (m, 3H, C(14)H, C(16)H, C(18)H), 4.38 (q, J = 7.1 Hz, 2H, C(10)H_2), 3.64 (s, 2H, C(5)H_2), 1.41 (t, J = 7.1 Hz, 3H, C(11)CH_3); ^{13}C NMR (101 MHz, $CDCl_3$) δ 191.15, 183.26, 166.68, 136.94, 129.71, 127.76, 124.06, 97.89, 60.54, 38.05, 14.48. IR (film $CDCl_3$/cm^{-1}) 3295, 1768, 1716, 1598, 1510, 1258, 1168, 2978, 760, 702. HR LC-MS (ESI+) found 264.1001 [M+H+]. Characterisation data obtained

was in agreement with the literature values.

8.0.19 2-(2-(2-hydroxyethoxy)ethoxy)ethyl-4-methyl-benzenesulphonate

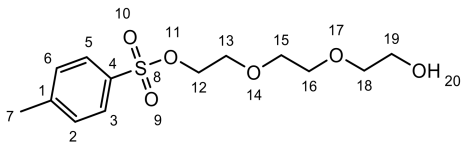

Following a literature procedure[306], to a solution of triethylene glycol (1 mL, 6.75 g, 44.9 mmol) in dichloro-methane, DCM (2 mL) was added tosyl chloride (0.2 g, 5.2 mmol, 1 eq.), and the reaction mixture was stirred at 0°C before triethyl amine, Et3N (0.3 mL, 10.4 mmol) was added dropwise. Solution was stirred overnight at room temperature and was extracted with aqueous sodium bicarbonate, $NaHCO_3$ aq. and DCM three times. The combined organic phase was dried over magnesium sulphate, $MgSO_4$ and concentrated to provide monotosylated-triethylene glycol (1.52 g, 95% yield). Colorless oil. ^{1}H NMR (600 MHz, $CDCl_3$) δ/ppm: 7.74–7.30 (dd, 4H, Ar–H, C(5)H, C(6)H, C(1)H, C(2)H), 4.09 (m, 2H, C(12)H_2), 3.64–3.50 (m, 10H, C(13)H_2, C(14)H_2, C(15)H_2, C(16)H_2, C(18)H_2), 2.38 (s, 3H, C(7)CH_3); ^{13}C NMR (101 MHz, $CDCl_3$) δ/ppm: 145.6, 137.0, 129.6, 127.7, 72.3, 70.9, 70.5, 70.2, 69.4, 62.0, 21.5. IR (film $CDCl_3$/cm^{-1}) 3350, 3030, 2955–2850, 1598, 1495, 1360, 1180, 1110–1065, 965–930, 820, 705. LR LC-MS (m/z): MS (ESI+) found 305.29. HR-LC MS (ESI, m/z): MS (ESI+) found 305.3012 [M+H+]. Characterisation

data obtained was in agreement with the literature values.

8.0.20 3-hydroxy-4-(2-(2-(2-hydroxyethoxy)ethoxy)ethoxy) benzaldehyde

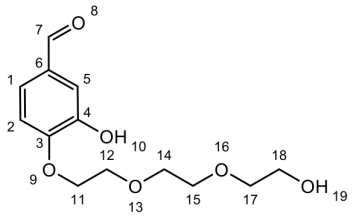

To a solution of NaH (0.84 mg, 60% oil dispersed, 21.0 mmol) in DMF (2 mL) was added a solution of 3,4-dihydroxybenzaldehyde (500 mg, 21.9 mmol) in DMF (2 mL) at 0 °C. After stirring for 30 minutes, TEG tosylate 2 (1.14g, 21.9 mmol) in DMF (2 mL) was added. The mixture was gradually warmed to room temperature, heated to 90°C and stirred overnight. The solvent was evaporated and residue so obtained was purified by silica gel column chromatography (Hexane:AcOEt=9:1-1:1) to yield product (250 mg, 54% based on recovery of the starting material). Tan-coloured solid. ^{1}H NMR (600 MHz, $CDCl_3$) δ/ppm: 9.86 (s, 1H, C(7)CHO), 7.46 (s, 1H, C(1)H), 7.37 (dd, J = 8.2, 2.0 Hz, 1H, C(5)H), 6.95 (dd, J = 12.3, 8.3 Hz, 1H, C(2)H), 4.29–4.21 (m, 2H, C(11)H_2), 3.91 (dt, J = 6.7, 2.8 Hz, 2H, C(12)HH_2), 3.81–3.70 (m, 10H, C(13)HH_2–C(18)HH_2), 3.70 (dt, J = 6.2, 2.0 Hz, 2H, C(19)H_2). ^{13}C NMR (101 MHz, $CDCl_3$) δ/ppm: 190.41, 151.63, 147.38, 146.85, 131.31, 123.85, 123.84, 72.33, 70.76, 70.41, 70.13, 69.34, 61.97. IR (film $CDCl_3$/cm^{-1}) 3508, 2894,

1682, 1285, 1129, 808. LR LC-MS (m/z): MS (ESI+) found 271.80 [M+H+]. HR LC-MS (ESI+) found 271.8010 [M+H+].

8.0.21 ethyl-5-(3-hydroxy-4-(2-(2-(2-hydroxyethoxy)ethoxy)ethoxy)benzylidene)-4-oxo-2-(phenylamino)-4,5-dihydrothiophene-3-carboxylate

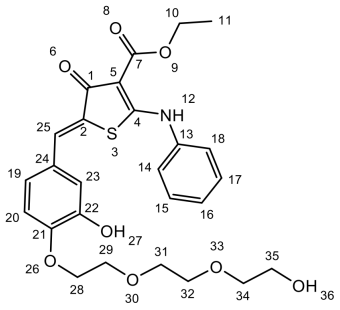

A solution of thiophene **4.1.1** (47.6 mg, 0.55 mmol), aldehyde **4.1.3** (150 mg, 0.55 mmol), and piperidine (169.5 uL, 0.55 mmol) in EtOH (1 mL) was heated at 80 °C by microwave for 4 hours. The solvent was evaporated and the product was purified by silica gel column chromatography (AcOEt only) to give product (208 mg, 72.6%). Yellow solid. ^{1}H NMR (600 MHz, $CDCl_3$) δ/ppm: 11.48 (s, 1H, N(12)H), 7.72 (s, 1H, C(5)H), 7.50–7.45 (m, 2H, C(14)H + C(18)H), 7.40–7.33 (m, 3H, C(15)H–C(17)H), 7.11 (d, J = 2.2 Hz, 1H, C(25)H), 6.99 (dd, J = 8.4, 2.2 Hz, 1H, C(20)H), 6.84 (d, J = 8.4 Hz, 1H, C(19)H), 4.40 (q, J = 7.1 Hz, 2H, C(10)H_2), 4.20–4.15 (m, 2H, C(28)H_2), 4.11 (q, J = 7.2 Hz, 1H, C(4)H), 3.88–3.82

(m, 2H, C(30)H_2), 3.78–3.66 (m, 8H, C(31)H_2, C(32)H_2, C(33)H_2, C(34)H_2), 2.03 (s, 2H, O–H (C(27)OH + C(36)OH)), 1.45–1.40 (m, 3H, C(11)CH_3). ^{13}C NMR (101 MHz, $CDCl_3$) δ/ppm: 182.25, 167.02, 166.99, 147.74, 147.41, 137.20, 137.16, 131.57, 130.08, 129.89, 124.07, 123.99, 123.56, 123.54, 117.07, 114.25, 113.30, 72.49, 70.79, 70.37, 70.15, 69.28, 61.99, 60.56, 14.20. IR (film $CDCl_3$/cm^{-1}) 2926, 1648, 1556, 1278, 1050. LR LC-MS (m/z): MS (ESI+) found 515.09 [M+]. HR-LC MS (ESI, m/z): MS (ESI+) found 515.1001 [M+].

8.0.22 ethyl-5-(3-hydroxy-4-(2-(2-(2-(((perfluorophenoxy) carbonyl)oxy)ethoxy)ethoxy)ethoxy)benzylidene)-4-oxo-2-(phenylamino)-4,5-dihydrothiophene-3-carboxylate

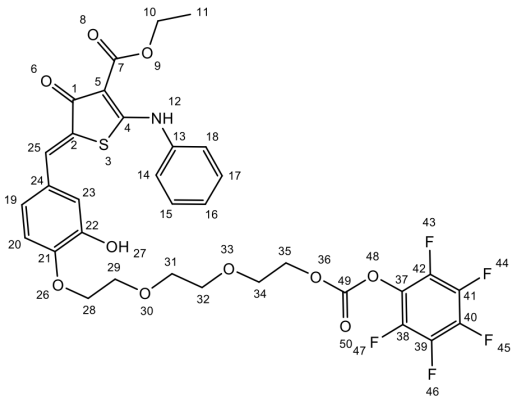

To a solution of thiophenaniline (20.0 mg, 0.38 mmol, 1 eq.) in dry DMF (0.5 mL) was added Bis(pentafluoro- phenyl)carbonate (35.2 mg, 0.76 mmol, 2 eq.)

and triethyl amine, NEt3 (39.0 µL, 0.278 mmol) and left stirring for 4h at room temperature. The solvent was evaporated and residue so obtained was purified by silica gel column chromatography (Hexane:AcOEt=1:2-0:1) to yield compound (19.9 mg, 0.28 mmol, 70%). Bright yellow oil. ^{1}H NMR (600 MHz, $CDCl_3$) δ/ppm: 11.52 (s, 1H, N(12)H), 7.87–7.77 (m, 5H, C(14–18)H, anilide ring), 7.73 (s, 1H, C(5)H), 7.57–7.37 (m, 2H, salicyl Ar–H), 7.08 (dd, J = 8.7, 5.2 Hz, 1H, salicyl Ar–H), 4.48–4.37 (m, 3H, C(10)H_2 + C(4)H), 4.35–4.22 (m, 2H, C(28)H_2), 3.90 (dt, J = 14.3, 4.9 Hz, 2H, C(30)H_2), 3.83–3.66 (m, 6H, C(31)H_2–C(35)H_2), 1.45 (t, 7 Hz, 3H, C(11)CH_3). ^{13}C NMR (101 MHz, $CDCl_3$) δ/ppm: 181.86, 175.98, 166.92, 152.27, 151.33, 149.88, 143.18 – 136.05, 132.45 – 128.78, 128.64 – 126.50, 124.5 – 123.27, 119.54, 118.90, 114.15, 97.87, 71.01, 70.77, 69.96 – 68.42, 68.80, 68.53, 60.70, 14.11. Pentafluorophenyl-carbons were not observed due to $^{13}C^{19}F$ coupling. ^{19}F NMR (471 MHz, $CDCl_3$) δ/ppm: -152.28 – -153.61 (m, 2F), -156.01 – -157.87 (m, 1F), -160.83 – -162.36 (m, 2F). IR (film $CDCl_3$/cm^{-1}) 2361, 1788, 1526, 1233, 1037, 724. HR-LC MS (ESI, m/z): MS (ESI+) found 748.1201 [M+Na+].

8.0.23 Nucleic acid sequences

All amine PS-modified oligonucleotides were purchased from IDT, HPLC-purified in lyophilised form and dissolved in 10 mM potassium phosphate buffer, pH 8. All unmodified oligonucleotides, such as qPCR primers, were purchased from IDT as desalted and lyophilised products — resuspended in 10 mM Tris pH 8.

Table 8.8: Sequence of amine-modified antisense oligonucleotides (ASOs) used for the synthesis of RNase L-ASO conjugates. * denotes phosphorothioate linkages.

Index	**Name**	**Sequence (5′–3′)**
1	siRNA ASO	T*G*G*A*G*T*A*G*G*T*T*C*T*G*C*T*T*T*T*C*T*T*

8.0.24 RNase L-ligand ASO conjugate synthesis, purification and characterisation

RNase L-ligand PFP-ester functionalisation

To a 0.5 mL Eppendorf DNA LoBind tube was added 1 µL of the PS-modified amine-DNA (100 µM stock concentration), 1 µL of NaHCO3 pH 8.5 (1 M), 2 µL of H_2O, 5 µL of a 50 mM solution of RNase L-ligand PFP-ester in dry DMF. The reaction was vortexed, spun down in a tabletop centrifuge and placed in a Thermomixer (Eppendorf) overnight, shaking at 800 rpm at 37 °C.

The excess hydrolysed small molecule was removed using Amicon 3K 0.5 mL spin columns, according to the manufacturer's instructions. Briefly, the reaction was made up to a volume of 500 µL with H_2O and spun at 14,700g for 10 minutes. The eluent was removed and the above process was repeated for a total of three times. The column was then inverted, inserted into a fresh collection tube and spun at 14,700g for 1 minute.

HPLC purification method for RNase L ligand PFP-ester modification

The eluent obtained was then purified by HPLC on an Agilent Polaris C18 column (150 x 4.6 mm), column heated to 50 °C using a gradient of 3-30% CH_3CN (indicated in Appendix Figures) over 20 minutes, flow rate of 1.5 mL/minute, with 10 mM triethylammonium bicarbonate (TEAB) pH 8.5 as an ion-pairing buffer throughout.

Oligonucleotide MS characterisation

Oligonucleotide Mass Spectra were recorded on a Waters Xevo G2 QTOF ESI-UPLC-MS system. A gradient of MeOH in Et3N and hexafluoroisopropanol (HFIP) was used (buffer A, 8.6 mM Et3N, 200 mM HFIP in 5% MeOH/H_2O (v/v); buffer B, 20% buffer A in MeOH). Data was then deconvoluted using MassLynx software v4.1 and recorded in Table 8.9.

Table 8.9: Expected and observed mass of the RNase L ligand-siRNA ASO conjugate, as determined by mass spectrometry following deconvolution.

S.No.	Name	Expected Mass	Mass after Deconvolution
1	RNase L ligand-siRNA ASO	7465.0	7465.5

8.0.25 PCR and Molecular cloning

Homologous recombination was used to create the MLL, AF4 and SEM MLL-AF4 plasmids with the truncated sequences – to serve as templates for in vitro transcription. The DHFR control plasmid obtained as a positive control for NEB PUR-

Express IVTT kit was used as the PCR template for the backbone of all plasmids. Inserts for the MLL and AF4 plasmid were PCR amplified from the hMLL-AF4 plasmid previously prepared by the Milne group. SEM insert was ordered as a 1498 kb gene from GeneArt Thermofischer services (full sequences in table z).

Separate PCR reactions were carried out to amplify the backbone and insert. The reactions were performed in 0.2 mL PCR tubes and contained the plasmid template (1 ng, 1 µL of 1 ng/µL), the forward and reverse primers (1.25 µL, 10 µM, sequences in Table 8.10), Phusion High-Fidelity PCR Master Mix with GC Buffer (12.5 µL, 2X), 0.5 uL, 0.75 uL DMSO and made up to 25 µL with MilliQ water. The same PCR protocol was followed for preparing linear templates for IVT. PCR reactions were carried out on a Peqlab peqSTAR 96X Universal thermal cycler using the following conditions: initial denaturation at 98 °C for 30 seconds; 35 cycles [denaturation at 98 °C for 10 seconds, annealing at different temperature (listed in Table 8.11)for 30 seconds, and extension at 72 °C for either 1.5 minutes. A final extension at 72 °C for 10 minutes was performed. The reactions were purified with a Genejet PCR column according to the manufacturer's protocol. Reactions were analysed with gel electrophoresis to confirm product bands.

Table 8.10: Primer sequences used for homologous recombination (HR)-based cloning of the MLL-AF4 plasmid. FWD and REV denote forward and reverse primers respectively.

Index	**Primer Name**	**Sequence (5′–3′)**
1	MLL HR FWD	CCGCGAAATTAATACGACTCACTATAGGGAAATAAAA GGCCAAAGCTCAGCTC
2	MLL HR REV	GTTATTGCTCAGCGGTGGCAGCAGCCAACCTTAAAG GCTGCTGATCATCCTG
3	AF4 HR FWD	CCGCGAAATTAATACGACTCACTATAGGGAAATAAA CTGCTTCGAATTAGAGAGAAGGAAAG
4	AF4 HR REV	TATTGCTCAGCGGTGGCAGCAGCCAACCTCTGCTGG CTTGGGTTCGTTGCTTGCTGC
5	SEM HR FWD	CCGCGAAATTAATACGACTCACTATAGGGAAATAGCT GCCAGGTGCCTGAGG
6	SEM HR REV	GCTCAGCGGTGGCAGCAGCCAACACTCACTGTGCCT GCTGCCTTCACTC
7	Backbone FWD	AGTTGGCTGCTGCCACCCGTGAGC
8	Backbone REV	CTATAGTGAGTCGTATTAATTTTCGC

Table 8.11: Annealing temperatures used for amplification of homologous recombination (HR) fragments during MLL-AF4 plasmid construction.

PCR product	**Annealing temperature for PCR (°C)**
MLL HR	60
AF4 HR	62
SEM HR	65
Backbone HR	47

A 4:1 insert : backbone ratio was used for homologous recombination and calculated according to NEBioCalculator. The backbone (100 ng) and insert were mixed in a 1.5 mL Eppendorf tube. XL-10 Gold competent E. coli cells (25 µL) were added to the reaction. The tube was kept on ice for 30 minutes and heat-shocked at 42°C for 30 seconds. SOC Outgrowth Medium (500 µL) was added and the tube was incubated at 37 °C with shaking at 225 rpm for 30 minutes. The tube was kept on ice for 2 minutes and 200 µL of the transformed bacteria were plated on LB agar plates containing ampicillin (100 µg/mL) at 37 °C for 14-16 hours. Colonies were then picked and grown in 50-mL Falcon tubes containing 5 mL LB media with ampicillin (100 µg/mL) at 37 °C and shaking at 225 rpm for 14-16 hours. 300 µL of the overnight cultures were combined with glycerol (300 µL, 50% v/v, filtered). The glycerol stocks were kept at -80 °C. The rest of the cultures were miniprepped using Qiagen's miniprep kit according to the manufacturer's protocol and eluted in their Elution Buffer (50 µL) and stored at -20 °C. Whole-plasmid nanopore sequencing was performed by Plasmidsaurus to confirm identity. The plasmids were resuspended in 10 mM Tris, pH 8.0 and stored at -20 °C.

8.0.26 In vitro transcription

In vitro transcription was performed with 10 ng/µL of linear template DNA (linear DNA prepared for homologous recombination to prepare plasmids, as mentioned above) using the HiScribe RNA Synthesis kit (NEB) in a total reaction volume of 10 µL. Samples were incubated at 37 °C for 4 hours prior to addition of DNAse I (1

µL) and further incubation for 30 minutes. The mRNA was then purified using the GeneJet RNA Cleanup following the manufacturer's protocol and eluted in H_2O.

8.0.27 RNase H assay

1 pmol of mRNA (prepared as above with *in vitro* transcription), 0.6 U/µL RNase H (recombinant E. Coli, Takara), and a concentration of 0.25 pmol of the ASO (sequences in Table 8.12) in a buffer system containing 30 mM HEPES pH 7, 100 mM KCl, 20 mM MgCl2 and 2 mM DTT in a total of 10 µL were incubated for 1 hour at 37 °C. RNA loading dye (NEB, B0363S) was then added, samples heated to 70 °C for 10 minutes and then analysed by agarose gel electrophoresis.

Table 8.12: Antisense oligonucleotide sequences designed for screening against the SEM breakpoint. * denotes phosphorothioate linkages.

Index	**Name**	**Sequence (5′–3′)**
1	ASO 20mer	T*A*G*G*T*C*T*G*C*T*T*T*T*C*T*T*T*T*G*G*
2	ASO 18mer	A*G*G*T*C*T*G*C*T*T*T*T*C*T*T*T*T*G*
3	ASO 16mer	G*G*T*C*T*G*C*T*T*T*T*C*T*T*T*T*

8.0.28 Cell culture

Cell culture and cell lines SEM (an MLL-AF4 B-ALL cell line) cells were cultured in IMDM with 10% FCS (Gibco) and Glutamax (ThermoFisher Scientific). HEK293T

cells were cultures in DMEM with 10% FCS and Glutamax. All cells were grown in 5% CO2 incubator at 37 °C.

8.0.29 Electroporation

SEM cells were resuspended at a density of 10^8 per mL and siRNA/ASO (sequences in Table 8.13) was added to a concentration of 250 nM. Cells were subjected to a 10 ms 330V electroporation using a rectangle pulse EPI 2500 electroporator (Fischer, Heidelberg), after which they were diluted to 10^6 per mL. Cells were harvested after 48 hours for an RT-qPCR readout.

Table 8.13: Sequences of siRNA and antisense oligonucleotides used for electroporation in SEM cells. * denotes phosphorothioate linkages. __ indicates 2′-O-Methoxy-ethyl modifications. + denotes 2′–4′ methylene bridges.

Index	**Name**	**Sequence (5′–3′)**
1	siMARS siRNA	sense: AAGAAAAGCAGACCUACUCCA antisense: UGGAGUAGGUCUGCUUUUCUUUU
2	siRNA ASO	T*G*G*A*G*T*A*G*G*T*C*T*T*G*C*T*T*T*C* T*T*
3	ASO 16mer	G*G*T*C*T*G*C*T*T*T*T*C*T*T*T*T*
4	LNA gapmer	+G*+G*+T*C*T*G*C*T*T*T*T*C*T*+T* +T*+T*
5	ASO 18mer	A*G*G*T*C*T*G*C*T*T*T*T*C*T*T*T*T*G*
6	ASO 20mer	T*A*G*G*T*C*T*G*C*T*T*T*T*C*T*T*T*T* G*G*
7	MOE gapmer	T*A*G*G*T*C*T*G*C*C*T*T*T*T*T*C*T*T*T*T*G*G*

8.0.30 RT-qPCR

RNA extraction, cDNA synthesis, and RT-qPCR were performed as previously described (see Section 8.0.12, 8.0.12). For this section, a different set of qPCR primers was used for quantifying knockdown of target genes, *MLL-AF4*, *MLL*, and *AF4*. The primer sequences are listed in Table 8.14.

Table 8.14: Primer sequences used for quantitative PCR analysis. FWD and REV refer to forward and reverse primer sequences respectively.

S. No.	**Name**	**Sequence (5′–3′)**
1	GAPDH FWD	TTGGCTACAGCAACAGGGTG
2	GAPDH REV	GGGGAGATTCAGTGTGGTGG
3	MLL FWD	ACAGAAAAAAGTGGCTCCCCG
4	MLL REV	GCAAACCACCCTGGGTGTTA
5	AF4 FWD	CAGAAGCCCACGGCTTATGT
6	AF4 REV	TATTGCTGTCAAAGGAGGCGG
7	MLL-AF4 FWD	ACAGAAAAAAGTGGCTCCCCG
8	MLL-AF4 REV	TATTGCTGTCAAAGGAGGCGG

Chapter 4: Designing small-molecule ASO conjugates to harness the lysosome for targeted mRNA degradation

8.0.31 Antisense oligonucleotide sequences

All unmodified oligonucleotides were purchased from IDT as desalted and lyophilised products – resuspended in 10 mM Tris pH 8. Amine-containing oligonucleotides were purchased from IDT, HPLC-purified in lyophilised form and dissolved in 10 mM potassium phosphate buffer, pH 8.

Table 8.15: Antisense oligonucleotide sequences used for all transfection and gymnosis experiments, with 5′-terminal amine modification functionalisation chemistry. * denotes phosphorothioate linkages; __ indicates 2′-O-Methoxy-ethyl sugars; *m* denotes 2′-O-Methyl sugars.

No.	**Name**	**Sequence (5′–3′)**
1	NCL1 2′-OMe ASO	mG*mU*mC*mA*mU*mC*mG*mU*mC*mA*mU*mC*mC*mU*mC*mA*mU*mC*mA*mU
2	NCL1 gapmer	G*T*C*A*T*C*G*T*C*A*T*C*C*T*C*A*T*C*A*T
3	MEN1 2′-OMe ASO	mA*mG*mC*mA*mG*mC*mC*mA*mG*mC*mA*mG*mA*mU*mG
4	MEN1 gapmer	A*G*C*A*G*C*A*G*C*A*G*C*U*U*C*U*G
5	NTC-ASO	T*A*G*T*G*C*G*G*A*C*C*T*A*C*C*C*A*C*G*A

8.0.32 Ispinesib-ASO conjugates synthesis, purification and characterisation

Dibenzylcyclooctyne (DBCO)-NHS ester functionalisation

To a 0.5 mL Eppendorf DNA LoBind tube was added 1 µL of the amine-modified ASO (100 µM stock concentration), 1 µL of NaHCO3 pH 8.5 (1 M), 2 µL of H_2O, 5 µL of a 50 mM solution of DBCO NHS in dry DMF. The reaction was vortexed, spun down in a tabletop centrifuge and placed in a Thermomixer (Eppendorf) overnight, shaking at 800 rpm at 37 °C.

The excess hydrolysed small molecule was removed using Amicon 3K 0.5 mL spin columns, as per the manufacturer's instructions. Briefly, the reaction was made up to a volume of 500 µL with H_2O and spun at 14,700g for 10 minutes. The eluent was removed, and the above process was repeated for a total of three times. The column was then inverted, inserted into a fresh collection tube and spun at 14,700g for 1 minute.

HPLC purification method for DBCO modification

The eluent obtained was then purified by HPLC on an Agilent Polaris C18 column (150 x 4.6 mm), column heated to 50 °C using a gradient of 3-30% CH_3CN (indicated in Appendix Figures) over 20 minutes, flow rate of 1.5 mL/minute, with 10 mM triethylammonium bicarbonate (TEAB) pH 8.5 as an ion-pairing buffer throughout.

Ispinesib-functionalisation with strain-promoted azide-alkyne click chemistry

To a 0.5 mL Eppendorf DNA LoBind tube was added, listed in order of addition, 1 µL of the DBCO-modified DNA (1 mM stock concentration), 1.5 µL of 1 mM ispinesib-azide (commercially obtained from MedChemExpress), 1.5 µL of 1X PBS pH 7.4 and finally, 6 µL of DMF. The reaction was vortexed, spun down in a tabletop centrifuge and placed in a Thermomixer (Eppendorf) overnight, shaking at 800 rpm at room temperature.

The crude reaction mixture was then made up to 500 µL with H_2O and first run through a Amicon 3K 0.5 mL column/tube as described above to remove the unreacted small molecule.

HPLC purification for ispinesib modification

The final eluent collected after inversion was then purified by HPLC on an Agilent Polaris C18 column (150 x 4.6 mm), column heated to 50 °C using a gradient of 3-50% CH_3CN (indicated in Appendix Figures) over 20 minutes, flow rate of 1.5 mL/minute, with 10 mM triethylammonium bicarbonate (TEAB) pH 8.5 as an ion-pairing buffer throughout.

Oligonucleotide MS characterisation

Oligonucleotide Mass Spectra were recorded on a Waters Xevo G2 QTOF ESI-UPLC-MS system. A gradient of MeOH in Et3N and hexafluoroisopropanol (HFIP) was used (buffer A, 8.6 mM Et3N, 200 mM HFIP in 5% MeOH/H_2O (v/v); buffer B, 20% buffer A in MeOH). Data was then deconvoluted using MassLynx software v4.1 and recorded in Table 8.16.

Table 8.16: Expected and observed mass of DBCO- and/or ispinesib-functionalised ASO conjugates, as determined by mass spectrometry following deconvolution.

No.	Name	Expected Mass	Mass after Deconvolution
1	DBCO-NCL1 2′-OMe ASO	7442.0	**7442.7**
2	NCL1 2′-OMe LyTON	8131.0	**8131.5**
3	Ispinesib-NTC-ASO	7240.0	**7239.0**
4	DBCO-NCL1 gapmer	7542.0	**7541.7**
5	NCL1 gapmer LyTON	8231.0	**8231.7**
6	DBCO-MEN1 2′-OMe ASO	7308.0	**7308.6**
7	MEN1 2′-OMe LyTON	7997.0	**7994.6**

8.0.33 Cell culture

HEK293T, A549, and HeLa cells were cultured in Dulbecco's Modified Eagle Medium with 1X GlutaMAX (Gibco) supplemented with 10% (v/v) FBS (Gibco) and) at 37 °C in a humidified incubator with 5% CO2.

8.0.34 Nucleic acid delivery: Lipid-based transfection and gymnosis

Transfection

For **transfection** with lipofectamine 2000, HEK293T / A549 / HeLa cells were seeded at 2.5×10^5 / 2.2×10^5 / 2.0×10^5 cells in 1 mL of culture media in 24-well plates 16 hours before transfection to reach 70-80% cell confluency. Prior to transfection, the culture media was replaced with 1 mL OptiMEM.

2 µL of Lipofectamine 2000 (Invitrogen) was added to 48 µL OptiMEM (Gibco) and incubated at room temperature for 5 minutes before mixing with 0.5 nmol of oligonucleotide dissolved in 50 µL of OptiMEM. The resulting mixture was incubated at room temperature for 20 minutes allowing complexation to occur. The complexes were then added to the cells at the required concentrations (with total volume of 1 mL per well). The cells were then incubated at 37 °C in a 5% CO2 incubator. After 6 hours the media was replaced with 1 mL of culture media and the cells were returned to the incubator for another 18 hours.

Gymnosis

For **gymnosis**, HEK293T / A549 / HeLa cells were seeded at a density of 5.0×10^4 / 4.7×10^4 / 4.5×10^4 cells/well in 1 mL of culture media in 24-well plates for 16 hours before gymnosis to reach 70-80% cell confluency. Prior to gymnosis, the

culture media was replaced with OptiMEM and the ASO was added at the desired concentration. After 6 hours, OptiMEM was replaced with 1 mL of complete culture media and the cells were returned to the incubator for a further 90 hours (total time of 96 hours).

8.0.35 CellTiter-Glo

Transfection experiments were carried out as outlined above. Cells were subjected to the CellTiter-Glo assay at the indicated time points following the manufacturer's guidelines. Briefly, 100 µL CellTiter-Glo Reagent was added to 100 µL of media containing cells in a white (Thermofischer Nunc MicroWell polystyrene, 236105) 96-well plate. Subsequently, the contents of the wells were mixed on an orbital shaker for 2 minutes to induce cell lysis. The plate was then incubated at room temperature for 10 minutes to stabilize the luminescent signal. The luminescence was measured using a CLARIOstar microplate reader (BMG Labtech). The luminescence values were normalised to the values for untreated cells.

8.0.36 Lysosome inhibition assays

Bafilomycin inhibition

Cell were plated at the above mentioned densities and transfection/gymnosis was carried out as above. Bafilomycin was added at 10 nM at the start of the transfection. When the OptiMEM was replaced with complete media, the 10 nM Bafilomycin

treatment was repeated. Cells were then harvested at 24 hours, and subjected to RNA extraction/western blotting for RNA/protein read-out.

Chloroquine inhibition

Cells were seeded at the above mentioned densities and transfection/gymnosis was performed as above. When the OptiMEM was replaced with complete media at 6 hours, cells were treated with 30 µM Chloroquine. Cells were then harvested at 24 hours (with 18 hours of chloroquine treatment), and subjected to RNA extraction for RNA read-out.

8.0.37 RT-qPCR

RNA extraction, cDNA synthesis, and RT-qPCR were performed as previously described (see Section 8.0.12, 8.0.12). For this section, a different set of qPCR primers was used for quantifying knockdown of target genes relevant to establishing the efficacy and selectivity of lysosomal trafficking ASOs. The primer sequences are listed in Table 8.14.

Table 8.17: Primer sequences used for quantitative PCR analysis. FWD and REV refer to forward and reverse primer sequences respectively.

S. No.	**Name**	**Sequence (5′–3′)**
1	GAPDH FWD	TTGGCTACAGCAACAGGGTG
2	GAPDH REV	GGGGAGATTCAGTGTGGTGG
3	NCL1 FWD	GCCTGTCAAAGAAGGCACCTGG
4	NCL1 REV	GAAAGCCGTAGTCGGTTCTGTG
5	MEN1 FWD	ATCGGGCCCATCCAGTCCC
6	MEN1 REV	GCCCCAACCACAGCAAAGGC
7	YWHAZ FWD	ACTTTTGGTACATTGTGGCTTCAA
8	YWHAZ REV	CCGCCAGGACAAACCAGTAT
9	UBC FWD	ATTTGGGTCGCAGTTCTTG
10	UBC REV	TGCCTTGACATTCTCGATGGT

8.0.38 Western blotting

Salt-soluble proteins were extracted from 1×10^6 cells by incubating cells in a high-salt lysis buffer (20 mM Tris-HCl pH 8.0, 300 mM KCl, 5 mM EDTA, 20% glycerol, 0.5% IGEPAL CA-630, protease inhibitor cocktail). Protein extracts were then run on a NuPAGE 4-12% BisTris gels (Life Technologies) for Menin and NuPAGE 12% BisTris gels for LC3 at 180V for 1 hour and blotted onto a polyvinylidene fluoride membrane (Immobilon) at 100V for 1 hour using a Tris-glycine blotting buffer[299]. The blots were then probed with 1:10,000 dilution of primary antibody for Menin

(Bethyl #A300-105A) and GAPDH (Bethyl, A300-641A) while LC3-I and LC3-II were probed with 1:10,000 dilution of primary antibody for LC3 (Sigma Aldrich, L8918) in 5% milk/TBS-tween at 4°C overnight. Menin / LC3 / GAPDH blots were then probed with secondary antibody (ab216773, IRDye 800CW) for 2 hours at room temperature, followed by imaging on the ChemiDoc MP system.

Chapter 6: Tunable control over PROTAC Activity via DNA Hybridization and Strand Displacement

8.0.39 General synthesis

As outlined in Section 8.0.1, all synthetic procedures were conducted using commercially sourced reagents without further purification, and solvents were employed as supplied or dried under nitrogen when necessary. Standard purification and analytical techniques, including column chromatography, TLC, NMR, MS, LC-MS, HPLC, and IR spectroscopy, were used as described previously. (+)-JQ1 alkyne for oligonucleotide modification was synthesised as outlined previously in Section 8.0.2, 8.0.3.

8.0.40 Oligonucleotide sequences used

All unmodified Oligonucleotides were purchased from IDT as desalted and lyophilised products — resuspended in 10 mM Tris pH 8. Amine-containing PS-oligonucleotides were purchased from IDT, HPLC-purified in lyophilised form and dissolved in 10 mM potassium phosphate buffer, pH 8.

Table 8.18: Sequences for OligoPROTAC ssDNA strands used in all transfection experiments. Toehold sequences are highlighted in violet, anti-toehold and scrambled anti-toehold complements in orange. * denotes phosphorothioate linkages; \Azide\ indicates an azide modification; \Alkyne\ indicates an alkyne modification.

S.No.	**Name**	**Sequence (5′– 3′)**
1	(+)-JQ1 ssDNA OligoPROTAC, [n=0]	T*C*G*T*G*G*G*T*A*G*G*T*C*C*G*C*A*C*T*A\Azide\
2	VH032 ssDNA OligoPROTAC, [n=0]	\Alkyne\T*A*G*T*G*C*G*G*A*C*C*T*A*C*C*C*A*C*G*A
3	(+)-JQ1 ssDNA OligoPROTAC, [n=1]	T*C*G*T*G*G*G*T*A*G*G*T*C*C*G*C*A*C*T*A*T\Azide\
4	VH032 ssDNA OligoPROTAC, [n=1]	\Alkyne\T*T*A*G*T*G*C*G*G*A*C*C*T*A*C*C*C*A*C*G*A
5	(+)-JQ1 ssDNA OligoPROTAC, [n=2]	T*C*G*T*G*G*G*T*A*G*G*T*C*C*G*C*A*C*T*A*T*T\Azide\
6	VH032 ssDNA OligoPROTAC, [n=2]	\Alkyne\T*T*T*A*G*T*G*C*G*G*A*C*C*T*A*C*C*C*A*C*G*A
7	(+)-JQ1 ssDNA OligoPROTAC, [n=3]	T*C*G*T*G*G*G*T*A*G*G*T*C*C*G*C*A*C*T*A*T*T*T\Azide\
8	VH032 ssDNA OligoPROTAC, [n=3]	\Alkyne\T*T*T*T*A*G*T*G*C*G*G*A*C*C*T*A*C*C*C*C*A*C*G*A

S.No.	Name	Sequence (5′ – 3′)
9	(+)-JQ1 ssDNA OligoPROTAC, [n=5]	T*C*G*T*G*G*G*T*A*G*G*T*C*C*G*C*A*C*T*A*T*T*T*T*T\Azide\
10	VH032 ssDNA OligoPROTAC, [n=5]	\Alkyne\T*T*T*T*T*T*A*G*T*G*C*G*G*A*C*C*T*A*C*C*C*A*C*G*A
11	(+)-JQ1 ssDNA OligoPROTAC, [n=10]	T*C*G*T*G*G*G*T*A*G*G*T*C*C*G*C*A*C*T*A*T*T*T*T*T*T*T*T*T*T \Azide\
12	VH032 ssDNA OligoPROTAC, [n=10]	\Alkyne\T*T*T*T*T*T*T*T*T*T*T*T*T*A*G*T*G*C*G*G*A*C*C*T*A*C*C*C*A*C*G*A
13	(8-base pair) Toehold-(+)-JQ1 ssDNA, [n=3]	T*C*A*A*C*A*T*C*T*C*G*T*G*G*G*T*A*G*G*T*C*C *G*C*A*C*T*A*T*T*T\Azide\
14	(8-base pair) Anti-toehold complement	A*A*A*T*A*G*T*G*C*G*G*A*C*C*T*A*C*C*C*A*C*G*A*G*A*T*G*T*T*G*A*
15	(8-base pair) Scrambled anti-toehold complement	A*A*C*A*A*T*C*A*C*T*T*C*T*T*A*A*C*A*A*T*T*C*C*T*T*T*T*C*C*
16	(7-base pair) Toehold ssDNA, [n=3]	T*C*A*A*C*A*T*T*C*G*T*G*G*G*T*A*G*G*T*C*C*G*C*A*C*T*A*T*T*T
17	(9-base pair) Toehold ssDNA, [n=3]	T*C*A*A*C*A*T*C*A*T*C*G*T*G*G*G*T*A*G*G*T*C*C*G*C*A*C*T*A*T*T*T
18	(10-base pair) Toehold ssDNA, [n=3]	T*C*A*A*C*A*T*C*A*G*T*C*G*T*G*G*G*T*A*G*G*T*C*C*G*C*A*C*T*A*T*T*T
19	(7-base pair) Anti-toehold complement	A*A*A*T*A*G*T*G*C*G*G*A*C*C*T*A*C*C*C*A*C*G*A*A*T*G*T*T*G*A*
20	(9-base pair) Anti-toehold complement	A*A*A*T*A*G*T*G*C*G*G*A*C*C*T*A*C*C*C*A*C*G*A*T*G*A*T*G*T*T*G*A
21	(10-base pair) Anti-toehold complement	A*A*A*T*A*G*T*G*C*G*G*A*C*C*T*A*C*C*C*A*C*G*A*C*T*G*A*T*G*T*T*G*A

8.0.41 (+)-JQ1- and VH032-oligonucleotide conjugates synthesis, purification and characterisation

(+)-JQ1-functionalisation with copper click chemistry

To a 0.5 mL Eppendorf DNA LoBind tube was added, listed in order of addition, 1 µL of the PS-modified DNA (1 mM stock concentration), 1.5 µL of 1 mM (+)-JQ1-alkyne (stock in DMF), 1 µL of 200 mM DIPEA, 5.5 µL of H_2O, 1 µL of 200 mM sodium ascorbate and finally, 1 µL of 200 mM $CuBrMe_2S$ (stock in DMSO). The reaction was vortexed, spun down in a tabletop centrifuge and placed in a Thermomixer (Eppendorf) overnight, shaking at 800 rpm at room temperature. An alternate protocol, listed in order of addition, used 1 µL of the PS-modified DNA (1 mM stock concentration), 1.5 µL of 1 mM (+)-JQ1-alkyne (stock in DMF), 0.4 µL of 100 mM sodium ascorbate, 1.6 µL of H_2O, and finally, 0.5 µL of 100 mM copper (I) sulphate pre-complexed with 100 mM Tris(3-hydroxypropyltriazolylmethyl)amine (1:1, final concentration of both at 50 mM), shaking at 800 rpm overnight at room temperature.

The reaction was quenched with 250 µL of 0.5 M EDTA pH 8, made up to 500 µL with H_2O and first run through a Amicon 3K 0.5 mL column/tube as described above to chelate excess copper and remove it along with the unreacted small molecule. The final eluent collected after inversion.

HPLC purification method for (+)-JQ1 modification

The final eluent collected was then purified by HPLC on an Agilent Polaris C18 column (150 x 4.6 mm), column heated to 50°C using a gradient of 3-30% CH_3CN (indicated in Appendix Figures) over 20 minutes, flow rate of 1.5 mL/min, with 10 mM triethylammonium bicarbonate (TEAB) pH 8.5 as an ion-pairing buffer throughout.

VH032-functionalisation with copper click chemistry

To a 0.5 mL Eppendorf DNA LoBind tube was added, listed in order of addition, 1 µL of the DNA (1 mM stock concentration), 1.5 µL of 1 mM VH032 azide (stock in DMF), 1 uL of 200 mM DIPEA, 4.5 µL of H_2O, 1 µL of 200 mM sodium ascorbate and finally, 1 µL of 200 mM $CuBrMe_2S$ (stock in DMSO). The reaction was vortexed, spun down in a tabletop centrifuge and placed in a Thermomixer (Eppendorf) overnight, shaking at 800 rpm at room temperature. An alternate protocol, listed in order of addition, used 1 µL of the PS-modified DNA (1 mM stock concentration), 1.5 µL of 1 mM VH032 azide (stock in DMF), 0.4 µL of 100 mM sodium ascorbate, 1.6 µL of H_2O, and finally, 0.5 µL of 100 mM copper (I) sulphate pre-complexed with 100 mM Tris(3-hydroxypropyltriazolylmethyl)amine (1:1, final concentration of both at 50 mM), shaking at 800 rpm overnight at room temperature.

The reaction was quenched with 250 µL of 0.5 M EDTA pH 8, made up to 500 µL with H_2O and first run through a Amicon 3K 0.5 mL column/tube as de-

scribed above to chelate excess copper and remove it along with the unreacted small molecule.

HPLC purification method for VH032 modification

The final eluent collected after inversion was then purified by HPLC on an Agilent Polaris C18 column (150 x 4.6 mm), column heated to 50°C using a gradient of 3-30% or 3-50% CH_3CN (indicated in Appendix Figures) over 20 minutes, flow rate of 1.5 mL/min, with 10 mM triethylammonium bicarbonate (TEAB) pH 8.5 as an ion-pairing buffer throughout.

Oligonucleotide MS characterisation

Oligonucleotide Mass Spectra were recorded on a Waters Xevo G2 QTOF ESI-UPLC-MS system. A gradient of MeOH in Et3N and hexafluoroisopropanol (HFIP) was used (buffer A, 8.6 mM Et3N, 200 mM HFIP in 5% MeOH/H_2O (v/v); buffer B, 20% buffer A in MeOH). Data was then deconvoluted using MassLynx software v4.1 and recorded in Table 8.19.

Table 8.19: Expected and observed (deconvoluted) molecular weights for the synthesized OligoPROTACs incorporating (+)-JQ1 or VH032 moieties. Variants with different linker lengths ([n]) and toehold designs are included.

S.No.	Name	Expected Mass	Mass after Deconvolution
1	(+)-JQ1 ssDNA OligoPROTAC, [n=0]	7238.5	7239.5
2	VH032 ssDNA OligoPROTAC, [n=0]	7108.7	7109.5
3	(+)-JQ1 ssDNA OligoPROTAC, [n=1]	7563.0	7561.0
4	VH032 ssDNA OligoPROTAC, [n=1]	7429.7	7429.0
5	(+)-JQ1 ssDNA OligoPROTAC, [n=2]	7888.5	7882.5
6	VH032 ssDNA OligoPROTAC, [n=2]	7751.2	7751.0
7	(+)-JQ1 ssDNA OligoPROTAC, [n=3]	8206.5	8201.5
8	VH032 ssDNA OligoPROTAC, [n=3]	8070.2	8068.0
9	(+)-JQ1 ssDNA OligoPROTAC, [n=5]	8841.0	8842.5
10	VH032 ssDNA OligoPROTAC, [n=5]	8710.0	8710.5
11	(+)-JQ1 ssDNA OligoPROTAC, [n=10]	10442.0	10445.0
12	VH032 ssDNA OligoPROTAC, [n=10]	10311.2	10312.5
13	Antisymmetric OligoPROTAC (+)-JQ1, [n=3]	8171.0	8170.5
14	Toehold-(+)-JQ1 ssDNA, [n=3]	10747.0	10745.5

8.0.42 Assembly of OligoPROTAC

3′-(+)-JQ1 ssDNA OligoPROTAC strand and complementary 5′-VH032 ssDNA OligoPROTAC strand were combined in an equimolar ratio at 50µM in buffer: 30 mM HEPES pH 7.5, 100 mM CH3COOK. The solution was then heated to 95°C in

a thermocycler and slowly cooled down to 25°C over 40 minutes. Duplex formation was verified by running a native PAGE gel.

8.0.43 Cell culture

HEK293T cells were both cultured in Dulbecco's Modified Eagle Medium with 1X GlutaMAX (Gibco) supplemented with 10% (v/v) FBS (Gibco) and) at 37 °C in a humidified incubator with 5% CO2.

8.0.44 Nucleic acid delivery via lipid-based transfection

For **transfection** with lipofectamine 2000, 2.5×10^5 HEK239T cells were plated in 1 mL of culture media in 24-well plates 16 hours before transfection to reach 70-80% cell confluency. Prior to transfection, the culture media was replaced with OptiMEM, 100 µL for the 96-well plates and 1 mL for the 24-well plates.

2 µL of Lipofectamine 2000 (Invitrogen) was added to 48 µL OptiMEM (Gibco) and incubated at room temperature for 5 minutes before mixing with 0.5 nmol of Oligonucleotide dissolved in 50 µL of OptiMEM. The resulting mixture was incubated at room temperature for 20 minutes allowing complexation to occur. The complexes were then added to the cells at the required concentrations (with total volume of 1 mL per well). The cells were then incubated at 37 °C in a 5% CO2 incubator. After 6 hours the media was replaced with 1 mL of culture media and the cells were returned to the incubator for another 18 hours.

8.0.45 CellTiter-Glo

Transfection experiments were carried out as outlined above. Cells were subjected to the CellTiter-Glo assay at the indicated time points following the manufacturer's guidelines. Briefly, 100 µL CellTiter-Glo Reagent was added to 100 µl of media containing cells in a white (Thermofischer Nunc MicroWell polystyrene, 236105) 96-well plate. Subsequently, the contents of the wells were mixed on an orbital shaker for 2 minutes to induce cell lysis. The plate was then incubated at room temperature for 10 minutes to stabilize the luminescent signal. The luminescence was measured using a CLARIOstar microplate reader (BMG Labtech). The luminescence values were normalised to the values for untreated cells.

8.0.46 RT-qPCR

RNA extraction, cDNA synthesis, and RT-qPCR were performed as previously described (see Section 8.0.12, 8.0.12). For this section, a different set of qPCR primers was used for quantifying knockdown of target genes relevant to establishing the efficacy of OligoPROTACs. The primer sequences are listed in Table 8.20.

Table 8.20: Primer sequences used for quantitative PCR analysis. FWD and REV refer to forward and reverse primer sequences respectively.

S. No.	**Name**	**Sequence (5′ – 3′)**
1	GAPDH FWD	TTGGCTACAGCAACAGGGTG
2	GAPDH REV	GGGGAGATTCAGTGTGGTGG
3	MYC FWD	TTCTAAGAGAAATGTCCTGAGCAATC
4	MYC REV	TCAAGACTCAGCCAAGGTTGTG

8.0.47 Western blotting

Salt-soluble proteins were extracted from 1×10^6 cells by incubating cells in a high-salt lysis buffer (20 mM Tris-HCl pH 8.0, 300 mM KCl, 5 mM EDTA, 20% glycerol, 0.5% IGEPAL CA-630, protease inhibitor cocktail). Protein extracts were then run on a NuPAGE 4-12% BisTris gels (Life Technologies) at 180V for 1 hour and blotted onto a polyvinylidene fluoride membrane (Immobilon) at 100V for 1 hour using a Tris-glycine blotting buffer[299]. The blots were then probed with 1:10,000 dilution of primary antibody for BRD4 (CST #13440, E2A7X) and GAPDH (Bethyl, A300-641A) in 5% milk/TBS-tween at 4 °C overnight. BRD4 blots were then probed with secondary antibody (ab216773, IRDye 800CW) for 2 hours or secondary antibody (LiChor IRDye 800 CW) for 2 hours at room temperature, followed by imaging on the ChemiDoc MP system.

8.0.48 Molecular Modelling

Experiment performed by Prof. Shozeb Haider, UCL

The structure of the PROTAC, MZ1 in complex with the second bromodomain of BRD4 (BRD44BD2) and Von Hippel-Lindau disease tumor suppressor:ElonginC:ElonginB (PDB ID: 5T353) was downloaded from the protein databank. The structure was cleaned to remove transcription elongation factor polypeptide 1 (chain C) and 2 (chain B). The PEG linker from MZ1 was removed such that MZ1 was split into VH032 and (+)-JQ1. The warhead groups of VH032 and (+)-JQ1 were restrained so that the original conformation in the crystal structure was retained. The linkers were extended from the point of cleavage that attached VH032 to the 5′-end of one DNA Oligonucleotide and (+)-JQ1 to the 3′-end to the complementary DNA Oligonucleotide. A further 3 unpaired thymidines were added on each strand, [n=3], followed by an extension of a 20 bp duplex DNA containing the sequence AG-CACCCATCCAGGCGTGAT on the 5′- 3′strand and its complementary sequence on the 3′- 5′strand. The final structure was minimized in situ for a 1000 steps conjugate gradient, to relieve any steric clashes between the side chains and the extended OligoPROTAC, [n=3]. All structural manipulation and construction of the molecular model was carried out in ICM-Pro suite software.

Appendix

A.1 NMR spectra

A.1.1 1H NMR

Chapter 2: Altering the subcellular localization of ASOs to improve their therapeutic engagement and efficacy

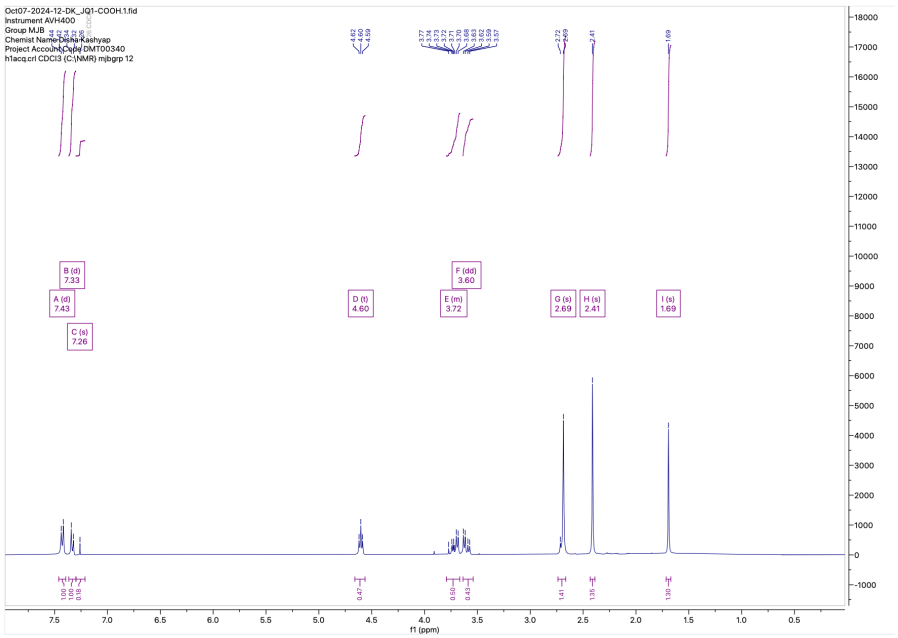

Figure A.1: **(S)-2-(4-(4-chlorophenyl)-2,3,9-trimethyl-6H-thieno[3,2-f][1,2,4]triazolo[4,3-a][1,4]diazepin-6-yl)acetic acid**, 1H NMR (400MHz, CDCl3)

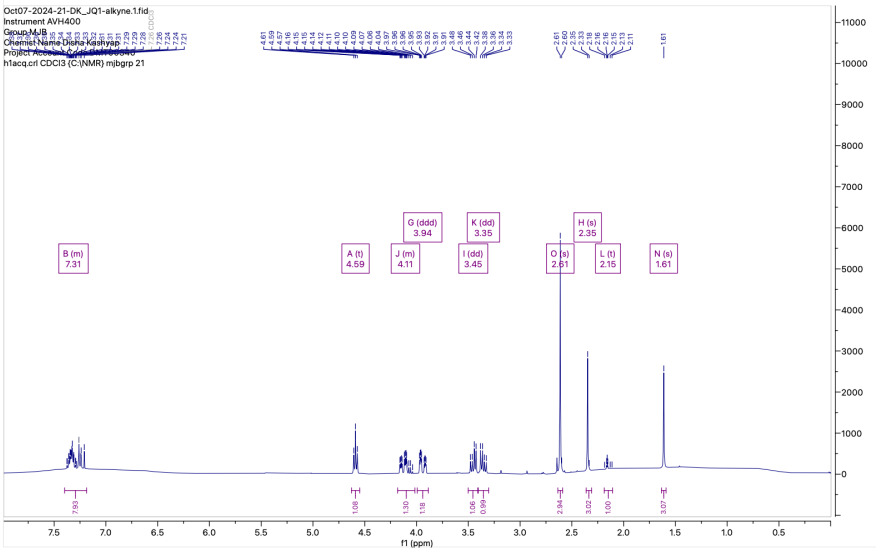

Figure A.2: **(S)-2-(4-(4-chlorophenyl)-2,3,9-trimethyl-6H-thieno[3,2-f][1,2,4]triazolo[4,3-a][1,4]diazepin-6-yl)-N-(prop-2-yn-1-yl)acetamide**, 1H NMR (600MHz, CDCl3)

Chapter 3: Exploring RNase L recruitment via an Activator-ASO conjugate for knockdown of the MLL-AF4 fusion oncogene

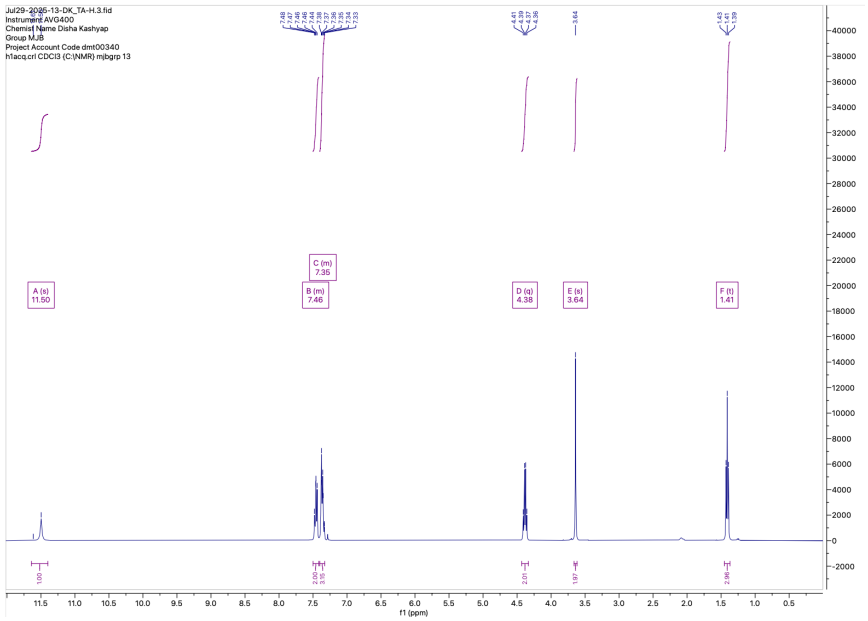

Figure A.3: **Ethyl 4-oxo-2-(phenylamino)-4,5-dihydrothiophene-3-carboxylate**, 1H NMR (400MHz, CDCl3)

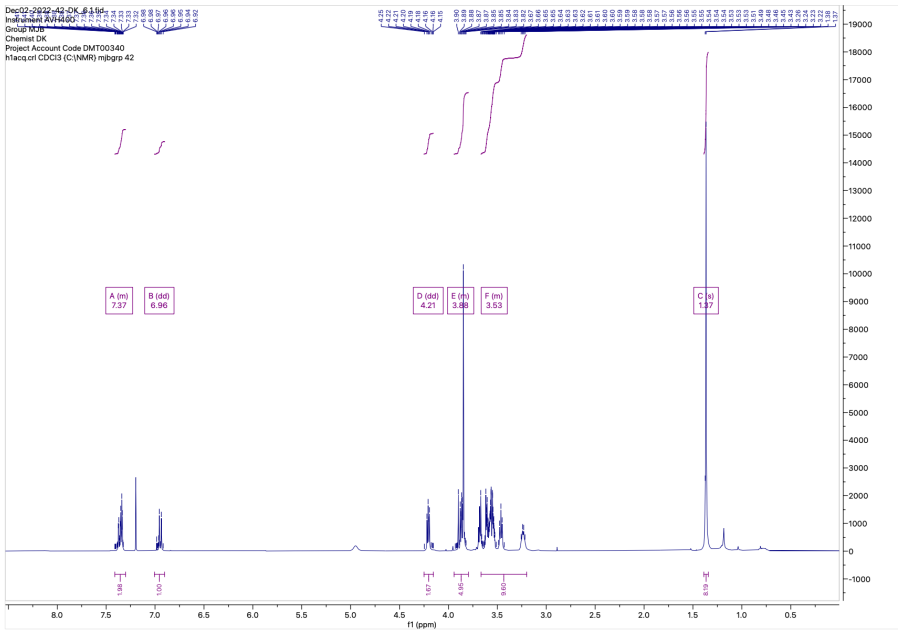

Figure A.4: **2-(2-(2-hydroxyethoxy)ethoxy)ethyl 4-methylbenzenesulphonate**, 1H NMR (400MHz, CDCl3

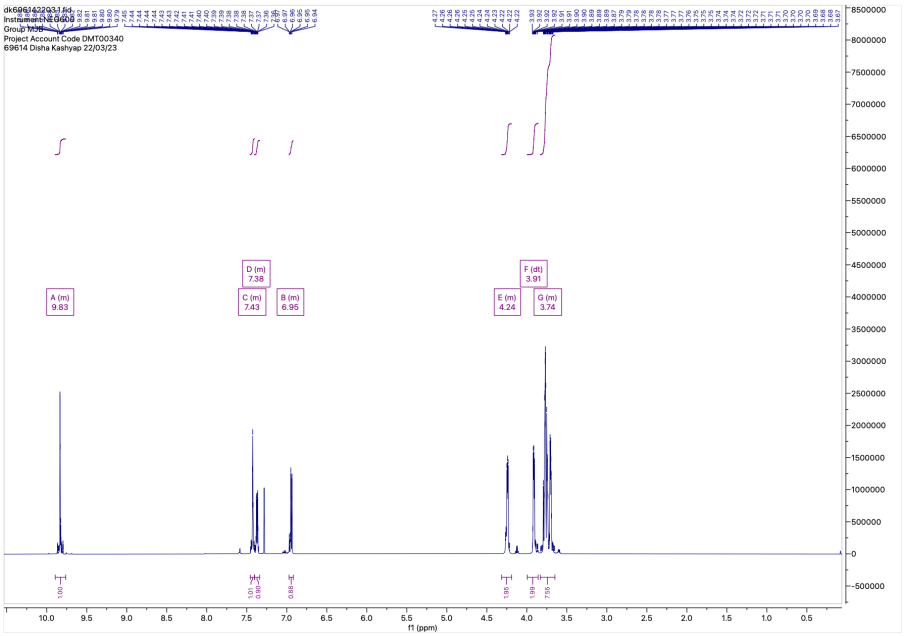

Figure A.5: **3-hydroxy-4-(2-(2-(2-hydroxyethoxy)ethoxy)ethoxy)benzaldehyde**, 1H NMR (600MHz, CDCl3)

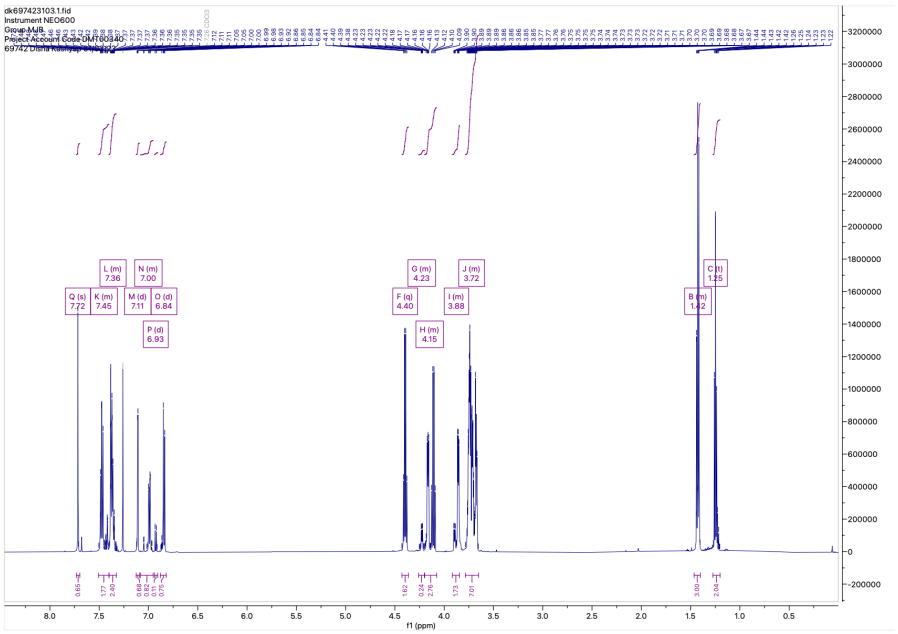

Figure A.6: **ethyl-5-(3-hydroxy-4-(2-(2-(2-hydroxyethoxy)ethoxy)ethoxy) benzylidene)-4-oxo-2-(phenylamino)-4,5-dihydrothiophene-3-carboxylate**, 1H NMR (600MHz, CDCl3)

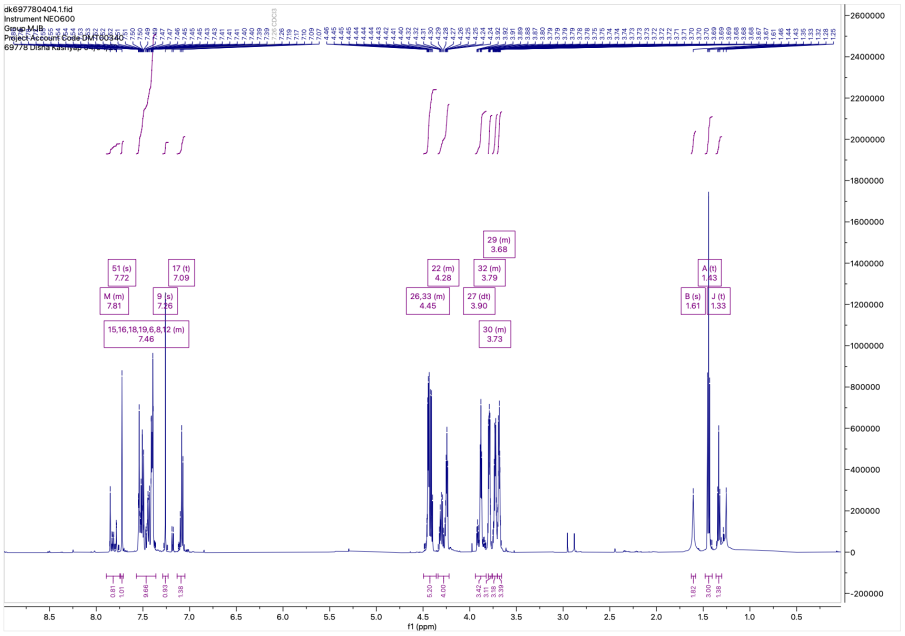

Figure A.7: **ethyl-5-(3-hydroxy-4-(2-(2-(2-(((perfluorophenoxy)carbonyl)oxy) ethoxy)ethoxy)ethoxy)benzylidene)-4-oxo-2-(phenylamino)-4,5-dihydrothiophene-3-carboxylate**, 1H NMR (600MHz, CDCl3)

A.1.2 13C NMR

Chapter 2: Altering the subcellular localization of ASOs to improve their therapeutic engagement and efficacy

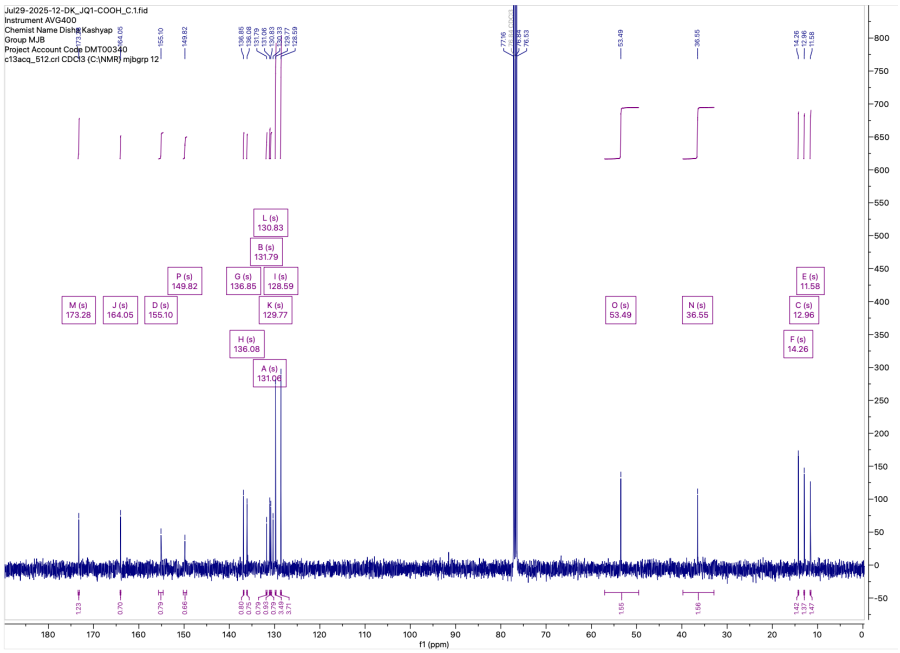

Figure A.8: **(S)-2-(4-(4-chlorophenyl)-2,3,9-trimethyl-6H-thieno[3,2-f][1,2,4]triazolo[4,3-a][1,4]diazepin-6-yl)acetic acid**, 13C NMR (256MHz, CDCl3)

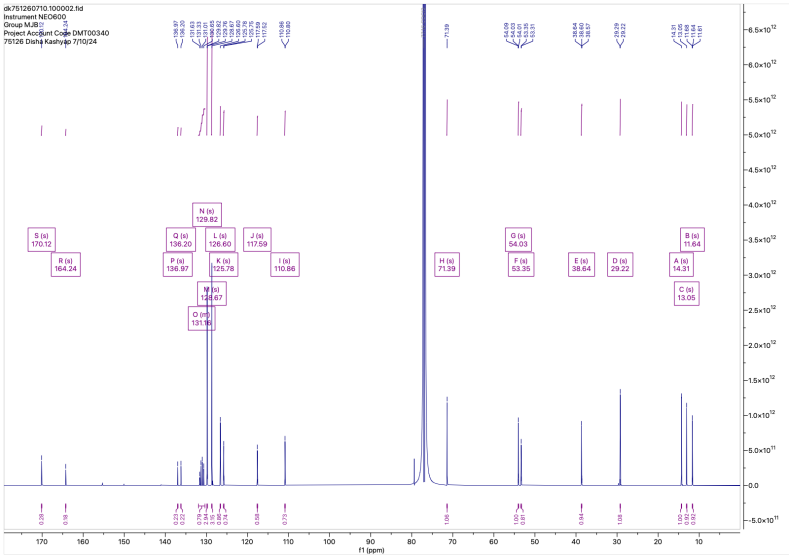

Figure A.9: **(S)-2-(4-(4-chlorophenyl)-2,3,9-trimethyl-6H-thieno[3,2-f][1,2,4]triazolo[4,3-a][1,4]diazepin-6-yl)-N-(prop-2-yn-1-yl)acetamide**, 13C NMR (256MHz, CDCl3)

Chapter 3: Exploring RNase L recruitment via an Activator-ASO conjugate for knockdown of the MLL-AF4 fusion oncogene

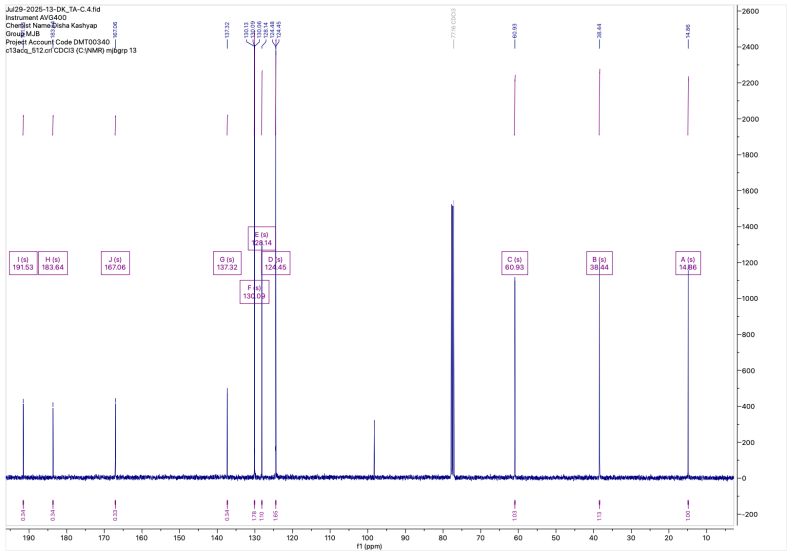

Figure A.10: **Ethyl 4-oxo-2-(phenylamino)-4,5-dihydrothiophene-3-carboxylate**, 13C NMR (256MHz, CDCl3)

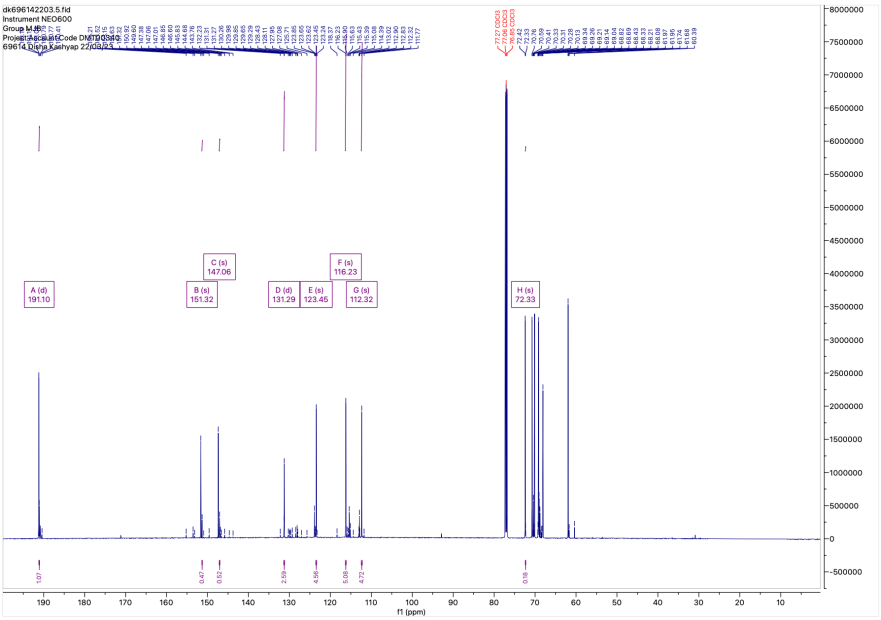

Figure A.11: **3-hydroxy-4-(2-(2-(2-hydroxyethoxy)ethoxy)ethoxy)benzaldehyde**, 13C NMR (256MHz, CDCl3)

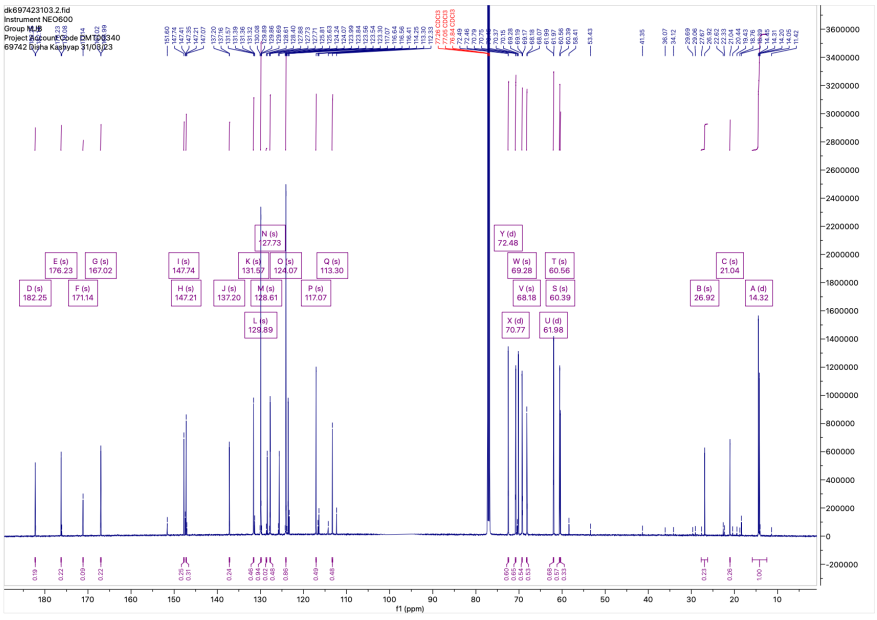

Figure A.12: **ethyl-5-(3-hydroxy-4-(2-(2-(2-hydroxyethoxy)ethoxy)ethoxy) benzylidene)-4-oxo-2-(phenylamino)-4,5-dihydrothiophene-3-carboxylate**, 13C NMR (256MHz, CDCl3)

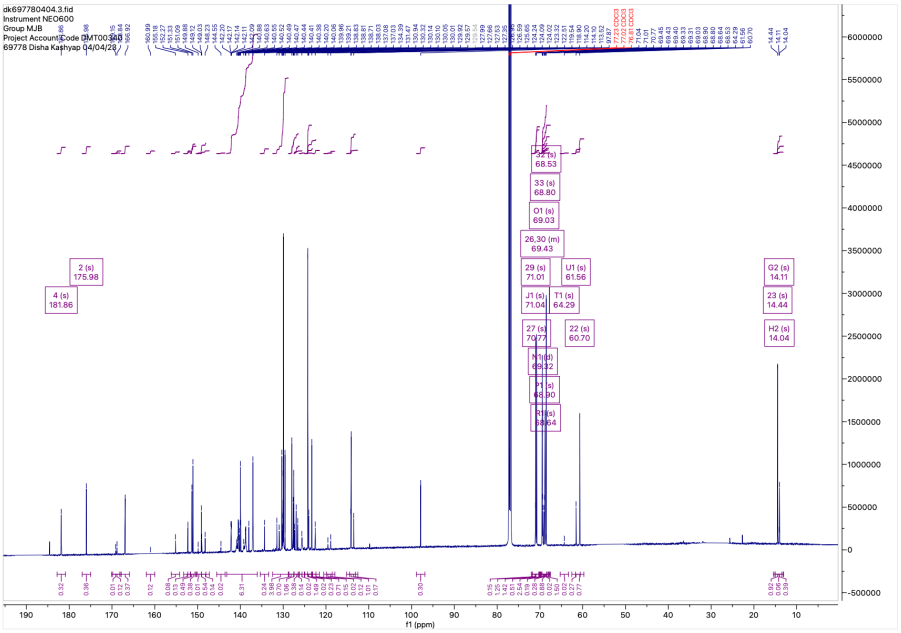

Figure A.13: **ethyl-5-(3-hydroxy-4-(2-(2-(2-(((perfluorophenoxy)carbonyl)oxy) ethoxy)ethoxy)ethoxy)benzylidene)-4-oxo-2-(phenylamino)-4,5-dihydrothiophene-3-carboxylate**, 13C NMR (256MHz, CDCl3)

A.1.3 19F NMR

Chapter 3: Exploring RNase L recruitment via an Activator-ASO conjugate for knockdown of the MLL-AF4 fusion oncogene

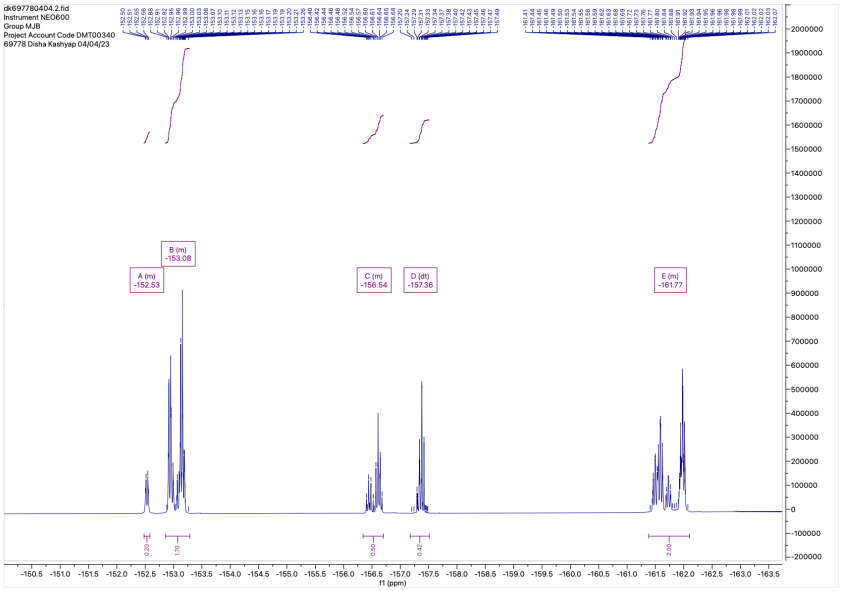

Figure A.14: **ethyl-5-(3-hydroxy-4-(2-(2-(2-(((perfluorophenoxy)carbonyl)oxy) ethoxy)ethoxy)ethoxy)benzylidene)-4-oxo-2-(phenylamino)-4,5-dihydrothiophene-3-carboxylate**, 19F NMR (600MHz, CDCl3)

A.2 Oligonucleotide reaction scheme, HPLC purification and MS characterisation

(+)-JQ1-ASO conjugates: synthesis, HPLC purification, and MS characterisation

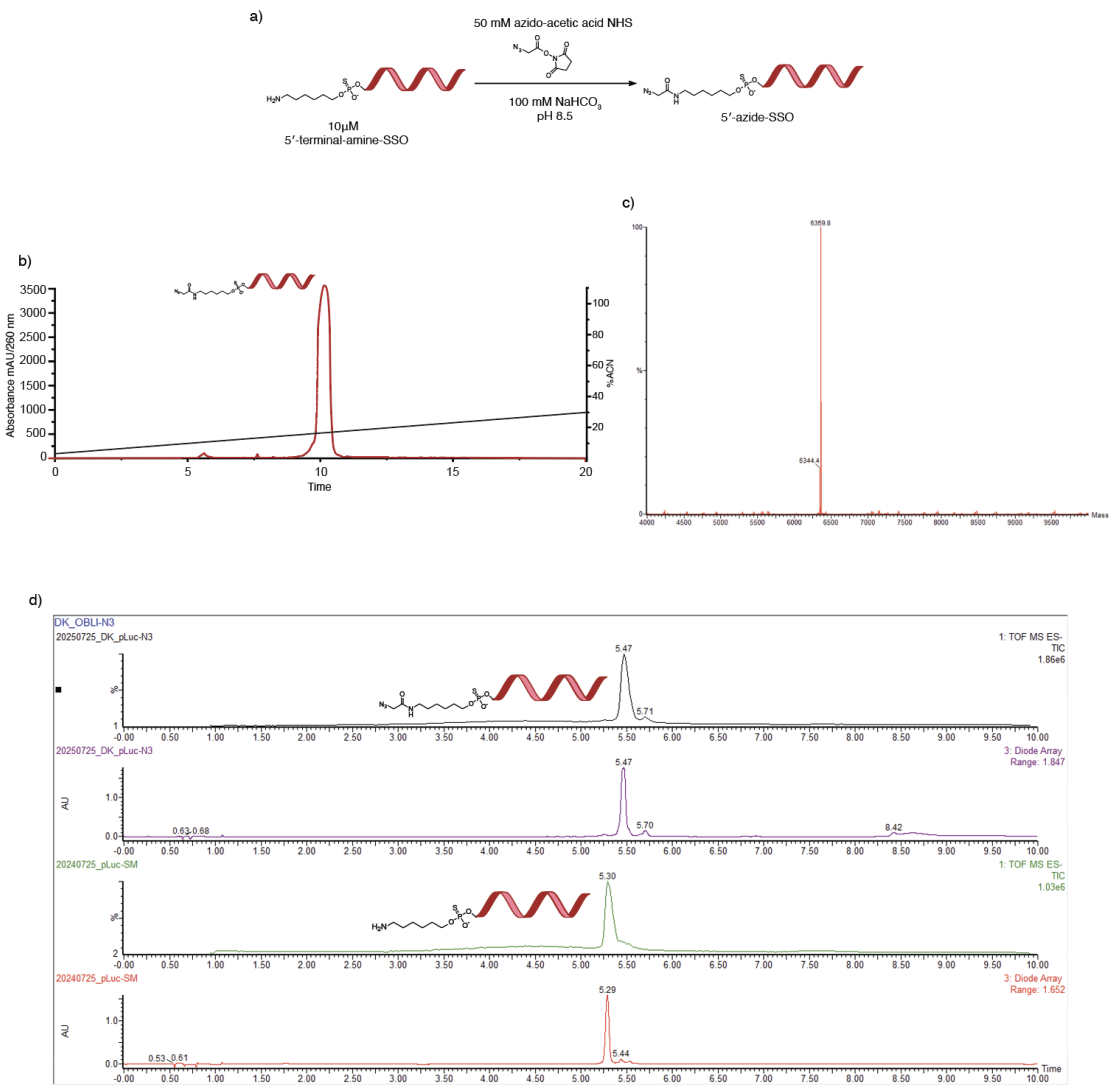

Figure A.15: Reaction and characterisation for azide modification of the SSO. (a) Reaction scheme for azide functionalisation of SSO. (b) HPLC purification for azide-SSO functionalisation. (c) Mass spectrum for HPLC-purified azide-SSO. (d) LC-MS characterisation for HPLC-purified azide-SSO.

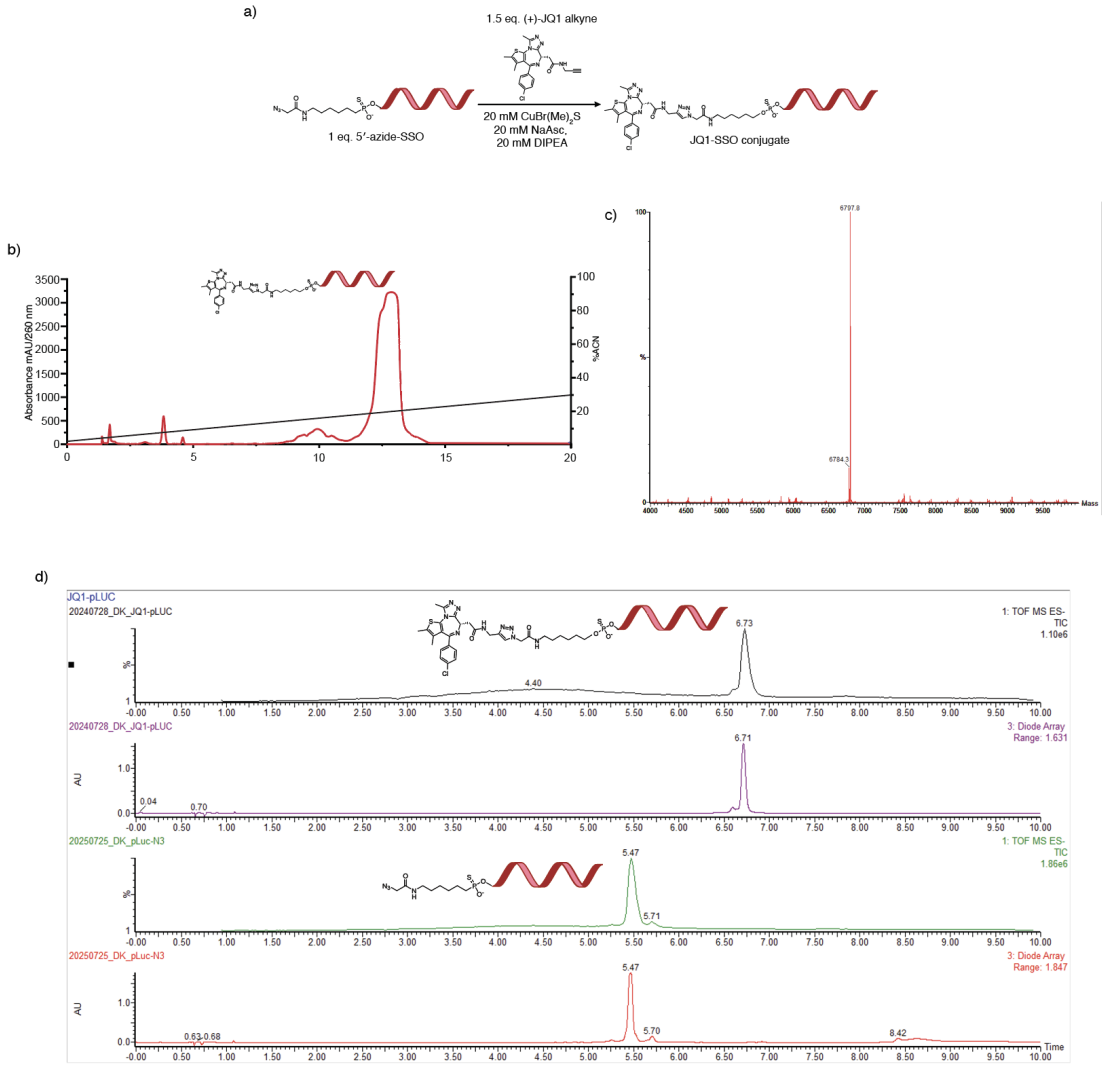

Figure A.16: Reaction and characterisation for JQ1 modification of the azido SSO. (a) Reaction scheme for copper click conjugation of JQ1-alkyne with azide-SSO. (b) HPLC purification for JQ1-SSO functionalisation. (c) Mass spectrum for HPLC-purified JQ1-SSO. (d) LC-MS characterisation for HPLC-purified JQ1-SSO.

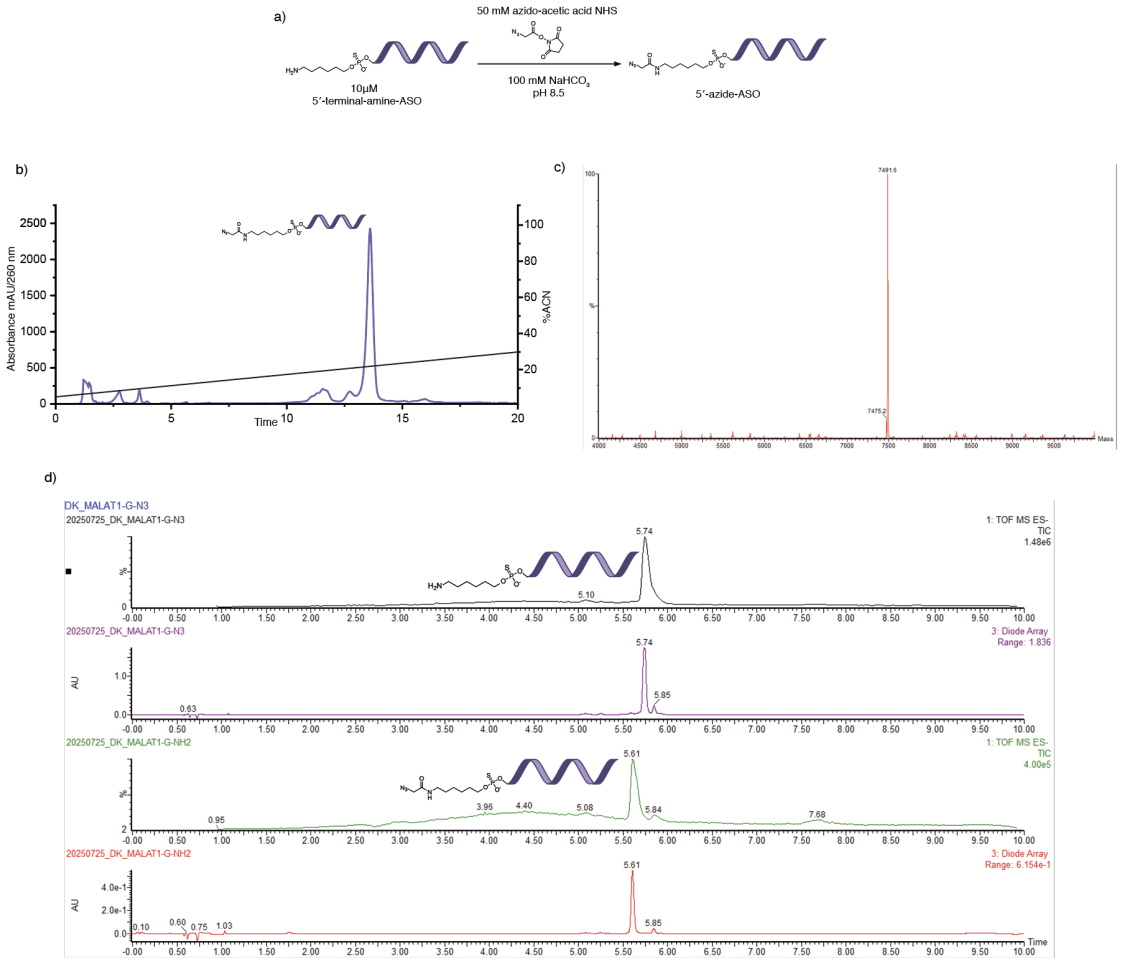

Figure A.17: Reaction and characterisation for azide modification of the MALAT1 gapmer. (a) Reaction scheme for azide functionalisation of the MALAT1 gapmer. (b) HPLC purification for azide-MALAT1 gapmer functionalisation.(c) Mass spectrum for HPLC-purified azide-MALAT1 gapmer. (d) LC-MS characterisation for HPLC-purified azide-MALAT1 gapmer.

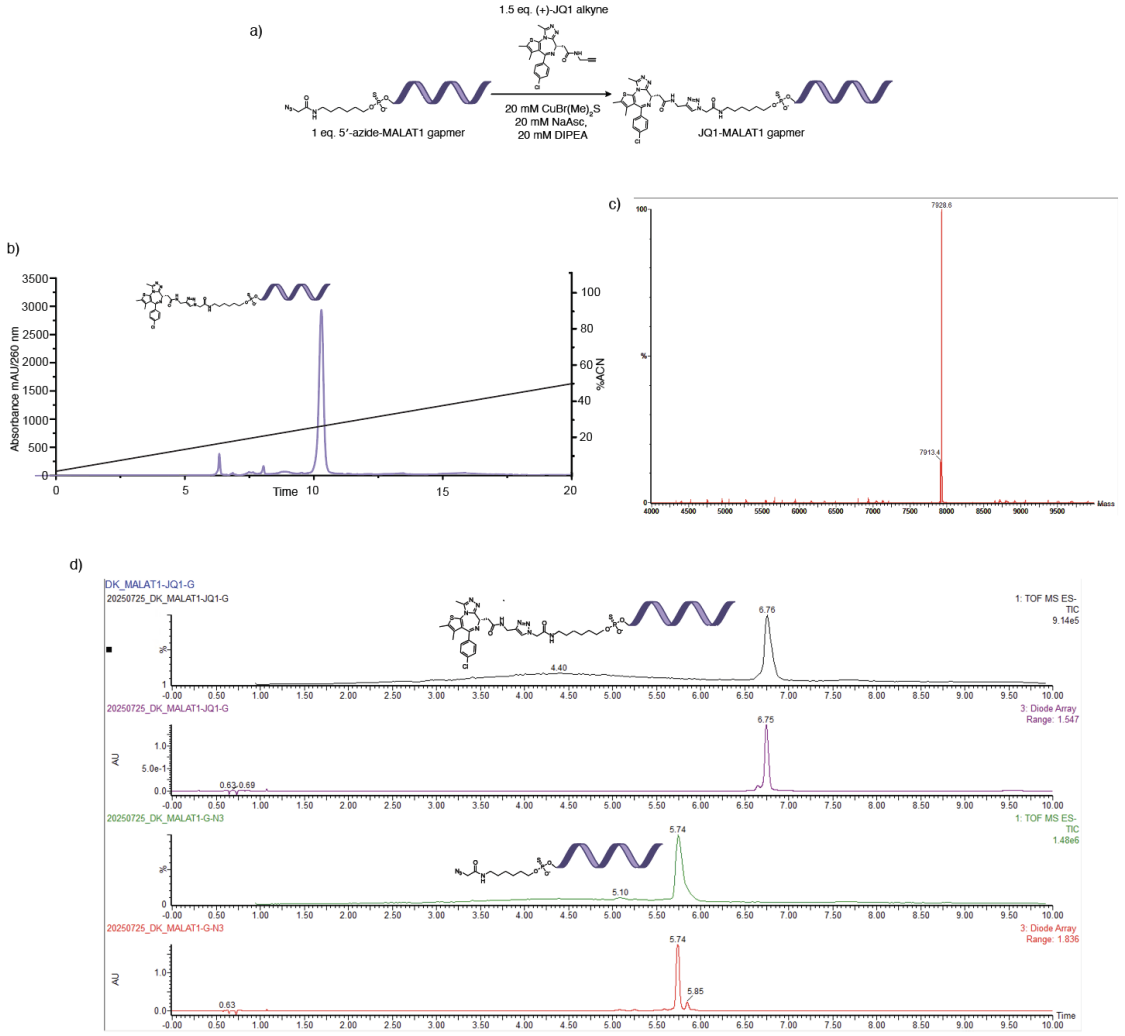

Figure A.18: Reaction and characterisation for JQ1 modification of the azido SSO. (a) Reaction scheme for copper click conjugation of JQ1-alkyne with azide-MALAT1 gapmer. (b) HPLC purification for JQ1-MALAT1 gapmer functionalisation. (c) Mass spectrum for HPLC-purified JQ1-MALAT1 gapmer. (d) LC-MS characterisation for HPLC-purified JQ1-MALAT1 gapmer.

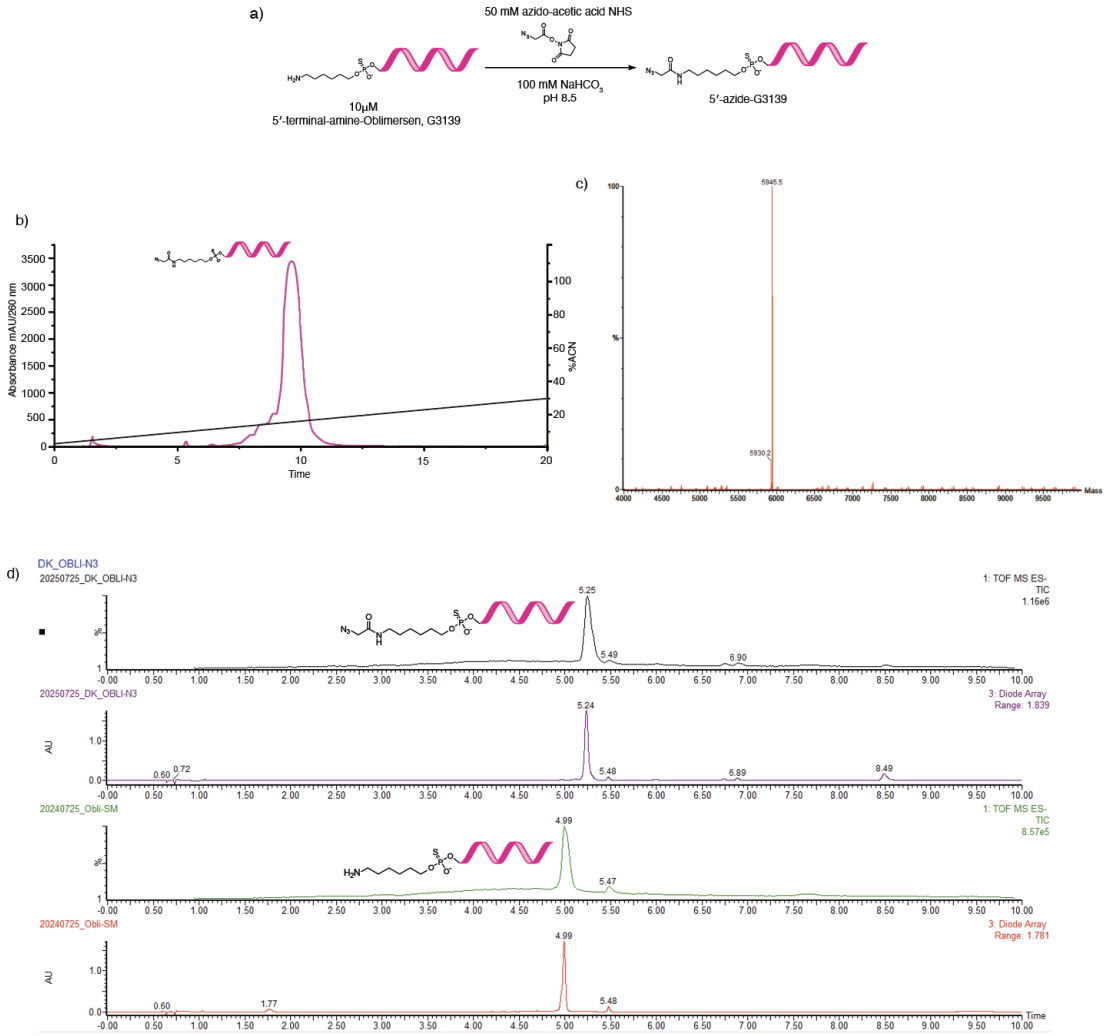

Figure A.19: Reaction and characterisation for azide modification of G3139. (a) Reaction scheme for azide functionalisation of the G3139. (b) HPLC purification for azide-G3139 functionalisation.(c) Mass spectrum for HPLC-purified azide-G3139. (d) LC-MS characterisation for HPLC-purified azide-G3139.

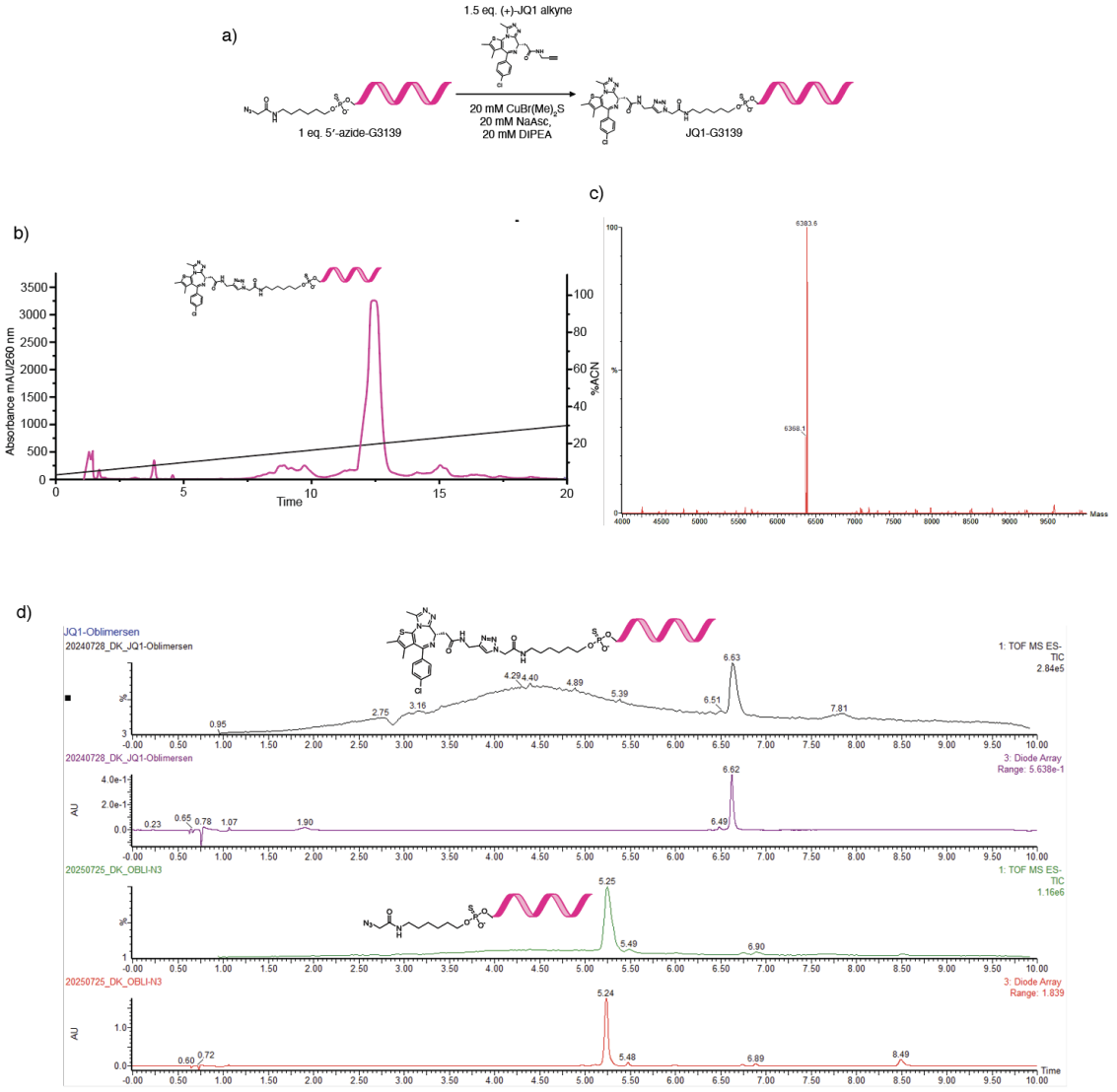

Figure A.20: Reaction and characterisation for JQ1 modification of azido G3139. (a) Reaction scheme for JQ1 functionalisation of G3139. (b) HPLC purification for JQ1-G3139 functionalisation.(c) Mass spectrum for HPLC-purified JQ1-G3139. (d) LC-MS characterisation for HPLC-purified JQ1-G3139.

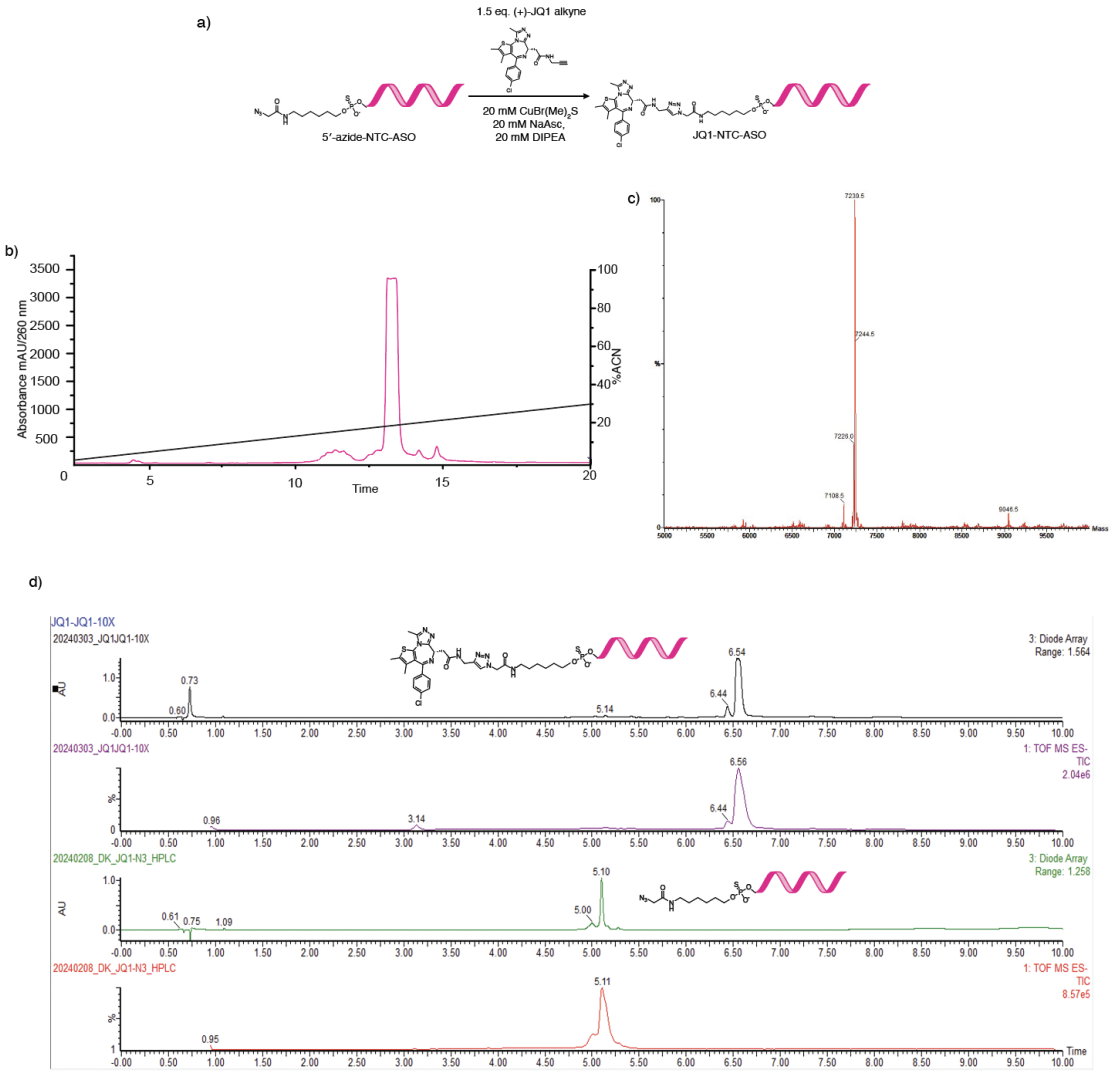

Figure A.21: Reaction and characterisation for JQ1 modification of the NTC-ASO. (a) Reaction scheme for JQ1 functionalisation of the NTC-ASO. (b) HPLC purification for JQ1-NTC-ASO functionalisation.(c) Mass spectrum for HPLC-purified JQ1-NTC-ASO. (d) LC-MS characterisation for HPLC-purified JQ1-NTC-ASO.

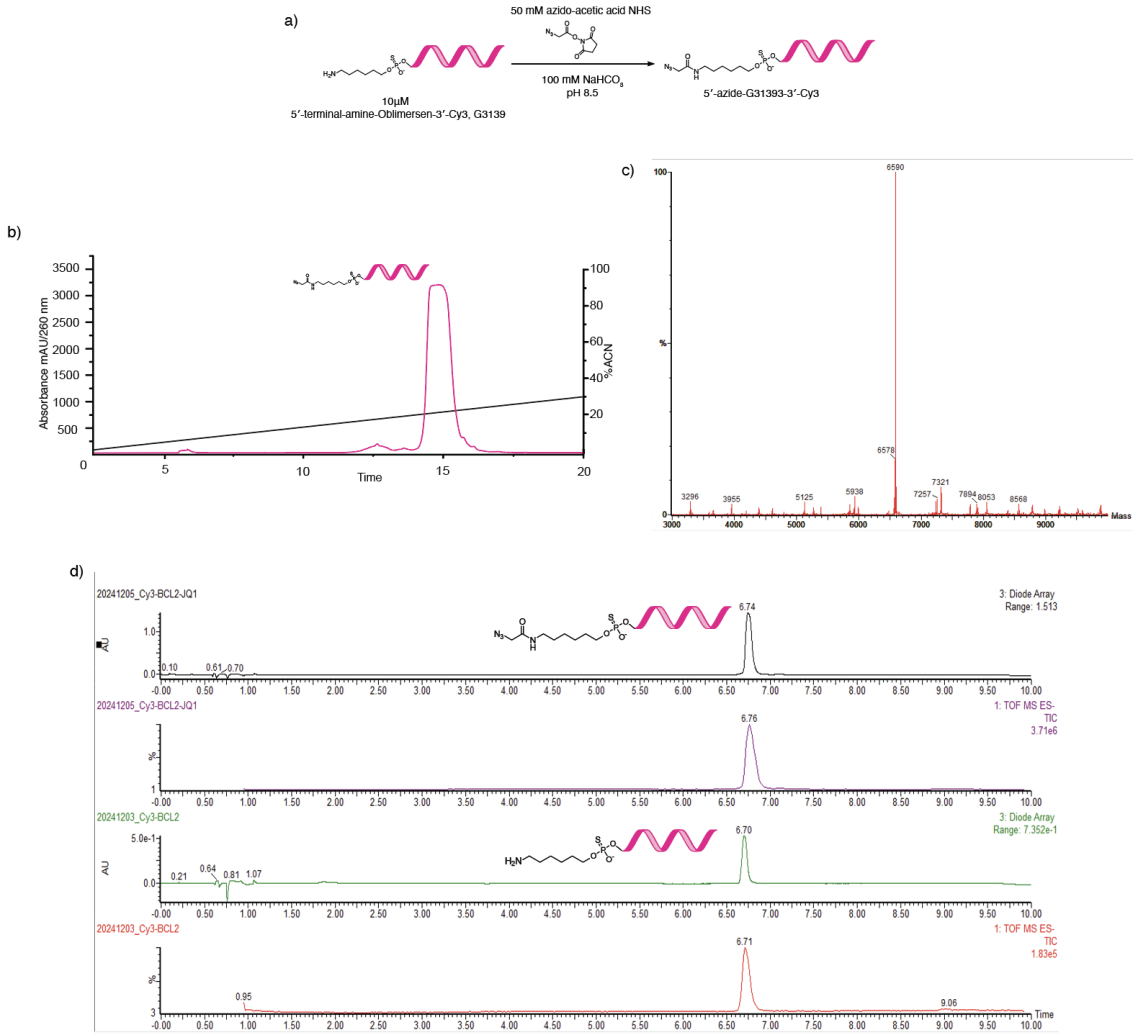

Figure A.22: Reaction and characterisation for azide modification of the Oblimersen (G3139)-Cy3 ASO. (a) Reaction scheme for azide functionalisation of G3139-Cy3. (b) HPLC purification for azide-G3139-Cy3 functionalisation. (c) Mass spectrum for HPLC-purified azide-G3139. (d) LC-MS characterisation for HPLC-purified azide-G3139-Cy3.

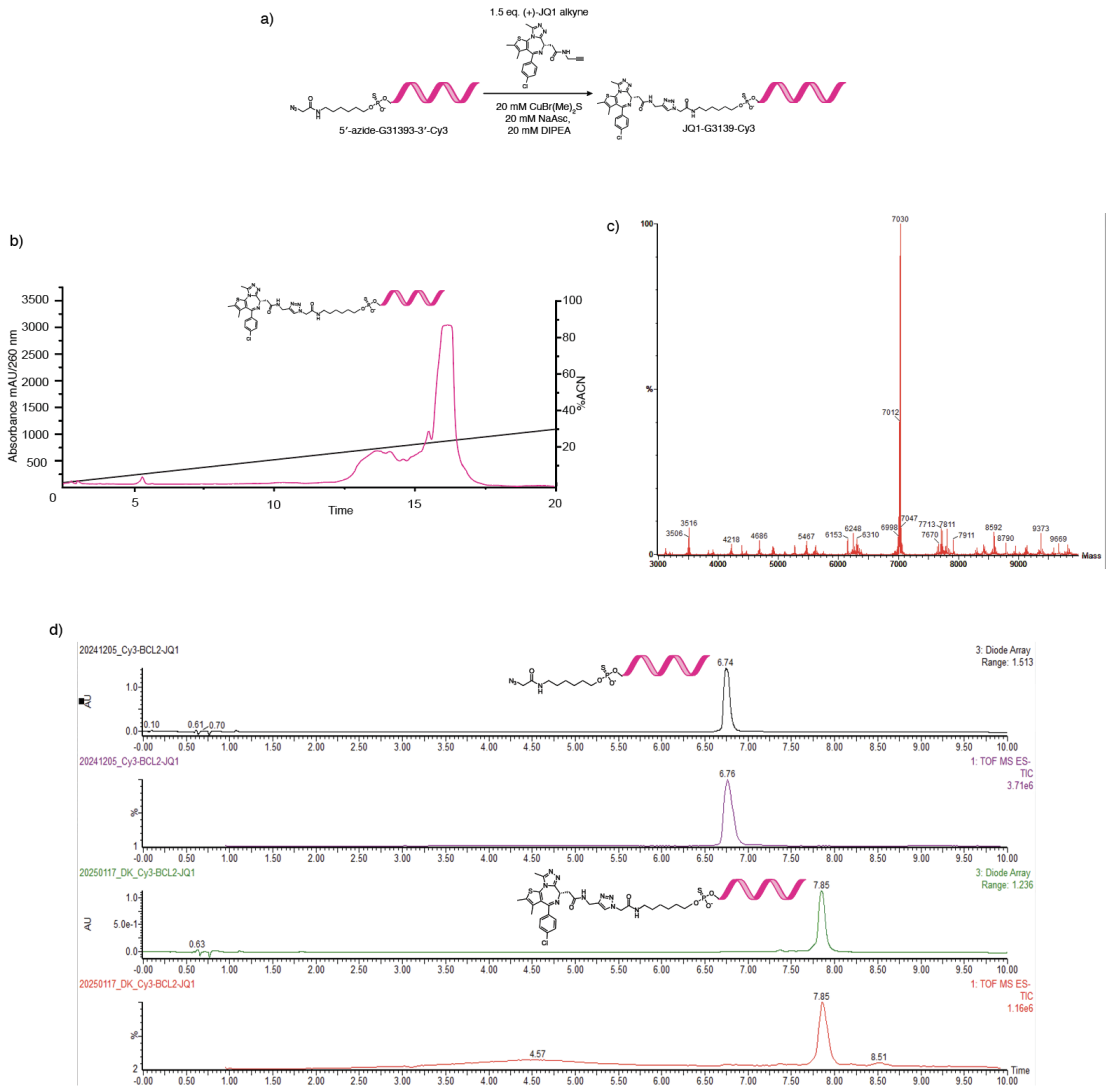

Figure A.23: Reaction and characterisation for JQ1 modification of the azido G3139-Cy3. (a) Reaction scheme for copper click conjugation of JQ1-alkyne with azido G3139-Cy3. (b) HPLC purification for JQ1-G3139-Cy3 functionalisation. (c) Mass spectrum for HPLC-purified JQ1-G3139-Cy3. (d) LC-MS characterisation for HPLC-purified JQ1-G3139-Cy3.

Ispinesib-ASO conjugates: synthesis, HPLC purification, and MS characterisation

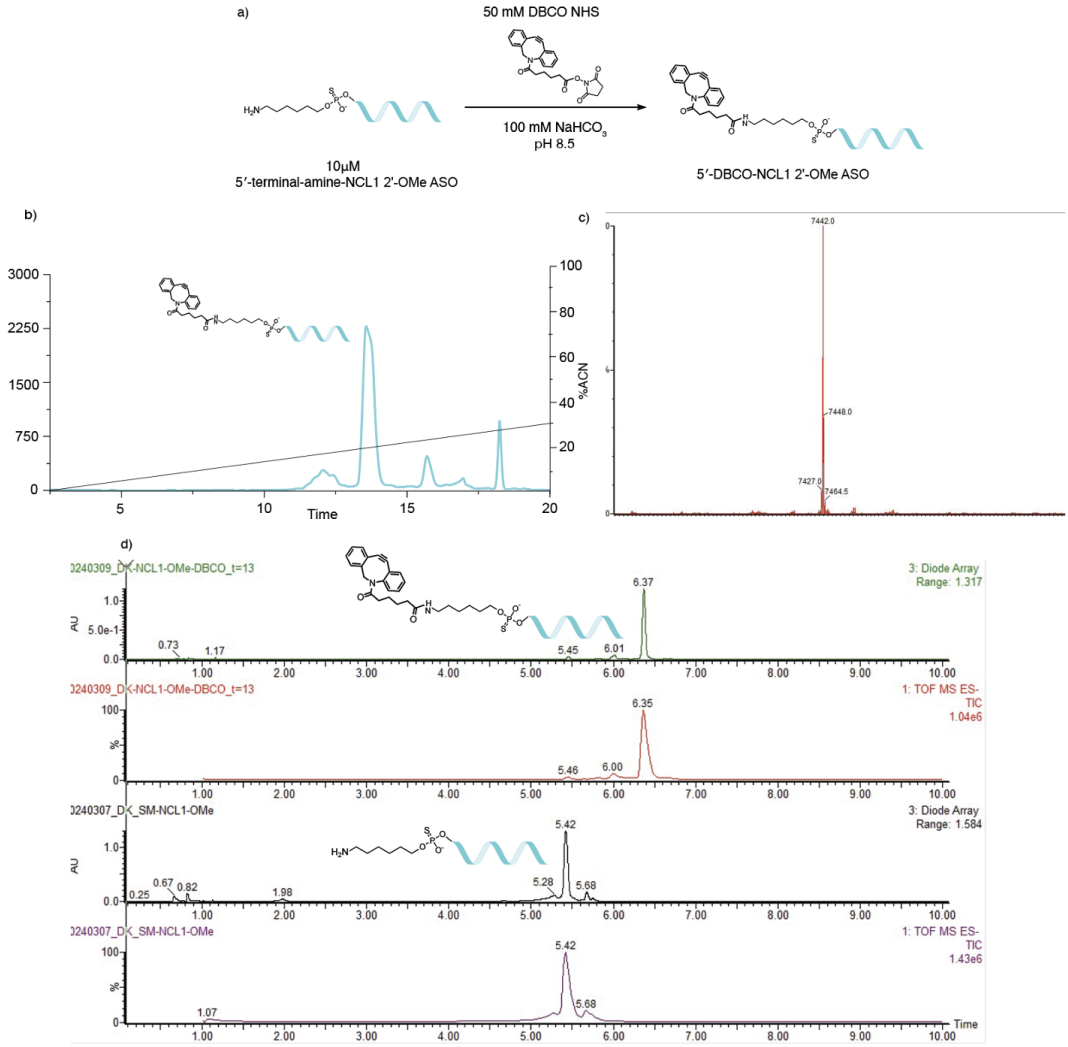

Figure A.24: Reaction and characterisation for DBCO modification of NCL1 2′-OMe ASO. (a) Reaction scheme for DBCO functionalisation of NCL1 2ÓMe ASO. (b) HPLC purification for DBCO-NCL1 2′- OMe ASO functionalisation. (c) Mass spectrum for HPLC-purified DBCO-NCL1 2′- OMe ASO. (d) LC-MS characterisation for HPLC-purified DBCO-NCL1 2′- OMe ASO.

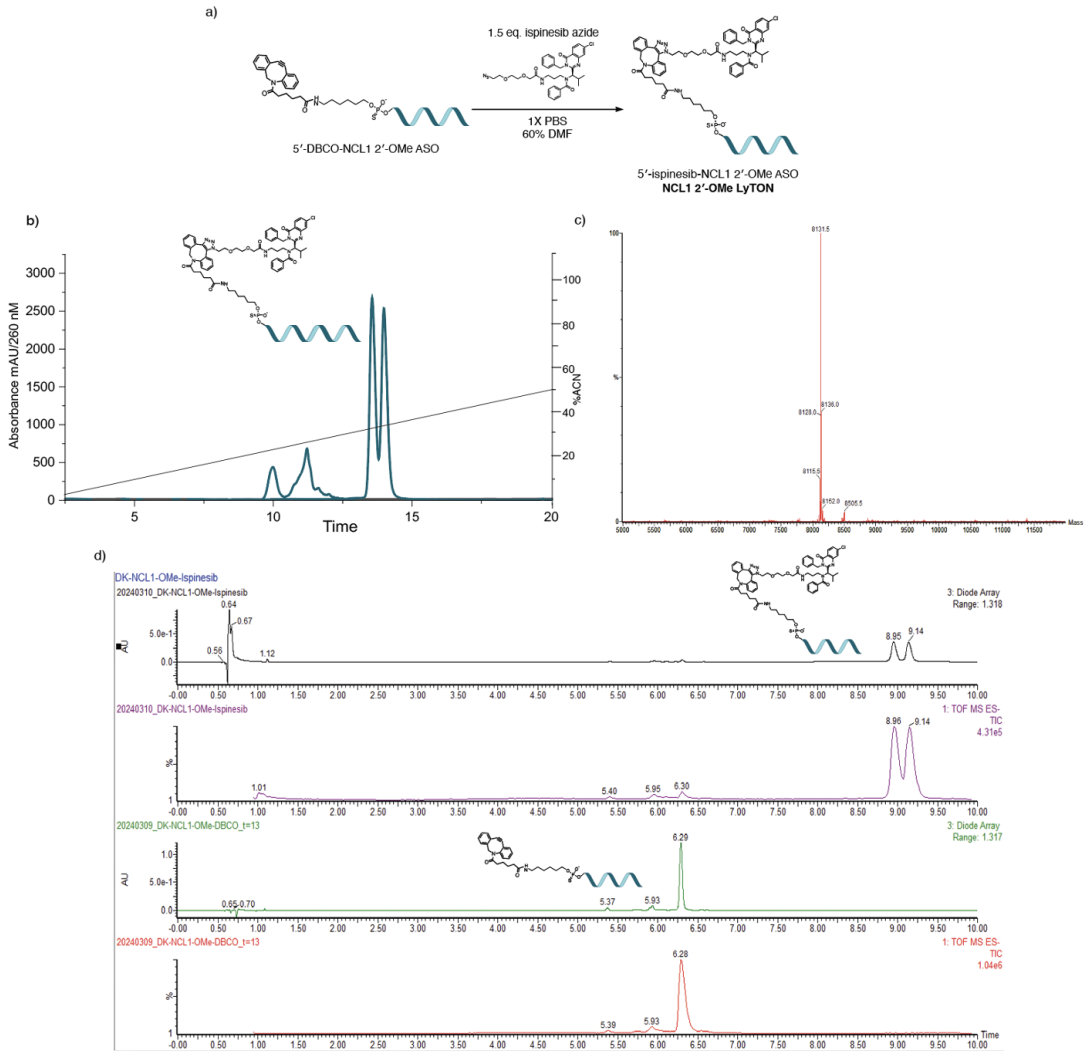

Figure A.25: Reaction and characterisation for ispinesib modification of NCL1 2′-OMe ASO. (a) Reaction scheme for ispinesib functionalisation of NCL1 2′- OMe ASO. (b) HPLC purification for Ispinesib-NCL1 2′- OMe ASO (NCL1 2′- OMe LyTON) functionalisation (two peaks represent regioisomer products from SPAAC). (c) Mass spectrum for HPLC-purified NCL1 2′- OMe LyTON. (d) LC-MS characterisation for HPLC-purified NCL1 2′- OMe LyTON.

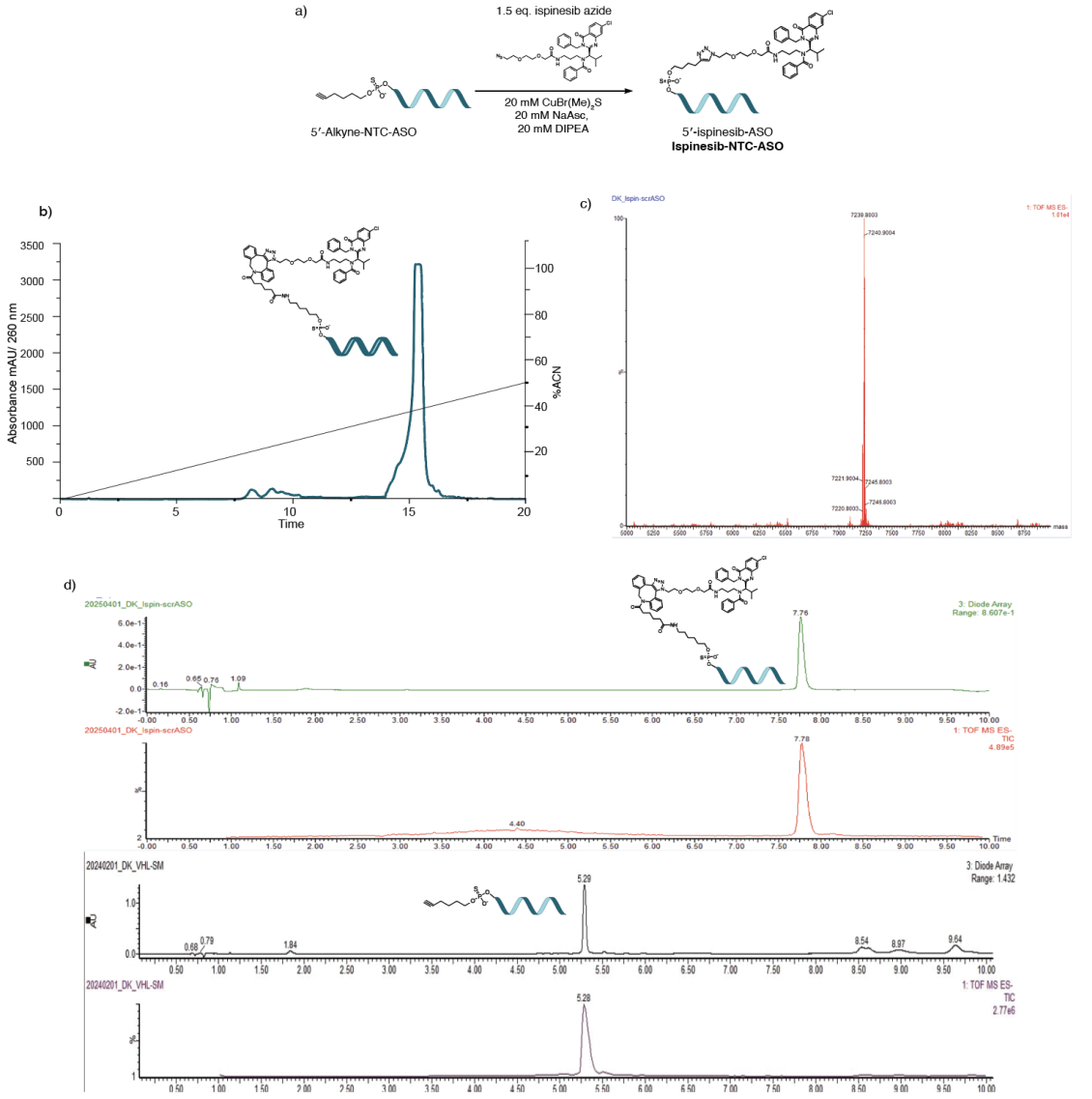

Figure A.26: Reaction and characterisation for ispinesib modification of NTC-ASO. (a) Reaction scheme for ispinesib functionalisation of NTC-ASO. (b) HPLC purification for Ispinesib-NTC-ASO functionalisation. (c) Mass spectrum for HPLC-purified Ispinesib-NTC-ASO. d) LC-MS characterisation for HPLC-purified Ispinesib-NTC-ASO.

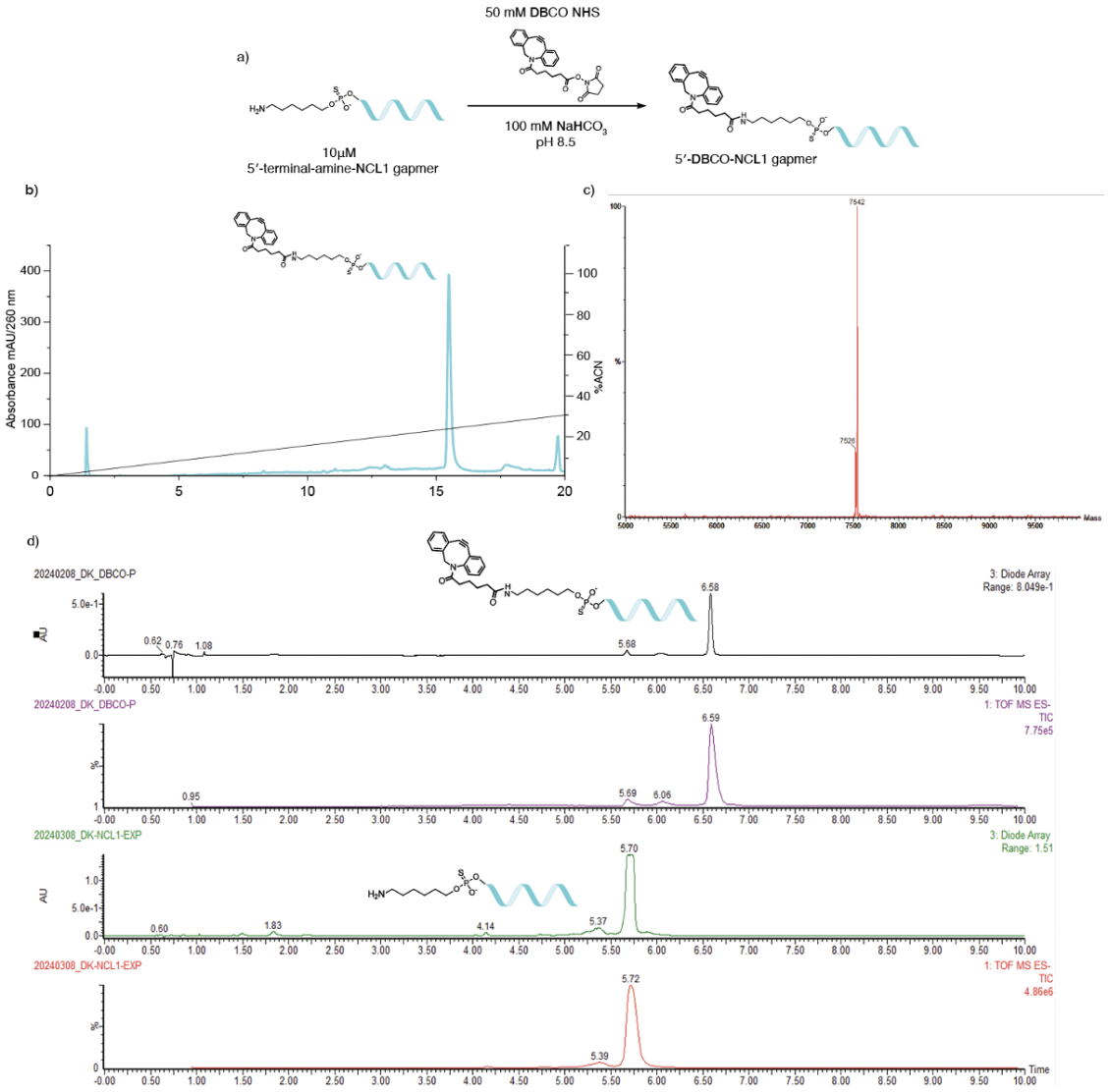

Figure A.27: Reaction and characterisation for DBCO modification of NCL1 gapmer ASO. a) Reaction scheme for DBCO functionalisation of NCL1 gapmer ASO. b) HPLC purification for DBCO-NCL1 gapmer ASO functionalisation. c) Mass spectrum for HPLC-purified DBCO-NCL1 gapmer ASO. d) LC-MS characterisation for HPLC-purified DBCO-NCL1 gapmer ASO.

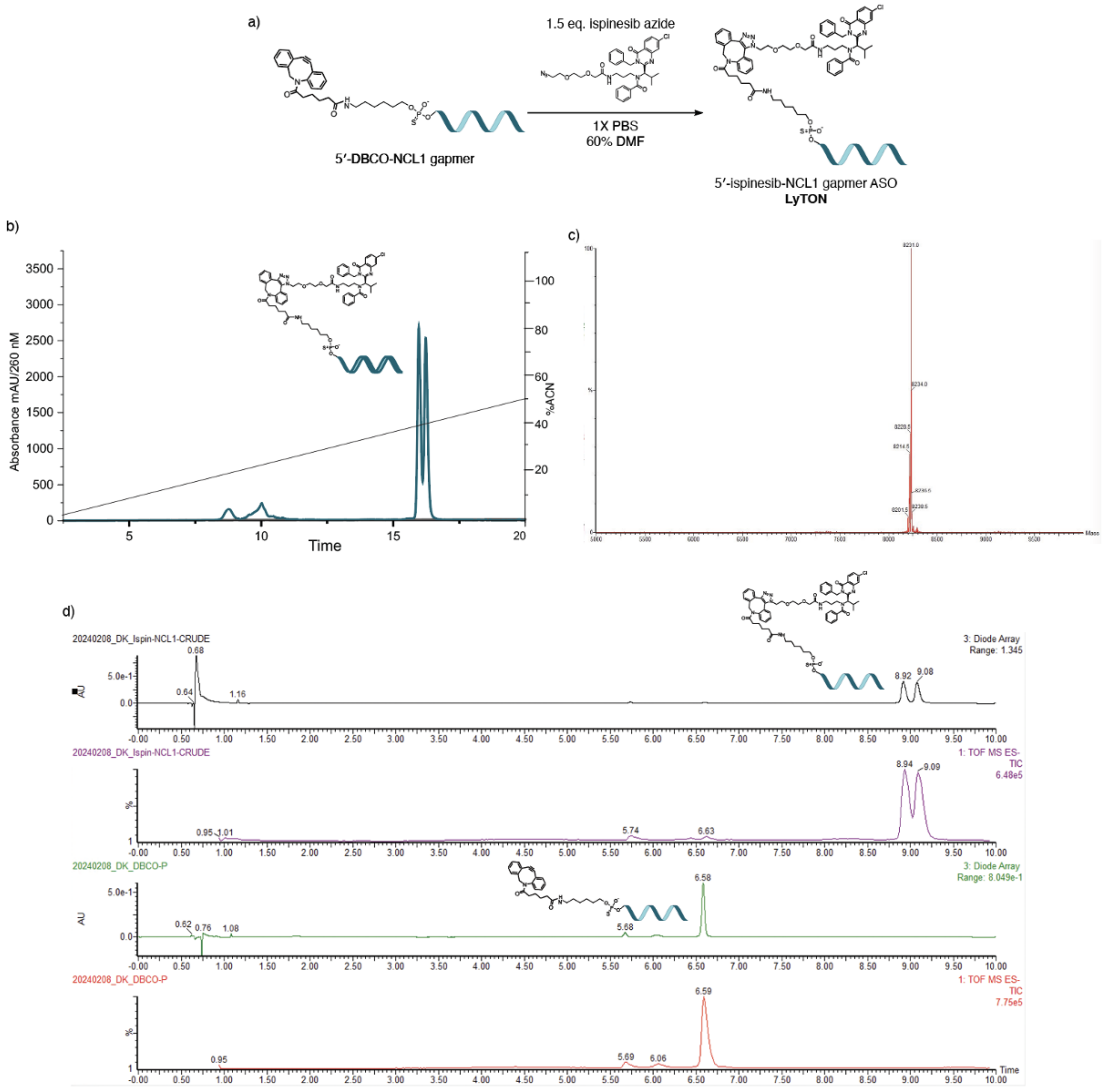

Figure A.28: Reaction and characterisation for ispinesib modification of NCL1 gapmer ASO. (a) Reaction scheme for ispinesib functionalisation of NCL1 gapmer ASO. (b) HPLC purification for Ispinesib-NCL1 gapmer ASO (NCL1 gapmer LyTON) functionalisation (two peaks represent regioisomer products from SPAAC). (c) Mass spectrum for HPLC-purified NCL1 gapmer LyTON. (d) LC-MS characterisation for HPLC-purified NCL1 gapmer LyTON.

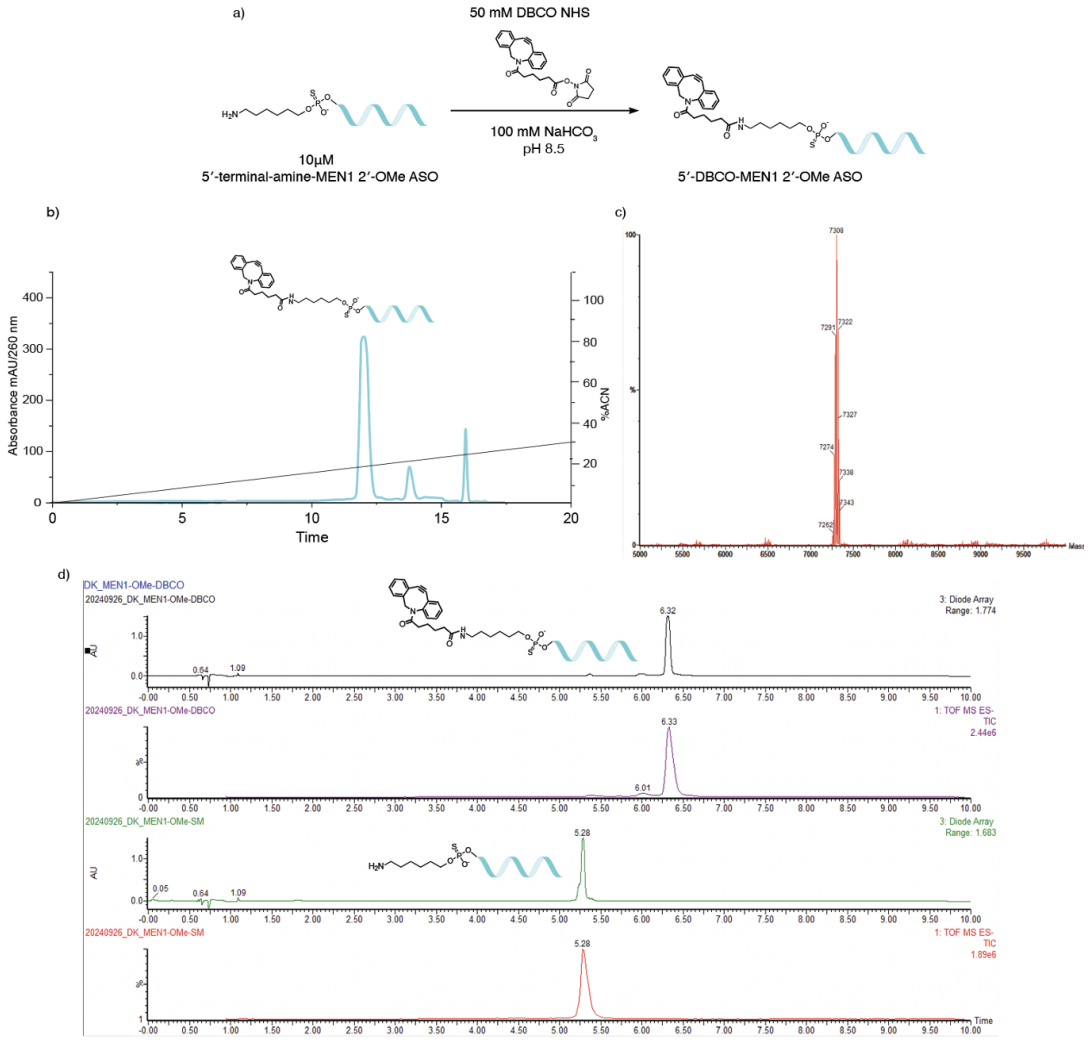

Figure A.29: Reaction and characterisation for DBCO modification of MEN1 2′-OMe ASO. a) Reaction scheme for DBCO functionalisation of MEN1 2′- OMe ASO. b) HPLC purification for DBCO-MEN1 2′- OMe ASO functionalisation. c) Mass spectrum for HPLC-purified DBCO-MEN1 2′- OMe ASO. d) LC-MS characterisation for HPLC-purified DBCO-MEN1 2′- OMe ASO.

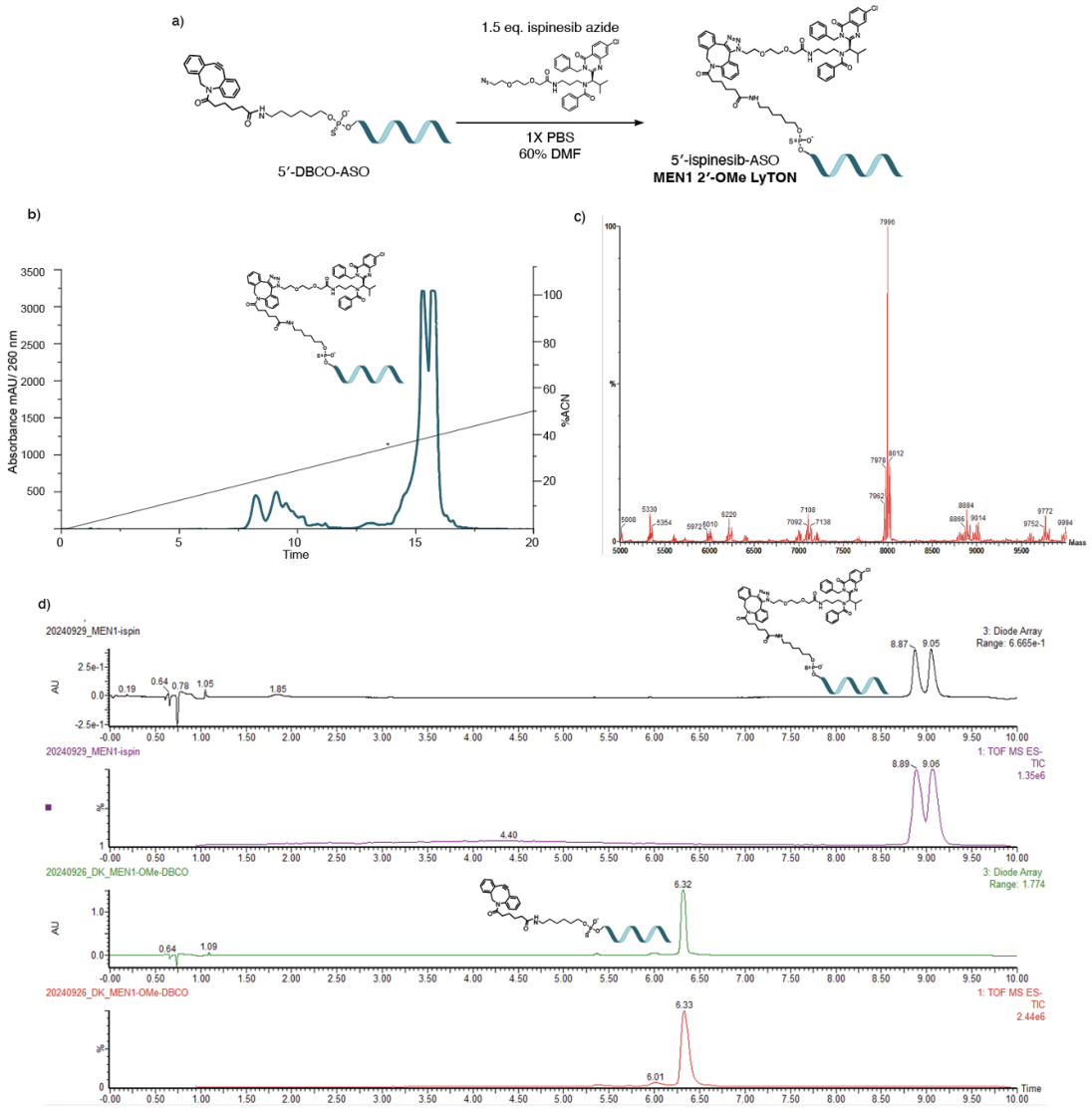

Figure A.30: Reaction and characterisation for ispinesib modification of MEN1 2′- OMe ASO. (a) Reaction scheme for ispinesib functionalisation of MEN1 2′- OMe ASO. (b) HPLC purification for Ispinesib-MEN1 2′- OMe ASO (MEN1 2′- OMe LyTON) functionalisation (two peaks represent regioisomer products from SPAAC). (c) Mass spectrum for HPLC-purified MEN1 2′- OMe LyTON. (d) LC-MS characterisation for HPLC-purified MEN1 2′- OMe LyTON.

OligoPROTACs, small molecule-oligonucleotide conjugates: synthesis, HPLC purification, and MS characterisation

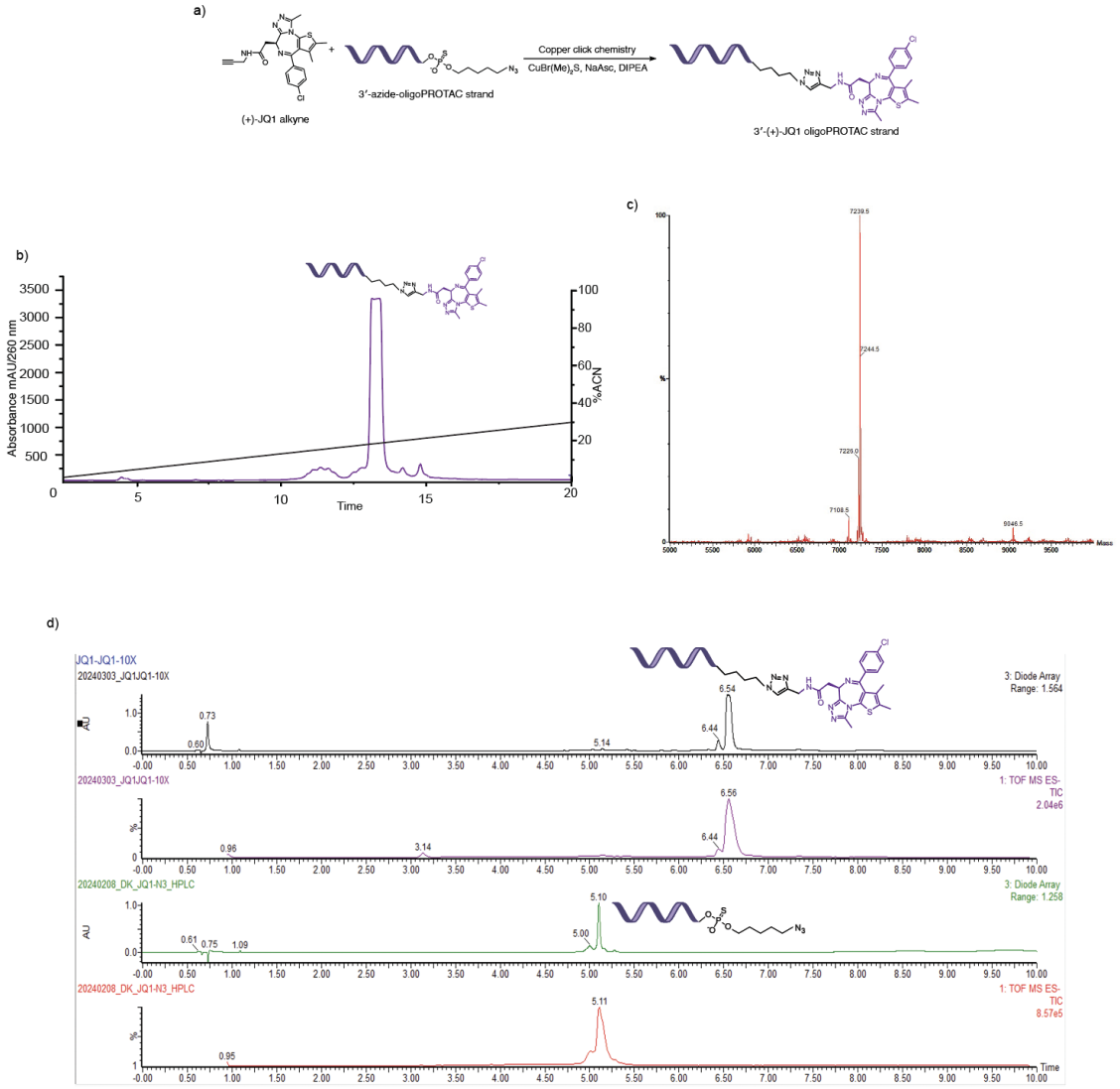

Figure A.31: Reaction and characterisation for (+)-JQ1 ssDNA OligoPROTAC, [n=0]. (a) Reaction scheme for copper click conjugation of (+)-JQ1-alkyne with azide-OligoPROTAC, [n=0]. (b) HPLC purification for (+)-JQ1 ssDNA OligoPROTAC, [n=0]. (c) Mass spectrum for HPLC-purified (+)-JQ1 ssDNA OligoPROTAC, [n=0]. (d) LC-MS characterisation for (+)-JQ1 ssDNA OligoPROTAC, [n=0].

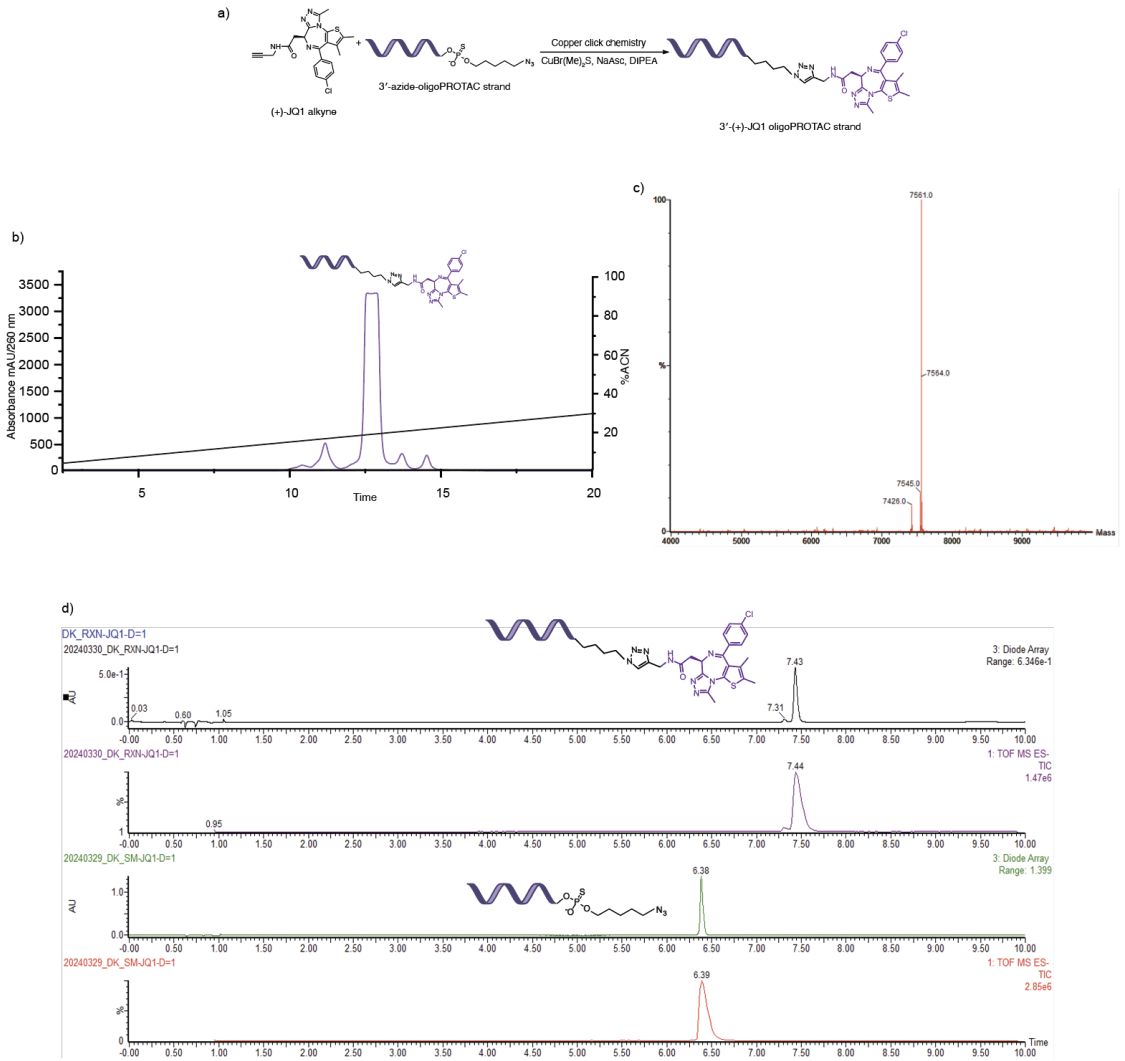

Figure A.32: Reaction and characterisation for (+)-JQ1 ssDNA OligoPROTAC, [n=1]. (a) Reaction scheme for copper click conjugation of (+)-JQ1-alkyne with azide-OligoPROTAC, [n=1]. (b) HPLC purification for (+)-JQ1 ssDNA OligoPROTAC, [n=1]. (c) Mass spectrum for HPLC-purified (+)-JQ1 ssDNA OligoPROTAC, [n=1]. (d) LC-MS characterisation for (+)-JQ1 ssDNA OligoPROTAC, [n=1].

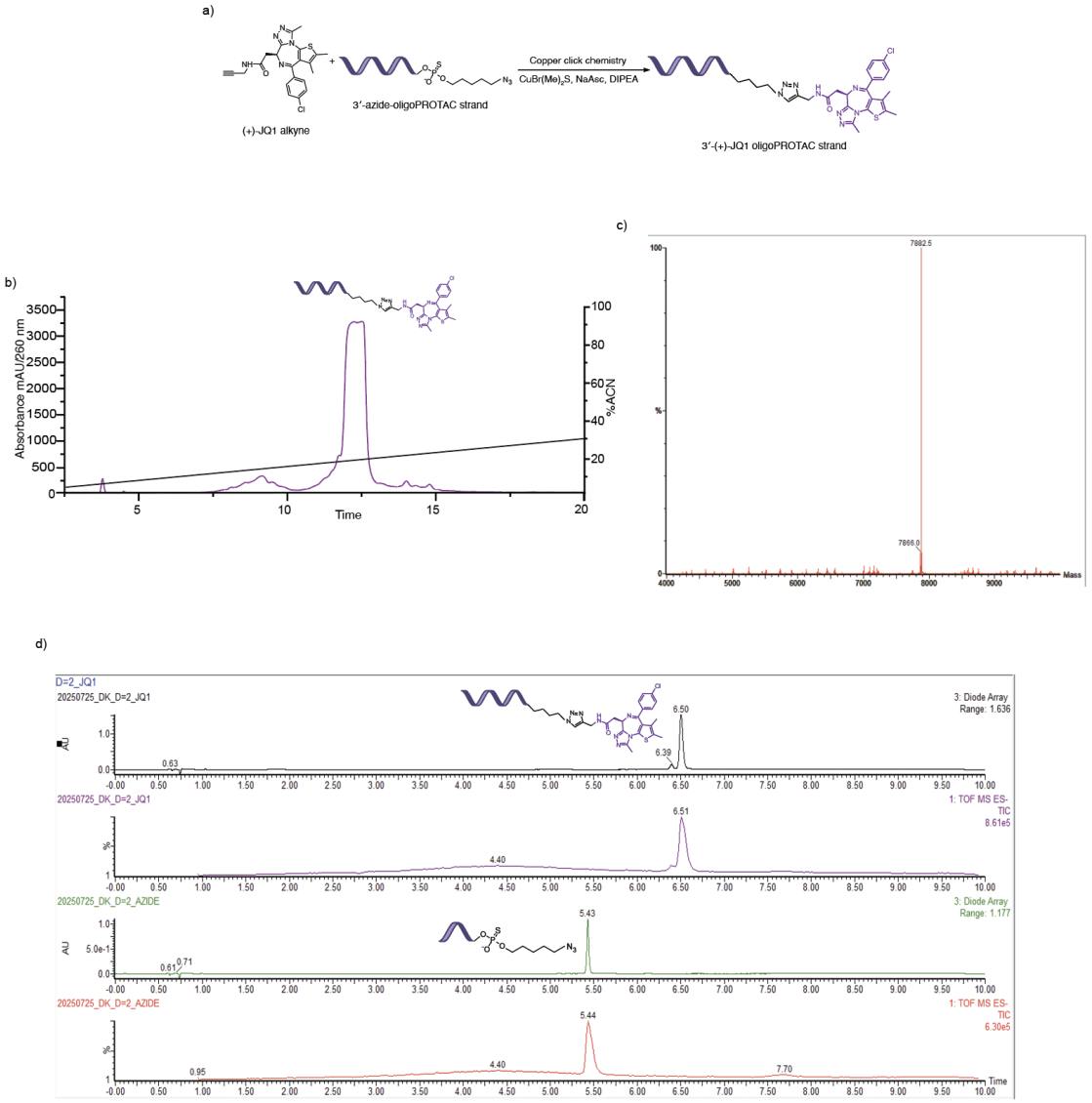

Figure A.33: Reaction and characterisation for (+)-JQ1 ssDNA OligoPROTAC, [n=2]. (a) Reaction scheme for copper click conjugation of (+)-JQ1-alkyne with azide-OligoPROTAC, [n=2]. (b) HPLC purification for (+)-JQ1 ssDNA OligoPROTAC, [n=2]. (c) Mass spectrum for HPLC-purified (+)-JQ1 ssDNA OligoPROTAC, [n=2]. (d) LC-MS characterisation for (+)-JQ1 ssDNA OligoPROTAC, [n=2].

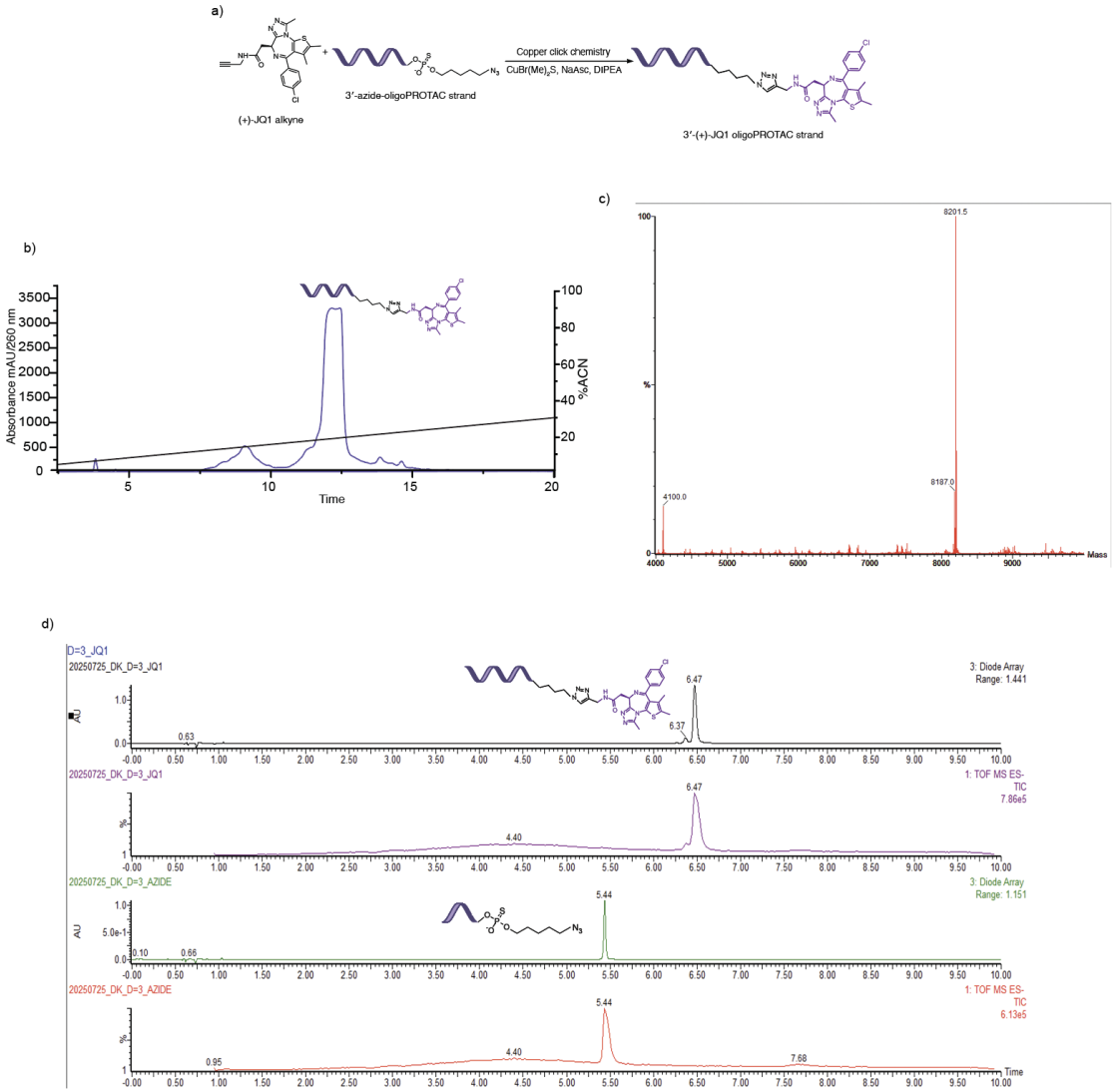

Figure A.34: Reaction and characterisation for (+)-JQ1 ssDNA OligoPROTAC, [n=3]. (a) Reaction scheme for copper click conjugation of (+)-JQ1-alkyne with azide-OligoPROTAC, [n=3]. (b) HPLC purification for (+)-JQ1 ssDNA OligoPROTAC, [n=3]. (c) Mass spectrum for HPLC-purified (+)-JQ1 ssDNA OligoPROTAC, [n=3]. (d) LC-MS characterisation for (+)-JQ1 ssDNA OligoPROTAC, [n=3].

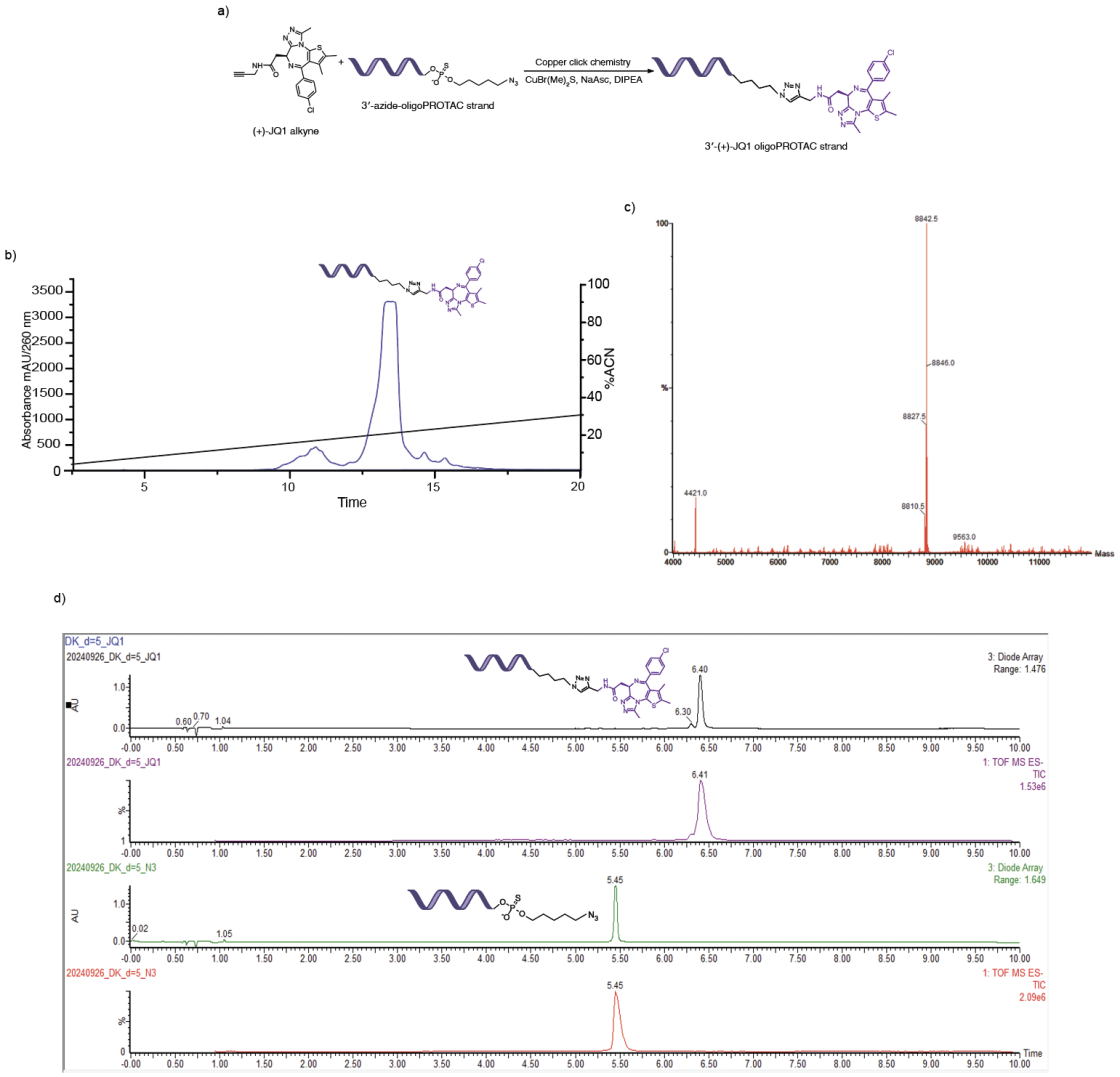

Figure A.35: Reaction and characterisation for (+)-JQ1 ssDNA OligoPROTAC, [n=5]. (a) Reaction scheme for copper click conjugation of (+)-JQ1-alkyne with azide-OligoPROTAC, [n=5]. (b) HPLC purification for (+)-JQ1 ssDNA OligoPROTAC, [n=5]. (c) Mass spectrum for HPLC-purified (+)-JQ1 ssDNA OligoPROTAC, [n=5]. (d) LC-MS characterisation for (+)-JQ1 ssDNA OligoPROTAC, [n=5].

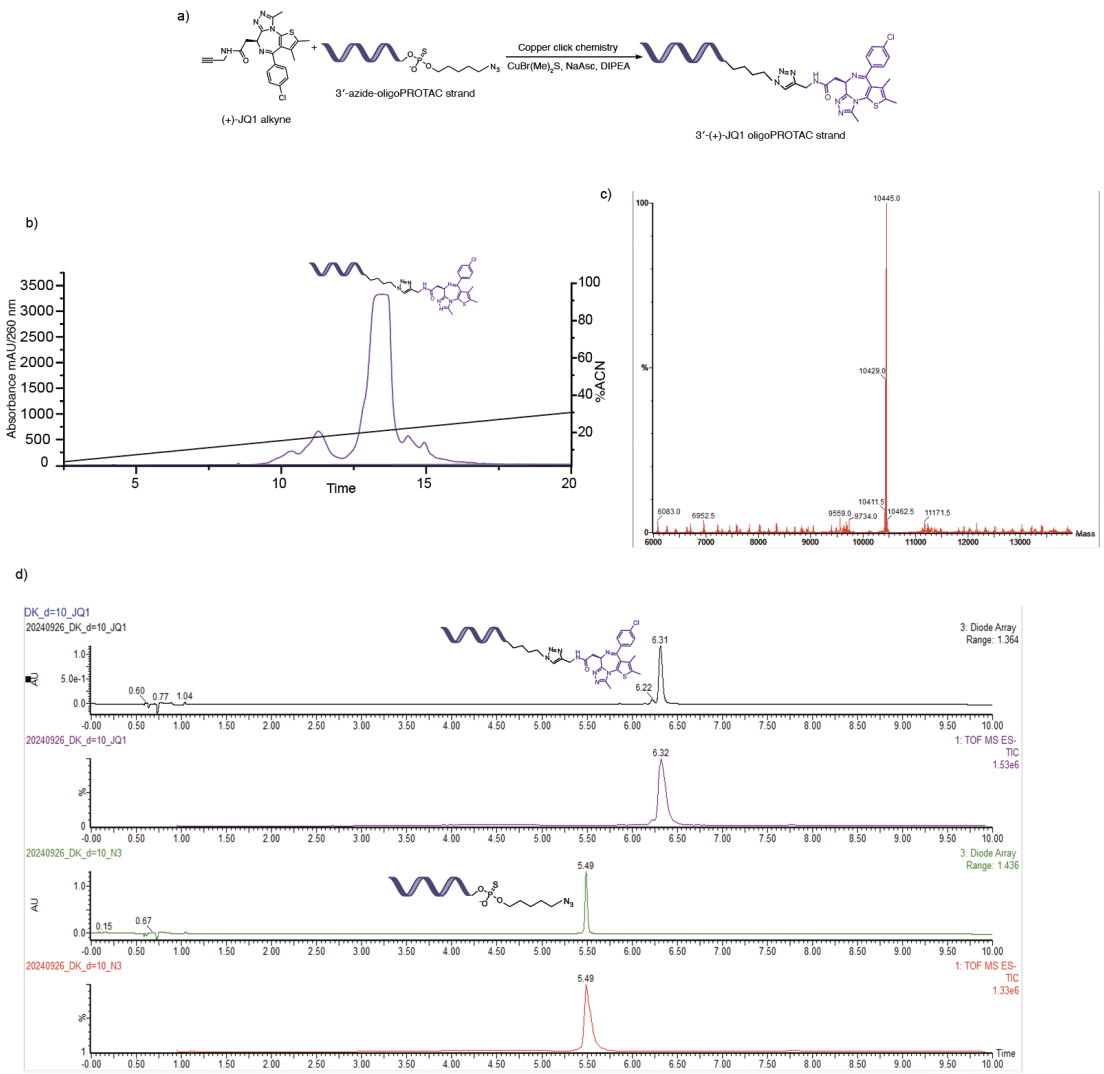

Figure A.36: Reaction and characterisation for (+)-JQ1 ssDNA OligoPROTAC, [n=10]. (a) Reaction scheme for copper click conjugation of (+)-JQ1-alkyne with azide-OligoPROTAC, [n=10]. (b) HPLC purification for (+)-JQ1 ssDNA OligoPROTAC, [n=10]. (c) Mass spectrum for HPLC-purified (+)-JQ1 ssDNA OligoPROTAC, [n=10]. (d) LC-MS characterisation for (+)-JQ1 ssDNA OligoPROTAC, [n=10].

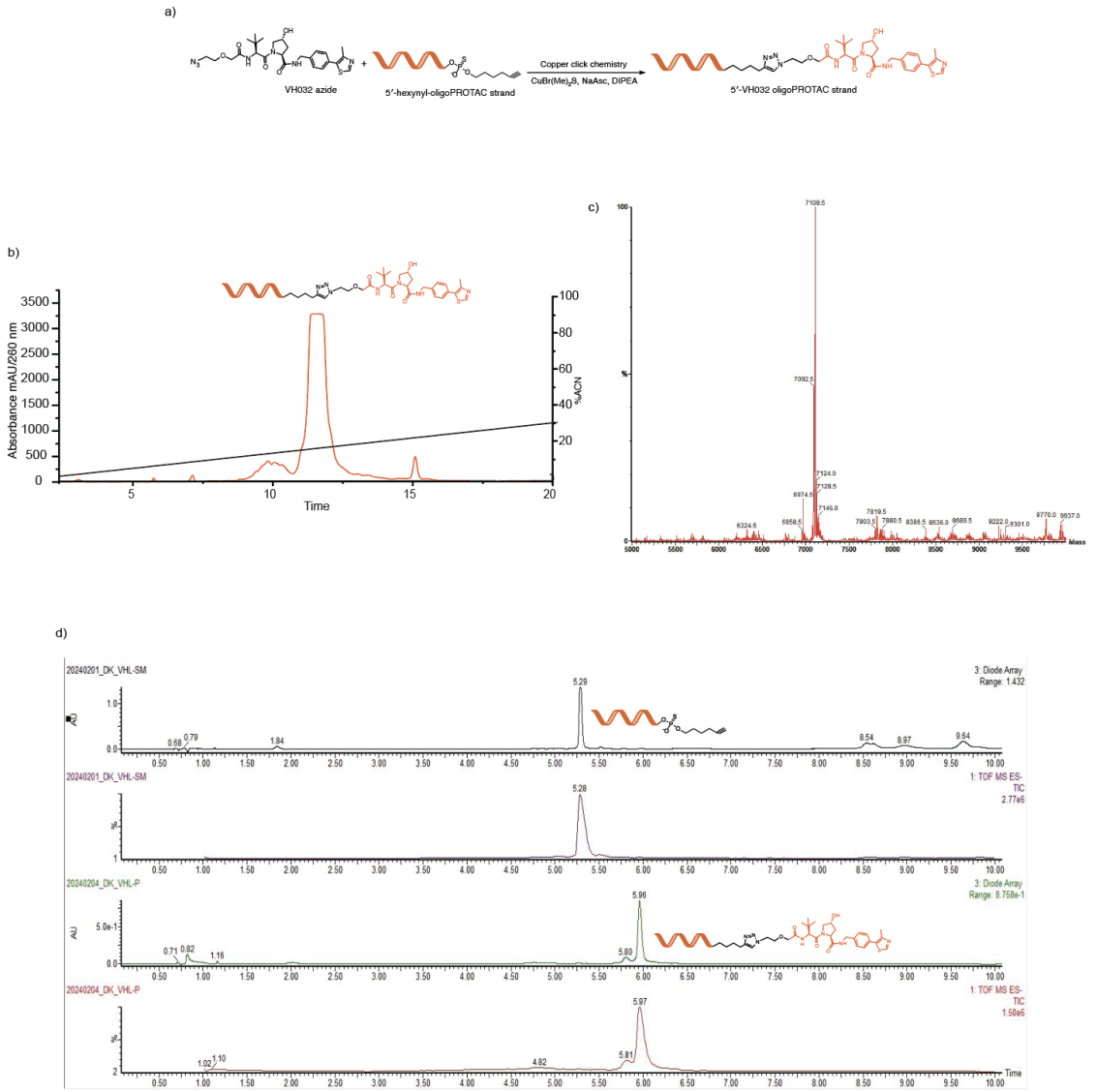

Figure A.37: Reaction and characterisation for VH032 ssDNA OligoPROTAC, [n=0]. (a) Reaction scheme for copper click conjugation of VH032 azide with alkyne-OligoPROTAC, [n=0]. (b) HPLC purification for VH032 ssDNA OligoPROTAC, [n=0]. (c) Mass spectrum for HPLC-purified VH032 ssDNA OligoPROTAC, [n=0].(d) LC-MS characterisation for VH032 ssDNA OligoPROTAC, [n=0].

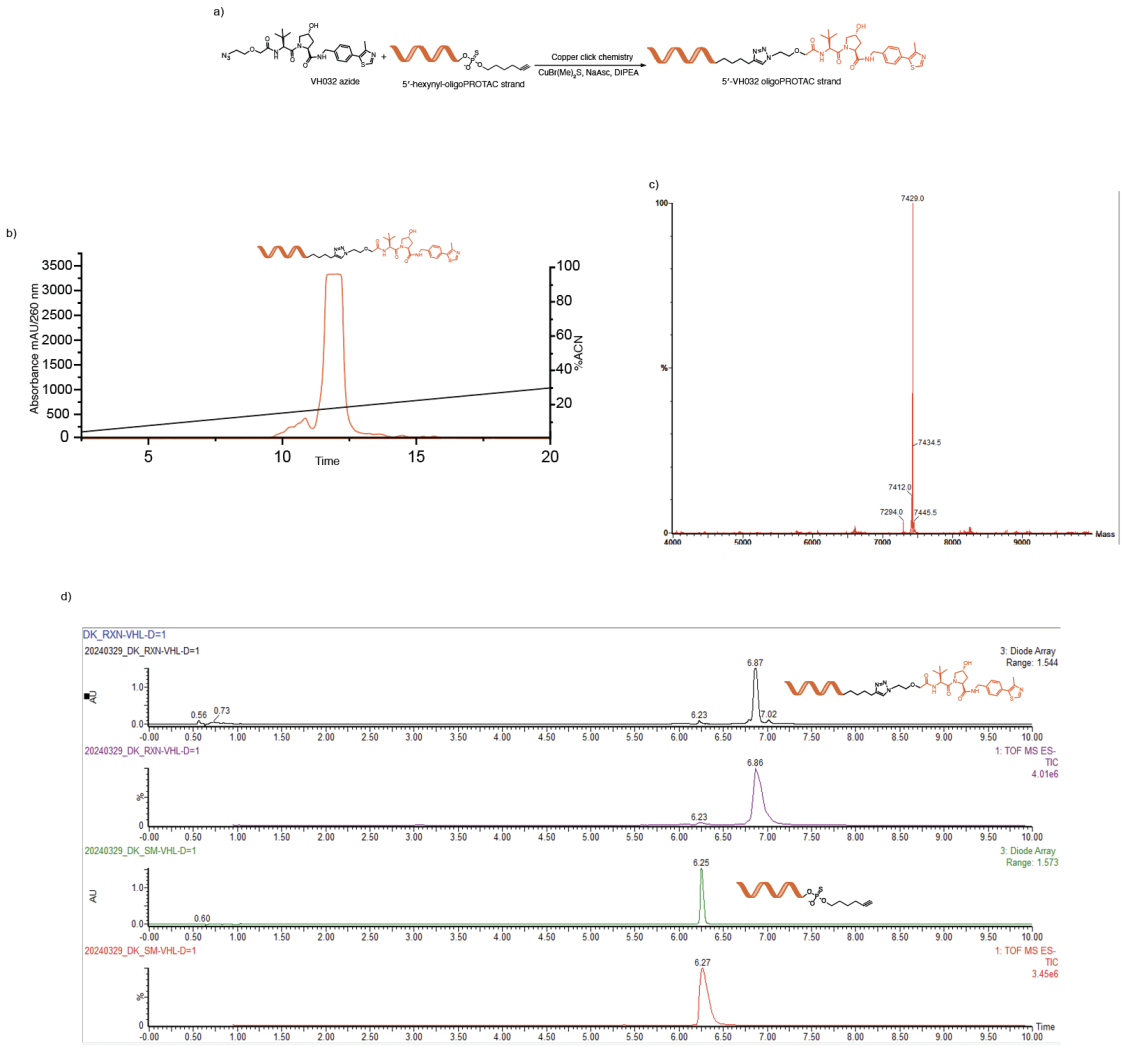

Figure A.38: Reaction and characterisation for VH032 ssDNA OligoPROTAC, [n=1]. (a) Reaction scheme for copper click conjugation of VH032 azide with alkyne-OligoPROTAC, [n=1]. (b) HPLC purification for VH032 ssDNA OligoPROTAC, [n=1]. (c) Mass spectrum for HPLC-purified VH032 ssDNA OligoPROTAC, [n=1].(d) LC-MS characterisation for VH032 ssDNA OligoPROTAC, [n=1].

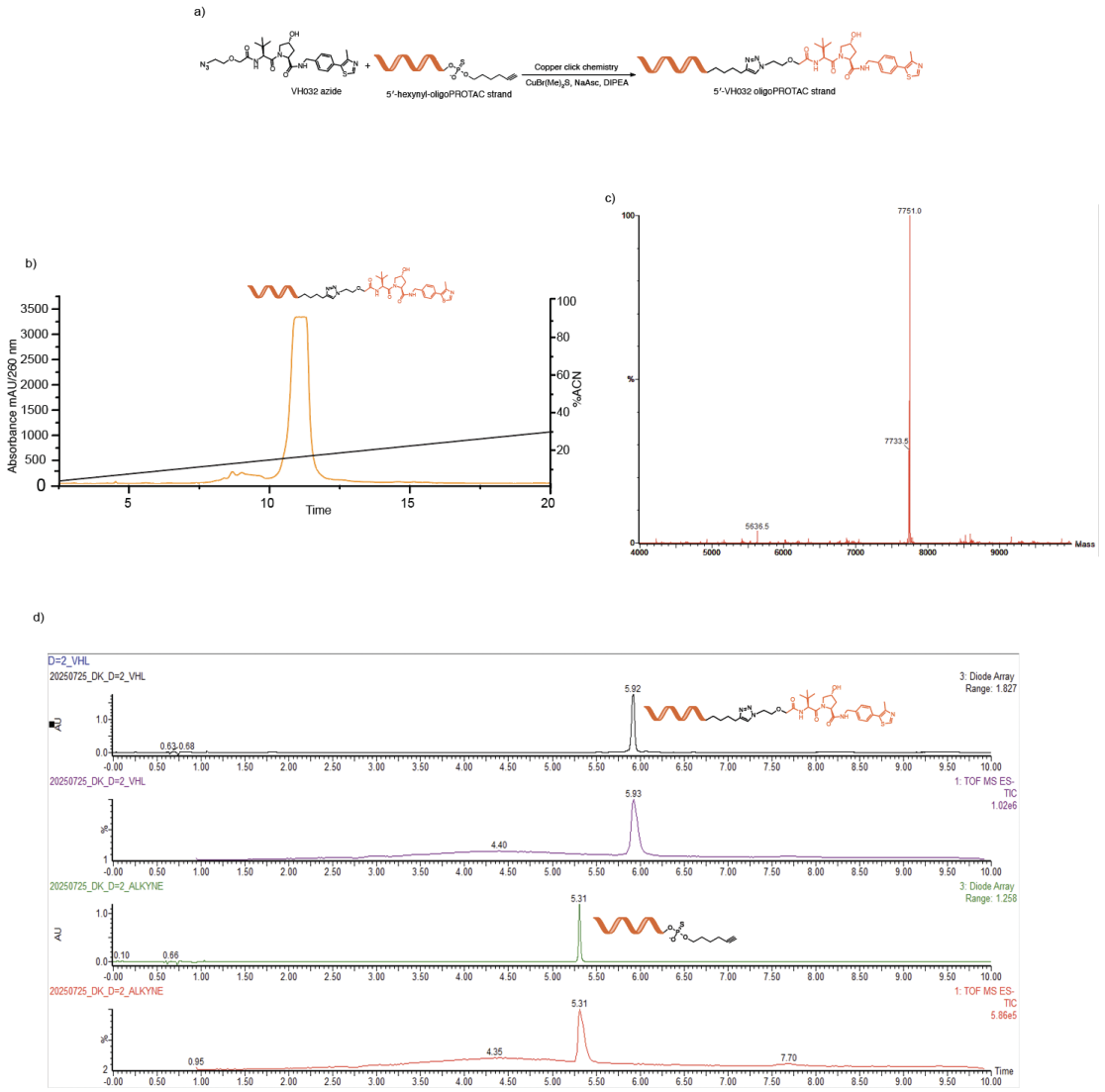

Figure A.39: Reaction and characterisation for VH032 ssDNA OligoPROTAC, [n=2]. (a) Reaction scheme for copper click conjugation of VH032 azide with alkyne-OligoPROTAC, [n=2]. (b) HPLC purification for VH032 ssDNA OligoPROTAC, [n=2]. (c) Mass spectrum for HPLC-purified VH032 ssDNA OligoPROTAC, [n=2].(d) LC-MS characterisation for VH032 ssDNA OligoPROTAC, [n=2].

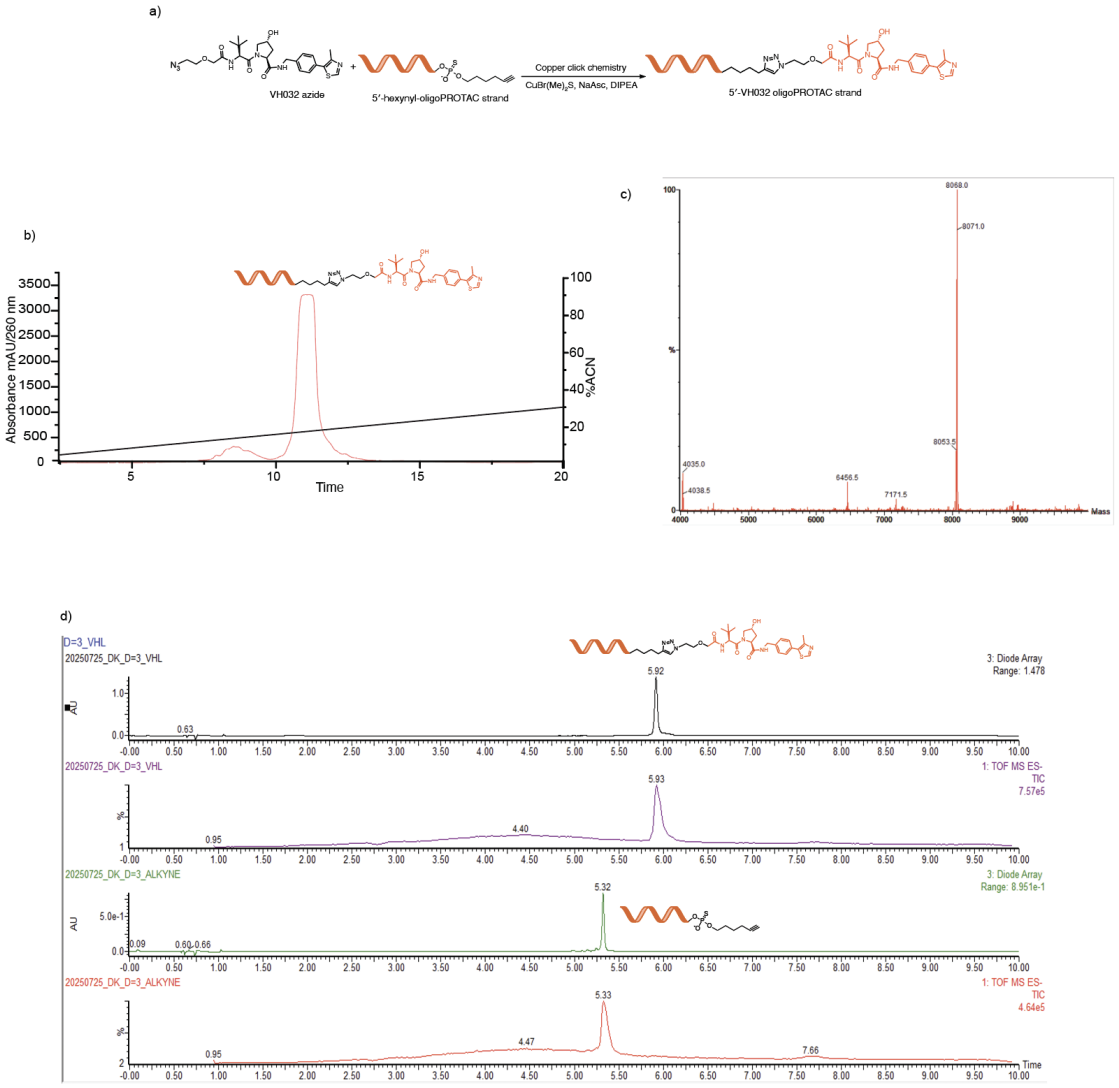

Figure A.40: Reaction and characterisation for VH032 ssDNA OligoPROTAC, [n=3]. (a) Reaction scheme for copper click conjugation of VH032 azide with alkyne-OligoPROTAC, [n=3]. (b) HPLC purification for VH032 ssDNA OligoPROTAC, [n=3]. (c) Mass spectrum for HPLC-purified VH032 ssDNA OligoPROTAC, [n=3].(d) LC-MS characterisation for VH032 ssDNA OligoPROTAC, [n=3].

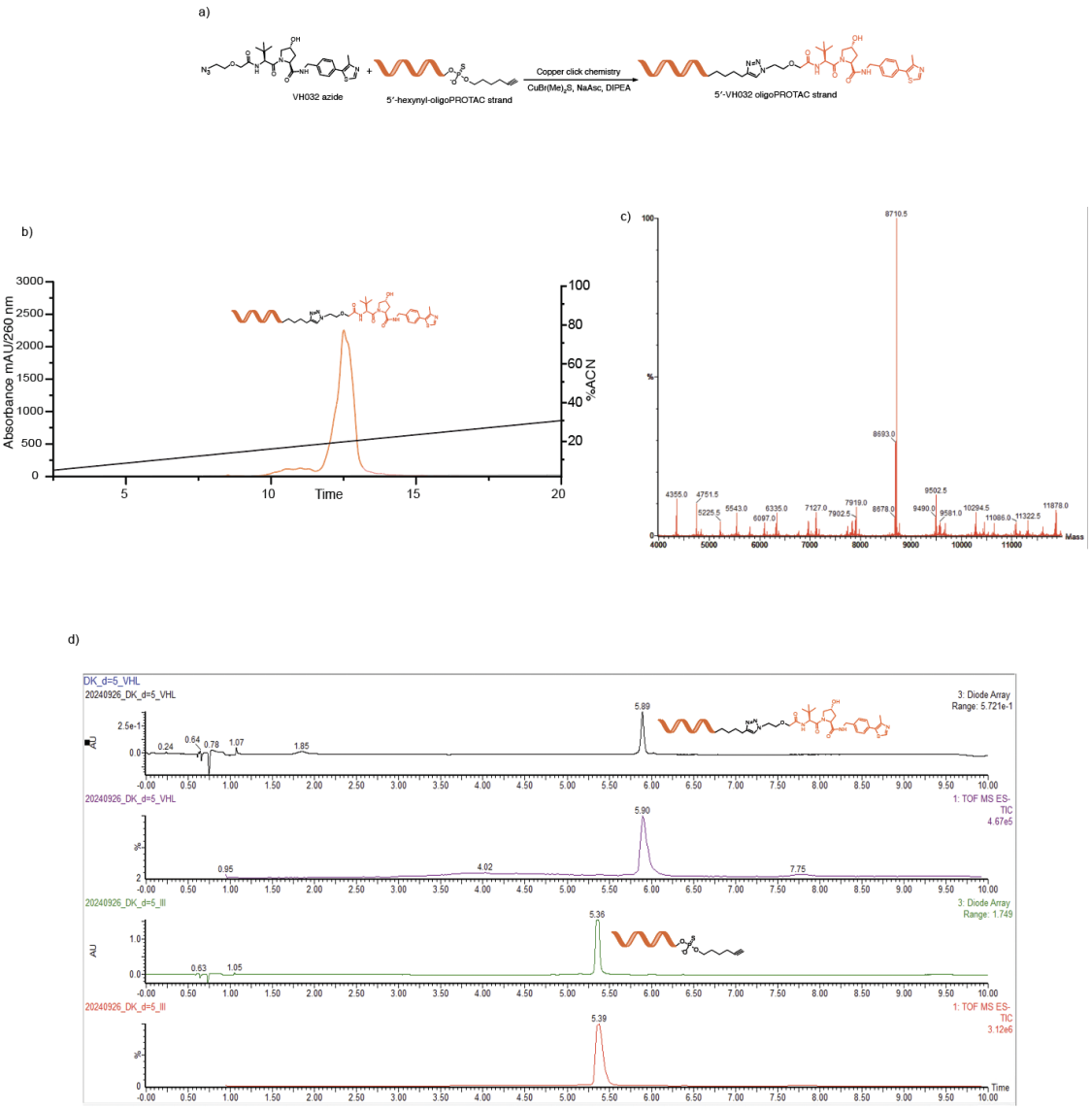

Figure A.41: Reaction and characterisation for VH032 ssDNA OligoPROTAC, [n=5]. (a) Reaction scheme for copper click conjugation of VH032 azide with alkyne-OligoPROTAC, [n=5]. (b) HPLC purification for VH032 ssDNA OligoPROTAC, [n=5]. (c) Mass spectrum for HPLC-purified VH032 ssDNA OligoPROTAC, [n=5].(d) LC-MS characterisation for VH032 ssDNA OligoPROTAC, [n=5].

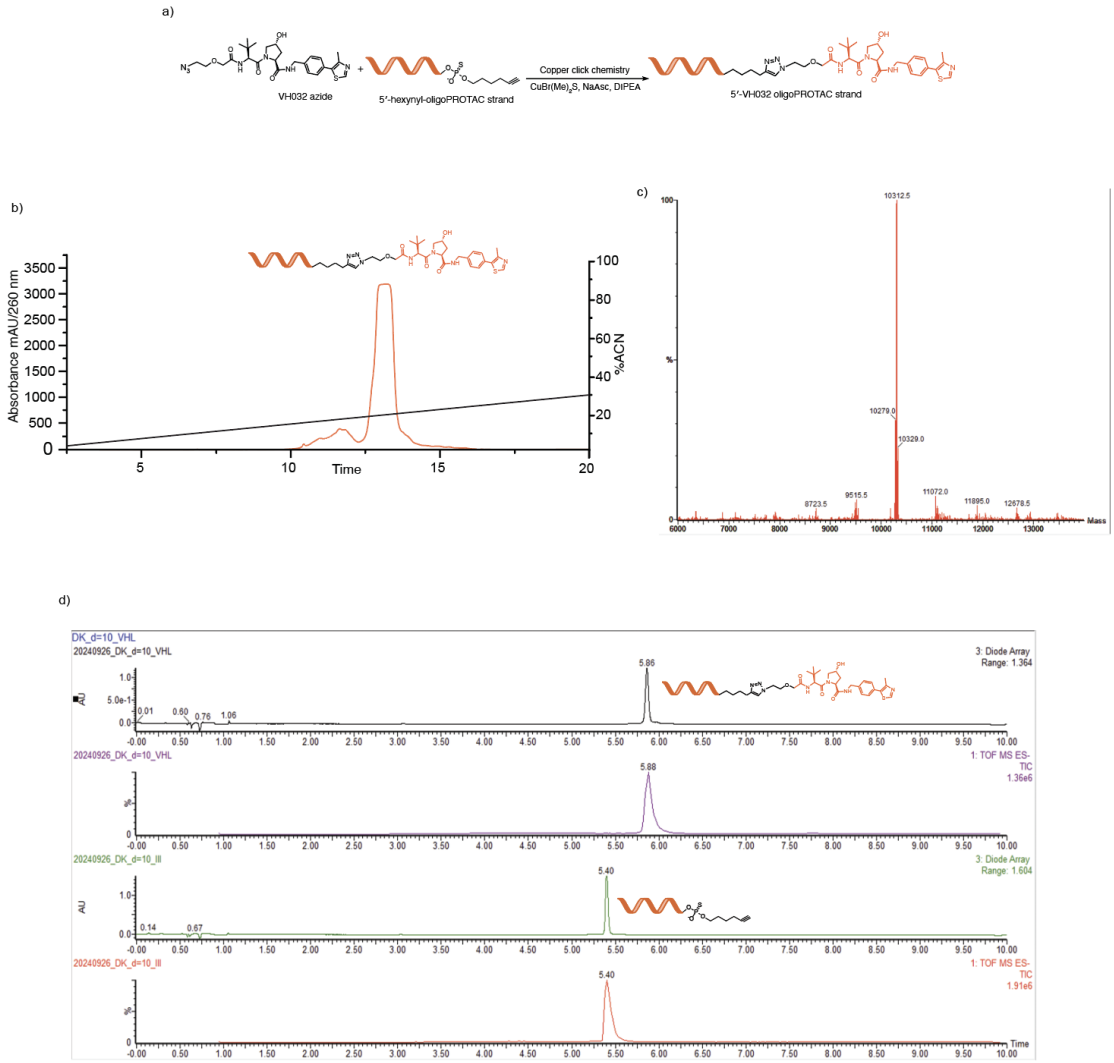

Figure A.42: Reaction and characterisation for VH032 ssDNA OligoPROTAC, [n=10]. (a) Reaction scheme for copper click conjugation of VH032 azide with alkyne-OligoPROTAC, [n=10]. (b) HPLC purification for VH032 ssDNA Oligo-PROTAC, [n=10]. (c) Mass spectrum for HPLC-purified VH032 ssDNA Oligo-PROTAC, [n=10].(d) LC-MS characterisation for VH032 ssDNA OligoPROTAC, [n=10].

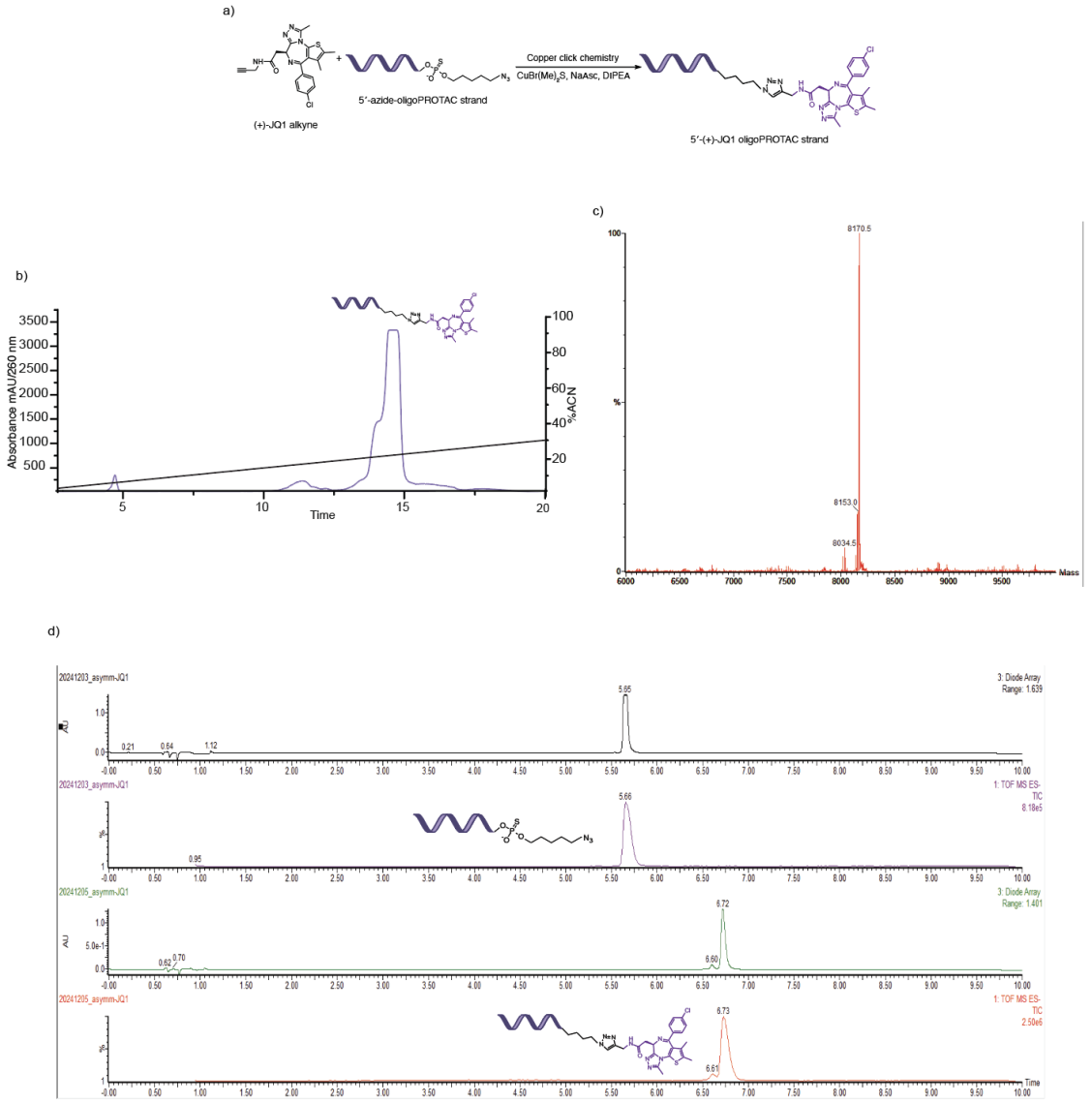

Figure A.43: Reaction and characterisation for asymmetric 5′- JQ1 ssDNA Oligo-PROTAC, [n=3]. (a) Reaction scheme for copper click conjugation of (+)-JQ1-alkyne with 5'-azide-OligoPROTAC, [n=10]. (b) HPLC purification for (+)-JQ1 asymmetric ssDNA OligoPROTAC, [n=3]. (c) Mass spectrum for HPLC-purified (+)-JQ1 asymmetric ssDNA OligoPROTAC, [n=3]. (d) LC-MS characterisation for (+)-JQ1 asymmetric ssDNA OligoPROTAC, [n=3].

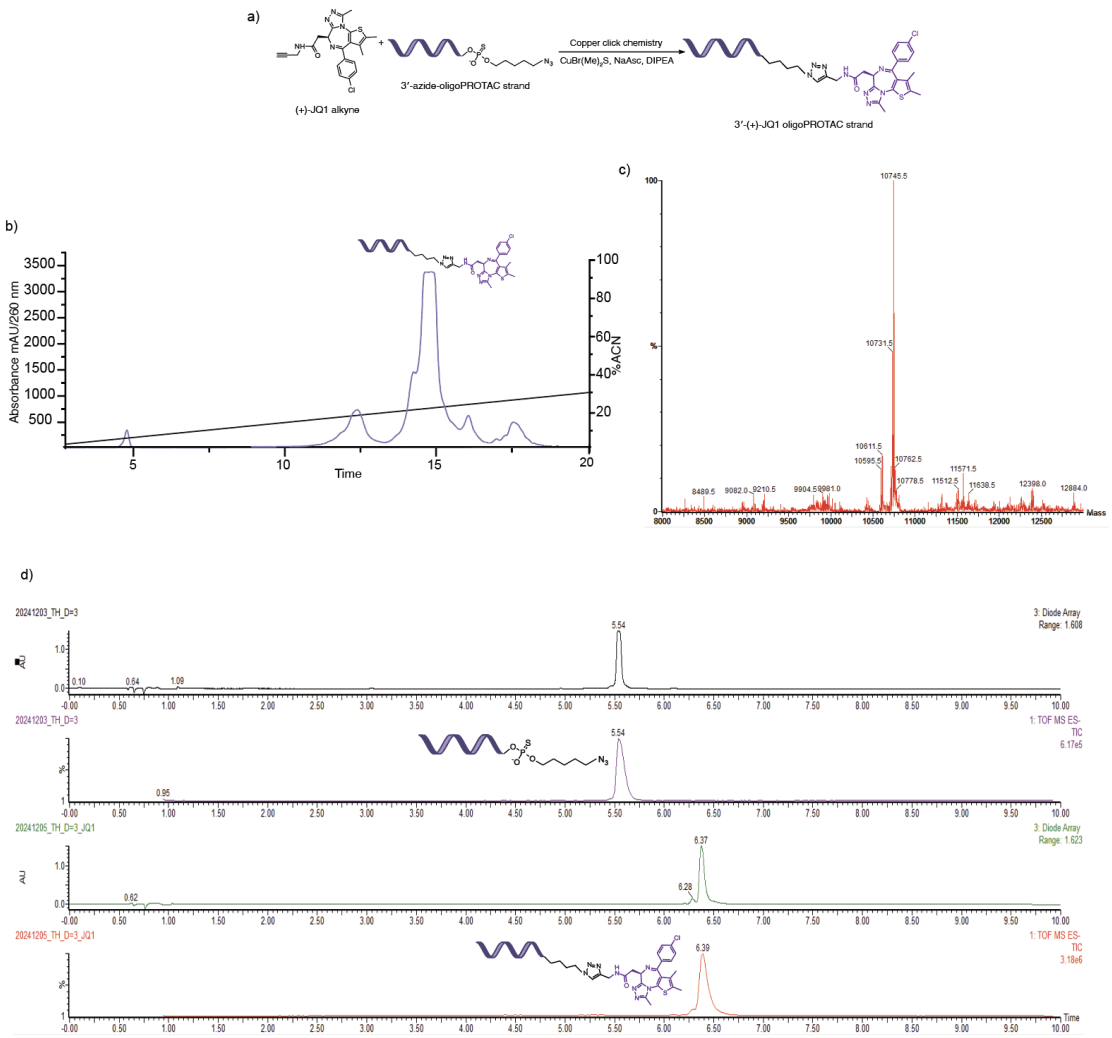

Figure A.44: Reaction and characterisation for toehold-(+)-JQ1 ssDNA OligoPROTAC, [n=3]. (a) Reaction scheme for copper click conjugation of (+)-JQ1-alkyne with azide-toehold-OligoPROTAC, [n=3]. (b) HPLC purification for toehold-(+)-JQ1 ssDNA OligoPROTAC, [n=3]. (c) Mass spectrum for HPLC-purified toehold-(+)-JQ1 ssDNA OligoPROTAC, [n=3]. (d) LC-MS characterisation for toehold-(+)-JQ1 ssDNA OligoPROTAC, [n=3].

A.3 Uncropped western blots

Chapter 2: Altering the subcellular localization of ASOs to improve their therapeutic engagement and efficacy

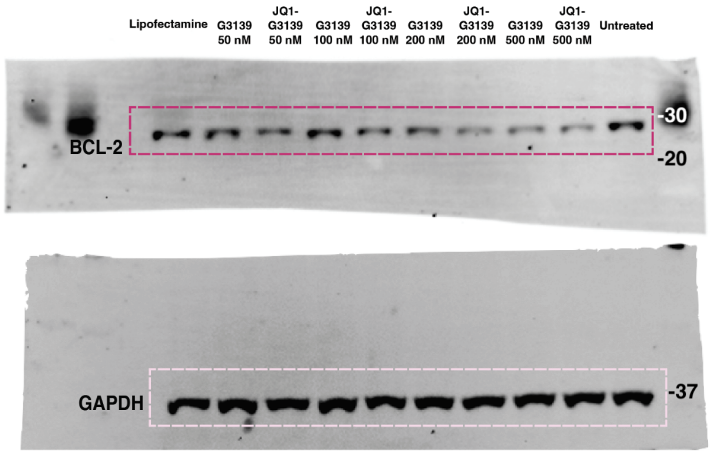

Figure A.45: Uncropped western blot of BCL-2 levels upon treatment with G3139 and (+)-JQ1-G3139 upon transfection with lipofectamine at 24 hours. Normalised to GAPDH expression levels.

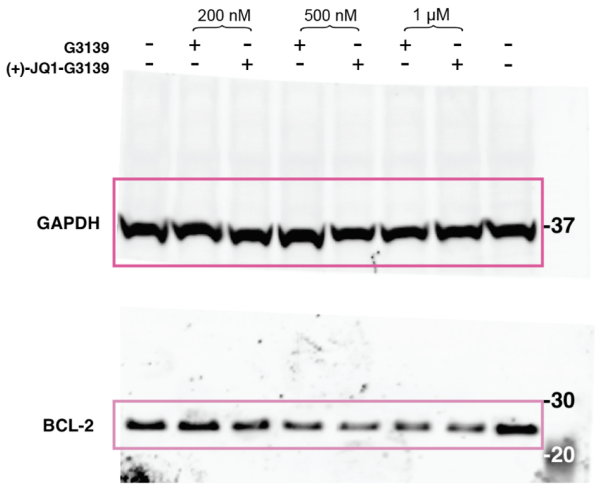

Figure A.46: Uncropped western blot of BCL-2 levels in THP-1s upon treatment with G3139 and (+)-JQ1-G3139, two rounds of electroporation at 96 hours at concentrations indicated. Normalised to GAPDH expression levels.

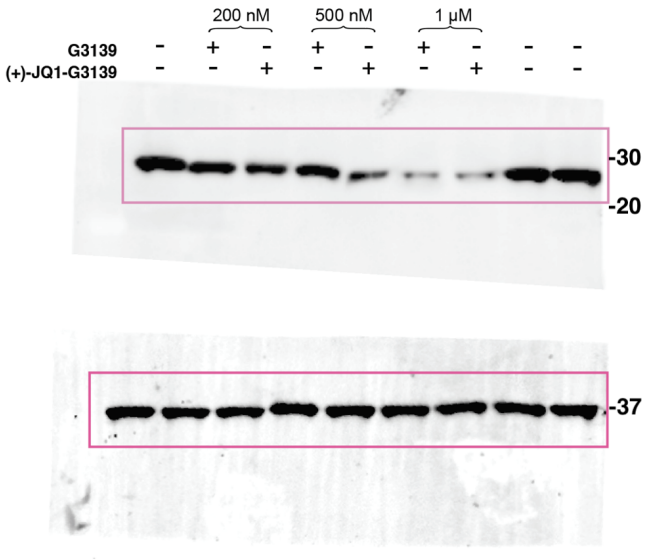

Figure A.47: Uncropped western blot of BCL-2 levels in THP-1s upon treatment with G3139 and (+)-JQ1-G3139, two rounds of electroporation at 96 hours at concentrations indicated. Normalised to GAPDH expression levels (biological replicate).

Chapter 4: Designing small-molecule ASO conjugates to harness the lysosome for targeted mRNA degradation

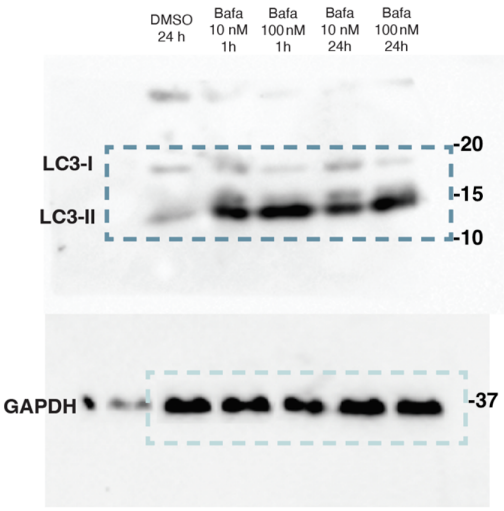

Figure A.48: Uncropped western for LC3-I and LC3-II levels upon treatment with bafilomycin at indicated concentrations and time points, in HEK293Ts. Normalised to GAPDH levels.

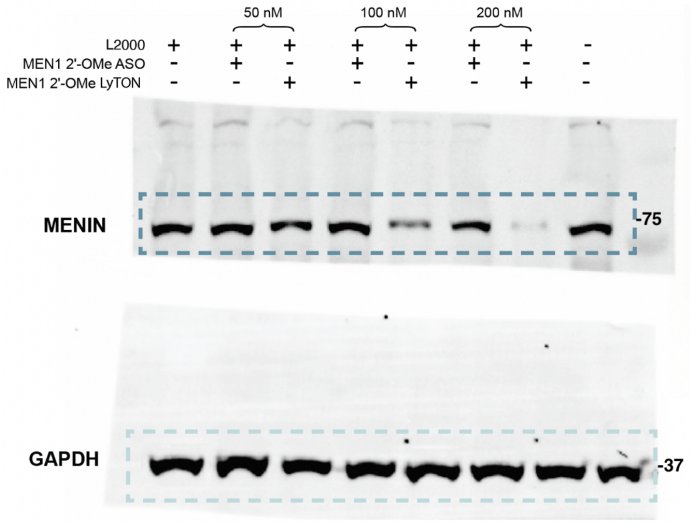

Figure A.49: Uncropped western blot of Menin levels upon treatment with MEN1 2'-OMe ASO and MEN1 2'-OMe LyTON upon transfection with lipofectamine, harvested at 48 hours in HEK293Ts. Normalised to GAPDH levels.

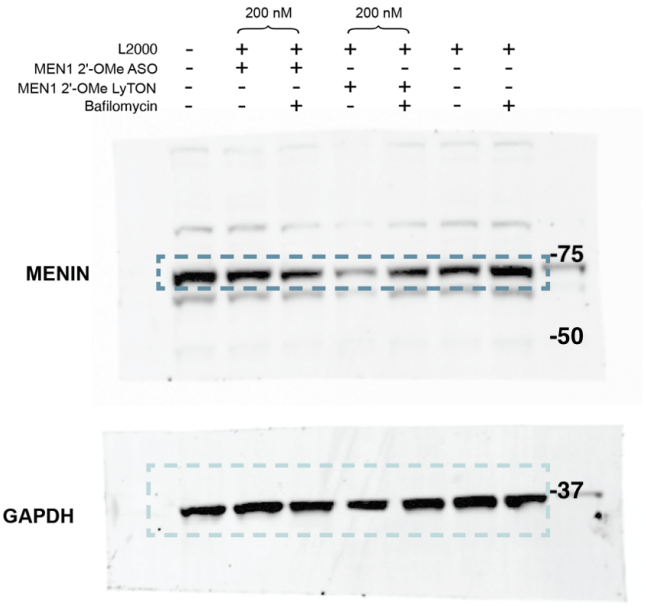

Figure A.50: Uncropped western blot of Menin levels upon treatment with MEN1 2'-OMe ASO and MEN1 2'-OMe LyTON – in presence and absence of 10 nM bafilomycin, upon transfection with lipofectamine, harvested at 48 hours in HEK293Ts. Normalised to GAPDH levels.

Chapter 6: Tunable control over PROTAC Activity via DNA Hybridization and Strand Displacement

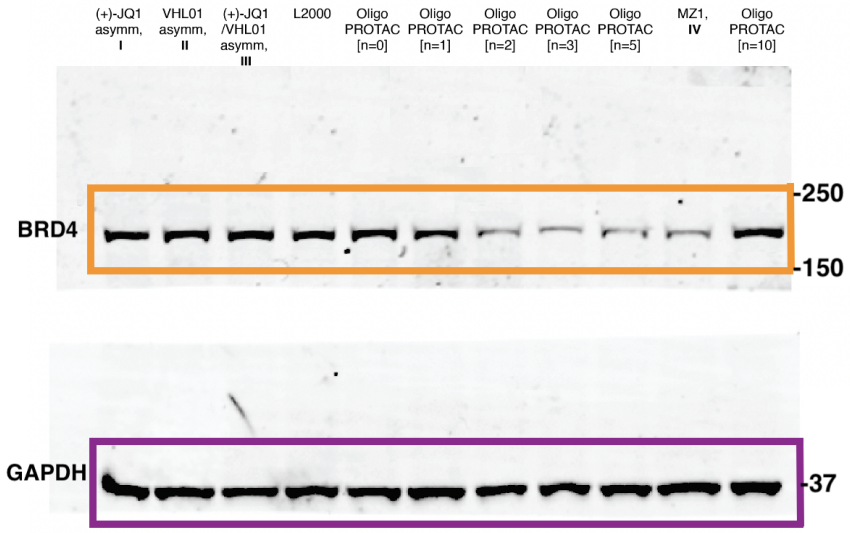

Figure A.51: Uncropped western blot of BRD4 levels upon lipofectamine 2000 transfection in HEK293T with OligoPROTACs of varying linker lengths and partial PROTAC control constructs.

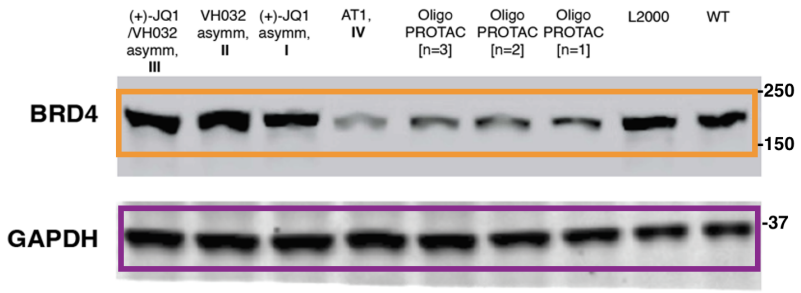

Figure A.52: Uncropped western blot of BRD4 levels upon lipofectamine 2000 transfection in HeLa with OligoPROTACs of varying linker lengths and partial PROTAC control constructs.

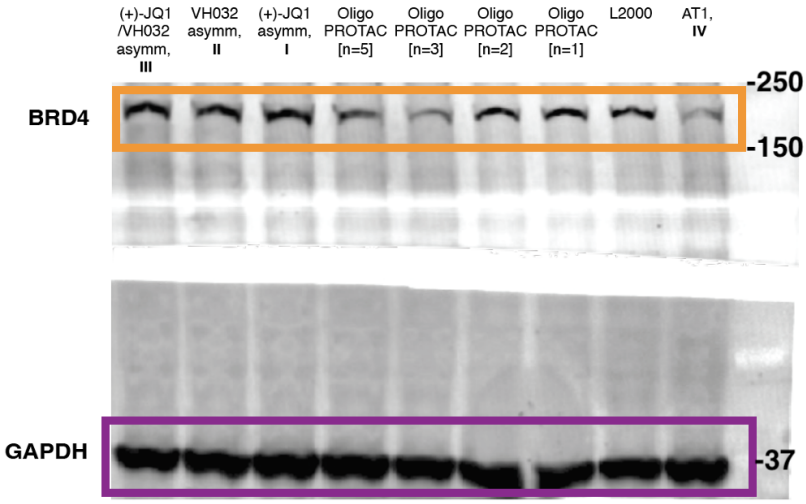

Figure A.53: Uncropped western blot of BRD4 levels upon lipofectamine 2000 transfection in A549 with OligoPROTACs of varying linker lengths and partial PROTAC control constructs.

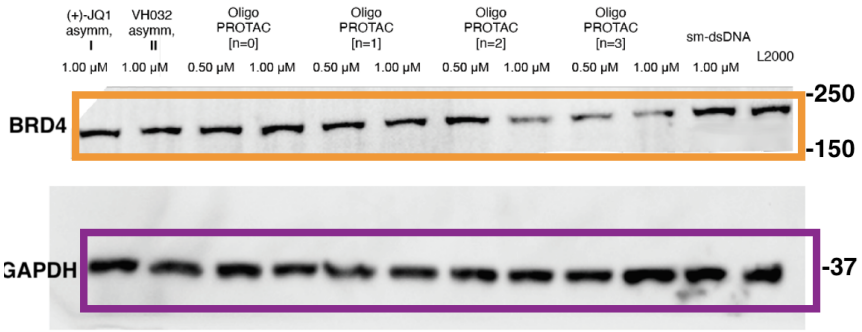

Figure A.54: Uncropped western blot of BRD4 levels upon lipofectamine 2000 transfection in HEK293T with OligoPROTAC of varying linker lengths, [n=1, 2, 3] and partial PROTAC control constructs.

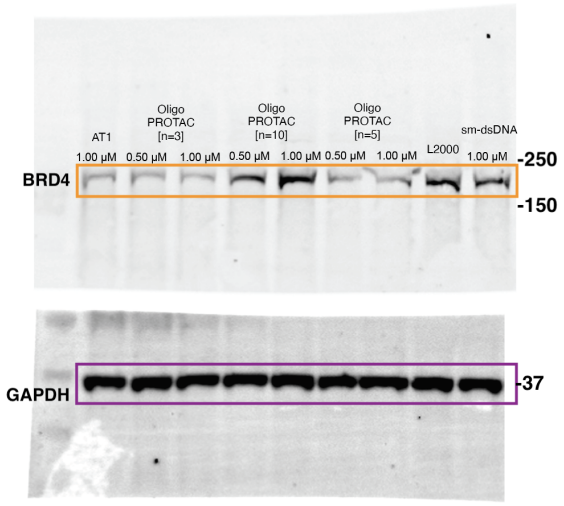

Figure A.55: Uncropped western blot of BRD4 levels upon lipofectamine 2000 transfection in HEK293T with OligoPROTAC of varying linker lengths, [n=3, 5, 10] and control constructs.

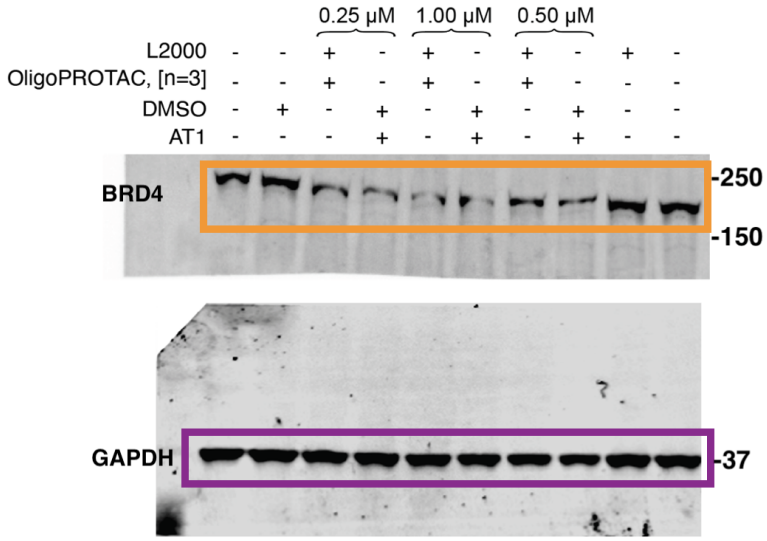

Figure A.56: Uncropped western blot for BRD4 levels upon treatment with [n=3] OligoPROTAC and small molecule PROTAC, AT1 at concentrations indicated over upon Lipofectamine 2000 transfection/DMSO treatment in HEK293T cells at 12 hours.

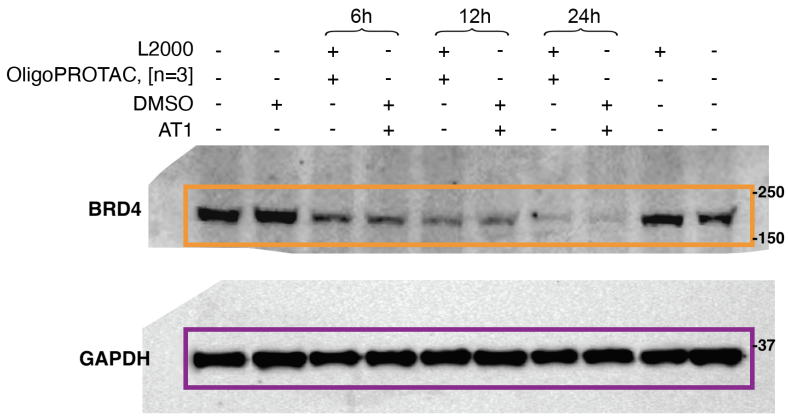

Figure A.57: Uncropped western blot for BRD4 levels upon treatment with [n=3] OligoPROTAC and small molecule PROTAC, AT1 at 1.00 µM over 6 hours, 12 hours, and 24 hours upon Lipofectamine 2000 transfection/DMSO treatment in HEK293T cells.

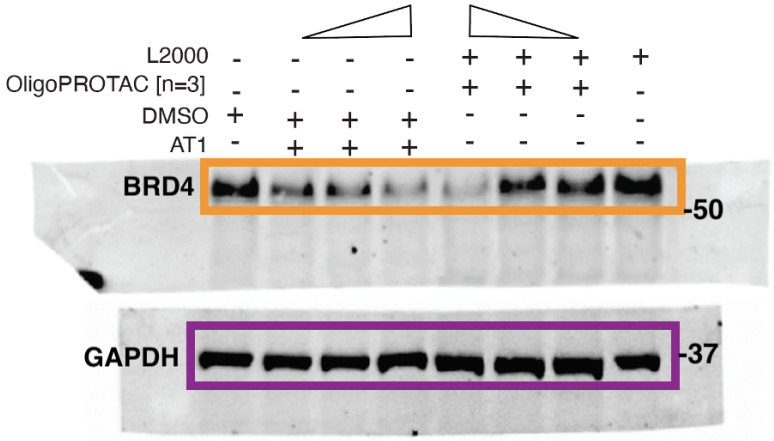

Figure A.58: Uncropped western blot for MYC levels upon treatment with [n=3] OligoPROTAC and small molecule PROTAC, AT1 at concentrations (0.25, 0.50, 1.00 µM) upon Lipofectamine 2000 transfection/DMSO treatment in HEK293T cells at 12 hours.

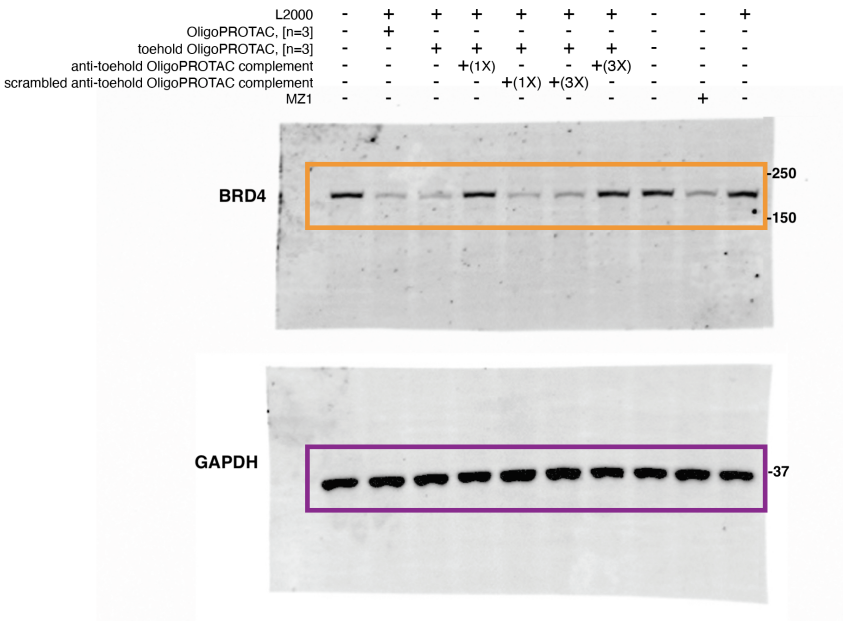

Figure A.59: Uncropped western blot of BRD4 levels upon treatment with toehold OligoPROTAC [n=3], along with anti-toehold complement and scrambled anti-toehold complement upon lipofectamine 2000 transfection in HEK293T cells.

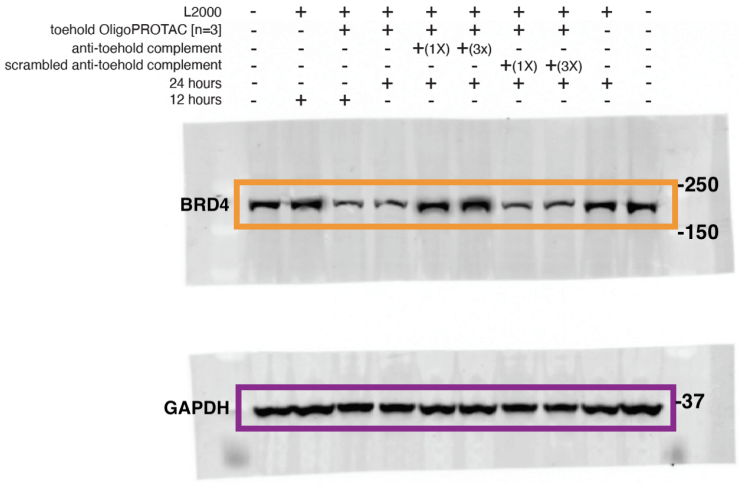

Figure A.60: Uncropped western blot of BRD4 levels upon treatment with toehold OligoPROTAC [n=3] for 12 hours, followed by anti-toehold complement and scrambled anti-toehold complement incubation for another 12 hours – harvest at 24 hours.

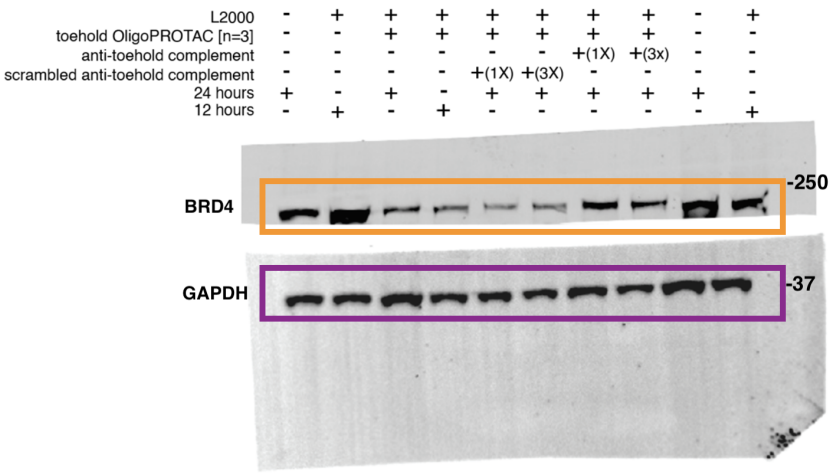

Figure A.61: Uncropped western blot of BRD4 levels upon treatment with toehold OligoPROTAC [n=3] for 12 hours, followed by anti-toehold complement and scrambled anti-toehold complement incubation for another 12 hours – harvest at 24 hours (biological replicate).

A.4 Nucleotide sequences for truncated gene constructs of *MLL-AF4*, *MLL*, and *AF4*

Table A.1: Sequences for truncated gene constructs of *MLL-AF4*, *MLL*, and *AF4* (5′- 3′)

S. No.	Name	Sequence (5′- 3′)
1	MLL	GGAAATAAAAGGCCAAAGCTCAGCTCTGCAAGA TTGAGAAGAGTAAGAGTCTTAAACAAACCGACC AGCCCAAAGCACAGGGTCAAGAAAGTGACTCAT CAGAGACCTCTGTGCGAGGACCCCGGATTAAAC ATGTCTGCAGAAGAGCAGCTGTTGCCCTTGGCC GAAAACGAGCTGTGTTTCCTGATGACATGCCCA CCCTGAGTGCCTTACCATGGGAAGAACGAGAAA AGATTTTGTCTTCCATGGGGAATGATGACAAGT CATCAATTGCTGGCTCAGAAGATGCTGAACCTCT TGCTCCACCCATCAAACCAATTAAACCTGTCACT AGAAACAAGGCACCCCAGGAACCTCCAGTAAAG AAAGGACGTCGATCGAGGCGGTGTGGGCAGTGT CCCGGCTGCCAGGTGCCTGAGGACTGTGGTGTT TGTACTAATTGCTTAGATAAGCCCAAGTTTGGT

S. No.	Name	Sequence (5′–3′)
1	MLL	GGTCGCAATATAAAGAAGCAGTGCTGCAAGATG AGAAAATGTCAGAATCTACAATGGATGCCTTCC AAAGCCTACCTGCAGAAGCAAGCTAAAGCTGTG AAAAAGAAAGAGAAAAAGTCTAAGACCAGTGAA AAGAAAGACAGCAAAGAGAGCAGTGTTGTGAAG AACGTGGTGGACTCTAGTCAGAAACCTACCCCA TCAGCAAGAGAGGATCCTGCCCCAAAGAAAAGC AGTAGTGAGCCTCCTCCACGAAAGCCCGTCGAG GAAAAGAGTGAAGAAGGGAATGTCTCGGCCCCT GGGCCTGAATCCAAACAGGCCACCACTCCAGCTT CCAGGAAGTCAAGCAAGCAGGTCTCCCAGCCAG CACTGGTCATCCCGCCTCAGCCACCTACTACAGG ACCGCCAAGAAAAGAAGTTCCCAAAACCACTCCT AGTGAGCCCAAGAAAAAGCAGCCTCCACCACCA GAATCAGGTCCAGAGCAGAGCAAACAGAAAAAA GTGGCTCCCCGCCCAAGTATCCCTGTAAAACAAA AACCAAAAGAAAAGGAAAAACCACCTCCGGTCA ATAAGCAGGAGAATGCAGGCACTTTGAACATCC TCAGCACTCTCTCCAATGGCAATAGTTCTAAGCA AAAAATTCCAGCAGATGGAGTCCACAGGATCAG AGTGGACTTTAAGGAGGATTGTGAAGCAGAAAA TGTGTGGGAGATGGGAGGCTTAGGAATCTTGAC TTCTGTTCCTATAACACCCAGGGTGGTTTGCTTT CTCTGTGCCAGTAGTGGGCATGTAGAGTTTGTG TATTGCCAAGTCTGTTGTGAGCCCTTCCACAAGT TTTGTTTAGAGGAGAACGAGCGCCCTCTGGAGG ACCAGCTGGAAAATTGGTGTTGTCGTCGTTGCA AATTCTGTCACGTTTGTGGAAGGCAACATCAGG CTACAAAGCAGCTGCTGGAGTGTAATAAGTGCC GAAACAGCTATCACCCTGAGTGCCTGGGACCAA ACTACCCCACCAAACCCACAAAGAAGAAGAAAG TCTGGATCTGTACCAAGTGTGTTCGCTGTAAGA GCTGTGGATCCACAACTCCAGGCAAAGGGTGGG ATGCACAGTGGTCTCATGATTTCTCACTGTGTCA TGATTGCGCCAAGCTCTTTGCTAAAGGAAACTTC TGCCCTCTCTGTGACAAATGTTATGATGATGAT GACTATGAGAGTAAGATGATGCAATGTGGAAAG TGTGATCGCTGGGTCCATTCCAAATGTGAGAAT CTTTCAGATGAGATGTATGAGATTCTATCTAATC TGCCAGAAAGTGTGGCCTACACTTGTGTGAACT GTACTGAGCGGCACCCTGCAGAGTGGCGACTGG CCCTTGAAAAAGAGCTGCAGATTTCTCTGAAGC AAGTTCTGACAGCTTTGTTGAATTCTCGGACTAC CAGCCATTTGCTACGCTACCGGCAGGCTGCCAA GCCTCCAGACTTAAATCCCGAGACAGAGGAGAG TATACCTTCCCGCAGCTCCCCCGAAGGACCTGAT CCACCAGTTCTTACTGAGGTCAGCAAACAGGAT GATCAGCAGCCTTTA

S. No.	Name	Sequence (5′–3′)
2	AF4	CCTACAAGACAGCAAAAGGTGATGAGCTGTCTA GTCGAATACAGAACATGTTGGGAAACTACGAAG AAGTGAAGGAGTTCCTTAGTACTAAGTCTCACA CTCATCGCCTGGATGCTTCTGAAAATAGGTTGG GAAAGCCGAAATATCCTTTAATTCCTGACAAAG GGAGCAGCATTCCATCCAGCTCCTTCCACACTAG TGTCCACCACCAGTCCATTCACACTCCTGCGTCT GGACCACTTTCTGTTGGCAACATTAGCCACAATC CAAAGATGGCGCAGCCAAGAACTGAACCAATGC CAAGTCTCCATGCCAAAAGCTGCGGCCCACCGG ACAGCCAGCACCTGACCCAGGATCGCCTTGGTC AGGAGGGGTTCGGCTCTAGTCATCACAAGAAAG GTGACCGAAGAGCTGACGGAGACCACTGTGCTT CGGTGACAGATTCGGCTCCAGAGAGGGAGCTTT CTCCCTTAATCTCTTTGCCTTCCCCAGTTCCCCC TTTGTCACCTATACATTCCAACCAGCAAACTCTT CCCCGGACGCAAGGAAGCAGCAAGGTTCATGGC AGCAGCAATAACAGTAAAGGCTATTGCCCAGCC AAATCTCCCAAGGACCTAGCAGTGAAAGTCCAT GATAAAGAGACCCCTCAAGACAGTTTGGTGGCC CCTGCCCAGCCGCCTTCTCAGACATTTCCACCTC CCTCCCTCCCCTCAAAAAGTGTTGCAATGCAGCA GAAGCCCACGGCTTATGTCCGGCCCATGGATGG TCAAGATCAGGCCCCTAGTGAATCCCCTGAACTG AAACCACTGCCGGAGGACTATCGACAGCAGACC TTTGAAAAAACAGACTTGAAAGTGCCTGCCAAA GCCAAGCTCACCAAACTGAAGATGCCTTCTCAGT CAGTTGAGCAGACCTACTCCAATGAAGTCCATT GTGTTGAAGAGATTCTGAAGGAAATGACCCATT CATGGCCGCCTCCTTTGACAGCAATACATACGCC TAGTACAGCTGAGCCATCCAAGTTTCCTTTCCCT ACAAAGGACTCTCAGCATGTCAGTTCTGTAACCC AAAACCAAAAACAATATGATACATCTTCAAAAAC TCACTCAAATTCTCAGCAAGGAACGTCATCCATG CTCGAAGACGACCTTCAGCTCAGTGACAGTGAG GACAGTGACAGTGAACAAACCCCAGAGAAGCCT CCCTCCTCATCTGCACCTCCAAGTGCTCCACAGT CCCTTCCAGAACCAGTGGCATCAGCACATTCCAG CAGTGCAGAGTCAGAAAGCACCAGTGACTCAGA CAGTTCCTCAGACTCAGAGAGCGAGAGCAGTTC AAGTGACAGCGAAGAAAATGAGCCCCTAGAAAC CCCAGCTCCGGAGCCTGAGCCTCCAACAACAAAC AAATGGCAGCTGGACAACTGGCTGACCAAAGTC AGCCAGCCAGCTGCGCCACCAGAGGGCCCCAGG AGCACAGAGCCCCCACGGCGGCACCCAGAGAGT AAGGGCAGCAGCGACAGTGCCACGAGTCAGGAG CATTCTGAATCCAAAGATCCTCCCCCTAAAAGCT CCAGCAAAGCCCCCCGGGCCCCACCCGAAGCCCC CCACCCCGGAAAGAGGAGCTGTCAGAAGTCTCC GGCACAGCAGGAGCCCCCACAAAGGCAAACCGT TGGAACCAAACAACCCAAAAAACCTGTCAAGGC CTCTGCCCCGGGCAGGTTCACGGACCAGCCTGCA GGGGGAAAGGGAGCCAGGGCTTCTTCCCTATGG CTCCCGAGACCAGACTTCCAAAGACAAGCCCAAG GTGAAGACGAAAGGACGGCCCCGGGCCGCAGCA AGCAACGAACCCAAGCCAGCAG

S. No.	Name	Sequence (5′–3′)
3	MLL-AF4	GGAAATACAATTGCTGGCTCAGAAGATGCTGAA CCTCTTGCTCCACCCATCAAACCAATTAAACCTG TCACTAGAAACAAGGCACCCCAGGAACCTCCAGT AAAGAAAGGACGTCGATCGAGGCGGTGTGGGCA GTGTCCCGGCTGCCAGGTGCCTGAGGACTGTGG TGTTTGTACTAATTGCTTAGATAAGCCCAAGTTT GGTGGTCGCAATATAAAGAAGCAGTGCTGCAAG ATGAGAAAATGTCAGAATCTACAATGGATGCCT TCCAAAGCCTACCTGCAGAAGCAAGCTAAAGCT GTGAAAAAGAAAGAGAAAAAGTCTAAGACCAGT GAAAAGAAAGACAGCAAAGAGAGCAGTGTTGTG AAGAACGTGGTGGACTCTAGTCAGAAACCTACC CCATCAGCAAGAGAGGATCCTGCCCCAAAGAAA AGCAGTAGTGAGCCTCCTCCACGAAAGCCCGTC GAGGAAAAGAGTGAAGAAGGGAATGTCTCGGCC CCTGGGCCTGAATCCAAACAGGCCACCACTCCAG CTTCCAGGAAGTCAAGCAAGCAGGTCTCCCAGC CAGCACTGGTCATCCCGCCTCAGCCACCTACTAC AGGACCGCCAAGAAAAGAAGTTCCCAAAACCAC TCCTAGTGAGCCCAAGAAAAAGCAGCCTCCACCA CCAGAATCAGGTCCAGAGCAGAGCAAACAGAAA AAAGTGGCTCCCCGCCCAAGTATCCCTGTAAAAC AAAAACCAAAAGAAAAGCAGACCTACTCCAATG AAGTCCATTGTGTTGAAGAGATTCTGAAGGAAA TGACCCATTCATGGCCGCCTCCTTTGACAGCAAT ACATACGCCTAGTACAGCTGAGCCATCCAAGTTT CCTTTCCCTACAAAGGACTCTCAGCATGTCAGTT CTGTAACCCAAAACCAAAAACAATATGATACATC TTCAAAAACTCACTCAAATTCTCAGCAAGGAACG TCATCCATGCTCGAAGACGACCTTCAGCTCAGTG ACAGTGAGGACAGTGACAGTGAACAAACCCCAG AGAAGCCTCCCTCCTCATCTGCACCTCCAAGTGC TCCACAGTCCCTTCCAGAACCAGTGGCATCAGCA CATTCCAGCAGTGCAGAGTCAGAAAGCACCAGT GACTCAGACAGTTCCTCAGACTCAGAGAGCGAG AGCAGTTCAAGTGACAGCGAAGAAAATGAGCCC CTAGAAACCCCAGCTCCGGAGCCTGAGCCTCCAA CAACAAACAAATGGCAGCTGGACAACTGGCTGA CCAAAGTCAGCCAGCCAGCTGCGCCACCAGAGG GCCCCAGGAGCACAGAGCCCCCACGGCGGCACC CAGAGAGTAAGGGCAGCAGCGACAGTGCCACGA GTCAGGAGCATTCTGAATCCAAAGATCCTCCCCC TAAAAGCTCCAGCAAAGCCCCCCGGGCCCCACCC GAAGCCCCCCACCCCGGAAAGAGGAGCTGTCAG AAGTCTCCGGCACAGCAGGAGCCCCCAC

A.5 Microscopy images

Chapter 2: Altering the subcellular localization of ASOs to improve their therapeutic engagement and efficacy

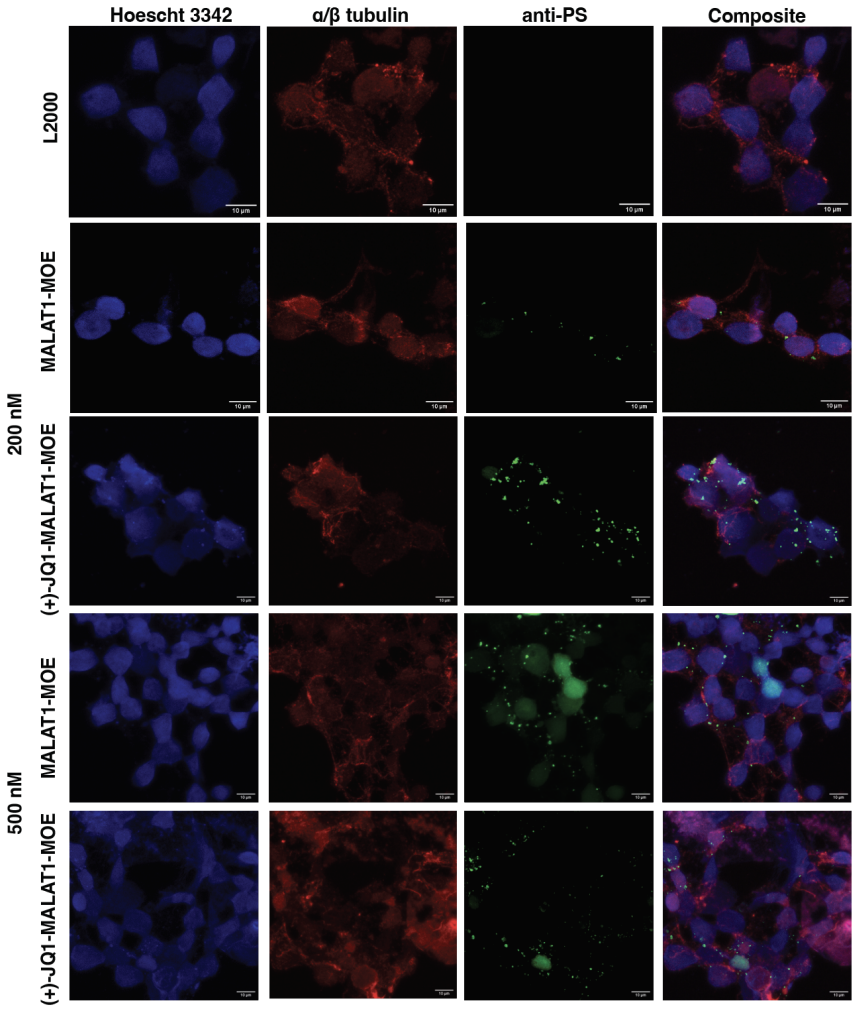

Figure A.62: Representative immunocytochemistry of HEK293 cells transfected with L2000 only, unconjugated and (+)-JQ1-modified MALAT1 gapmers at concentrations indicated for 24 hours using antibodies against the PS modifications (green) and α-/β- tubulin (red). Images are maximum intensity projections generated from Z-stacks; magnification 63x, scale bars as indicated.

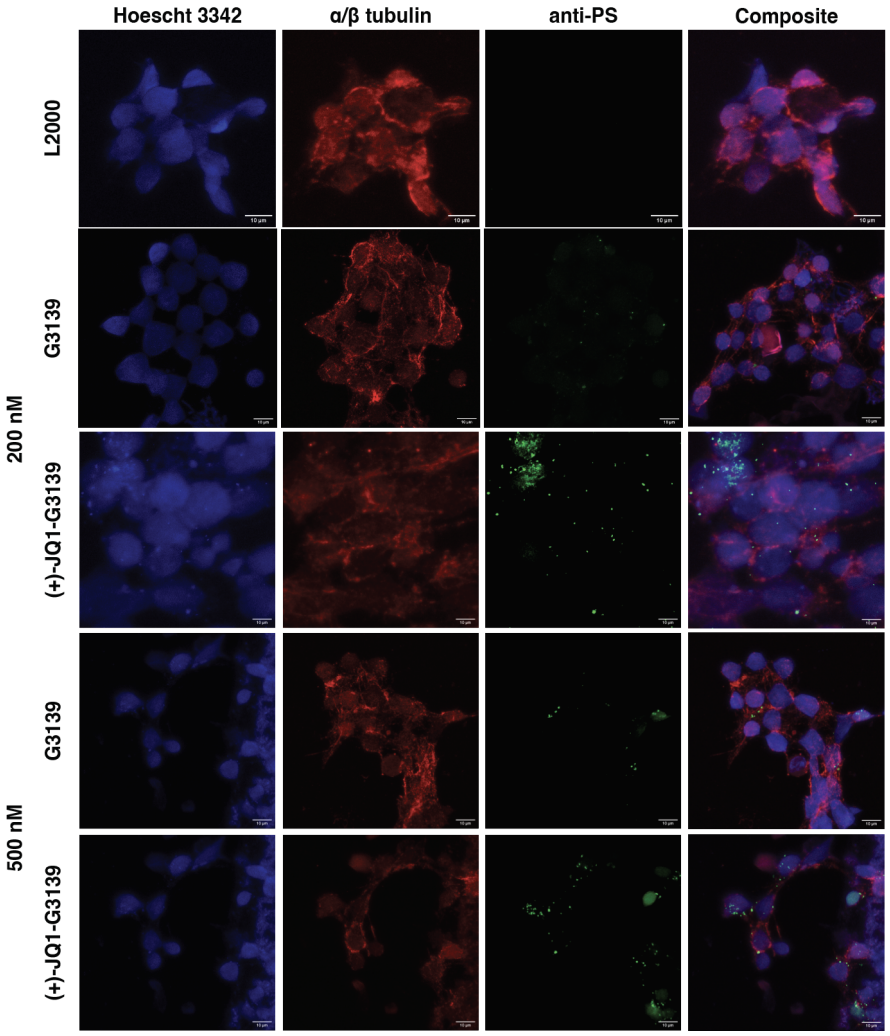

Figure A.63: Representative immunocytochemistry of HEK293 cells transfected with L2000 only, unconjugated and (+)-JQ1-modified G3139 at concentrations indicated for 24 hours using antibodies against the PS modifications (green) and α-/β-tubulin (red). Images are maximum intensity projections generated from Z-stacks; magnification 63x, scale bars as indicated.

Bibliography

[1] Friedrich Miescher. Ueber die chemische zusammensetzung der eiterzellen. *Hoppe-Seyler's Medizinisch-Chemische Untersuchungen*, 4:441–460, 1871.

[2] Phoebus A. Levene and Walter A. Jacobs. The structure of thymonucleic acid. *Journal of Biological Chemistry*, 40:415–424, 1919.

[3] Oswald T. Avery, Colin M. MacLeod, and Maclyn McCarty. Studies on the chemical nature of the substance inducing transformation of pneumococcal types: Induction of transformation by a desoxyribonucleic acid fraction isolated from pneumococcus type iii. *Journal of Experimental Medicine*, 79(2): 137–158, 1944. doi: 10.1084/jem.79.2.137.

[4] Rosalind Franklin and R. G. Gosling. Molecular configuration in sodium thymonucleate. *Nature*, 171(4356):740–741, 1953. doi: 10.1038/171740a0.

[5] James D Watson and Francis HC Crick. Molecular structure of nucleic acids: a structure for deoxyribose nucleic acid. *Nature*, 171(4356):737–738, 1953.

[6] David L Nelson and Michael M Cox. *Lehninger Principles of Biochemistry*. W. H. Freeman, 5th edition, 2008.

[7] W. J. Stec, A. Grajkowski, M. Koziolkiewicz, and B. Uznanski. Novel route to oligo(deoxyribonucleoside phosphorothioates). stereocontrolled synthesis of oligo(deoxyribonucleoside phosphorothioates). *J. Am. Chem. Soc.*, 113:1824–1826, 1991. doi: 10.1021/ja00005a065.

[8] R. T. Walker and H. T. Miles. The synthesis and properties of α- and β-anomers of nucleosides. *Biochemistry*, 12(9):1594–1600, 1973. doi: 10.1021/bi00733a022.

[9] Wolfram Saenger. *Principles of Nucleic Acid Structure*. Springer-Verlag, New York, 1984. ISBN 978-0387907623.

[10] J. Šponer, J. Leszczynski, and P. Hobza. Nature of nucleic acid–base stacking: Nonempirical ab initio and empirical potential characterization of 10 stacked base dimers. comparison of stacked and h-bonded base pairs. *J. Phys. Chem. A*, 105(22):6051–6061, 2001. doi: 10.1021/jp010176y.

[11] A. Rich and S. Zhang. Z-dna: the long road to biological function. *Nat. Rev. Genet.*, 4:566–572, 2003. doi: 10.1038/nrg1111.

[12] M. Egli and P. S. Pallan. Crystallographic studies of chemically modified nucleic acids: a backward glance. *Chem. Biodivers.*, 4:972–1029, 2007. doi: 10.1002/cbdv.200790082.

[13] Ignacio Tinoco and Carlos Bustamante. How rna folds. *Journal of Molecular Biology*, 293(2):271–281, 1999. doi: 10.1006/jmbi.1999.3001.

[14] Ronald R Breaker. Structure and function of riboswitches. *Cold Spring Harbor Perspectives in Biology*, 4(2):a003566, 2012. doi: 10.1101/cshperspect.a003566.

[15] Wolfram Saenger. *Principles of nucleic acid structure*. Springer-Verlag, 1984.

[16] CWA Pleij, K Rietveld, and L Bosch. A new principle of rna folding: the pseudoknot. *Nucleic Acids Research*, 13(5):1717–1731, 1985. doi: 10.1093/nar/13.5.1717.

[17] Eric Westhof and Pascal Auffinger. Rna folding and ribosome assembly. *Cold Spring Harbor Perspectives in Biology*, 2(2):a003366, 2010. doi: 10.1101/cshperspect.a003366.

[18] David W Staple and Samuel E Butcher. Pseudoknots: Rna structures with diverse functions. *PLoS Biology*, 3(6):e213, 2005. doi: 10.1371/journal.pbio.0030213.

[19] Aparna Bansal, Shikha Kaushik, and Shrikant Kukreti. Non-canonical dna structures: Diversity and disease association. *Frontiers in Genetics*, 13: 959258, 2022. doi: 10.3389/fgene.2022.959258.

[20] Rosalind E. Franklin. The structure of sodium thymonucleate fibres. I. The influence of water content. *Acta Crystallographica*, 6:673–678, 1953. doi: 10.1107/S0365110X53002044.

[21] Andrew H.-J. Wang, Gary J. Quigley, Francis J. Kolpak, James L. Crawford, Jacques H. van Boom, Gijs van der Marel, and Alexander Rich. Molecular structure of a left-handed double helical dna fragment at atomic resolution. *Nature*, 282:680–686, 1979. doi: 10.1038/282680a0.

[22] Alan Herbert. Flipons and small rnas accentuate the asymmetries of pervasive transcription by the reset and sequence-specific microcoding of promoter conformation. *Journal of Biological Chemistry*, 299(9):105140, 2023. doi: 10.1016/j.jbc.2023.105140.

[23] Karst Hoogsteen. The structure of crystals containing a hydrogen-bonded complex of purine and 1-methylthymine. *Acta Crystallographica*, 16(9):907–916, 1963.

[24] Evgenia N Nikolova, Eunae Kim, Abigail A Wise, Patrick J O'Brien, and Hashim M Al-Hashimi. Transient hoogsteen base pairs in canonical duplex dna. *Nature Structural & Molecular Biology*, 18(4):498–504, 2011.

[25] Patricia A Havre, Edward J Gunther, Glenn E Leverson, Deborah L Jaye, and Thomas J Kwoh. Triple helix formation inhibits dna synthesis and induces dna

strand breaks in a sequence-specific fashion. *Molecular and Cellular Biology*, 13(3):1572–1581, 1993.

[26] Maxim D Frank-Kamenetskii and Sergei M Mirkin. Triplex dna structures. *Annual Review of Biochemistry*, 64(1):65–95, 1995.

[27] A Jain, G Wang, and KM Vasquez. Structure and stability of dna triplexes containing 2'-o-methyl rna and phosphorothioate linkages. *Nucleic Acids Research*, 36(18):6377–6390, 2008.

[28] Dipankar Sen and Walter Gilbert. Formation of parallel four-stranded complexes by guanine-rich motifs in dna and its implications for meiosis. *Nature*, 334(6180):364–366, 1988.

[29] Shankar Balasubramanian, Laurence H Hurley, and Stephen Neidle. Targeting g-quadruplexes in gene promoters: a novel anticancer strategy? *Nature Reviews Drug Discovery*, 10(4):261–275, 2011.

[30] Daniela Rhodes and Hans J. Lipps. G-quadruplexes and their regulatory roles in biology. *Nucleic Acids Research*, 43(18):8627–8637, 2015. doi: 10.1093/nar/gkv862.

[31] J. Craig Venter, Mark D. Adams, Eugene W. Myers, Peter W. Li, Richard J. Mural, Granger G. Sutton, Hamilton O. Smith, Mark Yandell, Christopher A. Evans, Robert A. Holt, John D. Gocayne, Peter Amanatides, Robert M. Ballew, Daniel H. Huson, Jonathan R. Wortman, Qing Zhang, Cheryl D. Kodira, Xuehui Zheng, Lei Chen, Maya Skupski, Giri Subramanian, Paul D. Thomas, Jianzhong Zhang, George L. Gabor Miklos, Charles Nelson, Stephen Broder, Andrew G. Clark, Joseph Nadeau, Victor A. McKusick, Norton Zinder, Arnold J. Levine, Richard J. Roberts, Mel Simon, Charles Slayman, Michael Hunkapiller, Rodolfo Bolanos, Arthur Delcher, Igor Dew, Dave Fasulo, Mike Flanigan, Liliana Florea, Aaron Halpern, Sridhar Hannenhalli,

Seth Kravitz, Steven Levy, Christopher Mobarry, Kai Reinert, Kurt Remington, Jamal Abu-Threideh, Erica Beasley, Kimberly Biddick, Vincenza Bonazzi, Roy Brandon, Michelle Cargill, Indira Chandramouliswaran, Roderick Charlab, Kiran Chaturvedi, Zhenyu Deng, Vincenzo Di Francesco, Penelope Dunn, Karen Eilbeck, Christine Evangelista, Andrei E. Gabrielian, Wei Gan, Weiming Ge, Feng Gong, Zhiming Gu, Ping Guan, Theodore J. Heiman, Megan E. Higgins, Rongrong Ji, Zhihui Ke, Kristina A. Ketchum, Zemin Lai, Yanjun Lei, Zhen Li, Jian Li, Yu Liang, Xiaoyan Lin, Fei Lu, Gennady V. Merkulov, Natalia Milshina, Holly M. Moore, Ashok K. Naik, V. Anuradha Narayan, Bindu Neelam, Diane Nusskern, Douglas B. Rusch, Steven Salzberg, Wenyu Shao, Brian Shue, Jun Sun, Zheng Wang, Anqi Wang, Xin Wang, Jian Wang, Meizhong Wei, Roy Wides, Chunlin Xiao, Chao Yan, Anqiang Yao, Jin Ye, Ming Zhan, Wei Zhang, Hongwei Zhang, Qian Zhao, Lei Zheng, Fang Zhong, Wei Zhong, Shuli Zhu, Songnian Zhao, David Gilbert, Susan Baumhueter, Greg Spier, Catrina Carter, Alexei Cravchik, Thomas Woodage, Farid Ali, Hea An, Andrea Awe, Derek Baldwin, Henry Baden, Martha Barnstead, Irene Barrow, Kim Beeson, Diane Busam, Aaron Carver, Anne Center, Mei-Ling Cheng, Lee Curry, Sharon Danaher, Lisa Davenport, Richard Desilets, Sandra Dietz, Kim Dodson, Linda Doup, Sergio Ferriera, Neerja Garg, Andrew Gluecksmann, Barry Hart, Jack Haynes, Carolyn Haynes, Carrie Heiner, Suzanne Hladun, Dennis Hostin, Jennifer Houck, Terry Howland, Chike Ibegwam, Jeff Johnson, Frank Kalush, Lori Kline, Sudhakar Koduru, Andrea Love, Frederick Mann, Donna May, Sheila McCawley, Tina McIntosh, Irvin McMullen, Margaret Moy, Linda Moy, Bruce Murphy, Kelly Nelson, Christian Pfannkoch, Ellen Pratts, Vijay Puri, Hassan Qureshi, Mary Reardon, Rosalinda Rodriguez, Yvonne H. Rogers, Doug Romblad, Brian Ruhfel, Rona Scott, Cheryl Sitter, Michelle Smallwood, Erin Stewart, Rebecca Strong, Elizabeth Suh, Robert Thomas, Nghi Nguyen Tint, Sandy Tse, Christa Vech, Guangming Wang, Jason Wetter, Susan Williams, Mary

Williams, Steve Windsor, Edith Winn-Deen, Kathryn Wolfe, Jay Zaveri, Komal Zaveri, Jose F. Abril, Roderic Guigó, Michael J. Campbell, Kim V. Sjolander, Brett Karlak, Arun Kejariwal, Huaiyu Mi, Bella Lazareva, Laura Hatton, Aditi Narechania, Krista Diemer, Anand Muruganujan, Nan Guo, Shin Sato, Vineet Bafna, Sorin Istrail, Ross Lippert, Russell Schwartz, Brian Walenz, Shibu Yooseph, David Allen, Ashwin Basu, John Baxendale, Laura Blick, Marcio Caminha, Michael Carnes-Stine, Pat Caulk, Yu-Hui Chiang, Marie Coyne, Chuck Dahlke, Angela Deslattes Mays, Maria Dombroski, Maureen Donnelly, Donna Ely, Stefanie Esparham, Christine Fosler, Henry Gire, Kevin Glanowski, Karen Glasser, Ann Glodek, Mikhail Gorokhov, Kevin Graham, Bonnie Gropman, Mark Harris, Jeff Heil, Sue Henderson, Jeff Hoover, Dorothy Jennings, Cheri Jordan, James Jordan, Joseph Kasha, Lauren Kagan, Chris Kraft, Alexei Levitsky, Mike Lewis, Xiangqun Liu, Jesse Lopez, Dan Ma, William Majoros, Jason McDaniel, Scott Murphy, Michael Newman, Thuy Nguyen, Nathan Nguyen, Michael Nodell, Susan Pan, John Peck, Michele Peterson, William Rowe, Richard Sanders, James Scott, Martha Simpson, Tim Smith, Andrew Sprague, Tom Stockwell, Ray Turner, Ellen Venter, Mingfu Wang, Ming Wen, Dan Wu, Mei Wu, Anhua Xia, Ali Zandieh, and Xiaoyu Zhu. The sequence of the human genome. *Science*, 291(5507): 1304–1351, 2001. doi: 10.1126/science.1058040. Erratum in: Science 2001 Jun 5;292(5523):1838.

[32] Tom Misteli. The self-organizing genome: Principles of genome architecture and function. *Cell*, 183(1):28–45, 2020. doi: 10.1016/j.cell.2020.09.014.

[33] Karolin Luger, Armin W. Mäder, Robin K. Richmond, David F. Sargent, and Timothy J. Richmond. Crystal structure of the nucleosome core particle at 2.8 å resolution. *Nature*, 389:251–260, 1997. doi: 10.1038/38444.

[34] Tony Kouzarides. Chromatin modifications and their function. *Cell*, 128(4): 693–705, 2007. doi: 10.1016/j.cell.2007.02.005.

[35] CA Brackley, J Johnson, D Michieletto, et al. Non-equilibrium chromosome looping via molecular slip-links. *Physical Review Letters*, 117(1):018101, 2016.

[36] Alexander Buckle et al. Polymer simulations of heteromorphic chromatin predict the 3d folding of complex genomic loci. *Molecular Cell*, 72(5):786–797.e11, 2018.

[37] M. Jordan Rowley and Victor G. Corces. Organizational principles of 3d genome architecture. *Nature Reviews Genetics*, 19(12):789–800, 2018. doi: 10.1038/s41576-018-0060-8.

[38] Job Dekker and Leonid A Mirny. Loop extrusion: a mechanism for genome organization. *Nature Reviews Molecular Cell Biology*, 17(12):758–770, 2016.

[39] Suhas SP Rao, SC Huang, B Glenn St Hilaire, et al. Cohesin loss eliminates all loop domains. *Cell*, 171(2):305–320.e24, 2017.

[40] Geraldine Wutz et al. Topologically associating domains and chromatin loops depend on cohesin and are regulated by ctcf, wapl, and pds5 proteins. *EMBO Journal*, 36(24):3573–3599, 2017.

[41] Johannes Nuebler et al. Chromatin organization by an interplay of loop extrusion and compartmental segregation. *Science*, 357(6349):848–853, 2018.

[42] Tom Misteli. Beyond the sequence: cellular organization of genome function. *Cell*, 128(4):787–800, 2007. doi: 10.1016/j.cell.2007.01.028.

[43] MJ Rowley and VG Corces. Organizational principles of 3d genome architecture. *Nature Reviews Genetics*, 19(12):789–800, 2018.

[44] Peter Fraser and Wendy Bickmore. Nuclear organization of the genome and the potential for gene regulation. *Nature*, 447(7143):413–417, 2007. doi: 10.1038/nature05916.

[45] David L. Spector and Angus I. Lamond. Nuclear speckles. *Cold Spring Harbor Perspectives in Biology*, 3(2):a000646, 2011. doi: 10.1101/cshperspect.a000646.

[46] David Staněk and Archa H. Fox. Cajal bodies: facts, hypotheses, mysteries. *Trends in Cell Biology*, 27(6):498–510, 2017. doi: 10.1016/j.tcb.2017.01.004.

[47] Diego I. Cattoni, Ana M. Cardozo Gizzi, Marina Georgieva, Andrea Parmeggiani, and Marcelo Nollmann. Single-cell analysis of the 3d genome structure: challenges and perspectives. *Biophysical Journal*, 113(7):1273–1279, 2017. doi: 10.1016/j.bpj.2017.07.031.

[48] Erica H. Finn and Tom Misteli. Multiscale modeling of genome organization with chromatin extrusion and compartmental segregation. *Current Opinion in Cell Biology*, 58:76–85, 2019. doi: 10.1016/j.ceb.2019.03.003.

[49] Jorge Rodriguez, Guangming Ren, Catriona R. Day, Kai Zhao, Clement C. Chow, and Daniel R. Larson. Intrinsic dynamics of a human gene reveal the basis of expression heterogeneity. *Cell*, 176(1-2):213–226.e18, 2019. doi: 10.1016/j.cell.2018.11.026.

[50] Robert G Roeder. Transcriptional regulation and the role of diverse coactivators in animal cells. *Nature Reviews Genetics*, 6(3):179–190, 2005. doi: 10.1038/nrg1553.

[51] Aditi Kanhere and Manju Bansal. Structural properties of promoters: similarities and differences between prokaryotes and eukaryotes. *Nucleic Acids Research*, 33(10):3165–3175, 2005. doi: 10.1093/nar/gki627.

[52] Leighton J Core and John T Lis. Paused rna polymerase ii as a gateway to transcriptional regulation. *Nature Reviews Molecular Cell Biology*, 9(9): 612–623, 2008. doi: 10.1038/nrm2453.

[53] Job Dekker and Leonid Mirny. The 3d genome as moderator of chromosomal communication. *Cell*, 164(6):1110–1121, 2016. doi: 10.1016/j.cell.2016.02.007.

[54] Timothy W Nilsen and Brenton R Graveley. Diversity through alternative splicing: perspective on the significance of nonsense-mediated mrna decay. *Trends in Genetics*, 26(8):454–459, 2010. doi: 10.1016/j.tig.2010.05.001.

[55] Adam Ben-Shem, Nobuhiko Garreau de Loubresse, Shashi Bashan, Liliana Burakovsky, Andrei Zagryadskaya, Victoria Alexander, Pawel A. Agmon, Anat Bashan, and Ada Yonath. The structure of the eukaryotic ribosome at 3.0 å resolution. *Science*, 330(6008):1203–1209, 2010. doi: 10.1126/science.1194294.

[56] Richard J Jackson, Christopher U T Hellen, and Tatyana V Pestova. The mechanics of eukaryotic translation initiation. *Nature Reviews Molecular Cell Biology*, 11(2):113–127, 2010. doi: 10.1038/nrm2838.

[57] Tatyana V Pestova and Christopher U T Hellen. Eukaryotic ribosomes: structural and functional diversity. *Cell*, 131(4):660–670, 2007. doi: 10.1016/j.cell.2007.10.024.

[58] David P Bartel. Microrna: genomics, biogenesis, mechanism, and function. *Cell*, 116(2):281–297, 2004. doi: 10.1016/S0092-8674(04)00045-5.

[59] Mathieu Laplante and David M Sabatini. mtor signaling in growth control and disease. *Cell*, 149(2):274–293, 2012. doi: 10.1016/j.cell.2012.03.017.

[60] Carl P Anderson, Miao Shen, and Richard S Eisenstein. Post-transcriptional regulation of gene expression by iron regulatory proteins. *Biometals*, 25(4):687–698, 2012. doi: 10.1007/s10534-012-9544-z.

[61] Matthias Mann, Shao En Ong, Mads Grønborg, Hanno Steen, Ole N Jensen, and Akhilesh Pandey. Analysis of protein phosphorylation using mass spec-

trometry: deciphering the phosphoproteome. *Trends in Biotechnology*, 20(6): 261–268, 2002. doi: 10.1016/S0167-7799(02)01996-5.

[62] Noboru Mizushima, Beth Levine, Ana Maria Cuervo, and Daniel J Klionsky. Autophagy: renovation of cells and tissues. *Cell*, 147(4):728–741, 2011. doi: 10.1016/j.cell.2011.10.026.

[63] Martin Egli and Muthiah Manoharan. Chemistry, structure and function of approved oligonucleotide therapeutics. *Nucleic Acids Research*, 51(6):2529–2573, 2023. doi: 10.1093/nar/gkad067.

[64] S. T. Crooke. Molecular mechanisms of antisense oligonucleotides. *Nucleic Acid Therapeutics*, 27(2):70–77, 2017. doi: 10.1089/nat.2016.0656.

[65] H Wu, W F Lima, H Zhang, A Fan, H Sun, and S T Crooke. Determination of the role of the human rnase h1 in the pharmacology of dna-like antisense drugs. *Journal of Biological Chemistry*, 279(17):17181–17189, 2004. doi: 10.1074/jbc.M311683200.

[66] D Yu, H Pendergraff, J Liu, H. B. Kordasiewicz, D. W. Cleveland, E. E. Swayze, W. F. Lima, S. T. Crooke, T. P. Prakash, and D. R. Corey. Single-stranded rnas use rnai to potently and allele-selectively inhibit mutant huntingtin expression. *Cell*, 150(5):895–908, 2012. doi: 10.1016/j.cell.2012.08.002.

[67] T Suwanmanee, H Sierakowska, G Lacerra, S Svasti, S Kirby, C E Walsh, S Fucharoen, and R Kole. Restoration of human beta-globin gene expression in murine and human ivs2-654 thalassemic erythroid cells by free uptake of antisense oligonucleotides. *Molecular Pharmacology*, 62(3):545–553, 2002. doi: 10.1124/mol.62.3.545.

[68] SM Elbashir, J Harborth, W Lendeckel, A Yalcin, K Weber, and T Tuschl. Duplexes of 21-nucleotide rnas mediate rna interference in cultured mammalian cells. *Nature*, 411(6836):494–498, 2001. doi: 10.1038/35078107.

[69] J Liu, M A Carmell, F V Rivas, C G Marsden, J M Thomson, J J Song, S M Hammond, L Joshua-Tor, and G J Hannon. Argonaute2 is the catalytic engine of mammalian rnai. *Science*, 305(5689):1437–1441, 2004. doi: 10.1126/science.1102513.

[70] W E Salomon, S M Jolly, M J Moore, P D Zamore, and V Serebrov. Single-molecule imaging reveals that argonaute reshapes the binding properties of its nucleic acid guides. *Cell*, 162(1):84–95, 2015. doi: 10.1016/j.cell.2015.06.029.

[71] Craig Tuerk and Larry Gold. Systematic evolution of ligands by exponential enrichment: Rna ligands to bacteriophage t4 dna polymerase. *Science*, 249 (4968):505–510, 1990. doi: 10.1126/science.2200121.

[72] A. V. Lakhin, V. Z. Tarantul, and L. V. Gening. Aptamers: problems, solutions and prospects. *Acta Naturae*, 5(4):34–43, 2013.

[73] J. J. Senn, S. Burel, and S. P. Henry. Non-cpg-containing antisense 2'-methoxyethyl oligonucleotides activate a proinflammatory response independent of toll-like receptor 9 or myeloid differentiation factor 88. *Journal of Pharmacology and Experimental Therapeutics*, 314(3):972–979, 2005. doi: 10.1124/jpet.105.085712.

[74] S. T. Crooke, T. A. Vickers, and X. H. Liang. Phosphorothioate modified oligonucleotide-protein interactions. *Nucleic Acids Research*, 48(10):5235–5253, 2020. doi: 10.1093/nar/gkaa299.

[75] N. Harikai, H. Kakuda, T. Uchiyama, T. Yamamoto, K. Zaima, and K. Shinomiya. Detection of the phosphorothioate oligonucleotide fomivirsen using a ligase detection reaction with polymerase chain reaction. *Analytical Sciences*, 40(5):965–971, 2024. doi: 10.1007/s44211-024-00539-1.

[76] P. S. Miller, J. Yano, E. Yano, C. Carroll, K. Jayaraman, and P. O. Ts'o. Nonionic nucleic acid analogues. synthesis and characterization of dideoxyribonu-

cleoside methylphosphonates. *Biochemistry*, 18(23):5134–5143, 1979. doi: 10.1021/bi00590a017.

[77] J. Summerton and D. Weller. Morpholino antisense oligomers: Design, preparation, and properties. *Antisense and Nucleic Acid Drug Development*, 7(3): 187–195, 1997. doi: 10.1089/oli.1.1997.7.187.

[78] K. R. Q. Lim, R. Maruyama, and T. Yokota. Eteplirsen in the treatment of duchenne muscular dystrophy. *Drug Design, Development and Therapy*, 11: 533–545, 2017. doi: 10.2147/DDDT.S97635.

[79] Y.-A. Heo. Golodirsen: First approval. *Drugs*, 80(3):329–333, 2020. doi: 10.1007/s40265-020-01267-2.

[80] S. Imai, Y. Suda, J. Mori, Y. Sasaki, T. Yamada, and K. Kusano. Prediction of human pharmacokinetics of phosphorodiamidate morpholino oligonucleotides in duchenne muscular dystrophy patients using viltolarsen. *Drug Metabolism and Disposition*, 51(10):1428–1435, 2023. doi: 10.1124/dmd.123.001425.

[81] A. Milyard, G. Addison, Z. Meesam, M. H. Julia, and W. S. Brian. Casimersen (amondys 45™): An antisense oligonucleotide for duchenne muscular dystrophy. *Biomedicines*, 12:912, 2024.

[82] B. T. Le, S. Paul, K. Jastrzebska, H. Langer, M. H. Caruthers, and R. N. Veedu. Thiomorpholino oligonucleotides as a robust class of next generation platforms for alternate mrna splicing. *Proceedings of the National Academy of Sciences of the United States of America*, 119(36):e2207956119, 2022. doi: 10.1073/pnas.2207956119.

[83] S. Epple, C. Thorpe, Y. R. Baker, A. H. El-Sagheer, and T. Brown. Consecutive 5'- and 3'-amide linkages stabilise antisense oligonucleotides and elicit an efficient rnase h response. *Chemical Communications*, 56(41):5496–5499, 2020. doi: 10.1039/d0cc00444h.

[84] R. S. Finkel, E. Mercuri, B. T. Darras, A. M. Connolly, N. L. Kuntz, J. Kirschner, C. A. Chiriboga, K. Saito, N. Deconinck, E. Tizzano, and et al. Nusinersen versus sham control in infantile-onset spinal muscular atrophy. *New England Journal of Medicine*, 2017.

[85] M. E. Jung, T. A. Dwight, F. Vigant, M. E. Østergaard, E. E. Swayze, and P. P. Seth. Synthesis and duplex-stabilizing properties of fluorinated n-methanocarbathymidine analogues locked in the c3'-endo conformation. *Angewandte Chemie International Edition*, 53(37):9893–9897, 2014. doi: 10.1002/anie.201405283.

[86] L. J. Scott. Givosiran: First approval. *Drugs*, 80(3):335–339, 2020. doi: 10.1007/s40265-020-01269-0.

[87] S. F. Garrelfs, Y. Frishberg, S. A. Hulton, M. J. Koren, W. D. O'Riordan, P. Cochat, G. Deschênes, H. Shasha-Lavsky, J. M. Saland, W. G. Van't Hoff, and et al. Lumasiran, an rnai therapeutic for primary hyperoxaluria type 1. *New England Journal of Medicine*, 384(13):1216–1226, 2021. doi: 10.1056/NEJMoa2021712.

[88] P. B. Duell, R. D. Santos, B.-A. Kirwan, J. L. Witztum, S. Tsimikas, and J. J. P. Kastelein. Long-term mipomersen treatment is associated with a reduction in cardiovascular events in patients with familial hypercholesterolemia. *Journal of Clinical Lipidology*, 10(4):1011–1021, 2016. doi: 10.1016/j.jacl.2016.04.013.

[89] V. Mathew and A. K. Wang. Inotersen: new promise for the treatment of hereditary transthyretin amyloidosis. *Drug Design, Development and Therapy*, 13:1515–1525, 2019. doi: 10.2147/DDDT.S162913.

[90] J. Paik and S. Duggan. Volanesorsen: First global approval. *Drugs*, 79(12):1349–1354, 2019. doi: 10.1007/s40265-019-01168-z.

[91] M. Koizumi, K. Morita, M. Daigo, S. Tsutsumi, K. Abe, S. Obika, and T. Imanishi. Triplex formation with 2'-o,4'-c-ethylene-bridged nucleic acids (ena) having c3'-endo conformation at physiological ph. *Nucleic Acids Research*, 31(12):3267–3273, 2003. doi: 10.1093/nar/gkg416.

[92] M. Aboshi, K. Matsuda, D. Kawakami, K. Kono, Y. Kazami, T. Sekida, M. Komori, A. L. Morey, S. Suga, J. F. Smith, et al. Safety and immunogenicity of vlpcov-02, a sars-cov-2 self-amplifying rna vaccine with a modified base, 5-methylcytosine. *iScience*, 27(2):108964, 2024. doi: 10.1016/j.isci.2024.108964.

[93] A. L. Malinowska, H. L. Huynh, and S. Bose. Peptide-oligonucleotide conjugation: Chemistry and therapeutic applications. *Current Issues in Molecular Biology*, 46(10):11031–11047, 2024. doi: 10.3390/cimb46100655.

[94] A. Dasargyri, P. Hervella, A. Christiansen, S. T. Proulx, M. Detmar, and J.-C. Leroux. Findings questioning the involvement of sigma-1 receptor in the uptake of anisamide-decorated particles. *Journal of Controlled Release*, 224: 229–238, 2016. doi: 10.1016/j.jconrel.2016.01.021.

[95] M. Scherma, P. Masia, V. Satta, W. Fratta, P. Fadda, and G. Tanda. Brain activity of anandamide: a rewarding bliss? *Acta Pharmacologica Sinica*, 40 (3):309–323, 2019. doi: 10.1038/s41401-018-0075-x.

[96] J. M. Govan, D. D. Young, H. Lusic, Q. Liu, M. O. Lively, and A. Deiters. Optochemical control of rna interference in mammalian cells. *Nucleic Acids Research*, 41(22):10518–10528, 2013. doi: 10.1093/nar/gkt806.

[97] B. Zhao, Q. Tian, Y. Bagheri, and M. You. Lipid-oligonucleotide conjugates for simple and efficient cell membrane engineering and bioanalysis. *Current Opinion in Biomedical Engineering*, 13:76–83, 2020. doi: 10.1016/j.cobme.2019.12.006.

[98] T. Nagata, C. A. Dwyer, K. Yoshida-Tanaka, K. Ihara, M. Ohyagi, H. Kaburagi, H. Miyata, S. Ebihara, K. Yoshioka, T. Ishii, and et al. Cholesterol-functionalized dna/rna heteroduplexes cross the blood-brain barrier and knock down genes in the rodent cns. *Nature Biotechnology*, 39(12): 1529–1536, 2021. doi: 10.1038/s41587-021-00972-x.

[99] A. K. N. Chan and C. W. Chen. Rewiring the epigenetic networks in mll-rearranged leukemias: Epigenetic dysregulation and pharmacological interventions. *Frontiers in Cell and Developmental Biology*, 7:81, 2019. doi: 10.3389/fcell.2019.00081.

[100] X. H. Liang, H. Sun, J. G. Nichols, and S. T. Crooke. Rnase h1-dependent antisense oligonucleotides are robustly active in directing rna cleavage in both the cytoplasm and the nucleus. *Molecular Therapy*, 25(9):2075–2092, 2017. doi: 10.1016/j.ymthe.2017.06.002.

[101] S. F. Dowdy. Endosomal escape of rna therapeutics: How do we solve this rate-limiting problem? *RNA*, 29(4):396–401, 2023. doi: 10.1261/rna.079507.122.

[102] R. L. Juliano. Intracellular trafficking and endosomal release of oligonucleotides: What we know and what we don't. *Nucleic Acid Therapeutics*, 28(3):166–177, 2018. doi: 10.1089/nat.2018.0727.

[103] R. S. Geary, D. Norris, R. Yu, and C. F. Bennett. Pharmacokinetics, biodistribution and cell uptake of antisense oligonucleotides. *Advanced Drug Delivery Reviews*, 87:46–51, 2015. doi: 10.1016/j.addr.2015.01.008.

[104] Aaron D. Springer and Steven F. Dowdy. Galnac-sirna conjugates: Leading the way for delivery of rnai therapeutics. *Nucleic Acid Therapeutics*, 28(3): 109–118, 2018. doi: 10.1089/nat.2018.0736.

[105] O. Nakagawa, X. Ming, L. Huang, and R. L. Juliano. Targeted intracellular delivery of antisense oligonucleotides via conjugation with small-molecule lig-

ands. *Journal of the American Chemical Society*, 132(26):8848–8849, 2010. doi: 10.1021/ja102635c.

[106] J. Willibald, J. Harder, K. Sparrer, K. K. Conzelmann, and T. Carell. Click-modified anandamide sirna enables delivery and gene silencing in neuronal and immune cells. *Journal of the American Chemical Society*, 134(30):12330–12333, 2012. doi: 10.1021/ja303251f.

[107] K. Brunner, J. Harder, T. Halbach, J. Willibald, F. Spada, F. Gnerlich, K. Sparrer, A. Beil, L. Möckl, C. Bräuchle, and et al. Cell-penetrating and neurotargeting dendritic sirna nanostructures. *Angewandte Chemie International Edition*, 54(6):1946–1949, 2015. doi: 10.1002/anie.201409803.

[108] B. Frigerio, C. Bizzoni, G. Jansen, C. P. Leamon, G. J. Peters, P. S. Low, L. H. Matherly, and M. Figini. Folate receptors and transporters: biological role and diagnostic/therapeutic targets in cancer and other diseases. *Journal of Experimental Clinical Cancer Research*, 38(1):125, 2019. doi: 10.1186/s13046-019-1123-1.

[109] C. Dohmen, T. Fröhlich, U. Lächelt, I. Röhl, H. P. Vornlocher, P. Hadwiger, and E. Wagner. Defined folate-peg-sirna conjugates for receptor-specific gene silencing. *Molecular Therapy - Nucleic Acids*, 1(1):e7, 2012. doi: 10.1038/mtna.2011.10.

[110] D. S. Schade, L. Shey, and R. P. Eaton. Cholesterol review: A metabolically important molecule. *Endocrine Practice*, 26(12):1514–1523, 2020. doi: 10.4158/ep-2020-0347.

[111] J. Soutschek, A. Akinc, B. Bramlage, K. Charisse, R. Constien, M. Donoghue, S. Elbashir, A. Geick, P. Hadwiger, J. Harborth, and et al. Therapeutic silencing of an endogenous gene by systemic administration of modified sirnas. *Nature*, 432(7014):173–178, 2004. doi: 10.1038/nature03121.

[112] M. E. Østergaard, M. Jackson, A. Low, A. E. Chappell, R. G. Lee, R. Q. Peralta, J. Yu, G. A. Kinberger, A. Dan, R. Carty, and et al. Conjugation of hydrophobic moieties enhances potency of antisense oligonucleotides in the muscle of rodents and non-human primates. *Nucleic Acids Research*, 47(12): 6045–6058, 2019. doi: 10.1093/nar/gkz360.

[113] C. Wolfrum, S. Shi, K. N. Jayaprakash, M. Jayaraman, G. Wang, R. K. Pandey, K. G. Rajeev, T. Nakayama, K. Charrise, E. M. Ndungo, and et al. Mechanisms and optimization of in vivo delivery of lipophilic sirnas. *Nature Biotechnology*, 25(10):1149–1157, 2007. doi: 10.1038/nbt1339.

[114] A. Lacroix, H. H. Fakih, and H. F. Sleiman. Detailed cellular assessment of albumin-bound oligonucleotides: Increased stability and lower non-specific cell uptake. *Journal of Controlled Release*, 324:34–46, 2020. doi: 10.1016/j.jconrel.2020.04.020.

[115] K. M. Brown, J. K. Nair, M. M. Janas, Y. I. Anglero-Rodriguez, L. T. H. Dang, H. Peng, C. S. Theile, E. Castellanos-Rizaldos, C. Brown, D. Foster, and et al. Expanding rnai therapeutics to extrahepatic tissues with lipophilic conjugates. *Nature Biotechnology*, 40(10):1500–1508, 2022. doi: 10.1038/s41587-022-01334-x.

[116] Vignesh N. Hariharan, Minwook Shin, Ching-Wen Chang, Daniel O'Reilly, Annabelle Biscans, Ken Yamada, Zhiru Guo, Mohan Somasundaran, Qi Tang, Kathryn Monopoli, Pranathi Meda Krishnamurthy, Gitali Devi, Nicholas McHugh, David A. Cooper, Dimas Echeverria, John Cruz, Io Long Chan, Ping Liu, Sun-Young Lim, Jill McConnell, Satya Prakash Singh, Samuel Hildebrand, Jacquelyn Sousa, Sarah M. Davis, Zachary Kennedy, Chantal Ferguson, Bruno M. D. C. Godinho, Yann Thillier, Jillian Caiazzi, Socheata Ly, Manish Muhuri, Karen Kelly, Fiachra Humphries, Alyssa Cousineau, Krishna Mohan Parsi, Qi Li, Yang Wang, Rene Maehr, Guangping Gao,

Dmitry Korkin, William M. McDougall, Robert W. Finberg, Katherine A. Fitzgerald, Jonathan K. Watts, and Anastasia Khvorova. Divalent sirnas are bioavailable in the lung and efficiently block sars-cov-2 infection. *Proceedings of the National Academy of Sciences*, 120(11):e2219523120, 2023. doi: 10.1073/pnas.2219523120.

[117] Sarah M. Davis, Vignesh N. Hariharan, Agnes Lo, Anton A. Turanov, Dimas Echeverria, Jacquelyn Sousa, Nicholas McHugh, Annabelle Biscans, Julia F. Alterman, S. Ananth Karumanchi, Melissa J. Moore, and Anastasia Khvorova. Chemical optimization of sirna for safe and efficient silencing of placental sflt1. *Molecular Therapy - Nucleic Acids*, 29:542–552, 2022. doi: 10.1016/j.omtn.2022.06.009.

[118] A. Watanabe, M. Nakajima, T. Kasuya, R. Onishi, N. Kitade, K. Mayumi, T. Ikehara, and A. Kugimiya. Comparative characterization of hepatic distribution and mrna reduction of antisense oligonucleotides conjugated with triantennary n-acetyl galactosamine and lipophilic ligands targeting apolipoprotein b. *Journal of Pharmacology and Experimental Therapeutics*, 357(2):320–330, 2016. doi: 10.1124/jpet.115.230300.

[119] I. Dovgan, O. Koniev, S. Kolodych, and A. Wagner. Antibody-oligonucleotide conjugates as therapeutic, imaging, and detection agents. *Bioconjugate Chemistry*, 30(10):2483–2501, 2019. doi: 10.1021/acs.bioconjchem.9b00306.

[120] S. M. Hammond, F. Abendroth, L. Goli, J. Stoodley, M. Burrell, G. Thom, I. Gurrell, N. Ahlskog, M. J. Gait, M. J. Wood, and et al. Antibody-oligonucleotide conjugate achieves cns delivery in animal models for spinal muscular atrophy. *JCI Insight*, 7(24), 2022. doi: 10.1172/jci.insight.154142.

[121] A. E. Arnold, E. Malek-Adamian, P. U. Le, A. Meng, S. Martínez-Montero, K. Petrecca, M. J. Damha, and M. S. Shoichet. Antibody-antisense oligonucleotide conjugate downregulates a key gene in glioblastoma stem cells. *Molec-*

ular Therapy - Nucleic Acids, 11:518–527, 2018. doi: 10.1016/j.omtn.2018.04.004.

[122] N. Satake, C. Duong, S. Yoshida, M. Oestergaard, C. Chen, R. Peralta, S. Guo, P. P. Seth, Y. Li, L. Beckett, and et al. Novel targeted therapy for precursor b cell acute lymphoblastic leukemia: anti-cd22 antibody-mxd3 antisense oligonucleotide conjugate. *Molecular Medicine*, 22:632–642, 2016. doi: 10.2119/molmed.2015.00210.

[123] A. Muratovska and M. R. Eccles. Conjugate for efficient delivery of short interfering rna (sirna) into mammalian cells. *FEBS Letters*, 558(1-3):63–68, 2004. doi: 10.1016/s0014-5793(03)01505-9.

[124] R. P. Wu, D. S. Youngblood, J. N. Hassinger, C. E. Lovejoy, M. H. Nelson, P. L. Iversen, and H. M. Moulton. Cell-penetrating peptides as transporters for morpholino oligomers: effects of amino acid composition on intracellular delivery and cytotoxicity. *Nucleic Acids Research*, 35(15):5182–5191, 2007. doi: 10.1093/nar/gkm478.

[125] A. Amantana, H. M. Moulton, M. L. Cate, M. T. Reddy, T. Whitehead, J. N. Hassinger, D. S. Youngblood, and P. L. Iversen. Pharmacokinetics, biodistribution, stability and toxicity of a cell-penetrating peptide-morpholino oligomer conjugate. *Bioconjugate Chemistry*, 18(4):1325–1331, 2007. doi: 10.1021/bc070060v.

[126] V. Lafarga, O. Sirozh, I. Díaz-López, A. Galarreta, M. Hisaoka, E. Zarzuela, J. Boskovic, B. Jovanovic, R. Fernandez-Leiro, J. Muñoz, and et al. Widespread displacement of dna- and rna-binding factors underlies toxicity of arginine-rich cell-penetrating peptides. *EMBO Journal*, 40(13):e103311, 2021. doi: 10.15252/embj.2019103311.

[127] C. Betts, A. F. Saleh, A. A. Arzumanov, S. M. Hammond, C. Godfrey, T. Coursindel, M. J. Gait, and M. J. Wood. Pip6-pmo, a new generation

of peptide-oligonucleotide conjugates with improved cardiac exon skipping activity for dmd treatment. *Molecular Therapy - Nucleic Acids*, 1(8):e38, 2012. doi: 10.1038/mtna.2012.30.

[128] C. Ämmälä, W. J. Drury, L. Knerr, I. Ahlstedt, P. Stillemark-Billton, C. Wennberg-Huldt, E. M. Andersson, E. Valeur, R. Jansson-Löfmark, D. Janzén, and et al. Targeted delivery of antisense oligonucleotides to pancreatic β-cells. *Science Advances*, 4(10):eaat3386, 2018. doi: 10.1126/sciadv.aat3386.

[129] N. D. Abeydeera, M. Egli, N. Cox, K. Mercier, J. N. Conde, P. S. Pallan, D. M. Mizurini, M. Sierant, F. E. Hibti, T. Hassell, and et al. Evoking picomolar binding in rna by a single phosphorodithioate linkage. *Nucleic Acids Research*, 44(17):8052–8064, 2016. doi: 10.1093/nar/gkw725.

[130] S. I. Rudnick and G. P. Adams. Affinity and avidity in antibody-based tumor targeting. *Cancer Biotherapy and Radiopharmaceuticals*, 24(2):155–161, 2009. doi: 10.1089/cbr.2009.0627.

[131] J. W. Kotula, E. D. Pratico, X. Ming, O. Nakagawa, R. L. Juliano, and B. A. Sullenger. Aptamer-mediated delivery of splice-switching oligonucleotides to the nuclei of cancer cells. *Nucleic Acid Therapeutics*, 22(3):187–195, 2012. doi: 10.1089/nat.2012.0347.

[132] J. O. McNamara, E. R. Andrechek, Y. Wang, K. D. Viles, R. E. Rempel, E. Gilboa, B. A. Sullenger, and P. H. Giangrande. Cell type-specific delivery of sirnas with aptamer-sirna chimeras. *Nature Biotechnology*, 24(8):1005–1015, 2006. doi: 10.1038/nbt1223.

[133] Z. Zhao, A. Ukidve, J. Kim, and S. Mitragotri. Targeting strategies for tissue-specific drug delivery. *Cell*, 181(1):151–167, 2020. doi: 10.1016/j.cell.2020.02.001.

[134] A. Tewabe, A. Abate, M. Tamrie, A. Seyfu, and E. Abdela Siraj. Targeted drug delivery - from magic bullet to nanomedicine: Principles, challenges, and future perspectives. *Journal of Multidisciplinary Healthcare*, 14:1711–1724, 2021. doi: 10.2147/JMDH.S313968.

[135] S. Kadekar, G. N. Nawale, V. K. Rangasami, V. Le Joncour, P. Laakkonen, J. Hilborn, O. P. Varghese, and O. P. Oommen. Redox responsive pluronic micelle mediated delivery of functional sirna: a modular nano-assembly for targeted delivery. *Biomaterials Science*, 9(11):3939–3944, 2021. doi: 10.1039/d1bm00428j.

[136] M. Shi, X. Zhao, J. Zhang, S. Pan, C. Yang, Y. Wei, H. Hu, M. Qiao, D. Chen, and X. Zhao. ph-responsive hybrid nanoparticle with enhanced dissociation characteristic for sirna delivery. *International Journal of Nanomedicine*, 13: 6885–6902, 2018. doi: 10.2147/IJN.S180119.

[137] G. Hao, Z. P. Xu, and L. Li. Manipulating extracellular tumour ph: an effective target for cancer therapy. *RSC Advances*, 8(39):22182–22192, 2018. doi: 10.1039/C8RA02095G.

[138] C. Wang, T. Zhao, Y. Li, G. Huang, M. A. White, and J. Gao. Investigation of endosome and lysosome biology by ultra ph-sensitive nanoprobes. *Advanced Drug Delivery Reviews*, 113:87–96, 2017. doi: 10.1016/j.addr.2016.08.014.

[139] Z. Wang, X. Fan, G. Mu, X. Zhao, Q. Wang, J. Wang, and X. Tang. Cathepsin b-activatable cyclic antisense oligonucleotides for cell-specific target gene knockdown in vitro and in vivo. *Molecular Therapy - Nucleic Acids*, 33:548–558, 2023. doi: 10.1016/j.omtn.2023.07.022.

[140] C. Menge and A. Heckel. Coumarin-caged dg for improved wavelength-selective uncaging of dna. *Organic Letters*, 13(17):4620–4623, 2011. doi: 10.1021/ol201842x.

[141] D. Hartmann, J. M. Smith, G. Mazzotti, R. Chowdhry, and M. J. Booth. Controlling gene expression with light: a multidisciplinary endeavour. *Biochemical Society Transactions*, 48(4):1645–1659, 2020. doi: 10.1042/bst20200014.

[142] A. Deiters, R. A. Garner, H. Lusic, J. M. Govan, M. Dush, N. M. Nascone-Yoder, and J. A. Yoder. Photocaged morpholino oligomers for the light-regulation of gene function in zebrafish and xenopus embryos. *Journal of the American Chemical Society*, 132(44):15644–15650, 2010. doi: 10.1021/ja1053863.

[143] G. Mazzotti, D. Hartmann, and M. J. Booth. Precise, orthogonal remote-control of cell-free systems using photocaged nucleic acids. *Journal of the American Chemical Society*, 145(17):9481–9487, 2023. doi: 10.1021/jacs.3c01238.

[144] C. Ash, M. Dubec, K. Donne, and T. Bashford. Effect of wavelength and beam width on penetration in light-tissue interaction using computational methods. *Lasers in Medical Science*, 32(8):1909–1918, 2017. doi: 10.1007/s10103-017-2317-4.

[145] R. S. Riley, M. N. Dang, M. M. Billingsley, B. Abraham, L. Gundlach, and E. S. Day. Evaluating the mechanisms of light-triggered sirna release from nanoshells for temporal control over gene regulation. *Nano Letters*, 18(6):3565–3570, 2018. doi: 10.1021/acs.nanolett.8b00681.

[146] C. R. Brown, S. Gupta, J. Qin, T. Racie, G. He, S. Lentini, R. Malone, M. Yu, S. Matsuda, S. Shulga-Morskaya, and et al. Investigating the pharmacodynamic durability of galnac-sirna conjugates. *Nucleic Acids Research*, 48(21):11827–11844, 2020. doi: 10.1093/nar/gkaa670.

[147] C. He, M. T. Migawa, K. Chen, T. A. Weston, M. Tanowitz, W. Song, P. Guagliardo, K. S. Iyer, C. F. Bennett, L. G. Fong, and et al. High-resolution

visualization and quantification of nucleic acid-based therapeutics in cells and tissues using nanoscale secondary ion mass spectrometry (nanosims). *Nucleic Acids Research*, 49(1):1–14, 2021. doi: 10.1093/nar/gkaa1112.

[148] H. Makanai, T. Nishihara, M. Nishikawa, and K. Tanabe. Hoechst-modification on oligodeoxynucleotides for efficient transport to the cell nucleus and gene regulation. *Chembiochem*, 25(3):e202300645, 2024. doi: 10.1002/cbic.202300645.

[149] S. L. Schwartz and G. L. Conn. Rna regulation of the antiviral protein 2'-5'-oligoadenylate synthetase. *Wiley Interdisciplinary Reviews: RNA*, 10(4): e1534, 2019. doi: 10.1002/wrna.1534.

[150] N. M. Cirino, G. Li, W. Xiao, P. F. Torrence, and R. H. Silverman. Targeting rna decay with 2',5' oligoadenylate-antisense in respiratory syncytial virus-infected cells. *Proceedings of the National Academy of Sciences*, 94(5):1937–1942, 1997. doi: 10.1073/pnas.94.5.1937.

[151] X. Su, W. Ma, D. Feng, B. Cheng, Q. Wang, Z. Guo, D. Zhou, and X. Tang. Efficient inhibition of sars-cov-2 using chimeric antisense oligonucleotides through rnase l activation. *Angewandte Chemie International Edition*, 60 (40):21662–21667, 2021. doi: 10.1002/anie.202105942.

[152] X. Wang, Z. L. Qin, N. Li, M. Q. Jia, Q. G. Liu, Y. R. Bai, J. Song, S. Yuan, and S. Y. Zhang. Annual review of protac degraders as anticancer agents in 2022. *European Journal of Medicinal Chemistry*, 267:116166, 2024. doi: 10.1016/j.ejmech.2024.116166.

[153] K. T. G. Samarasinghe, E. An, M. A. Genuth, L. Chu, S. A. Holley, and C. M. Crews. Oligotraftacs: A generalizable method for transcription factor degradation. *RSC Chemical Biology*, 3(9):1144–1153, 2022. doi: 10.1039/d2cb00138a.

[154] A. Ghidini, A. Cléry, F. Halloy, F. H. T. Allain, and J. Hall. Rna-protacs: Degraders of rna-binding proteins. *Angewandte Chemie International Edition*, 60(6):3163–3169, 2021. doi: 10.1002/anie.202012330.

[155] R. Allen and T. Yokota. Endosomal escape and nuclear localization: Critical barriers for therapeutic nucleic acids. *Molecules*, 29(24), 2024. doi: 10.3390/molecules29245997.

[156] K. Klabenkova, A. Fokina, and D. Stetsenko. Chemistry of peptide-oligonucleotide conjugates: A review. *Molecules*, 26(17), 2021. doi: 10.3390/molecules26175420.

[157] Jonas Bucevičius, Gražvydas Lukinavičius, and Rūta Gerasimaitė. The use of hoechst dyes for dna staining and beyond. *Chemosensors*, 6(2):18, 2018. doi: 10.3390/chemosensors6020018. Submission received: 20 March 2018 / Revised: 15 April 2018 / Accepted: 17 April 2018 / Published: 18 April 2018.

[158] R. E. Durand and P. L. Olive. Cytotoxicity, mutagenicity and dna damage by hoechst 33342. *Radiation Research*, 30(2):194–210, 1982. doi: 10.1177/30.2.7061816.

[159] H. Ginisty, H. Sicard, B. Roger, and P. Bouvet. Structure and functions of nucleolin. *Journal of Cell Science*, 112(6):761–772, 1999. doi: 10.1242/jcs.112.6.761.

[160] J. J. Turner, G. D. Ivanova, B. Verbeure, D. Williams, A. A. Arzumanov, S. Abes, B. Lebleu, and M. J. Gait. Cell-penetrating peptide conjugates of peptide nucleic acids (pna) as inhibitors of hiv-1 tat-dependent trans - activation in cells. *Nucleic Acids Research*, 33(21):6837–6849, 2005. doi: 10.1093/nar/gki991.

[161] A. C. Hill, J. P. Becker, D. Slominski, F. Halloy, C. Søndergaard, J. Ravn, and J. Hall. Peptide conjugates of a 2-o-methoxyethyl phosphorothioate splice-switching oligonucleotide show increased entrapment in endosomes. *ACS Omega*, 8(43):40463–40481, 2023. doi: 10.1021/acsomega.3c05144.

[162] Maud Auger, Luis Sorroza-Martinez, Nadine Brahiti, Carole-Ann Huppé, Laurence Faucher-Giguère, Imen Arbi, Maxime Hervault, Xue Cheng, Bruno Gaillet, Frédéric Couture, David Guay, and Al-Halifa Soultan. Enhancing peptide and pmo delivery to mouse airway epithelia by chemical conjugation with the amphiphilic peptide s10. *Molecular Therapy - Nucleic Acids*, 34: 102290, 2024. doi: 10.1016/j.omtn.2024.102290.

[163] Tamami Miyagi, Koji Ueda, Masahiro Sugimoto, Takuya Yagi, Daisuke Ito, Rio Yamazaki, Satoshi Narumi, Yuhei Hayamizu, Hiroshi Uji-i, Masahiko Kuroda, and Kohsuke Kanekura. Differential toxicity and localization of arginine-rich c9orf72 dipeptide repeat proteins depend on de-clustering of positive charges. *Neurobiology of Disease*, 2023. doi: 10.1016/j.isci.2023.106957.

[164] W. J. Gibson, A. Sadagopan, V. M. Shoba, A. Choudhary, M. Meyerson, and S. L. Schreiber. Bifunctional small molecules that induce nuclear localization and targeted transcriptional regulation. *Journal of the American Chemical Society*, 145(48):26028–26037, 2023. doi: 10.1021/jacs.3c06179.

[165] P. Filippakopoulos, J. Qi, S. Picaud, Y. Shen, W. B. Smith, O. Fedorov, E. M. Morse, T. Keates, T. T. Hickman, I. Felletar, et al. Selective inhibition of bet bromodomains. *Nature*, 468(7327):1067–1073, 2010. doi: 10.1038/nature09504.

[166] E. Altendorfer, Y. Mochalova, and A. Mayer. Brd4: a general regulator of transcription elongation. *Transcription*, 13(1-3):70–81, 2022. doi: 10.1080/21541264.2022.2108302.

[167] K. L. Cheung, C. Kim, and M. M. Zhou. The functions of bet proteins in gene transcription of biology and diseases. *Front Mol Biosci*, 8:728777, 2021. doi: 10.3389/fmolb.2021.728777.

[168] B. Donati, E. Lorenzini, and A. Ciarrocchi. Brd4 and cancer: going beyond transcriptional regulation. *Molecular Cancer*, 17(1):164, 2018. doi: 10.1186/s12943-018-0915-9.

[169] A. Kotekar, A. K. Singh, and B. N. Devaiah. Brd4 and myc: power couple in transcription and disease. *Febs j*, 290(20):4820–4842, 2023. doi: 10.1111/febs.16580.

[170] Sung Ah Kim, Ara Go, Seung-Hyun Jo, Sun Jun Park, Young Uk Jeon, Ji Eun Kim, Heung Kyoung Lee, Chi Hoon Park, Chong-Ock Lee, Sung Goo Park, Pilho Kim, Byoung Chul Park, Sung Yun Cho, Sunhong Kim, Jae Du Ha, Jeong-Hoon Kim, and Jong Yeon Hwang. A novel cereblon modulator for targeted protein degradation. <*Journal Name*>, <Volume>(<Number>): <Page range>, 2023. doi: <DOIifknown>.

[171] S. He, G. Dong, Y. Li, S. Wu, W. Wang, and C. Sheng. Potent dual bet/hdac inhibitors for efficient treatment of pancreatic cancer. *Angewandte Chemie International Edition*, 59(8):3028–3032, 2020. doi: 10.1002/anie.201915896.

[172] S. H. Kang, M. J. Cho, and R. Kole. Up-regulation of luciferase gene expression with antisense oligonucleotides: implications and applications in functional assay development. *Biochemistry*, 37(18):6235–6239, 1998. doi: 10.1021/bi980300h.

[173] Sritama Bose and Peter L. Oliver. The chemistry and biology of oligonucleotide conjugation. *Nucleic Acid Insights*, 1(3):127–138, 2024. doi: 10.18609/nai.2024.018.

[174] Jianqing Zheng, Bifen Huang, Lihua Xiao, and Min Wu. Effects of brd4 inhibitor jq1 on the expression profile of super-enhancer-related lncRNAs and mRNAs in cervical cancer hela cells. *PeerJ*, 12:e17035, 2024. doi: 10.7717/peerj.17035.

[175] R. Yoshimoto, A. Mayeda, M. Yoshida, and S. Nakagawa. Malat1 long non-coding rna in cancer. *Biochim Biophys Acta*, 1859(1):192–199, 2016. doi: 10.1016/j.bbagrm.2015.09.012.

[176] A. A. Bhat, O. Afzal, M. Afzal, G. Gupta, R. Thapa, H. Ali, W. Hassan Almalki, I. Kazmi, S. I. Alzarea, S. Saleem, et al. Malat1: A key regulator in lung cancer pathogenesis and therapeutic targeting. *Pathol Res Pract*, 253: 154991, 2024. doi: 10.1016/j.prp.2023.154991.

[177] B. P. Monia, E. A. Lesnik, C. Gonzalez, W. F. Lima, D. McGee, C. J. Guinosso, A. M. Kawasaki, P. D. Cook, and S. M. Freier. Evaluation of 2'-modified oligonucleotides containing 2'-deoxy gaps as antisense inhibitors of gene expression. *J Biol Chem*, 268(19):14514–14522, 1993.

[178] Xinying Zong, Lulu Huang, Vidisha Tripathi, Raechel Peralta, Susan M. Freier, Shuling Guo, and Kannanganattu V. Prasanth. Knockdown of nuclear-retained long noncoding rnas using modified dna antisense oligonucleotides. In *Nuclear Bodies and Noncoding RNAs: Methods in Molecular Biology*, volume 1262, pages 321–331. Humana Press, 2014. doi: 10.1007/978-1-4939-2253-6_20.

[179] D. P. Chimento, A. L. Anderson, I. Fial, and C. A. Ascoli. Bioanalytical assays for oligonucleotide therapeutics: Adding antibody-based immunoassays to the toolbox as an orthogonal approach to lc-ms/ms and ligand binding assays. *Nucleic Acid Therapeutics*, 35(1):6–15, 2025. doi: 10.1089/nat.2024.0065.

[180] B. D. Cheson. Oblimersen for the treatment of patients with chronic lymphocytic leukemia. *Ther Clin Risk Manag*, 3(5):855–870, 2007.

[181] S. Qian, Z. Wei, W. Yang, J. Huang, Y. Yang, and J. Wang. The role of bcl-2 family proteins in regulating apoptosis and cancer therapy. *Front Oncol*, 12: 985363, 2022. doi: 10.3389/fonc.2022.985363.

[182] S. Frantz. Lessons learnt from genasense's failure. *Nature Reviews Drug Discovery*, 3(7):542, 2004. doi: 10.1038/nrd1464.

[183] A. R. Walker, G. Marcucci, J. Yin, W. Blum, W. Stock, J. Kohlschmidt, K. Mrózek, A. J. Carroll, A. K. Eisfeld, E. S. Wang, et al. Phase 3 randomized trial of chemotherapy with or without oblimersen in older aml patients: Calgb 10201 (alliance). *Blood Adv*, 5(13):2775–2787, 2021. doi: 10.1182/bloodadvances.2021004233.

[184] Katerina Tzelepis, Hisanori Koike-Yusa, Elise De Braekeleer, Yi Li, Eleftheria Metzakopian, Olga M. Dovey, Alberta Mupo, Valentyna Grinkevich, Mingfei Li, Alexandre Armache, Bin Chen, Chris Vadas, Ken Stegmaier, Alexander Bradley, K. C. Park, Henrik Johnsen, Philip J. Campbell, and Berthold Göttgens. Brd4 inhibition is synthetic lethal with parp inhibitors through the induction of homologous recombination deficiency in human thp-1 cells. In *Cancer Cell*, volume 33, pages 401–416.e6. Elsevier, 2018. doi: 10.1016/j.ccell.2018.01.019.

[185] Arvin M. Gouw, Katherine Margulis, Natalie S. Liu, Sudha J. Raman, Anthony Mancuso, Georgia G. Toal, Ling Tong, Adriane Mosley, Annie L. Hsieh, Delaney K. Sullivan, Zachary E. Stine, Brian J. Altman, Almut Schulze, Chi V. Dang, Richard N. Zare, and Dean W. Felsher. The myc oncogene cooperates with sterol regulated element-binding protein to regulate lipogenesis essential for neoplastic growth. *Cell Metabolism*, 30(3):556–572.e5, September 2019. doi: 10.1016/j.cmet.2019.07.004. Published online 2019 Aug 14.

[186] S. L. Schreiber. Molecular glues and bifunctional compounds: Therapeutic

modalities based on induced proximity. *Cell Chemical Biology*, 31(6):1050–1063, 2024. doi: 10.1016/j.chembiol.2024.05.004. Accessed 2024/10/07.

[187] T. C. Roberts, R. Langer, and M. J. A. Wood. Advances in oligonucleotide drug delivery. *Nature Reviews Drug Discovery*, 19(10):673–694, 2020. doi: 10.1038/s41573-020-0075-7.

[188] X. H. Liang, H. Sun, J. G. Nichols, and S. T. Crooke. Mechanisms of aso-mediated rna degradation. *Mol Ther*, 25:2075–2092, 2017.

[189] J. Kim, C. Hu, C. Moufawad El Achkar, and et al. Patient-customized genetic therapy. *N Engl J Med*, 381:1644–1652, 2019.

[190] P. E. Harrington, K. Biswas, D. Malwitz, and et al. Antisense drug discovery. *ACS Med Chem Lett*, 6:68–72, 2015.

[191] T. H. Ali, A. M. Mandal, T. Heidelberg, and R. S. D. Hussen. Synthetic modifications of nucleotides. *RSC Adv*, 12:13566–13579, 2022.

[192] C. S. Thakur, B. K. Jha, B. Dong, and et al. Mechanism of rnase l activation. *Proc Natl Acad Sci U S A*, 104:9585–9590, 2007.

[193] N. M. Cirino, G. Li, W. Xiao, and et al. Rnase l activation. *Proc Natl Acad Sci U S A*, 94:1937–1942, 1997.

[194] X. Su, W. Ma, D. Feng, and et al. Synthetic chemistry for rna targeting. *Angew Chem Int Ed Engl*, 60:21662–21667, 2021.

[195] M. G. Costales, Y. Matsumoto, S. P. Velagapudi, and M. D. Disney. Rna-binding small molecules. *J Am Chem Soc*, 140:6741–6744, 2018.

[196] Y. Tong, Y. Lee, X. Liu, and et al. Small molecule targeting of oncogenic rna. *Nature*, 618:169–179, 2023.

[197] C. S. Thakur, B. K. Jha, B. Dong, J. Das Gupta, K. M. Silverman, H. Mao, H. Sawai, A. O. Nakamura, A. K. Banerjee, A. Gudkov, et al. Small-molecule activators of rnase l with broad-spectrum antiviral activity. *Proceedings of the National Academy of Sciences of the United States of America*, 104(23): 9585–9590, 2007. doi: 10.1073/pnas.0700590104.

[198] C. Meyer, P. Larghero, B. Almeida Lopes, and et al. Mll rearranged leukemia. *Leukemia*, 37:988–1005, 2023.

[199] A. K. N. Chan and C. W. Chen. Developmental biology of leukemia. *Front Cell Dev Biol*, 7:81, 2019.

[200] Z. Luo, C. Lin, E. Guest, and et al. Transcriptional regulation by mll fusion proteins. *Mol Cell Biol*, 32:2608–2617, 2012.

[201] S. Rice, T. Jackson, N. T. Crump, and et al. Epigenetic modulation in mll leukemia. *Nat Commun*, 12:6905, 2021.

[202] A. Sanjuan-Pla, C. Bueno, C. Prieto, and et al. Leukemia stem cell identity. *Blood*, 126:2676–2685, 2015.

[203] E. Ferri, A. Le Thomas, H. A. Wallweber, and et al. Protein-rna interactions in cancer. *Nat Commun*, 11:6387, 2020.

[204] M. Thomas, A. Gessner, H. P. Vornlocher, and et al. sirna therapeutics in leukemia. *Blood*, 106:3559–3566, 2005.

[205] J. Greil, M. Gramatzki, R. Burger, R. Marschalek, M. Peltner, U. Trautmann, T. E. Hansen-Hagge, C. R. Bartram, G. H. Fey, and K. Stehr. The acute lymphoblastic leukaemia cell line SEM with t(4;11) chromosomal rearrangement is biphenotypic and responsive to interleukin-7. *British Journal of Haematology*, 86(2):275–283, 1994. doi: 10.1111/j.1365-2141.1994.tb04726.x.

[206] Peter Kerpedjiev, Stefan Hammer, and Ivo L. Hofacker. Forna (force-directed RNA): Simple and effective online RNA secondary structure diagrams. *Nucleic Acids Research*, 43(W1):W650–W654, October 2015. doi: 10.1093/nar/gkv456.

[207] Jon Kerry, Laura Godfrey, Emmanouela Repapi, Marta Tapia, Neil P. Blackledge, Helen Ma, Erica Ballabio, Sorcha O'Byrne, Frida Ponthan, Olaf Heidenreich, Anindita Roy, Irene Roberts, Marina Konopleva, Robert J. Klose, Huimin Geng, and Thomas A. Milne. MLL-AF4 spreading identifies binding sites that are distinct from super-enhancers and that govern sensitivity to DOT1L inhibition in leukemia. *Cell Reports*, 37(9):110058, 2021. doi: 10.1016/j.celrep.2021.110058.

[208] Johann Greil, Martin Gramatzki, Renate Burger, Rolf Marschalek, Markus Peltner, Udo Trautmann, Thomas E. Hansen-Hagge, Claus R. Bartram, Georg H. Fey, Klemens Stehr, and Jörn Beck. The acute lymphoblastic leukaemia cell line sem with t(4;11) chromosomal rearrangement is biphenotypic and responsive to interleukin-7. *British Journal of Haematology*, 86 (2):275–283, February 1994. doi: 10.1111/j.1365-2141.1994.tb04726.x. Cited by 93 as of July 2025.

[209] Samantha M. Meyer, Toru Tanaka, Patrick R. A. Zanon, Jared T. Baisden, Daniel Abegg, Xueyi Yang, Yoshihiro Akahori, Zainab Alshakarchi, Michael D. Cameron, Alexander Adibekian, and Matthew D. Disney. Dna-encoded library screening to inform design of a ribonuclease targeting chimera (ribotac). *Journal of the American Chemical Society*, 144(46):21096–21102, 2022. doi: 10.1021/jacs.2c07217.

[210] Y. Miao, C. Fu, Z. Yu, L. Yu, Y. Tang, and M. Wei. Current status and trends in small nucleic acid drug development: Leading the future. *Acta Pharm. Sin. B*, 14(9):3802–3817, 2024. doi: 10.1016/j.apsb.2024.05.008.

[211] J. Han, J. Xiong, D. Wang, and X. D. Fu. Pre-mrna splicing: where and when in the nucleus. *Trends Cell Biol.*, 21(6):336–343, 2011. doi: 10.1016/j.tcb.2011.03.003.

[212] W. Shen, H. Sun, C. L. De Hoyos, J. K. Bailey, X. H. Liang, and S. T. Crooke. Dynamic nucleoplasmic and nucleolar localization of mammalian rnase h1 in response to rnap i transcriptional r-loops. *Nucleic Acids Res.*, 45(18):10672–10692, 2017. doi: 10.1093/nar/gkx710.

[213] P. J. Thul, L. Åkesson, M. Wiking, D. Mahdessian, A. Geladaki, H. Ait Blal, T. Alm, A. Asplund, L. Björk, L. M. Breckels, and et al. A subcellular map of the human proteome. *Science*, 356(6340), 2017. doi: 10.1126/science.aal3321.

[214] Disha Kashyap, Martina Cadeddu, Peter L. Oliver, Thomas A. Milne, and Michael J. Booth. Harnessing bet-bromodomain assisted nuclear import for targeted subcellular localization and enhanced efficacy of antisense oligonucleotides. *Journal of the American Chemical Society*, August 2025. doi: 10.1021/jacs.5c09544.

[215] A. Karasik, G. D. Jones, A. V. DePass, and N. R. Guydosh. Activation of the antiviral factor rnase l triggers translation of non-coding mrna sequences. *Nucleic Acids Research*, 49(11):6007–6026, 2021. doi: 10.1093/nar/gkab036.

[216] M. A. Siddiqui, S. Mukherjee, P. Manivannan, and K. Malathi. Rnase l cleavage products promote switch from autophagy to apoptosis by caspase-mediated cleavage of beclin-1. *International Journal of Molecular Sciences*, 16(8):17611–17636, 2015. doi: 10.3390/ijms160817611.

[217] A. Ballabio and J. S. Bonifacino. Lysosomes as dynamic regulators of cell and organismal homeostasis. *Nature Reviews Molecular Cell Biology*, 21(2):101–118, 2020. doi: 10.1038/s41580-019-0185-4.

[218] C. Settembre and A. Ballabio. Lysosome: regulator of lipid degradation pathways. *Trends in Cell Biology*, 24(12):743–750, 2014. doi: 10.1016/j.tcb.2014.06.006.

[219] Y. Fujiwara, K. Wada, and T. Kabuta. Lysosomal degradation of intracellular nucleic acids-multiple autophagic pathways. *Journal of Biochemistry*, 161(2):145–154, 2017. doi: 10.1093/jb/mvw085.

[220] R. R. Paudel, D. Lu, S. Roy Chowdhury, E. Y. Monroy, and J. Wang. Targeted protein degradation via lysosomes. *Biochemistry*, 62(3):564–579, 2023. doi: 10.1021/acs.biochem.2c00310.

[221] S. M. Banik, K. Pedram, S. Wisnovsky, G. Ahn, N. M. Riley, and C. R. Bertozzi. Lysosome-targeting chimaeras for degradation of extracellular proteins. *Nature*, 584(7820):291–297, 2020. doi: 10.1038/s41586-020-2545-9.

[222] G. Ahn, S. M. Banik, C. L. Miller, N. M. Riley, J. R. Cochran, and C. R. Bertozzi. Lytacs that engage the asialoglycoprotein receptor for targeted protein degradation. *Nat. Chem. Biol.*, 17(9):937–946, 2021. doi: 10.1038/s41589-021-00770-1.

[223] Y. Miao, Q. Gao, M. Mao, C. Zhang, L. Yang, Y. Yang, and D. Han. Bispecific aptamer chimeras enable targeted protein degradation on cell membranes. *Angew Chem. Int. Ed. Engl.*, 60(20):11267–11271, 2021. doi: 10.1002/anie.202102170.

[224] L. J. Seabrook, C. N. Franco, C. A. Loy, J. Osman, C. Fredlender, J. Zimak, M. Campos, S. T. Nguyen, R. L. Watson, and S. R. Levine. Methylarginine targeting chimeras for lysosomal degradation of intracellular proteins. *Nat. Chem. Biol.*, 20(12):1566–1576, 2024. doi: 10.1038/s41589-024-01741-y.

[225] L. Lad, L. Luo, J. D. Carson, K. W. Wood, J. J. Hartman, R. A. Copeland,

and R. Sakowicz. Mechanism of inhibition of human ksp by ispinesib. *Biochemistry*, 47(11):3576–3585, 2008. doi: 10.1021/bi702061g.

[226] C. W. Lee, K. Bélanger, S. C. Rao, T. M. Petrella, R. G. Tozer, L. Wood, K. J. Savage, E. A. Eisenhauer, T. W. Synold, and N. Wainman. A phase ii study of ispinesib (sb-715992) in patients with metastatic or recurrent malignant melanoma: a national cancer institute of canada clinical trials group trial. *Invest. New Drugs*, 26(3):249–255, 2008. doi: 10.1007/s10637-007-9097-9.

[227] G. Dong, Y. Wu, J. Cheng, L. Chen, R. Liu, Y. Ding, S. Wu, J. Ma, and C. Sheng. Ispinesib as an effective warhead for the design of autophagosome-tethering chimeras: Discovery of potent degraders of nicotinamide phosphoribosyltransferase (nampt). *J. Med. Chem.*, 65(11):7619–7628, 2022. doi: 10.1021/acs.jmedchem.1c02001.

[228] Z. Li, C. Zhu, Y. Ding, Y. Fei, and B. Lu. Attec: a potential new approach to target proteinopathies. *Autophagy*, 16(1):185–187, 2020. doi: 10.1080/15548627.2019.1688556.

[229] S. A. Armstrong F. Perner, J. Y. Gadrey and M. W. M. Kühn. Targeting the menin-kmt2a interaction in leukemia: Lessons learned and future directions. *Int. J. Cancer*, 2025. doi: 10.1002/ijc.35332.

[230] A. M. Jawalekar, S. Malik, J. M. Verkade, B. Gibson, N. S. Barta, J. C. Hodges, A. Rowan, and F. L. van Delft. Oligonucleotide tagging for copper-free click conjugation. *Molecules*, 18(7):7346–7363, 2013. doi: 10.3390/molecules18077346.

[231] K. R. Q. Lim and T. Yokota. Invention and early history of gapmers. *Methods in Molecular Biology*, 2176:3–19, 2020. doi: 10.1007/978-1-0716-0771-8_1.

[232] P. R. Purnell and H. S. Fox. Autophagy-mediated turnover of dynamin-related protein 1. *BMC Neuroscience*, 14:86, 2013. doi: 10.1186/1471-2202-14-86.

[233] C. Mauvezin and T. P. Neufeld. Bafilomycin a1 disrupts autophagic flux by inhibiting both v-atpase-dependent acidification and ca-p60a/serca-dependent autophagosome-lysosome fusion. *Autophagy*, 11(8):1437–1438, 2015. doi: 10.1080/15548627.2015.1066957.

[234] E. Pandey and E. N. Harris. Chloroquine and cytosolic galectins affect endosomal escape of antisense oligonucleotides after stabilin-mediated endocytosis. *Molecular Therapy - Nucleic Acids*, 33:430–443, 2023. doi: 10.1016/j.omtn.2023.07.019.

[235] C. Cherif, D. T. Nguyen, C. Paris, T. K. Le, T. Sefiane, N. Carbuccia, P. Finetti, M. Chaffanet, A. E. Kaoutari, J. Vernerey, and et al. Menin inhibition suppresses castration-resistant prostate cancer and enhances chemosensitivity. *Oncogene*, 41(1):125–137, 2022. doi: 10.1038/s41388-021-02039-2.

[236] S. Matkar, A. Thiel, and X. Hua. Menin: a scaffold protein that controls gene expression and cell signaling. *Trends in Biochemical Sciences*, 38(8):394–402, 2013. doi: 10.1016/j.tibs.2013.05.005.

[237] Y. Wu, Z. J. Feng, S. B. Gao, S. Matkar, B. Xu, H. B. Duan, X. Lin, S. H. Li, X. Hua, and G. H. Jin. Interplay between menin and k-ras in regulating lung adenocarcinoma. *Journal of Biological Chemistry*, 287(47):40003–40011, 2012. doi: 10.1074/jbc.M112.382416.

[238] T. Cierpicki and J. Grembecka. Challenges and opportunities in targeting the menin-mll interaction. *Future Medicinal Chemistry*, 6(4):447–462, 2014. doi: 10.4155/fmc.13.214.

[239] W. Fiskus, S. Boettcher, N. Daver, C. P. Mill, K. Sasaki, C. E. Birdwell, J. A. Davis, K. Takahashi, T. M. Kadia, C. D. DiNardo, and et al. Effective menin inhibitor-based combinations against aml with mll rearrangement or npm1 mutation (npm1c). *Blood Cancer Journal*, 12(1):5, 2022. doi: 10.1038/s41408-021-00603-3.

[240] F. Perner, E. M. Stein, D. V. Wenge, S. Singh, J. Kim, A. Apazidis, H. Rahnamoun, D. Anand, C. Marinaccio, C. Hatton, and et al. Men1 mutations mediate clinical resistance to menin inhibition. *Nature*, 615(7954):913–919, 2023. doi: 10.1038/s41586-023-05755-9.

[241] Martin P. Schwalm, Johannes Dopfer, Adarsh Kumar, Francesco A. Greco, Nicolas Bauer, Frank Löhr, Jan Heering, Sara Cano-Franco, Severin Lechner, Thomas Hanke, Ivana Jaser, Viktoria Morasch, Christopher Lenz, Daren Fearon, Peter G. Marples, Charles W. E. Tomlinson, Lorene Brunello, Krishna Saxena, Nathan B. P. Adams, Frank von Delft, Susanne Müller, Alexandra Stolz, Ewgenij Proschak, Bernhard Kuster, Stefan Knapp, and Vladimir V. Rogov. Critical assessment of LC3/GABARAP ligands used for degrader development and ligandability of LC3/GABARAP binding pockets. *Nature Communications*, 15:5091, 2024. doi: 10.1038/s41467-024-42858-z.

[242] Zhaoyang Li, Cen Wang, Ziying Wang, Chenggang Zhu, Jie Li, Tian Sha, Lixiang Ma, Chao Gao, Yi Yang, Yimin Sun, Jian Wang, Xiaoli Sun, Chenqi Lu, Marian Difiglia, Yanai Mei, Chen Ding, Shouqing Luo, Yongjun Dang, Yu Ding, Yiyan Fei, and Boxun Lu. Allele-selective lowering of mutant HTT protein by HTT-LC3 linker compounds. *Nature*, 575(7781):203–209, 2019. doi: 10.1038/s41586-019-1722-1.

[243] Y. Fu, N. Chen, Z. Wang, S. Luo, Y. Ding, and B. Lu. Degradation of lipid droplets by chimeric autophagy-tethering compounds. *Cell Research*, 31(9): 965–979, 2021. doi: 10.1038/s41422-021-00532-7.

[244] S. Tan, D. Wang, Y. Fu, H. Zheng, Y. Liu, and B. Lu. Targeted clearance of mitochondria by an autophagy-tethering compound (attec) and its potential therapeutic effects. *Science Bulletin (Beijing)*, 68(23):3013–3026, 2023. doi: 10.1016/j.scib.2023.10.021.

[245] Gang Xue, Jianing Xie, Matthias Hinterndorfer, Marko Cigler, Lara Dötsch,

Hana Imrichova, Philipp Lampe, Xiufen Cheng, Soheila Rezaei Adariani, Georg E. Winter, and Herbert Waldmann. Discovery of a drug-like, natural product-inspired dcaf11 ligand chemotype. *Nature Chemical Biology*, 2023. Received: 20 March 2023; Accepted: 15 November 2023.

[246] Nadrian C. Seeman. Nucleic acid junctions and lattices. *Journal of Molecular Biology*, 173:789–816, 1982.

[247] Erik Winfree, Furong Liu, Lisa A. Wenzler, and Nadrian C. Seeman. Design and self-assembly of two-dimensional dna crystals. *Nature*, 394:539–544, 1998.

[248] Paul W. K. Rothemund, Nick Papadakis, and Erik Winfree. Algorithmic self-assembly of dna sierpinski triangles. *PLoS Biology*, 2(12):e424, 2004.

[249] Reid P. Goodman, Ryosuke M. Berry, and Nadrian C. Seeman. Rapid chiral assembly of rigid dna building blocks for molecular nanofabrication. *Science*, 310:1661–1665, 2005.

[250] Fan Zhang, Yonggang Ke, Shaojie Yan, Yonggang Ke, and Hao Yan. Complex wireframe dna origami nanostructures with multi-arm junction vertices. *Nature Nanotechnology*, 4:229–233, 2009.

[251] Paul W. K. Rothemund. Folding dna to create nanoscale shapes and patterns. *Nature*, 440:297–302, 2006.

[252] Ebbe S. Andersen, Mingdong Dong, Mette M. Nielsen, Kasper Jahn, Rolf Subramani, Wael Mamdouh, Monika M. Golas, Bjarne Sander, Holger Stark, Cristiano L. Oliveira, Jan K. Pedersen, Veit Birkedal, Flemming Besenbacher, Kurt V. Gothelf, and Jørgen Kjems. Self-assembly of a nanoscale dna box with a controllable lid. *Nature*, 459:73–76, 2009.

[253] David Y. Zhang and Erik Winfree. Control of dna strand displacement kinetics using toehold exchange. *Nature Chemistry*, 1:186–190, 2009.

[254] Peng Yin, Hari K. Sahu, and Jonathan H. Reif. Walking molecules can navigate a network of tracks. *Science*, 303(5658):538–541, 2004.

[255] Shawn M. Douglas, Ido Bachelet, and George M. Church. A logic-gated nanorobot for targeted transport of molecular payloads. *Science*, 335(6070): 831–834, 2012.

[256] Andrew J. Turberfield, Jonathan C. Mitchell, Bernard Yurke, Alexander P. Mills, Michael I. Blakey, and Friedrich C. Simmel. Dna fuel for free-running nanomachines. *Proceedings of the Royal Society of London. Series A: Mathematical, Physical and Engineering Sciences*, 361(1805):417–427, 2003.

[257] Qian Liu, Tianyu Zhang, and Chunhai Fan. A dna nanorobot functions as a cancer therapeutic in response to a molecular trigger in vivo. *Nature Biotechnology*, 36:258–264, 2018.

[258] Ralf Jungmann, Maier S. Avendaño, Johannes B. Woehrstein, Mireille Dai, William M. Shih, and Peng Yin. Multiplexed 3d cellular super-resolution imaging with dna-paint and exchange-paint. *Nano Letters*, 14:4270–4276, 2014.

[259] Joshua I. Cutler, Erin Auyeung, and Chad A. Mirkin. Spherical nucleic acids: novel agents for gene regulation and therapy. *Proceedings of the National Academy of Sciences*, 109:16510–16515, 2012.

[260] Lulu Qian, Erik Winfree, and Jehoshua Bruck. Neural network computation with dna strand displacement cascades. *Science*, 332:1196–1201, 2011.

[261] Dennis L. Buckley, Gregory E. Winter, and James E. Bradner. Targeting the undruggable genome with chemical degraders. *Nature Structural & Molecular Biology*, 22:386–391, 2015.

[262] Kazuhiro M. Sakamoto, Kris N. Kim, Bin Verma, Patricia A. Ransick, Scott Steinman, Craig M. Crews, and Raymond J. Deshaies. Development of

protacs to target cancer-promoting proteins for ubiquitination and degradation. *Molecular & Cellular Proteomics*, 2(N/A), 2003. doi: 10.1074/mcp.t300009-mcp200.

[263] Matthew D. Petroski and Raymond J. Deshaies. Function and regulation of cullin–ring ubiquitin ligases. *Nature Reviews Molecular Cell Biology*, 6(1): 9–20, January 2005. doi: 10.1038/nrm1547.

[264] K. M. Sakamoto, K. B. Kim, A. Kumagai, F. Mercurio, C. M. Crews, and R. J. Deshaies. Protacs: chimeric molecules that target proteins to the skp1-cullin-f box complex for ubiquitination and degradation. *Proceedings of the National Academy of Sciences*, 98(15):8554–8559, 2001. doi: 10.1073/pnas.141230798.

[265] Gregory E. Winter, Dennis L. Buckley, Jesse Paulk, Justin M. Roberts, Amanda Souza, Suresh Dhe-Paganon, and James E. Bradner. Drug development: Phthalimide conjugation as a strategy for in vivo target protein degradation. *Science*, 348:1376–1381, 2015.

[266] Christopher J. Burslem and Craig M. Crews. Proteolysis-targeting chimeras as therapeutics and tools for biological discovery. *Nature Reviews Drug Discovery*, 19:99–114, 2020.

[267] Michael S. Gadd, Craig M. Testa, Paul Lucas, David T. Chan, Owen T. Chen, David C. Strickland, John R. Shaginian, Paul J. Bondeson, Dennis L. Buckley, James E. Bradner, Nathanael S. Gray, and Eric S. Fischer. Structural basis of protac cooperative recognition for selective protein degradation. *Nature Chemical Biology*, 13:514–521, 2017.

[268] Li Zhou, Bin Yu, Mengqiu Gao, Rui Chen, Zhiyu Li, Yueqing Gu, Jinlei Bian, and Yi Ma. Dna framework-engineered chimeras platform enables selectively targeted protein degradation. *Nature Communications*, 14(1):4510, 2023. doi: 10.1038/s41467-023-40244-7.

[269] Jiayin Zhan, Xiang Li, Zhe Feng, Zheng Liu, Zhiyuan Feng, Jun-Jie Zhu, and Jingjing Zhang. Microrna-triggered programmable dna-encoded pre-protacs for cell-selective and controlled protein degradation. *Angewandte Chemie International Edition*, 63(41):e202415323, 2024. doi: 10.1002/anie.202415323.

[270] Yuzhe Shang, Longyi Zhu, Yang Xiao, Songyuan Du, Ruoyang Ji, Bin Li, Jialiang Chen, Shengyuan Deng, and Kewei Ren. Logic gate activated lysosome targeting dna nanodevice for controlled proteins degradation. *Advanced Functional Materials*, 34(12):23011722, 2024. doi: 10.1002/adfm.202311722.

[271] M. Schapira, M. F. Calabrese, A. N. Bullock, and C. M. Crews. Targeted protein degradation: expanding the toolbox. *Nature Reviews Drug Discovery*, 18(12):949–963, 2019. doi: 10.1038/s41573-019-0047-y.

[272] L. Gong, D. Cui, X. Xiong, and Y. Zhao. Targeting cullin-ring ubiquitin ligases and the applications in protacs. In *Advances in Experimental Medicine and Biology*, volume 1217, pages 317–347. 2020. doi: 10.1007/978-981-15-1025-0_19.

[273] D. P. Bondeson, A. Mares, I. E. Smith, E. Ko, S. Campos, A. H. Miah, K. E. Mulholland, N. Routly, D. L. Buckley, J. L. Gustafson, et al. Catalytic in vivo protein knockdown by small-molecule protacs. *Nature Chemical Biology*, 11(8):611–617, 2015. doi: 10.1038/nchembio.1858.

[274] C. Wang, C. Zheng, H. Wang, L. Zhang, Z. Liu, and P. Xu. The state of the art of protac technologies for drug discovery. *European Journal of Medicinal Chemistry*, 235:114290, 2022. doi: 10.1016/j.ejmech.2022.114290.

[275] Q. H. Chen, E. Munoz, and D. Ashong. Insight into recent advances in degrading androgen receptor for castration-resistant prostate cancer. *Cancers (Basel)*, 16(3), 2024. doi: 10.3390/cancers16030663.

[276] X. Lin, H. Xiang, and G. Luo. Targeting estrogen receptor α for degradation with protacs: A promising approach to overcome endocrine resistance. *European Journal of Medicinal Chemistry*, 206:112689, 2020. doi: 10.1016/j.ejmech.2020.112689.

[277] M. Xiao, J. Zhao, Q. Wang, J. Liu, and L. Ma. Recent advances of degradation technologies based on protac mechanism. *Biomolecules*, 12(9), 2022. doi: 10.3390/biom12091257.

[278] X. Dai, W. Gan, X. Li, S. Wang, W. Zhang, L. Huang, S. Liu, Q. Zhong, J. Guo, J. Zhang, et al. Prostate cancer-associated spop mutations confer resistance to bet inhibitors through stabilization of brd4. *Nature Medicine*, 23(9):1063–1071, 2017. doi: 10.1038/nm.4378.

[279] N. Pravin and K. Jóźwiak. Protac unleashed: Unveiling the synthetic approaches and potential therapeutic applications. *European Journal of Medicinal Chemistry*, 279:116837, 2024. doi: 10.1016/j.ejmech.2024.116837.

[280] H. Lebraud, D. J. Wright, C. N. Johnson, and T. D. Heightman. Protein degradation by in-cell self-assembly of proteolysis targeting chimeras. *ACS Central Science*, 2(12):927–934, 2016. doi: 10.1021/acscentsci.6b00280.

[281] T. C. Do, J. W. Lau, C. Sun, S. Liu, K. T. Kha, S. T. Lim, Y. Y. Oon, Y. P. Kwan, J. J. Ma, Y. Mu, et al. Hypoxia deactivates epigenetic feedbacks via enzyme-derived clicking proteolysis-targeting chimeras. *Science Advances*, 8 (50):eabq2216, 2022. doi: 10.1126/sciadv.abq2216.

[282] W. Cheng, S. Li, S. Han, R. Miao, S. Wang, C. Liu, H. Wei, X. Tian, and X. Zhang. Design, synthesis and biological evaluation of the tumor hypoxia-activated protacs bearing caged crbn e3 ligase ligands. *Bioorganic & Medicinal Chemistry*, 82:117237, 2023. doi: 10.1016/j.bmc.2023.117237.

[283] H. Liu, C. Ren, R. Sun, H. Wang, Y. Zhan, X. Yang, B. Jiang, and H. Chen. Reactive oxygen species-responsive pre-protac for tumor-specific protein degradation. *Chemical Communications*, 58(72):10072–10075, 2022. doi: 10.1039/d2cc03367d.

[284] J. Liu, H. Chen, L. Ma, Z. He, D. Wang, Y. Liu, Q. Lin, T. Zhang, N. Gray, H. Kaniskan, et al. Light-induced control of protein destruction by opto-protac. *Science Advances*, 6(8):eaay5154, 2020. doi: 10.1126/sciadv.aay5154.

[285] M. Reynders and D. Trauner. Photacs enable optical control of protein degradation. In *Methods in Molecular Biology*, volume 2365, pages 315–329. 2021. doi: 10.1007/978-1-0716-1665-9_17.

[286] Y. Zhang, X. Tian, Z. Wang, H. Wang, F. Liu, Q. Long, and S. Jiang. Advanced applications of dna nanostructures dominated by dna origami in antitumor drug delivery. *Frontiers in Molecular Biosciences*, 10:1239952, 2023. doi: 10.3389/fmolb.2023.1239952.

[287] D. Lien. The role of dna nanotechnology in medical sensing. *Analytical Methods*, 17(5):1148–1159, 2025. doi: 10.1039/d4ay01803f.

[288] A. R. Chandrasekaran, J. A. Punnoose, L. Zhou, P. Dey, B. K. Dey, and K. Halvorsen. Dna nanotechnology approaches for microrna detection and diagnosis. *Nucleic Acids Research*, 47(20):10489–10505, 2019. doi: 10.1093/nar/gkz580.

[289] C. N. Weller and J. Hall. Oligonucleotide-based protacs to degrade rna- and dna-binding proteins. *Chimia*, 79(3):167–173, 2025. doi: 10.2533/chimia.2025.167.

[290] L. Zhang, L. Li, X. Wang, H. Liu, Y. Zhang, T. Xie, H. Zhang, X. Li, T. Peng, X. Sun, J. Dai, J. Liu, W. Wu, M. Ye, and W. Tan. Development of a novel protac using the nucleic acid aptamer as a targeting ligand for tumor-selective

degradation of nucleolin. *Molecular Therapy Nucleic Acids*, 30:66–79, 2022. doi: 10.1016/j.omtn.2022.09.008.

[291] M. Zengerle, K. H. Chan, and A. Ciulli. Selective small molecule induced degradation of the bet bromodomain protein brd4. *ACS Chem Biol*, 10(8): 1770–1777, 2015. doi: 10.1021/acschembio.5b00216.

[292] L. Ma, J. Wang, Y. Zhang, F. Fang, J. Ling, X. Chu, Z. Zhang, Y. Tao, X. Li, Y. Tian, et al. Brd4 protac degrader mz1 exerts anticancer effects in acute myeloid leukemia by targeting c-myc and anp32b genes. *Cancer Biol Ther*, 23(1):1–15, 2022. doi: 10.1080/15384047.2022.2125748.

[293] P. Filippakopoulos, J. Qi, S. Picaud, Y. Shen, W. B. Smith, O. Fedorov, E. M. Morse, T. Keates, T. T. Hickman, I. Felletar, et al. Selective inhibition of bet bromodomains. *Nature*, 468(7327):1067–1073, 2010. doi: 10.1038/nature09504.

[294] C. J. Diehl and A. Ciulli. Discovery of small molecule ligands for the von hippel-lindau (vhl) e3 ligase and their use as inhibitors and protac degraders. *Chem Soc Rev*, 51(19):8216–8257, 2022. doi: 10.1039/d2cs00387b.

[295] K. Morihiro, S. Morita, N. Harada, M. Baba, J. Yum, M. Naito, K. Miyata, G. Nagae, and A. Okamoto. Rna oncological therapeutics: Intracellular hairpin rna assembly enables microrna-triggered anticancer functionality. *Journal of the American Chemical Society*, 146(2):1346–1355, 2024. doi: 10.1021/jacs.3c09524.

[296] J. E. Summerton. Morpholino, sirna, and s-dna compared: impact of structure and mechanism of action on off-target effects and sequence specificity. *Current Topics in Medicinal Chemistry*, 7(7):651–660, 2007. doi: 10.2174/156802607780487740.

[297] Doyeong Ku, Yewon Yang, and Yoosik Kim. Rna-associated nuclear condensates: Where the nucleus keeps its rnas in check. *BMB Reports*, TBD:TBD, 2025. doi: 10.1016/j.bbrc.2025.06.064. Minireview.

[298] Yvette R. Baker, Claire Thorpe, Jia Chen, Laura M. Poller, Laura Cox, Priya Kumar, Wei Feng Lim, Leo Lie, Graham McClorey, Sabine Epple, et al. An lna-amide modification that enhances the cell uptake and activity of phosphorothioate exon-skipping oligonucleotides. *Nature Communications*, 13(1): 4036, 2022. doi: 10.1038/s41467-022-31636-2.

[299] Adam C. Wilkinson, Erica Ballabio, Haixia Geng, Paul North, Manuel Tapia, John Kerry, Deba Biswas, Robert G. Roeder, C. David Allis, Ari Melnick, et al. Runx1 is a key target in t(4;11) leukemias that contributes to gene activation through an af4-mll complex interaction. *Cell Reports*, 3(1):116–127, 2013. doi: 10.1016/j.celrep.2012.12.016.

[300] Simon Andrews. Fastqc: A quality control tool for high throughput sequence data, 2010. Version 0.12.1.

[301] Felix Krueger. Trim galore: A wrapper tool around cutadapt and fastqc to consistently apply quality and adapter trimming to fastq files, 2012. Version 0.6.10.

[302] Alexander Dobin, Charles A. Davis, Felix Schlesinger, Jorg Drenkow, Chris Zaleski, Sonali Jha, Philippe Batut, Mark Chaisson, and Thomas R. Gingeras. Star: ultrafast universal rna-seq aligner. *Bioinformatics*, 29(1):15–21, 2013. doi: 10.1093/bioinformatics/bts635.

[303] Yang Liao, Gordon K. Smyth, and Wei Shi. featurecounts: an efficient general purpose program for assigning sequence reads to genomic features. *Bioinformatics*, 30(7):923–930, 2014. doi: 10.1093/bioinformatics/btt656.

[304] Michael I. Love, Wolfgang Huber, and Simon Anders. Moderated estimation of fold change and dispersion for rna-seq data with deseq2. *Genome Biology*, 15(12):550, 2014. doi: 10.1186/s13059-014-0550-8.

[305] Davide Risso, Katja Schwartz, Gavin Sherlock, and Sandrine Dudoit. Gc-content normalization for rna-seq data. *BMC Bioinformatics*, 12(1):480, 2011. doi: 10.1186/1471-2105-12-480. RUVSeq package: Version 1.36.0.

[306] Tammar Hussein Ali, Amar Mousa Mandal, Thorsten Heidelberg, and Rusnah Syahila Duali Hussen. Sugar based cationic magnetic core–shell silica nanoparticles for nucleic acid extraction. *RSC Advances*, 12(22):13566–13579, 2022. doi: 10.1039/D2RA01139E.